EVALUATION, RATING, AND NUMERICAL MODELING OF A SHOCK MITIGATION SEAT FOR HIGH-SPEED CRAFT BASED ON LABORATORY SINGLE IMPACT TESTING

By

Darren Benn

Bachelor of Science in Engineering – Mechanical Engineering
University of Nevada, Las Vegas
2012

Master of Science in Engineering – Mechanical Engineering
University of Nevada, Las Vegas
2015

A dissertation submitted in partial fulfillment
of the requirements for the

Doctor of Philosophy – Mechanical Engineering

Department of Mechanical Engineering
Howard R. Hughes College of Engineering
The Graduate College

University of Nevada, Las Vegas
May 2024

UNLV | GRADUATE COLLEGE

Dissertation Approval

The Graduate College
The University of Nevada, Las Vegas

March 21, 2024

This dissertation prepared by

Darren Benn

entitled

Evaluation, Rating, and Numerical Modeling of a Shock Mitigation Seat for High-Speed Craft Based on Laboratory Single Impact Testing

is approved in partial fulfillment of the requirements for the degree of

Doctor of Philosophy – Mechanical Engineering
Department of Mechanical Engineering

Douglas Reynolds, Ph.D.
Examination Committee Chair

Brendan O'Toole, Ph.D.
Examination Committee Member

Mohamed Trabia, Ph.D.
Examination Committee Member

Woosoon Yim, Ph.D.
Examination Committee Member

Nader Ghafoori, Ph.D.
Graduate College Faculty Representative

Alyssa Crittenden, Ph.D.
Vice Provost for Graduate Education & Dean of the Graduate College

Abstract

High-speed craft (HSC) are utilized in military and para-military maneuvers that are usually conducted in harsh environments. The Special Warfare Combatant-craft Crewmen (SWCC), a sub-unit of the United States Naval Special Warfare Command (NAVSOC), use an advanced HSC, known as the Combatant Craft Assault, to conduct coastal patrol and interdiction, and for infiltration and exfiltration of Navy SEALs. The United States Coast Guard, and the Drug Enforcement Agency (DEA), employ HSC for maritime patrol and to pursue 'go-fast' boats operated by contraband runners. In most of these intense applications, the mode of operation of the HSC results in planing. Planing occurs when the weight of the craft is largely supported by hydrodynamic lift, as opposed to hydrostatic lift. That is, the force that is normal to the fluid flow, not the buoyancy force (upthrust), is the force that sustains the partially immersed craft. The severity of these operations, in conjunction with the planing phenomena, create extreme dynamic environments that subject the HSC occupants to mechanical oscillations and shock pulses due to wave slam events. A wave slam is the violent impact between a waterborne craft and an incoming wave, and the shock created by the impact is the predominant cause of musculoskeletal injuries sustained by HSC operators and passengers.

Over the years, shock mitigation seats have been installed in HSC to diminish the rate of injury among on-board personnel. The consensus is that the design of a shock mitigation seat is based on finding a balance between comfort (from the seat cushion material) and shock mitigation capability. However, the varying characteristics of shock loads experienced at sea, makes it challenging for seat manufacturers to develop a seat that performs satisfactorily across the response spectrum of interest. In addition, currently, a universally accepted measurement system to classify, or rate, shock mitigation seats does not exist. Consequently, it is difficult for potential shock mitigation seat clientele to make an informed decision when considering seats for a specific operating environment. Ultimately, the goal of this study was to develop a repeatable procedure to quantify the performance capabilities of a shock mitigation seat that would facilitate identifying its operational envelope.

In addition, this endeavor also sought to develop a computer based numerical model of the system to validate the empirical results, and to characterize the dynamic response of the seat. The test protocol was based on requirements presented in a proposed ISO Standard, as well as guidance developed from research that was conducted by the United States Naval Surface Warfare Center Carderock Division (NSWCCD). However, en route to accomplishing the objectives, two questions – the answers to which were integral to the outcome of the study – had to be addressed.

The first query explored if the use of a single impact drop tower was a plausible method to simulate the rapidly applied vertical shock that is associated with a wave slam event experienced by an HSC. The NSWCCD has recommended using a mass-spring-damper model as the basis for the analytical representation of a shock mitigation seat. Hence, the second inquiry aimed to verify if the [HSC]-[seat-occupant]-[wave] global system could be appropriately modeled using the mass-spring-damper analytical representation of the seat.

Testing revealed that a drop tower, with certain hardware configurations, was a feasible option to simulate the vertical shock that is associated with a wave slam event. The tower was fully capable of testing to a severity threshold level of four (6.12 g), according to the recommended testing levels for military and commercial craft outlined in the ISO and NSWCCD documents. Using the tower, the seat was rated for use in vessels ranging from HSC Class 3 to HSC Class 4-3 for operating conditions that match severity threshold level four. The mass-spring-damper model proved to be a credible approach to the analytical representation of the shock mitigation seat.

A numerical analysis, conducted with SDOF and 2DOF models based on the mass-spring-damper concept, produced simulated acceleration data that agreed with the experimental data collected during the drop tests. The simulated acceleration and position data was effective in validating the empirical data, and a consolidated analysis using both the SDOF and 2DOF approaches provided an acceptable characterization of the dynamic response of the seat.

Acknowledgements

First, I would like to thank my Lord and Savior, Jesus Christ, for his continued guidance and blessings. I would like to thank Dr. Douglas Reynolds for his support and advice during this process. I would like to express my appreciation to Dr. Brendan O'Toole, Dr. Mohamed Trabia, Dr. Woosoon Yim, and Dr. Nader Ghafoori for agreeing to serve as members of my committee.

Thank you to Dr. Perrin for your guidance with Matlab®. Finally, a special thanks to Jeff Markle for going above and beyond to help me with getting the test hardware setup in the laboratory.

Thank you all.

Table of Contents

List of Tables

List of Figures

Chapter 1. High Speed Craft and Shock Mitigation

1.1 Background

In the past decade, a heightened focus has been placed on the repeated reports of musculoskeletal injuries sustained by the crew of military operated High-speed craft (HSC), attributed to the mechanical shock pulses caused by wave slam events. A research survey of Special Boat Operators (SBO) conducted by the United States Navy (USN) Naval Health Research Center, revealed that 64.9% of SBO operators reported at least one injury [1]. In the Community of Practice (CoP), several concepts have been proposed that address the initiative to reduce the effect of shock pulses on HSC crew members. The proposals range from retrofitting the deck of HSC with shock mitigating matting to redesigning the hull structure. However, the primary focus of these approaches was the HSC structure and not necessarily the shock mitigation seat system. Shock mitigating deck mats do not benefit seated occupants, and they are more effective in attenuating whole-body vibrations (WBV) rather than rapid changes in rigid body acceleration. Structural hull modifications are an effective course of action, but that approach does not represent a cost-effective solution. Therefore, shock mitigation seats are generally considered to be a direct and effective way to structurally isolate HSC occupants from the effects of shock pulses due to wave slam events.

The design of most shock mitigation seats is based on finding a balance between comfort and shock mitigation capability. However, the different classes of HSC have different shock mitigating requirements. Also, varying operational environments result in varying shock load characteristics. Thus, the challenge for seat manufacturers is to develop a seat that performs satisfactorily across the diverse classes of HSC as well as the varying operational environments. In addition, there is no current universally accepted measurement system to classify or rate shock mitigation seats. Consequently, it is difficult for potential shock mitigation seat clientele to make an informed decision when considering seats for a specific operational environment. Therefore, the objective of this study was to evaluate and rate a production line shock mitigation seat for use in specific operational environments. Subsequently, a numerical model of the seat was also developed.

In the upcoming sub-section of this chapter, the discussion will continue with a brief contextual history of when shock mitigation seats were first installed in naval combatant craft, and a summary of the types of shock mitigation seats that are currently manufactured will be covered. A subsequent sub-section will address the current concern within the CoP regarding the testing and evaluation of shock mitigation seats and an account of how that issue served as the impetus behind this study will be presented. Finally, the research objectives, the scope of this research, and the dissertation outline will follow.

1.2 Shock Mitigation Seats

High-speed craft (HSC) operating in rough open waters encounter wave impacts that can subject the occupants to unsafe conditions that result in discomfort and/or injury. High-speed Planing Boats (HSPB) are a class of United States Navy (USN) HSC in which the hull is designed so that the craft is mostly supported by hydrodynamic lift. The result is the occurrence of planing, an event in which the stern of the boat is partially immersed in the water and the bow of the boat is above the surface of the water. In certain extreme naval operational environments, the mode of operation for some of these boats results in a launch and free fall sequence of events [2]. On an encounter with a precursor head wave, the HSPB experiences a period of free fall, after which the stern of the craft enters the water first. This event is followed by a downward movement of the bow. The downward drive of the bow causes a forward acceleration into the incoming wave, leading to a bow impact with it. The result is an upward thrust in the bow accompanied by a rapid surge in vertical acceleration. Those sequence of events form the components of a wave slam and are the source of the shock pulses that lead to injury among the crew.

Documentation of shock mitigation seats being installed in naval combatant craft dates back to 1975 [3]. That early design concept was developed and patented by Pickford, Mahone, and Wolk for use in USN gun boats. The patent was described as a *"*mount for a chair that is exposed to rapid low-acceleration slams and intermittent high-acceleration shocks*."* The system consisted of two fundamental elements.

A spring to return the seat to its neutral position, and a hydraulic, or pneumatic, dashpot to absorb shocks. Figure 1-1 is an illustration of the sketch for US3912248A, the patent for the seat developed by Mahone et al.

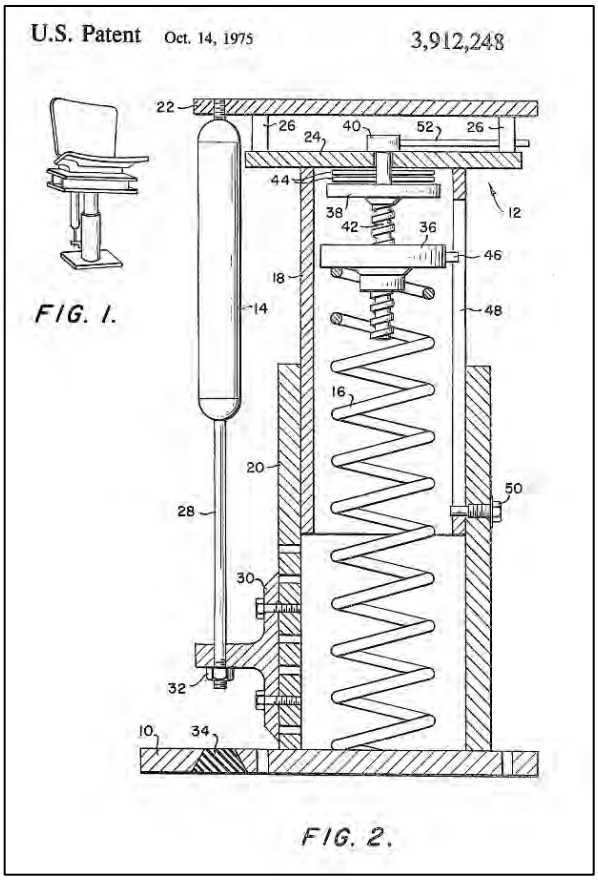

Figure 1-1: Schematic for Early Shock Isolation Seat [3]

While the seat form has progressed, present day concepts still employ the two primary functional components of a spring and a damper. The elements that have evolved in the contemporary designs revolve around the seat cushion material and the method by which the shock mitigating capability is implemented. One manifestation of the change in form is the jockey seat. In contrast to a conventional 'chair'

configuration in which the torso is near vertical to the deck and the upper legs are horizontal to the deck, the jockey seat is shaped like a saddle and occupants are required to straddle the seat with the knees slightly bent, and the entire body in a near vertical position. Other design updates include armrests and footrests. Figure 1-2 depicts an example of a jockey seat, and Figure 1-3 is a seat designed in the standard 'chair' form. Both seats were manufactured by Ullman Dynamics.

Although the response of the payload occurred above the seat cushion, the exploration of seat cushion technology was outside the scope of this analysis and is not addressed in this report. The three types of shock mitigation seats, also known as seat suspension systems, include active (semi and fully), adaptive, and passive systems. In the following section, a description of each of the three types of seats will be covered. The advantages and disadvantages of each system will be stated, after which the discussion will segue into introducing the concern that fueled the motivation behind this study.

Figure 1-2: Ullman Dynamics Jockey Shock Mitigation Seat

Figure 1-3: Ullman Dynamics Atlantic Crew Bolster Shock Mitigation Seat

1.2.1 Active Seat Systems

Active systems are the most complex of the three design concepts. The term ‘active’ refers to the system’s ability to dynamically adjust its shock mitigation capabilities based on the demands of the operating environment. Therefore, an external energy source is required to operate active systems. The category is sub-divided into semi-active and fully active systems based on where the energy is expended.

Semi-active systems employ a spring and a damper element just as the original concept shown earlier. However, the external energy source is required to continuously control the motion damping in real time. Essentially, the energy is consumed in actively changing the damping coefficient. An example of a semi-active concept are seats that use Magnetorheological (MR) damper fluid. The damper, which contains

the MR fluid, houses a magnetic coil. The energy source is used to alter the magnetic field which in turn changes the rheological properties of the MR fluid. The fluid can be manipulated from a free-flowing state with a linear viscosity profile to a semi-solid state with a more complex profile [4]. Fully active systems sometimes have more intricate elements than semi-active systems and often include sensors.

In fully active systems, some of the supplied external energy goes directly towards modifying the motion of the seat to counteract the motion of the environment. Certain designs deviate from the common spring-and-damper elements and utilize active rack and pinion concepts [4]. Sensors are employed to provide input to the system allowing the system to 'read' the environment and respond accordingly. Often, fully active systems possess shock mitigation capabilities in more than one degree of freedom. The complexity of design, the presence of electronic components, and the dependency on an external power supply make active seat systems expensive and a less attractive option to potential patrons. Hence, passive and adaptive seats are the more widely utilized shock mitigation seats.

1.2.2 Adaptive Seat Systems

Adaptive seat systems closely match the design of the early concepts in that they are usually comprised of a spring and a hydraulic, or pneumatic, damper. These systems do not employ sensors, and do not require an external power supply.

The adaptive characteristic stems from the fact that the stiffness (or damping) of the system can be adjusted. A typical means to modify the stiffness is by adjusting the pre-tension in the spring. Damping is modified by increasing, or decreasing, the internal pressure of the damper. Adjustments to the suspension system are made prior to use depending on the weight of the occupant and the expected operating conditions. The advantage of using an adaptive system is it offers the option to adjust the seat suspension to suit anticipated conditions before operation. However, the drawback is that if the operating conditions are not as predicted, the seat may actually amplify unwanted motion effects. The test seat for this research was designated as having 'progressive' damping by the manufacturer. However, its characteristics fell

within the adaptive system category. The notion that adaptive seats may magnify rather than mitigate shock pulses is also a concern associated with passive systems.

1.2.3 Passive Seat Systems

In terms of the fundamental structural components, passive suspension seats are the most closely related design to the early concept. The systems employ a spring and a hydraulic or pneumatic damper. It is the simplest form of shock mitigation seat systems. Thus, there are no means to adjust the stiffness of the system, there are no sensors or electrical components, and the system does not require an external power source. The simplicity of a passive system makes it the most commonly installed shock mitigation seat in HSC. However, the inability to adjust the stiffness (or damping) of passive systems is a downside. In the next section, the discussion introduces the setback associated with passive seats (and adaptive seats). The conversation explores the possible reasons and proposed solution for the predicament, and the mission statement that drives the motivation behind this study is introduced.

1.3 Motivation for this Study

As prevalent as passive seats (and adaptive seats) are in their use in HSC, such systems are not without their detractors. The main criticism is that, in some environments, these systems have been observed to amplify rather than attenuate shock loads. Observations notwithstanding, the issue may reside in how those seats are used. In other words, different operating environments produce different shock loads. Hence, a seat that mitigates shock loads in one environment with an occupant of a specific weight, that same seat may accentuate the shock loads generated in another environment with the same occupant, and therein lies the dilemma.

Several factors influence the operating environment, including the sea state, and the class of the craft. Naval military special operations, such as search and rescue (SAR), often require deployment in poor

weather conditions with rough to high sea states. Waves associated with rough to high sea states can range in height from 2.5 m to 6.0 m (8.2 ft to 19.7 ft) [5]. Waves within that range can generate severe impacts, especially in head seas. In addition, a mission may begin in a slight to moderate sea state (wave heights from 0.49 m to 2.5 m (1.6 ft to 8.2 ft)), but weather conditions my deteriorate to yield rough to high sea states. Therefore, a seat may be required to perform satisfactorily over a range of sea states. The other factor that defines the operating environment is the class of the craft.

A generic yet generally accepted craft classification scheme has been established to specify the severity of the environment that may be encountered when a certain type of craft is used [6]. The system assigns vessels to a class based on its intended use, as well as engine power. The severity of use for a specific class dictates if the use of a shock mitigation seat is required to protect on-board personnel. There are four classes of vessels with lengths ranging from 5 m to 10 m (16.4 ft to 32.8 ft). Of course, there are vessels outside of this range that may have similar requirements, but at sea trials in vessels within this range were used to establish the classes. The classes are itemized below.

1) Class 1: Low Speed Commercial/Leisure
2) Class 2: High Speed Commercial/Leisure
3) Class 3: Search and Rescue
4) Class 4: Military

Class 1 craft do not routinely operate in poor weather with rough to high sea states, and do not typically require the use of shock mitigation seats. Class 2 vessels may operate at speeds in excess of 20 knots (23.02 mi/hr.) in poor weather, so the potential for wave slams is more common. Hence, the use of shock mitigation seats in Class 2 craft is warranted. Class 3 and Class 4 craft can exceed speeds of 30 knots (34.52 mi/hr.) and are extensively operated in rough to high sea states. These vessels routinely encounter severe wave slams, so shock mitigations seats are required to avoid crew injury and to sustain the mission objectives. A seat that displays reasonable performance in a Class 2 craft may perform inadequately in a Class 3 or Class 4 HSC. The preceding information supports the fact that, shock load characteristics can

vary based on the operational environment and the class of vessel. This leads to the problem that operators have in choosing a seat that performs well across a variety of use case scenarios.

A proposed solution was to develop a procedure that would outline a method to quantify the shock mitigation characteristics of a seat and provide a means to categorize the seat for use in a specified application prior to installation in a craft. Therefore, the ambition of this work was to develop a repeatable laboratory testing procedure to quantify the performance capabilities of a shock mitigation seat that would facilitate identifying its operational envelope and its rating for use in specified classes of vessels. In the upcoming section the research scope and objectives are introduced. A related subtopic explores the benefit of developing the laboratory test procedure. Finally, the chapter closes with an outline of the report, which includes a brief look ahead to the topic of HSC dynamics and shock load characterization during wave slam events, which opens Chapter 2.

1.4 Research Scope and Objectives

1.4.1 Research Scope

The focus of this analysis is to conduct a series of laboratory single impact drop tests on a production line shock mitigation seat. The seat design did not include armrests or a footrest. The drop test was used to simulate a wave slam event with a single impact. During the drop tests, an inert payload was used to simulate the mass of a seated occupant. Nonetheless, modeling a human occupant to ascertain and analyze biomechanics and the effect of a mechanical shock pulse, or motion induced fatigue (MIF), on the biological health of a human was not within the breadth of this study. The primary goal was not to model a seat occupant, but to cultivate an analytical approach that would be conducive to evaluating the shock mitigating capabilities of the seat, and then develop a metric that would serve as a gauge of the seat's performance. The hope was that when the metric was matched to a particular criterion, it would provide insight that makes the assessment of the seat for a specific application more consequential.

All the research objectives were formulated for the main purpose of establishing an analytical protocol that aided in evaluating and rating the seat. As will be revealed later, that meant gleaning ideas from different schools of thought and combining parts of those philosophies to form a single executable methodology.

1.4.2 Research Objectives

The objectives were devised to achieve two primary high-level goals. The first goal was to appraise the ability of the drop tower to simulate the shock pulse associated with a wave slam event to test shock mitigation seats. The secondary aim of that task was to develop a protocol to evaluate to what level of consistency the drop tower performed that function. The second goal was to create a computer based numerical model that could be used to simulate the response of the seat, as well validate the empirical results generated from the drop tests.

The test protocol was partly based on requirements presented in a proposed International Organization for Standardization (ISO) standard ISO/WD 19470.6, *Laboratory evaluation of marine seat shock isolation* [7]. The ISO standard covered test hardware, instrumentation, data collection and processing, and other relevant test criteria. Test requirements presented in research that was conducted by the US Naval Surface Warfare Center Carderock Division (NSWCCD [2, 6]) were also incorporated into the analysis. Some aspects of the test procedure from the ISO standard were similar to the NSWCCD requirements, while their perspectives on other technical elements differed, so the intent was to combine the two approaches to create a hybrid protocol that represented a strategy that included the best test practices. The numerical model, based on the NSWCCD's recommendation of representing the seat as a mass-spring-damper mathematical concept, was created to corroborate the results generated from the experimental seat tests. Also, it allowed seat parameters, such as the spring constant and damping coefficient, to be modified to determine the effects on the simulated response of the system.

The aspiration was to ascertain whether the seat system could be adequately modeled using the single degree of freedom (SDOF) or two degree of freedom (2DOF) mass-spring-damper concept. The hope was that the model would accept the experimental test system state data as an input, and in return, generate an output response that would match the response of the experimental test system within an acceptable margin. The overarching goal was to develop a repeatable laboratory testing, and validation, procedure that would enable identifying the operational envelope of a shock mitigation seat prior to being installed in a HSC. A complimentary aim was to illustrate the viability of laboratory testing of shock mitigation seats in lieu of at sea testing.

At sea trials of shock mitigation seats is a method of testing that is conducted within the CoP. However, there are some barriers to at sea seat trials that do not affect laboratory testing.

At sea trials require some logistical effort to procure the use of boats and to enlist crew. Thus, one drawback is that equipment and personnel may not be readily available. Also, some look-ahead planning is required to schedule trials during the right sea state. Further, due to the unpredictability of wave motions, it is difficult to forecast when the ideal conditions will occur, and repeatability cannot be ensured. In contrast, laboratory testing, specifically single impact drop testing, does not require the coordination of boats and crew, does not solely rely on data collected from at sea trials as input data, and offers repeatability. Therefore, it is an appealing option for testing and evaluating shock mitigation seats. In the next section of this chapter, the report outline is summarized, and a brief synopsis of Chapter 2 is given.

1.5 Report Chapter Outline

There are seven subsequent chapters after this introductory chapter. Chapter 2 opens with a more in-depth look at the dynamics of a HSC in a wave slam, and the key parameters that define the shock load environment are introduced. An ensuing section goes over a survey of the literature in the canon. In addition to a review of past relevant work, that section explores ISO/WD 19470.6 and the applicable NSWCCD testing requirements in greater detail. In Chapter 3, the experimental test setup is presented, a

comprehensive account of the test elements such as hardware, data acquisition & processing, and a seat rating scheme are also covered. The chapter includes the steps for a test procedure based on the test criteria and the best test practices taken from the ISO standard and the NSWCCD sources, as well as an outline for procedures inherent to the specific test system.

The governing equations for the mass-spring-damper analytical concept are introduced in Chapter 4. Also, the state space representation of a dynamic system and the Newmark-Beta direct integration method used to develop the numerical model are addressed. In Chapter 5, the question of whether a single impact drop tower was a tenable method to replicate the shock that is associated with a wave slam event is resolved. The retort is presented through an exploration of the statistical analysis of the empirical results, and an effort to provide a rating or classification of the seat is presented. Additional ancillary topics in Chapter 5 includes using the impact method as a means to conduct a cursory evaluation of the system, and an analytical modal analysis procedure is discussed.

Chapter 6 explores the outcome of the undertaking of developing the numerical model based on the mass-spring-damper concept. A comparison of the simulated acceleration response generated by the state space and Newmark-Beta approaches is provided. The chapter also attempts to elucidate the inquiry of the validity of using the mass-spring-damper idea to analytically depict the seat, specifically, the notion of whether the seat could be appropriately characterized by the SDOF or 2DOF mass-spring-damper concept. The narrative pivots to the conclusion and closing remarks of the study in Chapter 7, and the proposal for future work is covered in Chapter 8.

Chapter 2. High-Speed Craft (HSC) Dynamics and Shock Pulse During Wave Impacts

In this chapter, the discussion opens with a look at the motion of a HSC and the resulting shock pulse from a wave slam event. The HSC rigid body acceleration associated with a wave slam is introduced. The discussion details the motion of the craft and introduce the dynamic factors that were used to characterize and analyze the change in vertical acceleration associated with a shock pulse. The recommended analytical representation that was used to correlate the analysis of shock mitigation seats with the HSC-wave global system, the mass-spring-damper model, is also covered. A later section of the chapter provides an account of the survey of the prior studies that have been conducted to evaluate the characteristics of shock mitigation seats for use in HSC applications.

Amongst the documentation that was reviewed, the two most common investigative approaches to conducting the seat evaluation process were drop testing to simulate the wave impact, and computer based numerical modeling using at sea test data as the input files. Some analyses employed both methods. For research that aimed at simulating the shock pulse caused by a wave slam, the use of a drop tower seemed to be the commonly practiced technique. Alternate approaches included using test structures equipped with actuator driven pistons that were fed with accelerometer data generated from at sea trials. Most of the analytical models were all based on the dynamic response of mass-spring-damper mathematical models of either one or two degrees of freedom. As part of the literature review, the chapter covers the two major sources that were consulted for the study presented in this report.

The International Organization for Standardization (ISO), Standard ISO/WD 19470.6 “Laboratory evaluation of marine seat shock isolation” covers test hardware, instrumentation, data collection and processing, and other relevant test criteria. Although the document was submitted by the Technical Committee (ISO/TC 108) at the time it was consulted, it was a working draft that was still in the review phase and was not considered an official ISO Standard. However, it did reference other established ISO standards. Several technical reports and memorandums covering the testing and evaluation of shock isolation seats by the Naval Surface Warfare Center Carderock Division (NSWCCD) can be found in the

literature. The topics of the NSWCCD documents included the characterization of HSC motion mechanics and wave impact dynamics, laboratory testing requirements, and the definition of seat performance parameters. The test measures from those reports were used as a framework for the test protocol and analysis discussed herein. This chapter closes with a summary of the vital topics that were discussed and a look into Chapter 3, which covers the test procedure and the steps that were developed to conduct the experimental analysis.

2.1 High Speed Craft Dynamics

In some military applications, the mode of operation of a HSC can be aggressive, usually involving high speeds in rough seas. In some cases, the stern of the craft remains immersed in the water while the bow pitches upward above the surface of the water about a rotational point closer to the stern. When that motion occurs, the craft experiences the phenomena of planing. Planing occurs when the weight of the craft is largely supported by hydrodynamic lift, as opposed to hydrostatic lift. The force that is normal to the fluid flow, not the buoyancy force (upthrust), is the force that sustains the partially immersed craft. When an HSC encounters a wave (of significant height), the forceful impact between the wave and the hull is known as a wave slam. The wave slam induces a rapid, and sudden, change in the upward vertical acceleration of the craft, which is characterized by a shock pulse. Data collected by the United States Navy (USN) from at sea trials have shown that, during a wave slam, the HSC is exposed to a series of events that subject the craft to motion in all six degrees of freedom at its longitudinal center of gravity (LCG) [2]. The translational motions (heave, surge, and sway) and the rotational motions (pitch, roll, and yaw) all occur during the series of events. However, some of the motions (or a combination of them) contribute more to the acceleration (and displacement) profiles of the craft. According to observations made by the NSWCCD, the contributions from the various modes of motion result in different features of the craft acceleration profile, which relate to three classes of wave slams.

Alpha Slam

An Alpha wave slam is characterized by a negative 1 g vertical free fall just prior to wave impact. This is usually due to an encounter with a low impact precursor wave resulting in a launch and free fall event. At the end of the free fall, the craft enters the water stern first, followed by a bow down motion that is accompanied by a forward increase in longitudinal acceleration. At that point, the craft contacts the incoming wave. The impact heaves the bow of the craft upward with a rapid surge in vertical acceleration characterized by the shock pulse. Alpha wave slams are usually the most severe of the wave slam events, with acceleration peaks in excess of 3 g. Figures 2-1 and 2-2, taken from [2], depict the craft acceleration profile during the low impact precursor wave and the subsequent Alpha slam, respectively. In the figures, the red curve represents the vertical acceleration, and the green curve is the longitudinal acceleration.

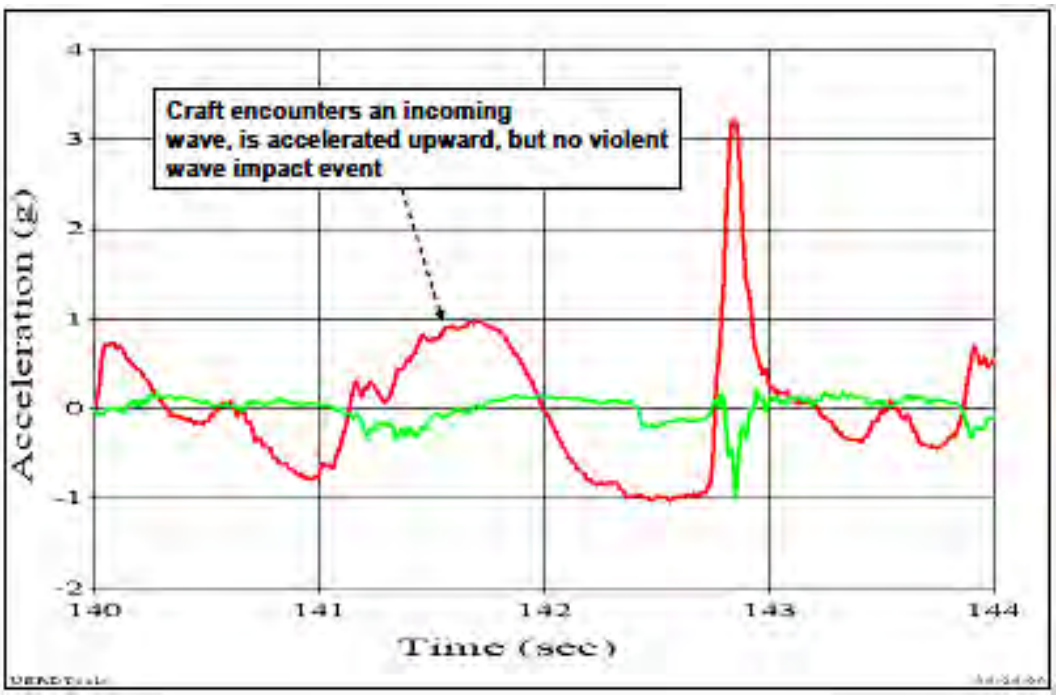

Figure 2-1: Acceleration Profile of HSC During Precursor Wave Encounter [2]

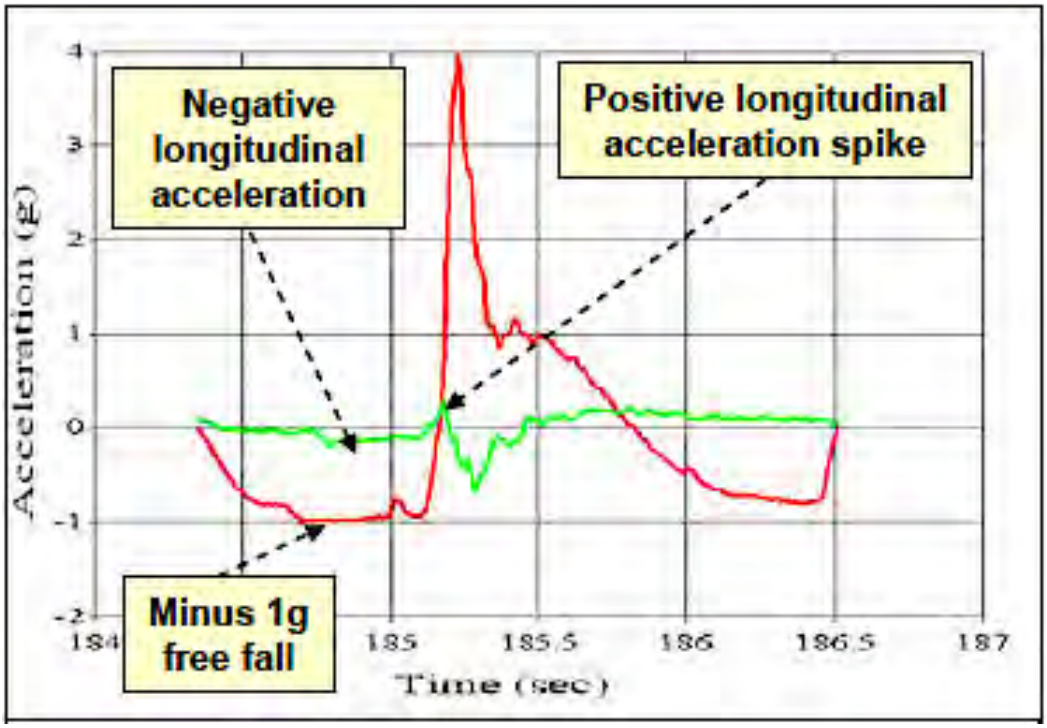

Figure 2-2: Acceleration Profile of HSC During Alpha Wave Slam [2]

Bravo Slam

The Bravo wave slam is observed as having a negative 1 g vertical free fall just prior to wave impact, similar to the Alpha slam. However, there is no sign of the craft entering the water stern first. The craft undergoes a decrease in longitudinal acceleration, and there is a slight downward rotation of the bow prior to impacting the incoming wave. Bravo slams are typically less severe than Alpha slams, with peak acceleration values between 2 g and 3 g. Figure 2-3 [2], shows the craft acceleration profile during the Bravo wave slam series of events. In the figure, the red curve represents the vertical acceleration, and the green curve is the longitudinal acceleration.

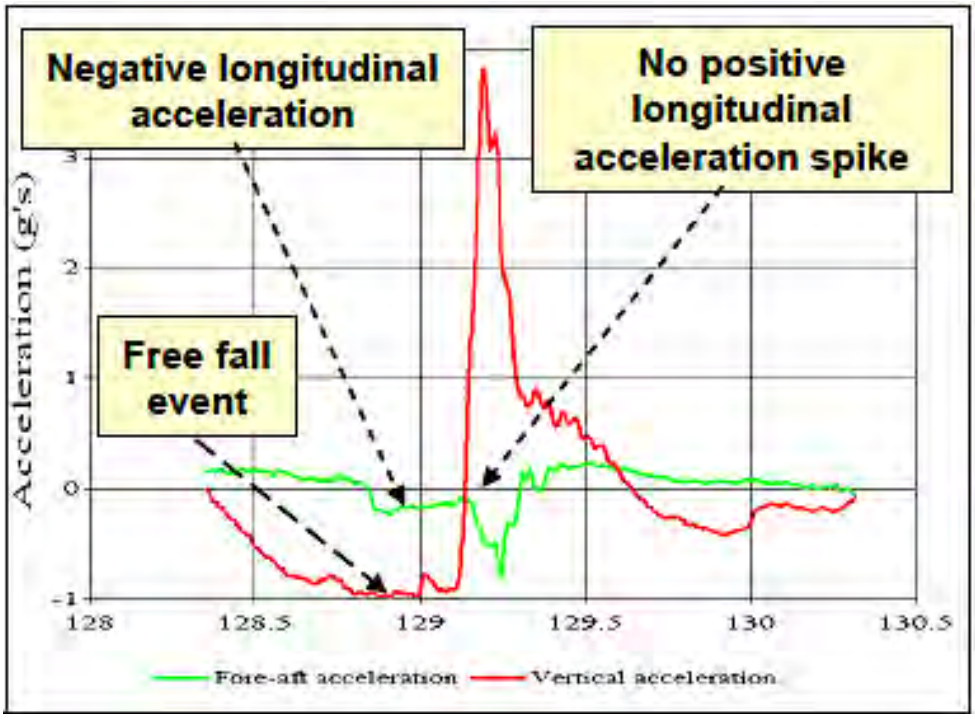

Figure 2-3: Acceleration Profile of HSC During Bravo Wave Slam [2]

Charlie Slam

The Charlie wave slam is identified by a steady nominal increase in longitudinal acceleration just before the impact. Similar to the Bravo slam, there is no sign of the craft entering the water stern first. Preceding the impact with the incoming wave, there is a slight downward rotation of the bow, with a minor (or no) occurrence of a free fall event. As there is a marginal vertical drop at the LCG of the craft, the energy generated during a Charlie slam is attributed to the forward velocity of the craft in the horizontal plane as it impacts the incoming wave, which creates the resultant shock pulse. The Charlie slam is the least severe of the three classes of wave slams. Figure 2-4 [2], shows the craft acceleration profile during the events of a Charlie slam. In the figure, the red curve represents the vertical acceleration, and the green curve is the longitudinal acceleration. The acceleration responses in Figures 2-1 to 2-4 were taken from at sea trials, and, in each figure, the spike in the vertical acceleration profile (red curve) signified the shock pulse associated with the wave slam.

Certainly, the motions described by the three wave slam events do not encompass every dynamic environment that a HSC may experience. However, they do account for the predominant force acting on the craft during a head on encounter with a wave, and there are two important factors to consider when examining the figures.

First, the shape of the shock pulse is similar for all three types of wave slams. It is somewhat reminiscent of a half-sine pulse. Second, and probably less obviously, is that the motion associated with the half-sine pulse is craft heave. The dynamic, vertical load associated with craft heave is the basis for the suggested use of the mass-spring-damper model as an analytical representation for the analysis of shock mitigation seats. The reason is that the vertical load can be readily simulated in that model. In the next section, the significance of the half-sine pulse for use in identifying the key factors used to analyze shock pulse acceleration data is covered.

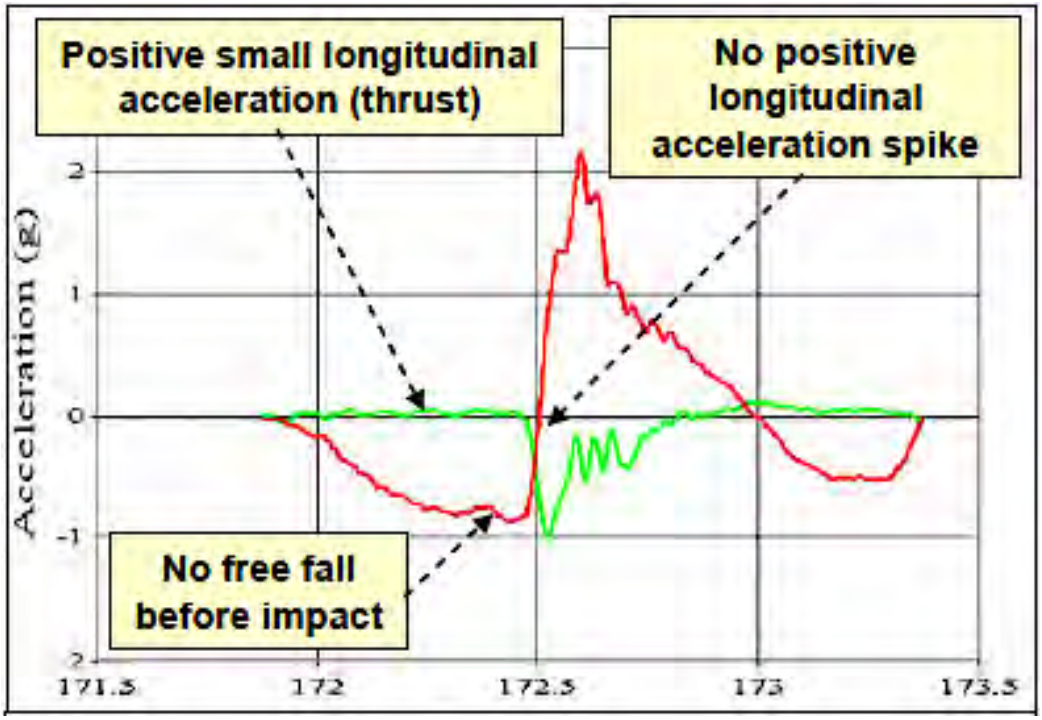

Figure 2-4: Acceleration Profile of HSC During Charlie Wave Slam [2]

2.1.1 Half-Sine Pulse

It is broadly accepted within the community of practice that the quasi-half-sine shape of the pulse in the acceleration response profile for a HSC during a wave impact is a suitable tool to form the basis for analyzing the performance of shock mitigation seats. In its research, the National Aeronautics and Space Administration (NASA) identified five factors on which human tolerance to rapidly applied accelerations depend on [8]. The factors are:

1) The direction in which the acceleration force is applied.
2) The magnitude of the acceleration force.
3) The duration of the acceleration force.
4) How rapidly the acceleration force is applied.
5) How the occupant's body is supported during the acceleration.

Four of the elements listed by NASA can be captured in a half-sine pulse curve. The acceleration force direction, magnitude, duration, and rate of applied acceleration (jerk) can all be determined in the half-sine pulse curve. The importance of these four parameters is that they can be used to establish a correlation between the empirical results from laboratory seat testing, with published severity threshold levels. The rate of the onset of the applied acceleration force, which is the derivative of acceleration (jerk), is presumed to be a second order phenomenon and its effects are insufficiently applicable to drop testing. Nevertheless, it is mentioned here for completeness. In regard to the seat cushion, NASA stated that firm seat padding/upholstery that distributes the forces over the largest surface area is the optimum choice to attenuate the applied shock load. The properties of the cushion for the test seat were not available, and an analysis of the seat cushion itself was not part of the scope of this study. Hence, as such, an exploration of the characteristics of the seat cushion material was not conducted.

The following sections provide some insight into the relevance of the force direction, magnitude, and duration in the analysis of an HSC motion during a wave slam event, and how they are captured in the half-sine pulse curve.

Acceleration Direction and Magnitude

As alluded to earlier, the direction of interest for the peak acceleration was in the vertical direction. In relation to the motion of the HSC, the vertical motion was equivalent to craft heave. The corresponding load for a shock mitigation seat was the upward force at the seat base transmitted through the spring-damper assembly. Vertical acceleration values of 7 g have been observed during at sea trials in rough seas with craft ranging in lengths from 10.06 m to 25 m (33 ft to 82 ft), and weights ranging from 6350.29 kg to 52616.71 kg (14,000 lb to 116,000 lb) [2]. However, there have been reports of wave slam impacts that measured above 20 g. The curves shown in Figures 2-1 through 2-4, display both direction and magnitude. The pulse duration is also accounted for in those plots of the HSC acceleration time histories.

Acceleration Pulse Duration

In at sea trials, several factors influence the duration of the impact, including the height of the wave, and the speed and size of the HSC. In general, severe wave impacts occur over a shorter duration, around 0.1 to 0.2 seconds. The less severe impacts transpire over a longer time frame, from approximately 0.1 to 0.4 seconds. Later, in laboratory single impact drop testing, the duration of the pulse is determined by the type of impact media (defined as a deformable surface) located at the base of the tower. The shape of the structure on the underside of the tower platform, that impacted the deformable surface, also influenced the pulse. In this study, the structure on the underside of the platform is defined as the pulse-shaping device. The minimum impact duration severity threshold for laboratory testing of shock mitigation seats as stated in the reference documents was 0.10 seconds.

Change in Velocity

The change in velocity was not explicitly referenced as one of the five factors listed earlier, but its calculation did serve as an optional analytical tool. During at sea trials, the change in velocity is a measure of the craft's kinetic energy of its vertical motion (heave) right before it impacts the incoming wave. In single impact laboratory drop testing, the change in velocity was replicated by relating the potential energy corresponding to a designated drop height to the kinetic energy of the system just prior to impacting the

deformable surface. Alternatively, the area under the acceleration pulse curve can be calculated, as that value represented the change in velocity.

The change in velocity was a valuable variable to calculate because it related the peak pulse acceleration value with the pulse duration, and provided additional information used to evaluate how much energy was absorbed in the impact media. A sample plot taken from a drop test conducted for this study, showing four of the five factors, is presented in Figure 2-5. Notice the similarity to the curves displayed in Figures 2-1 through 2-4 and the overall resemblance to a half-sine pulse (green dashed line). The relatively linear section from 0.4 to 0.45 seconds represents a segment of the -1 g period of free fall prior to the simulated HSC water entry.

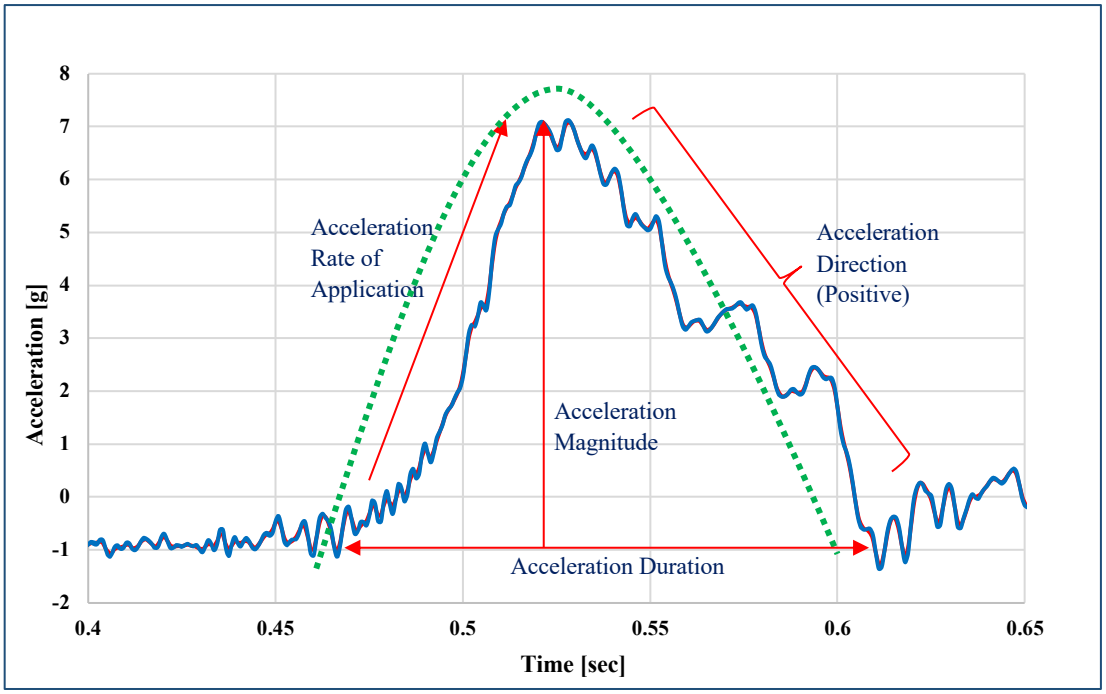

Figure 2-5: Partial Acceleration Time History for Drop Tower Seat Test

In a later section, when the documents on which the test protocol for this study is based on are covered, the role of these parameters is addressed. In the upcoming section, the mass-spring-damper model recommended for use as the mathematical representation of a shock mitigation seat is discussed.

2.2 Mass-Spring-Damper System

Envisioning the NSWCCD's recommendation of representing the seat as a mass-spring-damper for the purpose of an analytical assessment of the performance of a shock mitigation seat, required correlating the components of the model to the actual system. The HSC-seat-wave global system can be considered to be comprised of three primary sub-elements. The sub-elements include the wave, which provided the dynamic load, the deck of the HSC, which served as the point of application for the dynamic load (base), and the seat-occupant component, which served as the mass. Dissecting the HSC-wave global system into sub-parts, made it plausible to equate each subcomponent to an element of the mass-spring-damper model.

2.2.1 Single Degree of Freedom (SDOF) Mass-Spring-Damper

There were two primary reasons the mass-spring-damper model was an appropriate tool to assess the performance characteristics of a shock mitigation seat. First, the model facilitated investigating the response of a system to an input load, which benefited laboratory single impact testing of shock mitigation seats. Second, system variables, such as the spring and damping characteristics, could be modified in the numerical model to determine the effects on the system's response. The common, albeit less sophisticated mass-spring-damper model for investigating the response of a shock mitigation seat was the single degree of freedom (SDOF) model.

The elements of a SDOF model, and how it responded to an input, could have readily been used to correlate the sub-elements of the HSC-wave global system to a laboratory test of a shock mitigation seat. The classic SDOF system usually consists of a mass supported by a spring-damper assembly mounted on a

fixed base structure. It was imperative, and understood, that the mass of the fixed base structure was much greater than the combined mass of the human occupant and seat mass supported by the spring-damper assembly. Therefore, the dynamics (motion) of the collective mass did not influence the dynamics of the fixed base. To create the association between the HSC-wave global system and the shock mitigation seat, the analogous elements of each had to be matched to the SDOF model.

The deck of the HSC was be represented by the fixed base structure of the SDOF model. That was likened to a large rigid surface, such as the floor, on which the seat testing equipment was mounted on in the laboratory setting. The spring-damper assembly of the SDOF model was fittingly represented by the spring-damper assembly of the shock mitigation seat. The mass of the SDOF model was equated to the combined mass of the human occupant and the seat. Finally, in a laboratory environment, the impact force of the wave slam was simulated by using a drop tower. The impact generated when the seat was dropped from a designated height onto the impact surface, created the upward vertical acceleration associated with a wave slam. Using a drop tower to simulate the wave slam impact, assumed collinearity between the upward vertical force vector and the spring-damper assembly of the seat. As the impact occurred at the base of the seat system, that version of the SDOF model was considered to be a base excited model. Figures 2-1 to 2-5 show that neither actual at sea wave impact responses, nor drop tower impact responses perfectly simulate the quintessential, rounded half-sine pulse. However, those triangular shaped pulses fully captured the relationship between the pulse amplitude and the pulse duration in the exact way a pure half-sine pulse would. Moving forward, the triangular shaped pulses in the acceleration time histories are referred to as acceleration pulses.

Figure 2-6 illustrates an example of a SDOF model that was used to investigate the performance of the shock mitigation test seat, and to form the basis of the numerical model used for the computational analysis when the human occupant and seat were considered a lumped mass. The SDOF model is explored in greater depth in a later chapter, and the differential equations of motion that characterized the model are derived. In that later section, the notion of whether the SDOF model trivialized the seat analysis is also considered. Next, a brief account of a few prior studies that have been conducted to evaluate the

characteristics of shock mitigation seats for use in HSC applications is provided. The ISO and NSWCCD documents that provided guidance for this study are also covered.

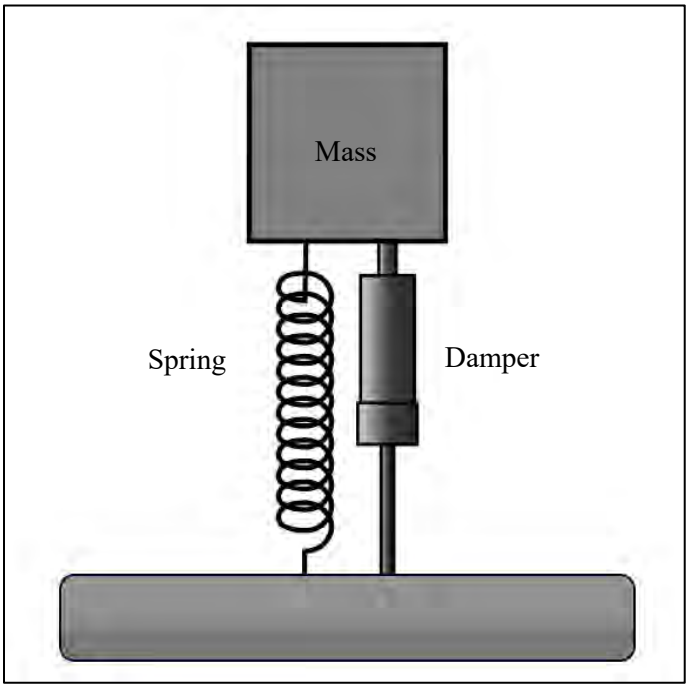

Figure 2-6: Single Degree of Freedom Mass-Spring-Damper System [9]

2.3 Survey of Relevant Research

The literature indicates that the testing of shock isolation seats to ascertain their capability to diminish damaging impact loads to occupants in human operated machinery dated as far back as the mid-to-late twentieth century. In 1965 and 1966, the United States Army Aviation Systems Command conducted drop tests to determine the response of UH-1B/D helicopter seats to vertical impact loads of 5 g and 15 g [10]. Recall, Chapter 1 mentions that seats designed to mitigate the effect of shock due to wave impacts were introduced to USN gun boats in 1975. However, it was not until a significant amount of time had

elapsed, possibly driven by the rise in reported crew injuries, that more attention was dedicated to researching the shock mitigation properties of seats intended for use on HSC. One of the early and heavily referenced studies focused on developing a reliable laboratory test method for evaluating shock isolation seats.

Drop Table

The study examined the shock environment created on HSC, the effects of prolonged exposure to shock on the human body, and methods to mitigate the effects of shock due to wave impact on HSC [11]. The main goal of that study was to devise, and validate, an inexpensive repeatable laboratory procedure to evaluate shock isolation seats for use in HSC. The test method employed a gravity drop table, with a stiffened platform, as the test machine. That method was deemed as an adequate technique to simulate the shock incurred on HSC due to wave slam. Once released for free fall, the base of the platform struck an absorbing moderator (Skydex® tiles) at the end of its motion. Thus, generating a shock pulse similar to those recorded on HSC. The test seat was described as an adaptive system, although it was equipped with a 5-volt power supply to adjust the damping. Lumped mass weights, ranging from 81.65 kg to 92.99 kg (180 lb to 205 lb), were used to represent the mass of the seat occupant, and drop heights ranged from 0.15 m to 0.46 m (6 in to 18 in).

The report concluded that a high level of repeatability (test-retest reliability) was achieved with the use of the drop table configuration in conjunction with the proposed test method. The drop table was able to generate shock pulse values similar to those observed on an HSC with shock values over 9 g. In addition, the test seat was successfully evaluated using the drop table with the test method. Another research effort that involved a single impact drop tower was performed later on. However, that study focused less on establishing testing procedure and more on seat evaluation.

A drop tower located at the Defence Research and Development Canada (DRDC), was used to evaluate a jockey style suspension seat [12]. The experimental component of that test was similar to the method described earlier with the exception of the hardware used to simulate the human occupant and the material used for the impact media (It was called the absorbing moderator in the study).

In contrast to using inert masses, a 78 kg (171.96 lb) anthropomorphic test device (ATD) outfitted with accelerometers was used to simulate the human occupant. The impact material used to generate the half-sine pulse was Alcore PAA-CORE™ aluminum honeycomb. A separate study using the same test equipment was conducted later [13]. In that analysis, five heights ranging from 0.836 m to 2.931 m (2.74 ft to 9.62 ft) were used for the drop heights. The thickness of the aluminum honeycomb was kept constant at 0.1016 m (0.33 ft), but two different density values of 25.63 kg/m^3 to 72.08 kg/m^3 (1.6 lb/ft^3 and 4.5 lb/ft^3) were used. The main objective of that study was to evaluate the shock mitigation capabilities of the seat. To quantify the performance of the seat, a metric known as the shock response spectra (SRS) mitigation ratio $MR_{(SRS)}$ was used. The $MR_{(SRS)}$ was simply the ratio of the SRS for the acceleration history of the seat to the SRS of the base input's acceleration history. An additional project that employed a drop tower to simulate a single wave impact placed an emphasis on special techniques to post process the empirical data as a means to establish a viable test procedure.

A drop tower with a similar design concept as the previous studies was used to simulate a single wave impact and resultant shock pulse to the test seat. However, the ideology behind that research was to post process the seat response signals to generate impulse response functions (IRFs), which were subsequently used as input for the Eigensystem Realization Algorithm (ERA) [14]. The ERA was used to extract the modal parameters of the seat. The report compared the modal parameters of two different seats (passive and adaptive) and concluded that the indicators generated by the ERA could be cataloged with other seat performance metrics to form a reference for seat characterization. These studies were experimental approaches that relied on a drop table to create the input to the shock mitigation seat, but they did not involve any computer modeling of the seat itself. In other research, a combined approach was taken that relied on experimental seat testing as well as the formulation of a numerical model.

Hydraulic Actuation System and Numerical Modeling

This research involved an experimental exercise and a numerical analysis, both of which relied on input data derived from at sea trials. The objective of the study was to construct a 'shake rig' that would be

used to excite the seat system, and to develop a computer model that simulated the response of the seat to user inputs [15].

The test structure used to simulate the wave impact was not a drop table; instead, a rigid frame with a moveable inner carriage (shake rig) was constructed. The test seat was mounted on the moveable inner carriage, and the bottom of the structure housed a hydraulic actuation system that drove a piston. In order to replicate wave slam events, accelerometer data from USN at sea trials was used as the input to the hydraulic actuation system that drove the piston. In turn, the piston drove the moveable inner carriage on which the seat was mounted, thus, providing the excitation to the seat. The at sea trial data was collected from three separate USN HSC, each of a different class. The test seat was described as an adaptive system equipped with a 5-volt power supply to adjust the damping, and lumped masses ranging from 68.04 kg to 113.4 kg (150 lb to 250 lb) were used to simulate the occupant's mass. The computer model was based on a two degree of freedom mass-spring-damper system.

The seat coil suspension system represented the first spring-damper element, while the seat cushion served as the second spring-damper element. Matlab Simulink® was used to model the equations of motion for the two degree of freedom system. The computer model was used to verify the experimental data generated by the shake rig and relied on the same input data that was used for the shake rig actuator. However, it offered the added benefit of determining the effect of changes made to the spring rate and the damping value on the system's response. Thus far, the review of prior relevant work has covered research that incorporated an experimental element for testing shock mitigation seats. However, some past research was solely numerical.

Numerical Modelling

Within the community of practice (CoP), there were some projects in which the research on shock mitigation seats focused exclusively on numerical modeling. One such study sought to develop a numerical model of a shock mitigation seat that would accommodate an efficient method for seat analysis and seat parameter tuning. The research involved the development of a model that investigated the effects of angular, lateral, and longitudinal input motions to the seat, as well as the effect of rail-bearing friction on the seat

from drop tower testing [16]. The study evaluated four seats, and the analysis included modeling the visco-elastic properties of the seat cushions and the occupant-seat interactions. The model required two types of input data, including configuration data and input motion data.

As there was no component of the analysis that included experimental testing of the seats, the configuration and input motion data was obtained from previously conducted seat testing. The configuration information included impulse response functions (IRF) that were derived from processing the seat response data generated from the single impact drop testing conducted in a separate research effort. The input motion data were obtained from the seat responses from previously conducted at sea trials.

In this section, past work that focused on studying the characteristics of shock mitigation seats was covered. The review revealed that in lieu of real time at sea trials, there were two major approaches to seat analysis. Early research involved experimental laboratory testing that relied on impact drop towers (or drop tables) to simulate the shock pulse associated with wave slam events. In more recent studies, numerical modeling of the seat system has become more prevalent. Customarily, the numerical analyses have used either seat response data generated from previously performed experimental seat testing or data from at sea trials for input to the numerical model to validate the empirical results. Then, some endeavors incorporated both experimental and numerical components. That approach seemed to be the most comprehensive method, as it offered the benefit of generating empirical data for comparison with numerical results. In addition, seat parameters that could not be experimentally altered, could be modified in the numerical model to determine the effect of the changes on the simulated response. The analysis that formed the subject of this report utilized that comprehensive approach. The details of the computer-based analysis are covered in a later chapter. In the next section, the reference information that was consulted to foster the development of the experimental test protocol is discussed.

2.4 Requirements for a Test Protocol

The consistent theme in the literature was that the use of a drop tower was an accepted method to simulate the shock pulse associated with wave slam events during the laboratory testing of a shock mitigation seat. Yet, what was not apparent were the steps of the implemented test methods and the reference documentation on which the methods were based. In addition, the objective of some tests was to establish the repeatability of the drop tower procedure, while others evaluated the characteristics of the seat. However, there was no indication that any of those efforts focused on evaluating the performance traits of the seat to determine its rating for use in a specific class of HSC. That is where the ideology of this analysis deviates from those studies. In this section, the test method and analysis recommendations from three reference documents are explored.

The upcoming information will cover the guidance for the laboratory testing of a shock mitigation seat. Reference information was gleaned from three documents. One document was from the International Organization for Standardization (ISO), ISO/WD 19470.6, titled *Laboratory evaluation of marine seat shock isolation*, which will be identified as ISO-19470 [7]. Also, two documents from the Naval Surface Warfare Center Carderock Division (NSWCCD). One document was titled NSWCCD-80-TR-2015/010 Rev A, *Laboratory Test Requirements For Marine Shock Isolation Seats*, denoted to as NSWCCD-80 [6], and the other was NSWCCD-83-TM-2013/26, *The Simulation of Wave Slam Impulses to Evaluate Shock Mitigation Seats for High-Speed Planing Craft*, referred to as NSWCCD-83 [2]. At the time this report was written, the ISO-19470 document was still in the review stage and had not been officially released. Nonetheless, its suggested test requirements aligned well with those outlined in NSWCCD-80 and NSWCCD-83.

All three documents provided recommendations on test methods and practices, instrumentation systems, data processing, and test severity threshold levels. The ISO-19470 document outlined procedures that were applicable to passive seats installed in HSC that were typically less than 30 m (98.425 ft) in length.

Its recommended test procedures did not consider the effect of the seat occupant using the arms or legs to actively brace against impact. The scope of both NSWCCD reports was also restricted to passive seats.

The NSWCCD reports were pertinent to passive seats, with or without footrests, installed in HSC ranging from 7 m to 30 m (22.9 ft to 98.425 ft). The reports specifically stated that the suggested methods were not considered applicable to jockey seats. The three documents offered clarifying statements on content covering the forces acting on a HSC during a wave slam, seat attributes other than shock isolation, and the potential for occupant discomfort or injury.

The references noted that while forces in directions other than the vertical direction were present in wave slam events, the most severe contribution to the shock associated with a wave slam was in the upward vertical direction, and as such it was the emphasis of each report. In addition, each reference stated that seat attributes associated with seat ergonomics, seat cushion material, comfort, operational temperature, and response to non-vertical impact loads were beyond the scope of its account. Finally, the standard and other two reports affirmed that the proposed test methods did not address or provide methods to analyze the adverse health effects to human occupants from exposure to shock due to wave slam impacts.

The laboratory seat testing procedures proposed in the reference documents did not purport to address all the possible real world dynamic environments that an HSC could encounter. Instead, they formed a compendium of the best practices based on prior research that, when implemented, was in service of quantifying the seat performance and determining its subsequent rating for use in an HSC. The following section begins with the hardware items, including instrumentation, then follows with test severity thresholds, data processing, and finally the method to quantify shock mitigation.

2.4.1 Test Hardware

With the exception of a few select items, the majority of the test requirements and procedures in the ISO-19470 and NSWCCD-80/83 documents were in accordance with each other. Therefore, in the interest of clarity and when necessary, only the differences are highlighted.

Test Seat

As stated in the reference documents, the test seat should be a production line seat, or a seat that accurately represents a seat that is installed in currently operating HSC. The seat shall not be modified or refined prior to testing. If seat modifications are necessary, the effect of the changes on the dynamic performance of the seat or its shock mitigation capabilities should be negligible. Further, the modifications should be annotated in the test procedures. A full description of the seat, including dimensions, sub-parts, weight, and operational characteristics, such as position adjustment options, should be provided.

The adjustment options (if available) should be set as if an occupant with the specified payload weight were occupying the seat. The seat should be rigidly mounted to the test platform as it would be to the deck of the craft.

Payload

The payload simulating the human occupant should consist of inert rigid masses. It is acceptable to place individual ballast weights or sandbags inside a larger rigid container. The payload should be securely fastened to the test seat with the seatbelts or a seat harness, so that it does not become loose during testing. For seats without seatbelts or harnesses, ratchet-type straps can be used to secure the payload. However, the payload should be restrained in such a way as to allow at least 25 mm (0.98 in) of vertical movement between it and the seat surface. It shall be positioned on the seat so that its center of mass is within 10 mm (0.39 in) of the vertical axis of the motion of the spring-damper assembly. It is recommended that three different payload weights be tested.

There is some discrepancy between the way ISO-19470 and NSWCCD-80 assign values to the three weight categories. The ISO-19470 standard listed the three weight classes as light, medium, and heavy, while the NSWCCD-80 document listed the weights by population percentile. The NSWCCD-80 contended that the weights should correspond with the 5^{th}, 50^{th}, and 95^{th} percentile weights of male occupants. For tests of seats that are used in HSC intended for both male and female crew members, it was recommended that the 5^{th} percentile male weight was replaced by the 5^{th} percentile female weight. In addition, neither document specified whether the listed weights should include the weight of equipment

worn (or carried) by the seat occupant. From a procedural perspective, both reference documents advised that for a test to qualify as valid, three successive drops at each weight should be conducted. Table 2-1 itemizes the three weight categories recommended by two of the documents.

Table 2-1: Payload Weight Requirements for Seat Test [6, 7]

Payload Weight Requirements							
ISO-19470			NSWCCD-80				
Category			Population	Male		Female	
	(lb)	(kg)	Percentile	(lb)	(kg)	(lb)	(kg)
Light occupant	138.9	63	5th	135.8	61.6	109.3	49.6
Medium occupant	207.2	94	50th	184.0	83.5	145.2	65.9
Heavy occupant	275.6	125	95th	248.6	112.8	195.3	88.6

The use of an anthropomorphic test device (ATD) was recommended by NSWCCD-80. However, ATDs usually have a fixed weight, and as three separate occupant weights are stipulated by the requirements, the use of several ATDs may not be cost effective.

Drop Test Device

Both documents recommend the drop tower method to simulate the shock pulse associated with a wave slam impact. The requirements stated that the seat with the payload should be mounted to a rigid platform and dropped from a height designated for the specific impact severity. NSWCCD-80 stated that the impact surface should be able to deform in order to produce the desired pulse shape, amplitude, and duration. ISO-19470 provided some informative guidelines for the design concept of the drop tower, and both documents propose suggestions for the shape of the base of the platform that contacts the deformable impact surface.

As an example for a design, ISO-19470 cited that the platform should be constructed of steel plates with dimensions of 510 mm by 510 mm (20.1 in by 20.1 in) and a thickness of 60 mm (2.4 in). The platform should have a mass of at least 66 kg (145.5 lb) and should be guided by a four-leg wire sling. One leg of

the sling should be attached to each corner of the platform. The four-leg wire sling should not come into contact with the test seat. The two documents cite a test platform with an impact wedge attached to its underside as an acceptable mechanism to simulate the desired properties of the shock pulse reminiscent of the wave slam impact. Sand was suggested as the impact medium/deformable surface.

According to both documents, the platform with the wedge attached to the bottom should be dropped into a box of dry loose sand. Prior tests have shown that when a wedge impacts the sand, following a period of free fall, a shock pulse, similar to those created during an HSC encounter with a wave slam, can be generated. ISO-19470 states that the sand should be at least 0.36 m (1.2 ft) deep with a sieve size appropriate to produce the desired pulse shape, duration, and amplitude.

Figure 2-7 is a picture, available from both documents, showing a platform with a wedge attached to the bottom and a box filled with loose sand to serve as the impact surface.

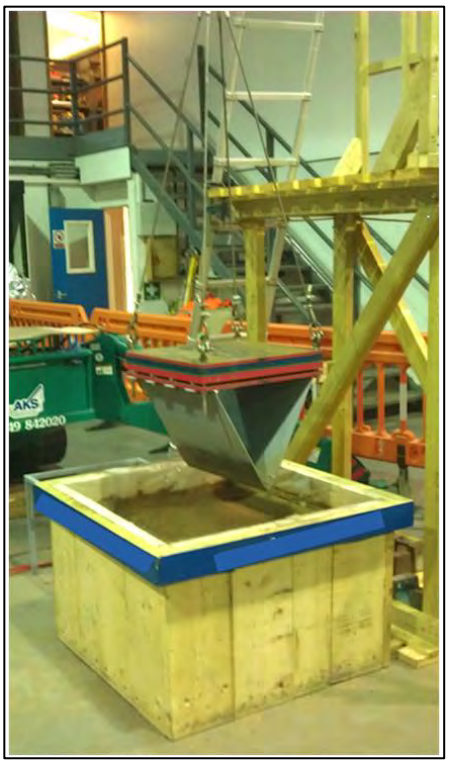

Figure 2-7: Example of Sand and Impact Wedge used for Drop Tower [6 ,7]

Instrumentation

It was recommended that piezoresistive or micro electro-mechanical systems (MEMS) accelerometers be used because of their dc response and the ability to operate at a frequency range of 0 Hz. ISO-19470 states the accelerometer frequency response should have a range of dc to 250 Hz, a nominal full-scale range of at least ± 20 g, and a minimal sensitivity of 50 mV/g or greater. NSWCCD-80 suggests a range of dc to 1000 Hz, a nominal full-scale range of ± 25 g, and a minimal sensitivity of 50 mV/g or greater. At least two accelerometers should be used in the test setup. One should be placed on the test platform, at the base of the test seat, as close as possible to the load path. The second should be placed on the surface of the test seat cushion between the inert payload and the seat cushion. It should be positioned directly under the payload center of mass and as close as possible to the vertical axis of the seat motion (collinear with the seat spring-damper assembly). An optional third accelerometer can be located on the seat pan above the spring-damper assembly and as close as possible to the load path. Comparing the response of the accelerometer located between the payload and the cushion with the response of the accelerometer installed on the seat pan offers insight into the effects of the cushion. In the drop-tower-seat coordinate system, vertical motion upward corresponded to the positive Z direction.

Data Acquisition System

There was some difference between the two references with regard to the properties and configuration of the data acquisition (DAQ) system. The consensus was that the DAQ system should be capable of analog-to-digital conversion. The ISO-19470 document postulates that the minimum measurement bandwidth should be 80 Hz with a sampling rate of 512 samples per second. A minimum measurement bandwidth of 100 Hz and a minimum sampling rate of 512 samples per second was proposed by NSWCCD-80. An anti-alias filter was required by both sources, and ISO-19470 required that all recorded accelerations should have the offset adjusted so that the recorded acceleration at rest was zero. Table 2-2 lists the DAQ configuration criteria for each reference.

Table 2-2: Data Acquisition System Requirements for Seat Test

Data System Requirements		
DAQ Property	Setting	
	ISO-19470	NSWCCD-80
A/D Bit rate	Minimum 12-bit	Minimum 16-bit
Bandwidth	dc to 80 Hz	dc to 100 Hz
Sample rate	Minimum 512 s/s	Minimum 512 s/s
Minimum resolution	0.1 m/s^2 (0.010 g) *	0.001 g (0.009 m/s^2) **
Anti-alias filter	Fixed low-pass hardware pre-filters	4-pole Butterworth/100 Hz low-pass
Offset at rest	0 g	0 g
* Based on ± 20 g accelerometer with 12-bit DAQ system.		
** Based on ± 25 g accelerometer with 16-bit DAQ system.		

2.4.2 Data Processing

The overarching goal for testing a shock mitigation seat was to evaluate its performance characteristics, and subsequently rate it for use in a specific class (or classes) of HSC. However, as was discussed earlier, not all wave slams are created equal. Therefore, it stands to reason that a measurement system to scale the severity (intensity) of the shock pulse should be developed. The scale, commonly referred to as the 'Test Severity Threshold' with the aid of the amplitude and duration of the shock pulse provided a means to gauge laboratory generated shock pulses against observed at sea shock pulses. In the upcoming sections, the topic pivots to the requirements for processing the test data, and the subject of a seat performance parameter is introduced.

Test Severity Thresholds and Tolerance Envelopes

A test severity threshold level for a single impact drop tower test was determined by the peak amplitude and impact duration recorded in the acceleration response pulse. The documents suggested that it was standard practice for the acceleration data generated from a drop tower to be post-processed using a low-pass 4-pole Butterworth filter. However, there was some discrepancy between the documents regarding the filter cut-off frequency. The ISO document suggested a cut-off frequency of 20 Hz, while the

NSWCCD-80 report recommended a 100 Hz low-pass filter. Thus, the pulse amplitude and duration information for the severity threshold designation was not garnered from raw acceleration data.

The documents listed six test severity threshold levels. Each level had the same acceleration pulse duration stipulation of 100 ms (0.10 s), but the peak acceleration ranged from 3.05 g to 10.19 g (3.00 g to 10.00 g for NSWCCD-80). In addition to the severity threshold levels, the reference documents also prescribed tolerance envelopes.

The tolerance envelopes established one of the criteria for a valid drop test. The values for the envelopes were based on the low-pass filtered (cut-off frequency of 20 Hz) vertical acceleration recorded at the base of the seat. The tolerances were intended to envelope the seat base movement that occurred due to spring-damper oscillation after the impact. Table 2-3 itemizes the criteria for the peak input acceleration amplitude (pulse) and pulse duration for the six severity thresholds from each reference document. ISO-19470 also presented the nominal drop height to achieve each severity threshold. The tolerance envelopes can be seen in Table 2-4. In both sources, the variable, 'A', represented the peak low-pass filtered (cut-off frequency of 20 Hz) vertical acceleration recorded at the base of the seat. The values in Table 2-4 can be viewed as coordinates for the points that plot the trace of the envelope. The variable T_2, as presented by ISO-19470, was derived by way of (2-1).

Table 2-3: Test Severity Thresholds for Drop Tower Test [6, 7]

Test Severity Threshold						
	ISO-19470				NSWCCD-80	
Threshold Level	Peak Input Acceleration (g)	Impact Duration (s)	Drop Height (ft)	(m)	Peak Acceleration (g)	Impact Duration (s)
6	10.19	0.10	6.78	2.07	10.00	0.10
5	8.15	0.10	4.34	1.32	8.00	0.10
4	6.12	0.10	2.44	0.74	6.00	0.10
3	5.09	0.10	1.69	0.51	5.00	0.10
2	4.08	0.10	1.08	0.33	4.00	0.10
1	3.05	0.10	0.61	0.18	3.00	0.10

Table 2-4: Acceleration Tolerance Envelopes for Drop Tower Test [6, 7]

Acceleration Tolerance Envelopes for Drop Tests				
Time (s)	ISO-19470		NSWCCD-80	
	Acceleration (g)		Acceleration (g)	
	Lower Envelope	Upper Envelope	Lower Envelope	Upper Envelope
-0.075		0		0
-0.02		1.15 A		1.2 A
0.02		1.15 A		1.2 A
$\mathbf{T_2}$	-2			
0.06		0.6 A		0.6 A
0.01	-2			
0.5	-0.15	1.5		0.15
≥ 0.6	-1.5	1.5		0.15
-0.09			-2	
(A+2)/(2A)				
0			A	
0.09			-2	
(A+2)/(2A)				

$$T_2 = \frac{0.1}{\pi} \sin^{-1}\left(\frac{-2}{A}\right) \tag{2-1}$$

2.4.3 Quantifying Shock Mitigation Performance

Since the goal of testing a shock mitigation seat is to evaluate its shock mitigation characteristics, there must be an established method to quantify the seat's performance. Some techniques take the compression of the human spine into consideration to ascertain the seat occupant's risk of injury. However, if the objective is to solely evaluate the seat mitigation performance, without analyzing the adverse health effects on the human occupant due to exposure to shock impact, then the collectively accepted method within the CoP is to calculate the mitigation ratio (MR).

The MR is the quotient of the ratio of the low-pass filtered maximum response acceleration of the seat to the low-pass filtered maximum base input acceleration. There are two versions of the MR currently

in use. The distinction stems from the information used in the ratio. In the following paragraphs, the MR approaches is introduced, beginning with the rigid body acceleration form of the formula.

MR: Peak Acceleration

The MR based on the peak acceleration was simply the ratio of the low-pass filtered seat rigid body (RB) peak response acceleration to the low-pass filtered RB peak base input acceleration [17]. The MR_{PEAK} was given by (2-2). Based on (2-2), if the MR was less than unity (1.0), then mitigation occurred; if the MR was equal to or greater than 1.0, then no mitigation or amplification of the input occurred. The response of a shock mitigation seat plotted as acceleration versus time does not accurately portray the motion phenomena related to frequency. For example, an acceleration plot may show that at some point in the time history, the peak response acceleration of the seat may exceed the peak base input acceleration. However, an alternate form of data processing (and visualization) may reveal that the seat peak response occurred outside the frequency range of interest. Hence, a MR that utilized frequency-based information was an additional analytical tool.

$$MR_{PEAK} = \frac{Seat\ RB\ peak\ response\ acceleration}{Base\ (Deck)\ RB\ peak\ input\ acceleration} \tag{2-2}$$

MR: Shock Response Spectra

The deck of a HSC during operation is a very dynamic environment. The crew and equipment are subjected to different sources of mechanical vibration, occurring across a spectrum of frequency ranges. Although, it was not the intent of this study to analyze the effects of whole-body vibration (WBV) on the seat occupant, an assessment of the seat would not be complete or valid if the frequency range of interest for a human occupant was not identified and established.

According to ISO-2631-1, a study that examined the effects on the comfort of a seated individual exposed to WBV, the frequency range of interest for the human body response is 4 Hz to 8 Hz [18]. Therefore, in the analysis of shock mitigation seats, it was customary to evaluate the performance of the

seat within a range that encompassed the natural frequency of the body. Hence, an alternate approach used to derive the MR was the shock response spectrum (SRS), as it offered insight to the behavior of the system across a specified frequency spectrum.

The SRS was a representation of the maximum responses of an array of linear SDOF systems to a base excitation such as a shock, or other transient base acceleration input. The SRS can be graphically illustrated as a plot of the maximum response of each SDOF system in the array to the specific input versus frequency. The natural frequency of each system is the center frequency of a pre-determined proportional octave bandwidth, and customarily, each system is assumed to have 5% damping. The benefit of using the SRS as an analytical tool was that it was based on SDOF systems, and it accounted for the peak acceleration response of those systems at varying natural frequencies. In that sense, it was aptly suited for analyzing seat systems for which the natural frequency was unknown and for determining the seat behavior in the frequency range of the human body response. One fundamental point to be kept in mind is that the measured (or calculated) SRS did not represent the spectrum of the actual measured impulse. Instead, it was a spectral portrayal of the response of a hypothetical SDOF system that had one or more resonances in the frequency range of interest. The MR_{SRS} was given by (2-3). In the closing section of this chapter, a recap of a few of the important concepts is given and a brief outline of the proposed test protocol is offered. The final thoughts include a look ahead at the upcoming chapter.

$$MR_{SRS} = \frac{SRS\ of\ Seat\ response\ acceleration}{SRS\ of\ Base\ (Deck)\ input\ acceleration} \tag{2-3}$$

2.5 Summary

During transit across rough seas, HSC encounter three categories of wave slam events. An Alpha wave slam is the most severe of the wave slams, inducing sudden upward vertical accelerations in excess of 3 g. Bravo slams have been observed to produce shock pulses in the range of 2 g to 3 g. Charlie slams

are the least intense class of wave slams, and are usually associated with a 1 g sudden, rapid rise in vertical acceleration. Analytically, the HSC-seat-wave global system is comprised of three primary sub-elements. The sub-elements are the wave as the dynamic load, the deck of the HSC as the point of application for the dynamic load (base), and the seat-occupant component above the seat's spring-damper assembly. Based on that premise, the HSC-wave global system can be modeled as a mass-spring-damper system. Throughout a wave slam encounter, HSC experience motion in all six degrees of freedom. However, it is the translational motion of heave (vertical upthrust) that serves as the primary component of the shock due to a wave slam. Using the mass-spring-damper model and exemplifying the heave associated with the shock pulse as a base excitation, laboratory single impact testing was recognized as a valid approach to simulate the shock associated with a wave slam event during the evaluation of shock mitigation seats. Past studies have shown that there are two main approaches to testing and analyzing shock mitigation seats.

Some experimental tests utilized drop towers to simulate the shock pulse. Computer based analytical evaluations of seats relied on numerical methods that used the mass-spring-damper mathematical model as the basis for that technique. There were numerous references in the literature that broached the subject of how an experimental test of a seat should be conducted, but there was little consistency amongst the CoP on the protocol to execute the test.

The three references that were used as guidance for test procedures were the ISO-19470 and the NSWCCD-80/83 reports. Those three documents shared a lot of the same best practices, including procedural test elements, and data processing practices. Thus, the information contained in those sources was used to formulate the experimental test procedure for this study. In Chapter 3, the details of the experimental test procedure are submitted. The chapter follows a similar structure as Section 2.4. It begins with an account of the hardware, including the test seat and the drop tower, and progresses towards detailing the instrumentation and the data processing effort. A small diversion from the flow of Section 2.4 is inserted to cover procedures that were conducted to identify traits inherent to the specific test system. Chapter 3 culminates with a proposed method to rate seats for use on specific classes of HSC based on the holistic approach of the test protocol.

Chapter 3. Procedure for the Experimental Analysis of the Shock Mitigation Seat

This chapter provides details about the experimental test setup and analysis that this report was based on. The framework of the test constituted the test requirements and criteria outlined in the ISO-19470 and NSWCCD-80/83 reference documents. The opening topic introduces the specifics about the hardware elements, including the test seat and the drop tower. Subsequently, the attention shifts to the method that was used for the data processing effort. In the concluding section, the subject transitions to the steps that made up the test protocol and some insight into the seat rating technique is offered.

3.1 Test Hardware

The drop tower used in the experimental analysis was constructed prior to this study and not specifically for this research. The calibration, configuration, and placement of hardware items was based on the recommendations proposed in the three reference documents. In addition to the proposal of using a wedge at the base of the tower platform, tines were attached to the underside of the tower platform for a series of drop tests. In past tests, tines have also been shown to generate acceleration pulses (similar to those shown earlier) on impact with the impact media, which was fine grain sand in this study.

3.1.1 Test Seat

The test seat was a production line shock mitigation seat from Ullman Dynamics [19]. The seat was part of Ullman's Atlantic Crew product line. The seat was manufactured from reinforced plastic, aluminum (5077) and stainless steel (EN1.4462). The cushion was upholstered with marine vinyl (or leather) covering a fire-resistant foam. The seat was not equipped with armrests or footrests. The isolation system was defined as a semi-active progressive shock mitigation system with twin progressive dampers. However, the seat did not require any external power. Therefore, the isolation system possessed qualities

that were more consistent with the characteristics of an adaptive system. Further, unlike some active seats, the test seat was designed to mitigate shock loads in the vertical direction only. The dampers were fabricated from aluminum (5077) and stainless steel (316). The term 'progressive' in the description was based on the fact that they had adjustable compression. The dampers were equipped with an adjustable dial with six levels (1-6) of damping. The manufacturer listed the six damping levels as ranging from soft (1) to stiff (6). The spring was a leaf spring manufactured from composites and stainless steel (316). Information from other unconfirmed sources described the spring as nonlinear. However, no actual values for the characteristics of the spring, nor for the dampers, was provided by the seat manufacturer. Chapter 5 provides more insight on the experimental analysis used to determine the spring and damping features of the seat. The spring housing was mounted to a reinforced plastic pedestal, which in turn was bolted to the tower platform via the bolt holes in the base of the pedestal. Table 3-1 itemizes the properties of the seat, Figure 3-1 shows the seat mounted to the platform of the drop tower, and Figure 3-2 depicts the spring and damper of the suspension system. The inset is an image of the dial showing the six settings.

Table 3-1: Properties of Ullman Dynamics Atlantic Crew Shock Mitigation Seat

Specifications of Ullman Dynamics Atlantic Crew Seat	
Property	Description
Suspension type	Semi-active progressive shock mitigation*
Spring	Composite and stainless-steel leaf spring
Damping	Twin progressive: 1 - 6 [Soft - Stiff] (Aluminum and stainless steel)
Seat stroke	150 mm - 200 mm (5.91 in - 7.87 in)
Height (Deck to seat cushion)	721 mm (28.38 in)
Base width	426 mm (16.5 in)
Base length	447 mm (17.59 in)
Weight	41.9 kg (92 lb)
Total height	1509 mm (59.41 in)
*System required no external power and had characteristics of an adaptive system.	

Figure 3-1: Ullman Dynamics Test Seat for Experimental Analysis

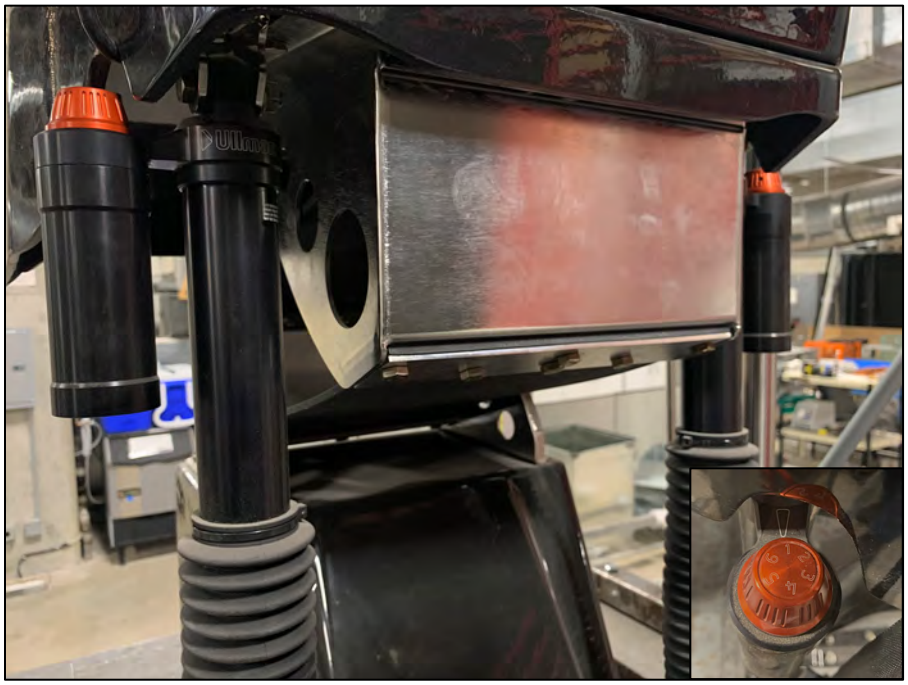

Figure 3-2: Spring and Damper Assembly of the Test Seat

3.1.2 Payload

The payload was made up of lead ballast weights packed into Polyvinyl Chloride (PVC) pipe sections. The payload consisted of three segments fabricated to represent a torso (vertical to the seat cushion) and two legs (parallel to the seat cushion). The upper segment (torso) had a length of 0.479 m (1.573 ft) and a circumference of 0.8636 m (2.833 ft). Each leg portion was 0.2667 m (0.875 ft) in length with a circumference of 0.3619 m (1.1875 ft). The two leg segments were fused to the base of the torso section to form a single unit. The individual ballast weights measured between 4.989 kg to 5.579 kg (11 lb to 12.33 lb). The total number of weights in the torso section was adjusted to modify the weight of the payload. The torso of the payload was secured to the seat with two ratchet straps, one around the top section (circumference) of the tube and the upper part of the seat back, and another around the lower section of the tube and the lower portion of the seat back. Two eye hooks, one on each side, were fastened to the upper lateral sides of the torso cap (lid). Two straps, one through each eye hook, were used to prevent the cap from becoming loose during a drop test. As per the reference material, the payload was secured in such a way that at least 0.025 m (0.08 ft) of vertical movement was allowed between the base of the payload and the rest position of the surface of the seat cushion. The three payload weights were designated based on the 5th percentile of female, and the 50th and 95th percentile weights of male occupants. Table 3-2 lists the three payload test weights, as well as the total weight when the weight of the seat was taken into consideration. Figure 3-3 displays the payload secured to the test seat.

Table 3-2: Payload Test Weights and Total Weight of Payload and Seat

Recommended Payload Test Weights				
Population Percentile	Payload Weight			
	Male (*Women)		Total Weight (including seat)	
	(lb)	(kg)	(lb)	(kg)
*5th	*109.3	*49.6	*201.3	*91.3
50th	184.0	83.5	276.0	125.2
95th	248.6	112.8	340.6	154.5

Figure 3-3: Test Payload Secured to the Test Seat

3.1.3 Drop Tower

The main structural components of the drop tower consisted of a vertical four-post outer frame, a top plate, a moveable platform, and a metal box which housed the impact media (sand) mounted on a bottom plate. The ancillary components included twin guide rails, the hoist frame, and the DC powered hoist. The

tower was predominantly constructed from aluminum parts; though, some components were made from steel.

Each of the four vertical posts that formed the frame was 3.6576 m (12 ft) with a 0.0508 m^2 (0.1667 ft^2) cross section. Approximately 0.4572 m (1.5 ft) down from the top plate, were two horizontal aluminum bars that were used to brace the four vertical posts. One bar was used to brace the two left vertical posts, and the other was used to support the two right vertical posts. The vertical posts were attached to the top and base plates with two 9-bolt pattern gussets at each corner. The top plate was made from an aluminum slab with a planar area of 0.9144 m^2 (3 ft^2) and a thickness of 0.0254 m (0.0833 ft). A hole was cut in the middle of the top plate to house the DC powered hoist. The base plate was also an aluminum slab with the same planar area as the top plate, but its thickness was 0.0508 m (0.1667 ft). The moveable platform was comprised of four separate pieces bolted together.

The platform was basically a square casing with an aluminum upper surface, two steel sides, and a lower steel surface. The total height (thickness) of the platform was 0.1397 m (0.4583 ft). When viewing the platform from the front (positive X direction), the left and right sides were not sealed off with steel plates. The aluminum upper surface was 0.0254 m (0.0833 ft) thick, and it was bolted to the front and back facing steel plates, which were 0.00635 m (0.0208 ft) thick. Holes were machined into the upper plate for the purpose of attaching the seat. In addition, a frame consisting of two vertical steel guide rods (0.00635 m (0.0208 ft) in diameter) and a horizontal aluminum bar were also attached to the upper surface of the platform.

A hook, bolted to the horizontal bar of the hoist frame, was the attachment point for the cable from the hoist. The lower surface of the platform was made from a steel plate with similar dimensions as the top aluminum plate, and it was bolted to the front and back facing steel plates in a comparable fashion. The upper aluminum plate, and the lower steel plate each had a two-dimensional area of 0.9144 m x 0.7874 m (3 ft x 2.583 ft). Hollow, vertically aligned 0.4128 m (1.345 ft) long steel bars were welded to the left and right sides of the platform. Two guide brackets were bolted to each of those steel bars. Each guide bracket moved along a guide rail that was attached to the top and base plates. The guide rails restricted the platform

to vertical motion only (no lateral movement). The platform (with the horizontal bar and guide brackets) had a mass of approximately 270.35 kg (596.026 lb) which complied with the minimum value stated in the ISO reference document. Holes were machined in the lower plate of the platform for the purpose of attaching the steel wedge and the tines pulse-shaping devices.

Using guidance outlined in the reference documents, a steel wedged was designed as the pulse-shaping device to create the acceleration pulse associated with the shock load. The wedge was constructed from steel plates that were 0.6096 m x 0.3556 m (2 ft x 1.1667 ft) and 0.00635 m (0.0208 ft) thick. The base of the wedge was approximately 0.2032 m (0.6667 ft) in width and also 0.3556 m (1.1667 ft) in length. The angle formed by the wedge was approximately 21°. The total weight of the wedge was 30.264 kg (66.5 lb). In addition to the wedge, a series of test were conducted with tines.

Prior tests had proven that tines generated the required acceleration pulse, albeit with a shorter duration. In general, the tines created higher amplitude pulses than the wedge at the same drop height and payload mass, but with shorter pulse durations. The tines were 0.6159 m (2.0208 ft) in length with a cross sectional area of 0.0508 m^2 (0.1667 ft^2). The tines were attached to the underside of the platform with the same bolts used to attach the wedge. Each tine weighed 5.126 kg (11.3 lb). A steel box with height-width-depth dimensions of 0.6096 m x 0.6858 m x 0.7747 m (2 ft x 2.25 ft x 2.542 ft) was mounted on the base plate of the tower to hold the dry, loose sand that was used as the impact surface.

The guidance in the reference documents notwithstanding, visualizing a drop tower as a wave slam simulator seemed like a challenge, but heeding the events of a wave slam event helped establish a correlation between the drop tower dynamics and the wave slam dynamics.

In Figures 2-1 to 2-4, three major elements can be identified, including a period of free fall, a rapidly applied vertical impact, and an acceleration with a high g measurement. In practice, a drop tower replicated those events well. The design of a drop tower inherently allowed for the occurrence of the period of free fall before impact. The vertical impact was applied rapidly, and it was collinear with the seat isolation system, assuring that most of the incoming load was directed to the seat isolation system. In addition, a drop tower, with a significant height, provided a way to simulate high g accelerations. Finally, when the

pulse-shaping device and deformable surface were chosen appropriately, the acceleration pulse shape possessed four of the five characteristics outlined by NASA as a prerequisite for the analysis of rapidly applied acceleration forces. Of course, detractors may contend that a drop tower did not account for the rotational forces (or surge and sway) imparted on the HSC, but it has been clearly documented that the translational, vertical force of heave is the dominant contributor to a wave slam event. Therefore, while the preceding discourse was not meant to advocate for a drop tower, it served to offer an alternate viewpoint. Figure 3-4 depicts the tower with the seat mounted on the platform, the wedge, and the steel box for the sand. Figures 3-5 and 3-6 show the wedge and the tines, respectively.

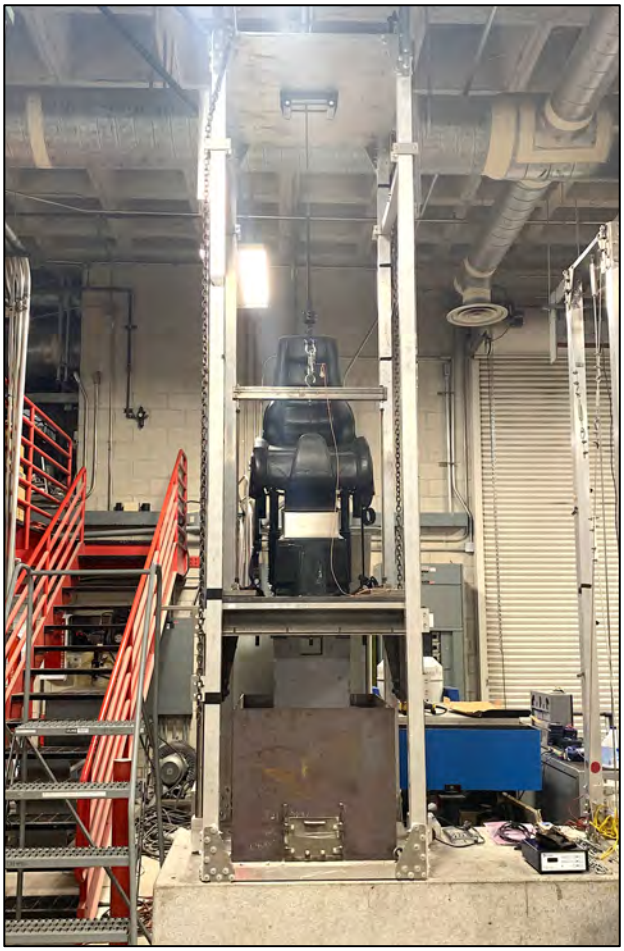

Figure 3-4: Drop Tower used for Single Impact Experimental Tests

Figure 3-5: Wedge Attached to the Underside of the Tower Platform

Figure 3-6: Tines Attached to Underside of the Tower Platform

3.1.4 Data Acquisition and Instrumentation

The main hardware component of the data acquisition (DAQ) system was the Quattro® signal analyzer from Data Physics [20]. The system had a 24-bit ADC resolution (Analog AAF) and a 32-bit sample resolution (Digital AAF). The maximum useful frequency (bandwidth) was 80 kHz. The minimum sample rate capability was <1 Hz, and the maximum was 204.8 kHz. The accelerometers were the micro electro-mechanical systems (MEMS) type with a frequency response of dc to 10000 Hz and a measurement range of ±100 g. The broadband resolution was 0.004 g rms (0.04 m/s^2 rms). Two accelerometers were used during testing. One was placed at the base of the seat pedestal, which served as the input signal. The second one was attached to the payload at a location that represented the base of the spinal column of a hypothetical seat occupant; it represented the response signal. In accordance with the suggested coordinate system layout in the reference documents, the positive Z axis was defined as vertical motion upward, while the X and Y directions were designated as the horizontal plane (parallel to the platform). Positive X was in the direction of the line of sight of a theoretical seat occupant, and positive Y was in the direction to the left of the conjectural seat occupant. The objective was to place the accelerometer located on the seat pedestal as close to the load path as possible.

The load path was considered to be the vertical line (Z axis) through the center of the seat. Hence, in relation to the coordinate system and the horizontal plane parallel to the seat pedestal, the lower accelerometer was approximately located at a position of 0.1715 m (0.56 ft) from the front edge (positive X direction) of the platform. Its Y coordinate was 0.0508 m (0.1667) from the edge of the platform that was considered to be in the positive Y direction. Finally, its Z location was 0 m (0 ft) from the top surface of the platform. Both accelerometers were positioned so that the positive vertical Z axis faced the top of the tower, with approximately 0.721 m (2.365 ft) vertical distance between them. Additional specifications for the DAQ and instrumentation are provided in Table 3-3. The hardware in Table 3-3 from top to bottom are the Dytran® signal conditioner, the Data Physics Quattro® signal analyzer, and the Dytran® accelerometer. Figure 3-7 is a picture of the seat with arrows illustrating the coordinate position of the accelerometers.

In Figure 3-7, the upper accelerometer is shown positioned on the surface of the seat cushion. However, in actuality, it was fitted into a hollowed cut-out in the payload at the position that replicated where the base of the spinal column of a seated occupant would be in relation to the surface of the seat cushion.

Table 3-3: Specifications for the Data Acquisition System and Instrumentation

Data Acquisition Specifications [20, 21]		
Hardware	Property	Specification
Dytran® Signal Conditioner	Input channels	4
	ADC resolution (Analog AAF)	24-bit
	Sample resolution (Digital AAF)	32-bit (floating point)
Data Physics Quattro® Signal Analyzer	Residual offset	±0.1% (≤ 3 mV DC)
	Minimum sample rate	< 1 Hz
	Maximum sample rate	204.8 kHz
	Maximum useful frequency	80 kHz
	Maximum input voltage	80 v Peak (2.5 V rms)
Dytran® Accelerometers	Sensitivity (±15%)	10 mV/g (1.0 mV/m/s^2)
	Measurement range	±100 g
	Frequency range (±5%)	1.00to 10000 Hz
	Resonant frequency	≥ 50 kHz
	Broadband resolution	0.004 g rms (0.04 m/s^2 rms)
	Excitation voltage	18 to 30 VDC

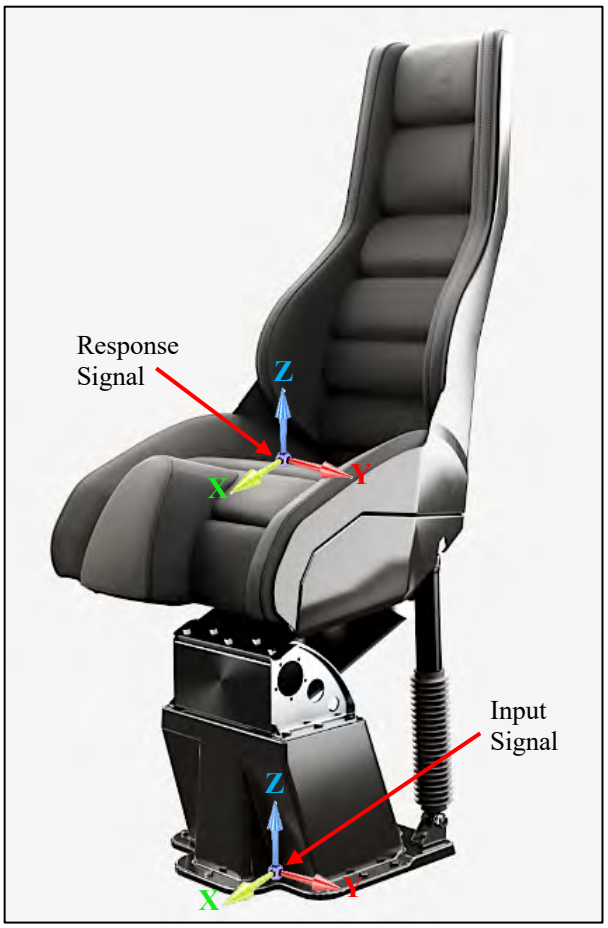

Figure 3-7: Location of Accelerometers on Test Seat [19]

3.2 Data Processing

The data processing effort was comprised of two primary tasks. The first action was to establish two frequency limits, including the frequency range within which the signal was to be recorded (sampling rate) and the low-pass filter cut-off frequency. The second undertaking was to implement a data processing technique that would not only produce the required MR values and help satisfy the objectives of the analysis, but one that aided in representing the results in a meaningful and useful manner. The following account commences with the introduction of the data recording frequency range of interest and progress towards providing an outline of the determination of the MR.

Recorded Data Frequency Range and Filter Cut-off Frequency

The literature revealed that most of the energy associated with the shock pulse that accompanied a wave slam was within the dc to 100 Hz frequency bandwidth. Signal information above that range was mostly attributed to local structural vibrations. Also, the human vertical frequency response range can be up to approximately 80 Hz. The reference documents recommended a sampling rate of 512 Hz or higher, but two sampling rates were used for comparison.

A series of tests were conducted in which the DAQ system was set to record the signals as transfer function measurements. Taking the rigidity of the tower (and actually the test seat as well) into consideration, the sampling rate for those tests was set to 500 Hz. As covered in one of the NSWCCD reports, most of the analysis of data from at sea trials was concerned with signal information below 80 Hz. Consequently, the decision was made that it was unnecessary to sample beyond 500 Hz, as anything above that frequency did not provide any value-added information. Nonetheless, in the interests of completeness, some of the tests were sampled at a greater frequency value.

For a series of higher amplitude tests, which were tests conducted using tines at the highest payload weight, the DAQ system was set to record the signals in the time domain (transfer function measurements) as well as in the frequency domain (shock response spectrum (SRS) measurements). The sampling rate was set to 1000 Hz for a subset of the transfer functions measurements. The SRS measurements were taken spanning a range of 1 Hz to 5000 Hz with a damping value of 0.05. The filters were placed with $1/24^{th}$ octave spacing with a reference frequency of 500 Hz. The SRS measurements were taken to satisfy the goal of determining the MR_{SRS}. An additional test criterion that required some consideration was the filter cut-off frequency.

The guidance offered in the documents agreed regarding the filter cut-off frequency. The NSWCCD-80 report recommended using a 4-pole Butterworth low-pass filter with a cut-off frequency of 20 Hz to post-process the collected data prior to analysis. The ISO draft standard did not explicitly recommend a post-processing filter cut-off frequency, but it did note that the test severity tolerances outlined in the document for input accelerations at the base of a test seat should be established using a 4-

pole Butterworth filter with a 20 Hz cut-off frequency. As stated earlier, at sea test data analysis presented in NSWCCD-83 focused on signal information below 80 Hz.

That report had examples of data that was filtered down to 10 Hz. Though, it did caution that filtering to such low frequency ranges affected the amplitude of the peak accelerations. Consequently, with all those reservations in mind and in the interest of a comparison, a 4-pole Butterworth filter with cut-off frequencies of 20 Hz, 80 Hz, 100 Hz, and 150 Hz were used to process the raw data prior to analysis. Later, in Chapter 5, it is shown that cut-off frequencies of 80 Hz and below alter the shape of the acceleration pulse due to a significant amount of information being lost from the raw data. Next, the process to develop the mitigation ratio (MR) is outlined.

Mitigation Ratio (MR)

The mitigation ratio (MR) was the focal point of the analysis to appraise the characteristics of the seat, and it was calculated using both (2-2) and (2-3). The tests that were conducted using transfer function measurements were used in (2-2) and the SRS tests were used in (2-3). The MR was the metric that was intended to encapsulate and relay the seat's performance. However, it seemed reductive to distill the data down to a single number. Therefore, to make the results more meaningful, the MR_{SRS} was a computed for a frequency range of interest rather than at a single frequency value.

The transfer function measurements were taken in the time domain, so MR_{PEAK} values calculated using (2-2) were based on the peak response-input acceleration ratio at an instance in time. That approach assigned a single MR value for each test. In contrast, the MR_{SRS} developed using (2-3) was used to create a range of values. The SRS was captured in the frequency domain, so computing a range of values with (2-3) provided a way to see how the system behaved across a range of frequencies (4 Hz to 10 Hz), which was considered to be valuable information that complimented the single number derived from (2-2). A statistical evaluation was applied to the post-processed data to facilitate establishing two facets of the study.

One aspect was to ascertain if a laboratory procedure intended to simulate a wave slam event with the use of a drop tower offered a level of repeatability in how it performed its function. The other course of action aimed at identifying the seat's probability of mitigating a shock impact across the different payload

masses and acceleration amplitudes. Ultimately, the goal of the data processing effort was to develop a complete and meaningful picture of the seat's characteristics. A picture that would help to fulfil the principal objective stated in Chapter 1. The DAQ system and instrumentation setup is shown in Figure 3-8. In the figure, the upper accelerometer is shown positioned on the surface of the seat cushion. However, in actuality it was fitted into a hollowed cut-out in the payload at the position that represented where the base of the spinal column of a seated occupant would be in relation to the surface of the seat cushion. In the following section, the steps of the test procedure are discussed, and the seat rating concept is expressed.

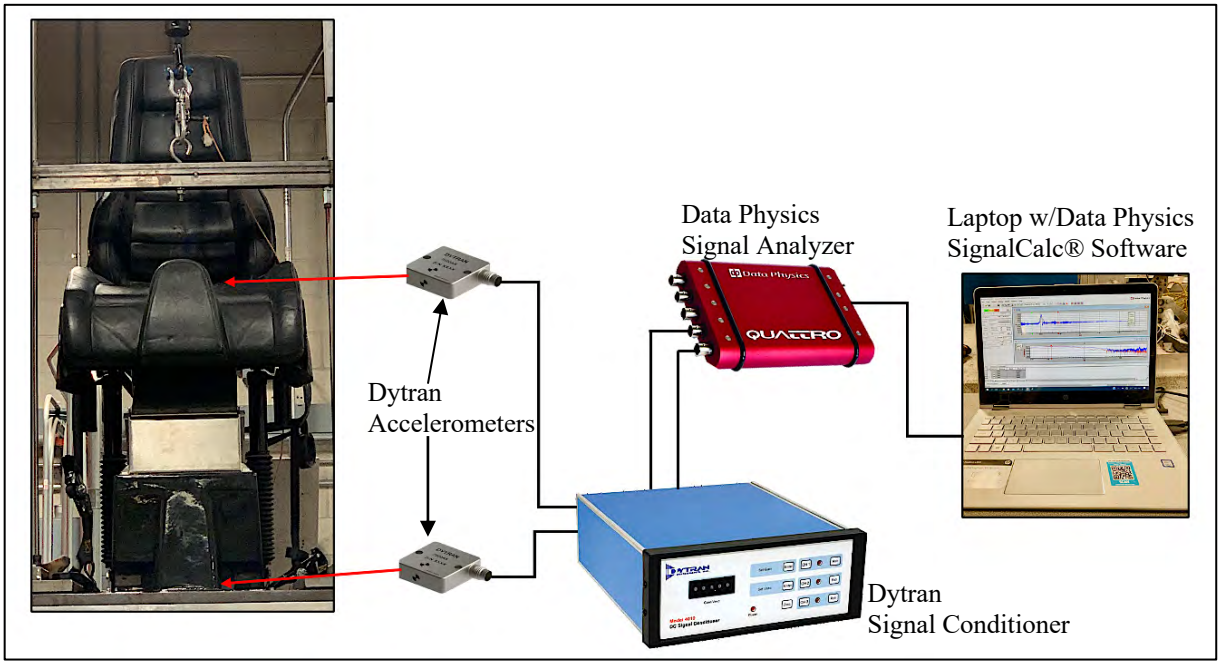

Figure 3-8: DAQ and Instrumentation Configuration

3.3 Test Procedure and Seat Rating

Although the reference documents recommended dropping from heights corresponding to all the severity threshold levels, only severity threshold levels four, five, and six were considered. The desire was

to test at the levels that matched acceleration pulse amplitudes that have been observed on Class 3 and Class 4 HSC. The steps of the laboratory test procedure are listed in Table E-1 in Appendix E. The tasks began with initializing the DAQ system and ended with raising the platform in preparation for conducting the next drop test. Some of the tasks in between included activating the data collection sequence in the DAQ software, inspecting and exporting the collected data, and raking the surface of the sand to remove divots. The entries in Table E-1 applied to the actions taken after the designated payload was properly secured, and the DAQ system, including the instrumentation, was connected and operational.

The test procedure itemized in Table E-1 incorporated measures from each of the reference sources. However, an additional step that was not covered in the reference documents but was specific to the test seat involved adjusting the damping to one of three different levels for specific tests.

In order to assess the effect of damping on the response of the seat, each test configuration as listed in the guidance criteria (height/payload) was conducted at three different damping levels. Earlier, it was noted that the seat was equipped with a dial (ranging from one to six) to adjust the damping, but no actual values for the damping were available. Consequently, each test setup was conducted at levels one, three, and six. In the absence of authentic values, it was presumed that those values corresponded to the lowest (softest), midpoint, and highest (stiffest) damping settings, respectively. Once the data were examined, and the tests were deemed to be valid based on the criteria outlined in ISO-19470 and NSWCCD-80/83, the method for rating the seat was developed.

At each weight category, three factors contributed to the seat rating, namely the MR value, the severity threshold level to which it was tested (the seat was raised to the maximum height allowed by the tower), and the corresponding HSC class for the specific level. However, before the subject of how those three elements worked together to form a rating, it is worth revisiting HSC Classes 3 and 4.

Vessels that were described as Class 3 and Class 4 fell into the search and rescue (SAR) and Military categories, respectively. Three sub-classes existed within Class 4 [6]. The three sub-classes in increasing order of operations in progressively more severe wave impact environments were 4-1 (4-1 had the same criteria as Class 3), 4-2, and 4-3. These HSC were usually operated in rough to high seas at speeds

in excess of 30 knots (34.52 mi/hr.). Hence, seats that could effectively mitigate shocks in laboratory tests at severity threshold levels that correspond to shock loads observed in these HSC would probably perform satisfactorily in environments experienced by those HSC. An abridged version of Table 2-3 is repeated below as Table 3-4. The table shows severity threshold levels four through six, and the corresponding class of HSC that could be expected to be operated in environments where the associated acceleration pulse loads have been observed. The 'Required' entry in the table stipulates that a test at that specific severity threshold level was required to rate the seat for use in that class of HSC. The 'Not Required' entry meant that a test at that specific severity threshold level exceeded the maximum expected shock load associated with the operational environment in which that class of HSC typically operated in. The maximum safe drop height allowed by the tower was 1.397 m (4.583 ft) above the top edge of the sandbox, which corresponded to a level between severity threshold levels five and six.

Table 3-4: Test Severity Threshold Levels and Corresponding Class of HSC [6, 7]

Test Severity Threshold Level versus HSC Class								
Severity Threshold					HSC Class			
Level	Peak Input Acceleration (g)	Impact Duration (s)	Recommended Drop Height (ft)	(m)	Class 4 Military 4-3	4-2	4-1	Class 3 SAR
6	10.19	0.10	6.78	2.07	Required	Not Required	Not Required	Not Required
5	8.15	0.10	4.34	1.32	Required	Required	Not Required	Not Required
4	6.12	0.10	2.44	0.74	Required	Required	Required	Required

The seat was rated based on a MR value, at a specific severity threshold level, for a specific class of HSC. Therefore, as an example, a MR_{PEAK} value of 0.90 at a severity threshold level of four would indicate that the seat mitigated 10% of the shock load, or stated differently, the seat reduced the rigid body

acceleration by 10%. Based on Table 3-4, a seat with a MR_{PEAK} value of 0.90, which was tested at a severity threshold level of four, would be rated for use in a Class 3 HSC and a Class 4-1 HSC. That same seat would require testing at a higher severity threshold level to be rated for use in a Class 4-2 HSC and a Class 4-3 HSC that intend to operate in environments with higher expected peak acceleration amplitudes. The MR_{SRS} value, which was calculated at each $1/24^{th}$ octave from 1 Hz to 5000 Hz, was also taken into consideration in the seat rating.

The response frequency range of interest for the MR_{SRS} was between 4 Hz and 10 Hz, as that was the frequency range for human response to rapidly applied accelerations. That data was used as supplemental information to institute the overall rating of the seat. Finally, a MR_{PEAK} value of less than one at a specific severity threshold level in more than one weight category suggested that the seat should perform satisfactorily across that range of payload weights. Therefore, the higher mass served as the upper limit of the range.

3.4 Summary

In this chapter, an account of the experimental test procedure is presented. The hardware elements of the test and the subsequent steps of the test procedure were based on recommendations and criteria submitted in ISO-19470 and NSWCCD-80/83. The impetus behind developing the test protocol was founded in the fact that there was no universally accepted experimental test procedure that incorporated all the best practices, which was aimed at rating a shock mitigation seat for use in a specific class of HSC. Consequently, the objective of the analysis was to develop such a procedure, one that utilized input from a proposed ISO Standard and from Naval research reports, to establish a seat rating method. The rating was based on the MR_{PEAK} value, the severity threshold level, and the class of HSC that corresponded to that severity threshold level. After testing, a seat that yielded a MR_{PEAK} value of less than one for a specific severity threshold level was deemed adequate for installation and use in the matched class of HSC. Of

course, the study would not have been complete without a numerical analysis to support the validation of the empirical results and to help characterize the dynamic response of the seat.

The benefit of the numerical model was when the same conditions in the experimental analysis were implemented in the model, the simulated responses were compared with the empirical results for validation. Also, the numerical model provided a way to ascertain if the mass-spring-damper concept was a feasible approach to characterizing the dynamic response of the seat. In the forthcoming chapter, the equations of motion for mass-spring-damper dynamic systems are presented, as well as other equations that facilitate analyzing such systems. In the closing section of the chapter, the developmental details of the numerical model are explored.

Chapter 4. Analytical Representation of the Seat and the Basis for the Numerical Model

In the preceding chapter, the experimental test setup of the seat system and its physical components is outlined. The experimental test procedure was developed to be a controlled process that helped ensure test repeatability. The numerical model was a valuable tool to validate the empirical data generated from the experimental test. However, it also served as the required tool to achieve one of the study's main objectives, which was to determine if the mass-spring-damper method formed an appropriate analytical representation of a shock mitigation seat.

This chapter opens with an in-depth look at the mass-spring-damper concept used to form the mathematical basis for the seat system. Two versions of the mass-spring-damper system are explored. The single degree of freedom (SDOF) mass-spring-damper system was the analytical representation of the seat system in which the seat and occupant were considered as a single lumped-mass entity. The SDOF model did not provide any consideration for treating the seat cushion as an active translational energy-dissipating element. The two degree of freedom (2DOF) model characterized the seat and occupant as separate entities (separated by the seat cushion) that experienced dynamic interaction. The 2DOF model adopted the notion that the seat cushion functioned as an active translational element with spring-like and damping capabilities.

The equations of motion derived from the free body diagrams of both models are developed. In addition, the expressions that correspond to physical system properties, such as damping, and how they were used to assess the physical system are introduced. In the closing sections of the chapter, the state space approach and the Newmark-Beta method for direct numerical integration that were implemented in the numerical model are discussed. Also, the assumptions that were made that facilitated simulating the physical system are presented.

4.1 Analytical Representation of the Mass-Spring-Damper Models

The accepted methodology for analyzing most dynamic systems is by applying Newton's second law of motion to the system components. That classical approach includes a procedure that begins with creating the free body diagrams of the system components and ends with the development of one or more equations of motion in the form of differential equations. Subsequently, the solutions to those equations, along with the theories associated with free and forced vibration, can be used to discern the system's behavior.

In the upcoming sections, Newton's method is applied to both mass-spring-damper models. Initially, the free response of each system is used to establish the fundamental equations of motion. Afterward, the equations used to evaluate each system's response to a forced vibration is introduced. In the context of this study, the forced vibration was generated by the base excitation due to the acceleration pulse created when the pulse-shaping device contacted the impact surface after a period of free fall. Later, an account of the impact method is presented. That method makes it convenient to carry out a cursory analysis on a seat when it is modeled as a SDOF mass-spring-damper system and tested with a drop tower.

4.1.1 Single Degree of Freedom (SDOF) Model

The three primary components of the SDOF mass-spring-damper system are shown in Figure 4-1. Figure 2-6 is repeated on the left side of the figure. It displays the elements of the SDOF model that represented the seat-occupant and suspension subsystems. The right side shows the forces acting on the system based on free vibration. Those forces were used to develop the equations of motion. Table 4-1 itemizes the nomenclature that is used for elements and characteristics of the system throughout this section.

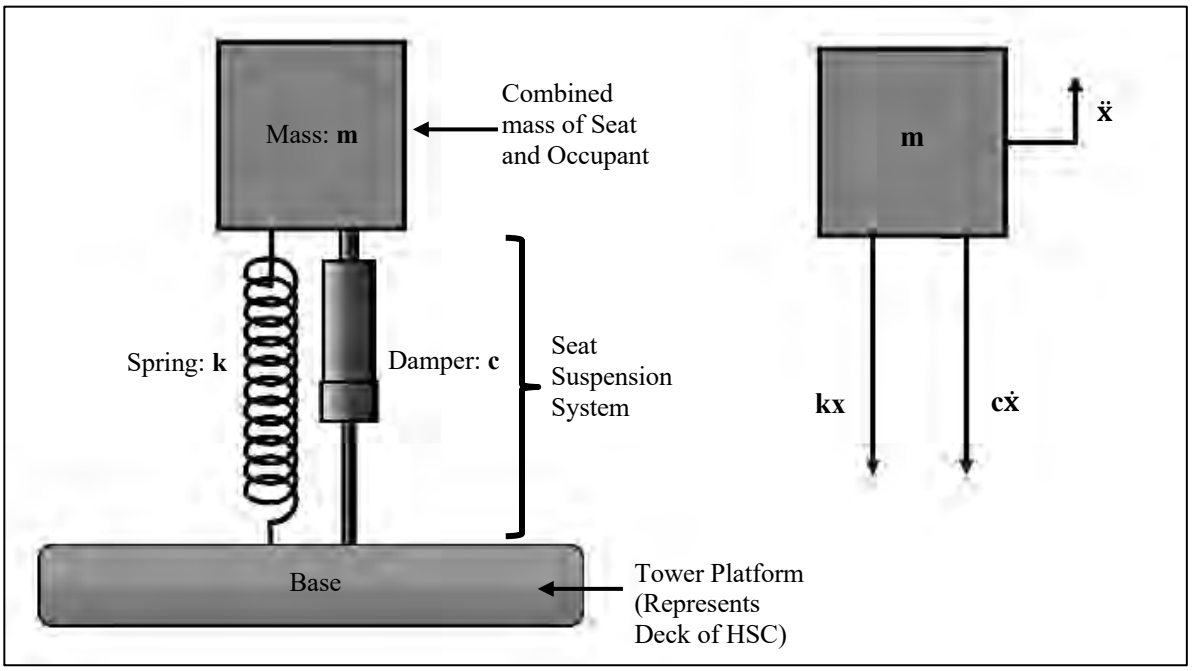

Figure 4-1: SDOF Mass-Spring-Damper System and Associated Free Body Diagram

Table 4-1: Nomenclature for the SDOF System Variables

Nomenclature for SDOF Variables	
Variable	Description
m	Mass of the seat-occupant subsystem
k	Spring stiffness of the seat suspension system
c	Viscous damping of the seat suspension system
x	Displacement of the seat-occupant subsystem
$\dot{x}$	Velocity of the seat-occupant subsystem
$\ddot{x}$	Acceleration of the seat-occupant subsystem
ω_n	Natural frequency of the system
ξ	Damping ratio
ω_d	Damped natural frequency of the system

Free Vibration

Using Newton's law and considering that there is no external force acting on the system, the sum of the forces based on the free body diagram is as follows:

$$\sum F = m\ddot{x} \tag{4-1}$$

The above equation can be rewritten using the summation of the vertical forces acting on the mass.

$$m\ddot{x} = -c\dot{x} - kx \tag{4-2}$$

$$m\ddot{x} + c\dot{x} + kx = 0 \tag{4-3}$$

It is customary to divide (4-3) by m.

$$\ddot{x} + \frac{c}{m}\dot{x} + \frac{k}{m}x = 0 \tag{4-4}$$

The coefficients of the velocity and displacement terms in (4-4) have an important meaning in the dynamics of the system. As is shown next, they help establish certain traits of the system that are crucial to its analysis.

$$\frac{c}{m} = 2\xi\omega_n \rightarrow \xi = \frac{c}{2\sqrt{km}} \tag{4-5}$$

$$\frac{k}{m} = \omega_n^2 \tag{4-6}$$

In (4-5), the system natural frequency is given by ω_n, and ξ represents the system damping ratio. The square of the natural frequency appears in (4-6). By substitution, (4-4) can be rewritten as follows:

$$\ddot{x} + 2\xi\omega_n \dot{x} + \omega_n^2 x = 0 \tag{4-7}$$

The solution to (4-7) can be obtained by first assuming a solution in the following form.

$$x(t) = Xe^{st} \tag{4-8}$$

Then, using the Laplace transform, and implementing (4-8), the revised governing equation is as follows.

$$(s^2 + 2\xi\omega_n\, s + \omega_n^2\,)\, Xe^{st} = 0 \tag{4-9}$$

Alternatively, the term in the parenthesis in (4-9) can be rewritten to facilitate defining the damped natural frequency.

$$\left\{(s + \xi\omega_n)^2 + \omega_n^2\left(1 - \xi^2\right)\right\} Xe^{st} = 0 \tag{4-9b}$$

The quadratic equation can be used to solve for s_1 and s_2 in (4-9).

$$s_{1,2} = \left(-\xi \pm \sqrt{\xi^2 - 1}\right)\omega_n \tag{4-10}$$

The form of the solution to (4-9, 4-9b) is based on the value of the damping ratio, ξ, in (4-10). From a theoretical perspective, the desired solution for these equations is the variable x(t). From a physical standpoint, x(t) represents the displacement of the system mass, m, in Figure 4-1, which represents the seat-occupant subsystem. There are three cases in which the value of ξ must be considered, as each yields a different form of the solution for x(t).

Less Than Critical Damping: $\xi < 1$

In this case, the damping ratio is less than 1, and the roots of (4-10) are complex expressions with real and imaginary parts. Thus, (4-10) takes the form shown below.

$$s_{1,2} = \left(-\xi \pm i\sqrt{1 - \xi^2}\right)\omega_n \tag{4-11}$$

In (4-11) the product of the natural frequency and the expression in the radical is defined as the damped natural frequency of the system and is given by the following expression:

$$\omega_d = \omega_n \sqrt{1 - \xi^2} \tag{4-12}$$

The general displacement response of the system with less than critical damping is given below.

$$x(t) = X_1\, e^{\left(-\xi + i\sqrt{1-\xi^2}\right)\omega_n t} + X_2\, e^{\left(-\xi - i\sqrt{1-\xi^2}\right)\omega_n t} \tag{4-13}$$

If Euler's formula $\left(e^{ix} = \cos x + i \sin x\right)$ is implemented, as well as the definition of ω_d, the displacement of the system becomes:

$$x(t) = e^{-\xi\omega_n t}\left\{[x(0)]\, \cos(\omega_d t) + \left[\frac{\dot{x}\,(0) + (\xi\omega_n)\, x(0)}{\omega_d}\right] \sin(\omega_d t)\right\} \tag{4-14}_{22}$$

Critical Damping: $\xi = 1$

In the second case, when the damping ratio is equal to 1, the roots of (4-10) are real and equal, and the damped natural frequency is equal to zero. Hence, $s_{1,2} = -\omega_n$. The resulting equation for displacement is then given as shown below.

$$x(t) = e^{-\omega_n t}\{\,[x(0)] + [\dot{x}\,(0) + \omega_n\, x(0)]\, t\} \tag{4-15}$$

Greater Than Critical Damping: $\xi > 1$

In the third and final scenario, the roots of the equation are real and negative. Using the Laplace transform of (4-9) and solving for X(s) results in the following.

$$X(s) = \left\{ \frac{\dot{x}(0) + [s + 2\xi\omega_n]\, x(0)}{s^2 + 2\xi\omega_n\, s + \omega_n^2} \right\} \tag{4-16}_{22}$$

Using equation (4-10) as the denominator of (4-16) and subtracting s_2 from s_1 yields:

$$s_1 - s_2 = \left(-\xi + \sqrt{\xi^2 - 1}\right)\omega_n + \left(\xi + \sqrt{\xi^2 - 1}\right)\omega_n \tag{4-17a}$$

$$s_1 - s_2 = 2\omega_n\sqrt{\xi^2 - 1} \tag{4-17b}$$

Next, following through with the Laplace transform, and implementing partial fractions, (4-16) becomes:

$$X(s) = \left\{\frac{1}{-s_2 + s_1}\right\}\left[\left\{\frac{x(0)\, s_1 + [\dot{x}(0) + 2\xi\omega_n\, x(0)]}{s - s_1}\right\} + \left\{\frac{-x(0)\, s_2 - [\dot{x}(0) + 2\xi\omega_n\, x(0)]}{s - s_2}\right\}\right] \tag{4-18}$$

Finally, take the inverse Laplace transform, and substitute in the expressions derived from (4-17a) and (4-17b) to achieve the general response for the system with greater than critical damping.

$$x(t) = \left\{\frac{1}{2\omega_n\sqrt{\xi^2 - 1}}\right\}\left\{X_1\, e^{\left(-\xi + \sqrt{\xi^2 - 1}\right)\omega_n t} + X_2\, e^{\left(-\xi - \sqrt{\xi^2 - 1}\right)\omega_n t}\right\} \tag{4-19}_{22}$$

The expressions for X_1 and X_2 are given below.

$$X_1 = \dot{x}(0) + x(0)\left(\xi + \sqrt{\xi^2 - 1}\right)\omega_n \tag{4-20}_{22}$$

$$X_2 = -\dot{x}(0) + x(0)\left(-\xi + \sqrt{\xi^2 - 1}\right)\omega_n \qquad (4\text{-}21)_{22}$$

In a laboratory setting, during system testing, it may not be conceivable to ascertain the damping of the system through analytical methods. In circumstances where the damping of the system is unavailable, the empirical data (system response) can be used to calculate the damping ratio. The method to determine the system damping ratio by evaluating the maxima of peak responses is presented next. This technique is especially suited to systems in which the damping ratio is less than critical, $\xi < 1$.

Logarithmic Decrement

The logarithmic decrement is the natural logarithm of the ratio of the maximum amplitude of two successive cycles of oscillation in the response of the damped free vibration of a system. The expression for the logarithmic decrement begins with an alternate form of the displacement of the underdamped system denoted by (4-13), as shown below.

$$x(t) = X\, e^{-\xi\omega_n t}\cos(\omega_d t + \phi) \qquad (4\text{-}22)_{23}$$

The time interval between two consecutive response peaks can be represented by the damped natural frequency and the difference in time (t) as follows.

$$t_2 - t_1 = \frac{2\pi}{\omega_d} = \frac{2\pi}{\omega_n\sqrt{1 - \xi^2}} \qquad (4\text{-}23)_{23}$$

Taking the term for the time interval into consideration, and with the use of (4-22) as the expression for the system response, the ratio of two consecutive response peak maxima can be represented by the following expression.

$$\frac{X_1}{X_2} = e^{\frac{2\pi\xi}{\sqrt{1-\xi^2}}} \tag{4-24}$$

Taking the natural logarithm of both sides of the equation yields:

$$\ln\left(\frac{X_1}{X_2}\right) = \frac{2\pi\xi}{\sqrt{1-\xi^2}} \tag{4-25}$$

It is customary to define the left side of (4-25) as α or, in some references, as Δ. Therefore, the logarithmic decrement can be defined as:

$$\alpha = \frac{2\pi\xi}{\sqrt{1-\xi^2}} \tag{4-26}_{23}$$

The system damping ratio was resolved by solving the preceding equation for ζ, to yield:

$$\xi = \frac{\alpha}{\sqrt{(2\pi)^2 + \alpha^2}} \tag{4-27}_{23}$$

An alternate form of (4-27) can be extended to ascertain the system damping ratio by using the ratio of the maxima of two non-successive response peaks separated by n cycles of oscillation.

The alternate versions for the expressions for the logarithmic decrement and the damping ratio are provided below. In each case, n is the number of cycles between the response peaks.

$$\alpha_n = \frac{2n\pi\xi}{\sqrt{1-\xi^2}} \tag{4-28}_{23}$$

$$\xi = \frac{\alpha_n}{\sqrt{(2n\pi)^2 + {\alpha_n}^2}} \tag{4-29}_{23}$$

The preceding equations were all based on (4-22), which is the expression for displacement. However, sometimes in experimental laboratory procedures, such as the one explored in this study, accelerations are easier to measure than displacements. Therefore, in cases where the acceleration is readily available, the damping ratio can be derived from (4-30), where 'n' is the number of cycles between the acceleration peaks.

$$\xi = \frac{1}{2\pi n} ln \frac{\ddot{x}_i}{\ddot{x}_{i+n}} \qquad (4\text{-}30)_{24}$$

The logarithmic decrement is an invaluable tool for calculating the damping ratio of a system with unpublished damping information. The equations that have been developed thus far were all derived from the equation of motion that did not include an external force acting on the system. A set of equations that support the analysis of a system that has been exposed to an external excitation is of more use in practical applications. In the next section, the equations that can be used to assess the response of a SDOF system exposed to a base excitation are presented. The representative force (for the purpose of demonstrating an input to the system) in the upcoming analysis is a half-sine pulse with an amplitude of A. Recall that the acceleration pulse associated with a wave slam event is reminiscent of a half-sine pulse. The first order of business was to set up the free body diagram to develop the equation of motion.

Forced Vibration

The motion of the base to which the system was attached introduced the notion of relative characteristics. That is, the response of the system was evaluated based on its displacement (position), velocity, and acceleration relative to the base. In Figure 4-2, the system and its free body diagram are illustrated. The forces were depicted as the difference between the position and velocity of the mass relative to the position and velocity of the base. The sum of the forces based on the free body diagram yielded a slightly different equation than that given by (4-2), as shown below.

$$m\ddot{x} = -c(\dot{x} - \dot{y}) - k(x - y) \qquad (4\text{-}31)$$

The conventional approach for developing the ensuing equations based on (4-31) was to use a third variable to represent the relative relationships between the mass and the base. Table 4-2 below lists the relative expressions as outlined in [25], and they are used for the remainder of the analysis. The 'y' variable related to the base (tower platform) and the 'x' variable corresponded to the payload (combined seat-occupant mass).

Table 4-2:Variables Used to Represent the Relative Relationships for SDOF [25]

SDOF Base Excitation Variables Relative Relationship	
Variable	Relative Relationship
z	x - y
$\dot{z}$	$\dot{x} - \dot{y}$
$\ddot{z}$	$\ddot{x} - \ddot{y}$
$\ddot{x}$	$\ddot{z} + \ddot{y}$

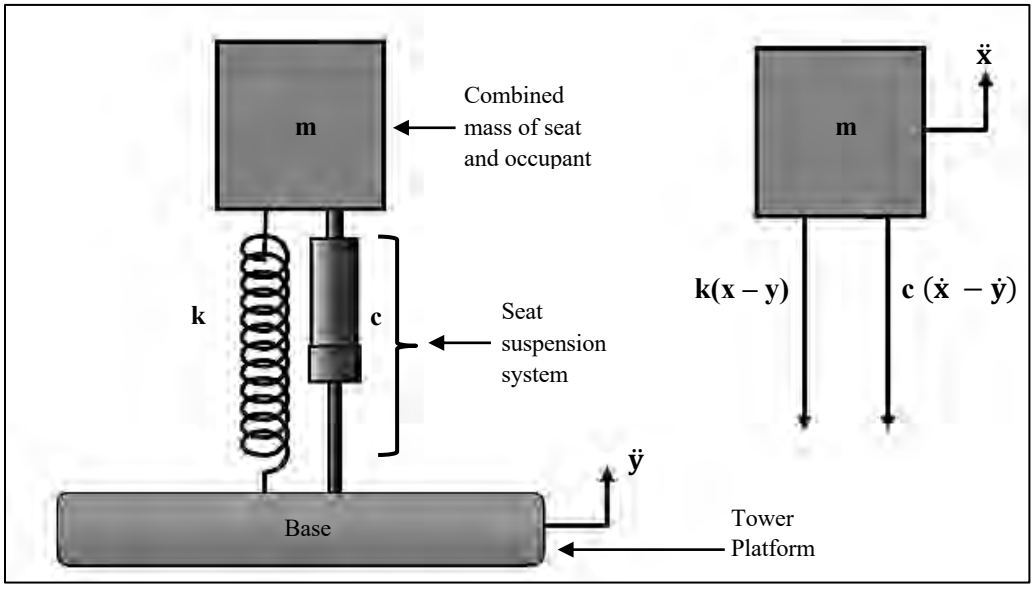

Figure 4-2: Mass-Spring-Damper System Exposed to a Base Excitation and Free Body Diagram

Substituting the relative terms into (4-31), making the necessary algebraic manipulations, and dividing by m yields:

$$\ddot{z} + \frac{c}{m}\dot{z} + \frac{k}{m}z = -\ddot{y} \tag{4-32}$$

The coefficients of the relative velocity and relative position terms had the same meaning as presented earlier, and the equivalent of (4-7) is given below.

$$\ddot{z} + 2\xi\omega_n z + \omega_n^2 z = -\ddot{y} \tag{4-33}$$

If the base input excitation was a half-sine pulse, as covered in [25], then the governing equation was given by the following expression:

$$\ddot{z} + 2\xi\omega_n z + \omega_n^2 z = -A\sin(\omega t) \rightarrow \omega = \frac{\pi}{T} \tag{4-34}_{25}$$

The 'A' in the equation represented the amplitude of the half-sine pulse, and 'T' was the pulse duration. The above expression was resolved by taking the Laplace transform of both sides to develop the complimentary and particular solutions. The total solution was the sum of the complimentary and particular solutions. According to [25], the complete expression for the solution takes the form of the following term.

$$Z(s) = Z_n(s) + Z_f(s) \tag{4-35}_{25}$$

Where the complimentary term, $Z_n(s)$, was given by:

$$Z_n(s) = \left\{\frac{\dot{z}(0) + [s + 2\xi\omega_n]\, z(0)}{s^2 + 2\xi\omega_n s + \omega_n^2}\right\} \quad (4\text{-}36)_{25}$$

and the particular term, $Z_f(s)$, was given by:

$$Z_f(s) = \left\{\frac{A\omega}{s^2 + \omega^2}\right\}\left\{\frac{1}{s^2 + 2\xi\omega_n s + \omega_n^2}\right\} \quad (4\text{-}37)_{25}$$

The steps involved in the algebraic manipulation of (4-36) and (4-37), and the subsequent inverse Laplace transform process are detailed in [25]. However, the relative displacement of the system for the complimentary and particular solutions, respectively, are given below.

$$z_n(t) = e^{(-\xi\omega_n t)}\left\{z(0)\, \cos(\omega_d t) + \left[\frac{\dot{z}(0) + [\xi\omega_n]\, z(0)}{\omega_d}\right]\sin(\omega_d t)\right\} \quad (4\text{-}38)_{25}$$

$$z_f(t) = \frac{A}{[(\omega^2 - \omega_n^2)^2 + (2\xi\omega\omega_n)^2]}\,[(2\xi\omega\omega_n)\, \cos(\omega t) + (\omega^2 - \omega_n^2)\, \sin(\omega t)] - \frac{\frac{A\omega}{\omega_d}\left[e^{(-\xi\omega_n t)}\right]}{\left[[(\omega^2 - \omega_n^2)^2 + (2\xi\omega\omega_n)^2]\right]}\left[(2\xi\omega_n\omega_d)\, \cos(\omega_d t) + \left(\omega^2 - \omega_n^2(1 - 2\,\xi^2)\right)\, \sin(\omega_d t)\right] \quad (4\text{-}39)_{25}$$

The solution for the total relative displacement of the system exposed to a half-sine pulse base excitation is the sum of (4-38) and (4-39). The expressions for the system's relative velocity and relative acceleration are derived by taking the first and second derivatives of the total relative displacement.

Before the discussion segues to introducing the 2DOF model, it is noteworthy to explore an approach that was suited to the analysis of a shock mitigation seat system through the use of a drop tower. As the drop tower used free fall due to gravity to generate the impact, the SDOF model was used to develop equations based on the acceleration due to gravity and the drop height that facilitated the experimental analysis of the seat system. The development began with a few assumptions, which are listed next.

Impact Method for SDOF Model in Drop Testing

According to [26], in order to develop the expressions for the impact (shock) method, some assumptions had to be made for the seat and the physical set up as follows:

1) The seat-occupant subsystem can be modeled as a SDOF system.
2) The seat-occupant subsystem was dropped from rest (initial velocity is zero).
3) The seat remained attached to the impact surface after initial contact.
4) The seat-occupant subsystem freely vibrated at its natural frequency after contact.
5) The system had a linear response.
6) There was no energy dissipation during the collision.

The list above required some scrutiny in order to determine the applicability of the method to this study. Items two and four were actualities. Item one did not seem like an unreasonable inference, and it was one of the primary inquiries that this analysis aimed to resolve. Hence, in the interest of developing the technique, item one seemed acceptable. Previously, it was noted that to generate the acceleration pulse, the impact surface was required to be deformable. Accordingly, the impact surface at the bottom of the tower was sand, which introduced some reservations about items three and six.

The impact that occurred when the wedge (or tines) attached to the underside of the platform contacted the sand was not a near elastic collision. That is, the total kinetic energy of the seat system was not conserved. After the impact, the seat remained attached to the platform, and the wedge/tines remained in contact with the sand, but energy was dissipated into the sand. Consequently, items three and six could not be explicitly attained, but with known information such as the drop height and the depth of the sand, the impact method was still used to determine the amount of energy expended in the sand. Item five was the sole supposition that required some experimental exploration, as the traits of the seat suspension system were unavailable. Indeed, if the system response was nonlinear, added complexities would be introduced into the analysis. Subsequently, that would abate the veracity of the equations that were based on the acceleration due to gravity and the drop height, as they applied to this study. Later, results from an

experimental evaluation of the seat spring revealed that a section of the suspension system profile was linear.

Despite the physical traits of the test setup that may have presented drawbacks to the impact analysis approach, there was some consolation to be had based on the type of information sought from a drop test. The impact analysis (and therefore shock analysis) of shock mitigation seat systems was primarily concerned with maximum values. Specifically, those values included peak acceleration, velocity, displacement, and to some extent, impulse. Hence, using equations that were based on the acceleration due to gravity and the drop height, combined with empirical acceleration data collected from the instrumentation, provided a less computationally demanding approach. That approach served as a sanity check (information for comparison) for evaluating the system. The process began with equating the system's kinetic energy with its potential energy.

Equating the system's kinetic energy through its mass, m, velocity, $\dot{x}$, the acceleration due to gravity, g, and its drop height, h, led to the following equation:

$$\frac{1}{2}m\dot{x}^2 = mgh \tag{4-40}$$

Dividing by m and multiplying by 2 gave the velocity of the system at impact (just as the wedge/tines contacted the sand), as shown in the term below.

$$\dot{x}(0) = \sqrt{2gh} \tag{4-41}$$

In the preceding equation, all the variables on the right-hand side were known values. Thus, (4-41) provided a straightforward way to calculate velocity upon impact. Revisiting the case for an underdamped system, (4-13) could be rewritten in the following form:

$$x(t) = e^{\left(\frac{-ct}{2m}\right)}(X_1 \sin \omega_d t + X_2 \cos \omega_d t) \tag{4-42}$$

The variable, X_2, was the value of x at time t = 0. This approach assumed that the seat system was dropped from rest, with an initial displacement of zero. Therefore, X_2 was initially equal to zero. Consequently, the expressions for x(t) and $\dot{x}(t)$ were as follows:

$$x(t) = e^{\left(\frac{-ct}{2m}\right)}(X_1 \sin \omega_d t) \tag{4-43}$$

$$\dot{x}(t) = X_1 e^{\left(\frac{-ct}{2m}\right)}\left(\omega_d \cos \omega_d t - \frac{\sin \omega_d t}{2m}\right) \tag{4-44}$$

Equating (4-41) and (4-44) at t = 0 gave the two following equations:

$$\dot{x}(0) = \sqrt{2gh} = X_1 \omega_d \tag{4-45}$$

$$X_1 = \frac{\sqrt{2gh}}{\omega_d} \tag{4-46}$$

The term for X_1 can be substituted into (4-43) to give the displacement of the system using the acceleration due to gravity, the drop height, and the damped natural frequency, as follows:

$$x(t) = e^{\left(\frac{-ct}{2m}\right)} \frac{\sqrt{2gh}}{\omega_d}(\sin \omega_d t) \tag{4-47}$$

The damping coefficient, c, and damped natural frequency, ω_d, could be determined by using the logarithmic decrement, as explained earlier. The second derivative provided the acceleration as shown below:

$$\ddot{x}(t) = e^{\left(\frac{-ct}{2m}\right)} \frac{\sqrt{gh}}{\sqrt{2}} \left[\frac{c^2 \sin \omega_d t}{2m^2 \omega_d} - \frac{2c \cos \omega_d t}{m} - 2\omega_d \sin \omega_d t \right] \quad (4\text{-}48)$$

Considering the force through the spring as $f_s(t) = kx$ and seeing that $k = \omega_n^2 m$, the force through the spring was given as shown below.

$$f_s(t) = \omega_n m \, e^{\left(\frac{-ct}{2m}\right)} \frac{\sqrt{2gh}}{\sqrt{1-\xi^2}} (\sin \omega_d t) \quad (4\text{-}49)$$

The force through the spring could be integrated from 0 to π/ω_n to yield the impulse over a half-sine pulse. However, based on the above equation, the term for the impulse was elaborate. Consequently, it negated the simplicity of this approach. Nonetheless, pulse durations usually occur over a small period of time, so the trigonometric term will tend to one or zero. The negative value of the damping coefficient in the exponential term will also tend to cause that term to go to a small value as well. When both criteria hold, the following simplified versions for the equations for maximum displacement, x_{max}, maximum acceleration, $\ddot{x}_{max}$, and the total impulse for the acceleration pulse period, I_t, can be utilized. Those equations are as follows:

$$x_{max} = \sqrt{\frac{2mgh}{k}} \quad (4\text{-}50)_{26}$$

$$\ddot{x}_{max} = \sqrt{\frac{2kgh}{m}} \quad (4\text{-}51)_{26}$$

$$I_t = 2m\sqrt{2gh} \qquad (4\text{-}52)_{26}$$

To emphasize on the point alluded to earlier, the preceding equations were simplified versions of the equations used for forced vibration analysis. These terms were not expected to replace the expressions that were derived earlier, they simply provided a modest method to supplement the experimental analysis and offer a rough estimate of the system characteristics. Next, the equations of motion that related to the 2DOF mass-spring-damper system are addressed. The equations were developed in a similar fashion to the SDOF system, beginning with Newton's law and the free body diagram.

4.1.2 Two Degree of Freedom (2DOF) Model

In contrast to the SDOF mass-spring-damper model, the 2DOF model considered the mass of the occupant and the mass of the seat as separate entities. In the scope of this research, the second mass and the second spring-damper subsystem were analogous to the human occupant and the seat cushion, respectively. The 2DOF model was the preferable option when it was desirable to identify the effect of the spring-damping properties of the seat cushion on the dynamics of the system. Often, in a laboratory setting, determining the spring-damping properties of a seat cushion poses a challenge. Thus, an alternative procedure was to use the published spring and damping properties of polyurethane foam as a starting point for the numerical model. The idea was to use an iterative process in which the values for the seat cushion spring constant and damping value were repeatedly modified until the simulated response closely matched the response from the empirical data.

In the examination of the 2DOF model, the free vibration equations are initially presented, but the final equations are based on the forced vibration concept because it generated expressions that were relevant to practical applications. However, the first step in the inquiry still began with applying Newton's law to the system, as is introduced next.

The representative force in the upcoming analysis, as shown in Figure 4-3, was applied to the base of the system. The left side of Figure 4-3 depicts the components of the 2DOF model that corresponded to the tower platform, the seat main suspension system, the seat pan, the seat cushion, and the human occupant subsystems of the experimental setup.

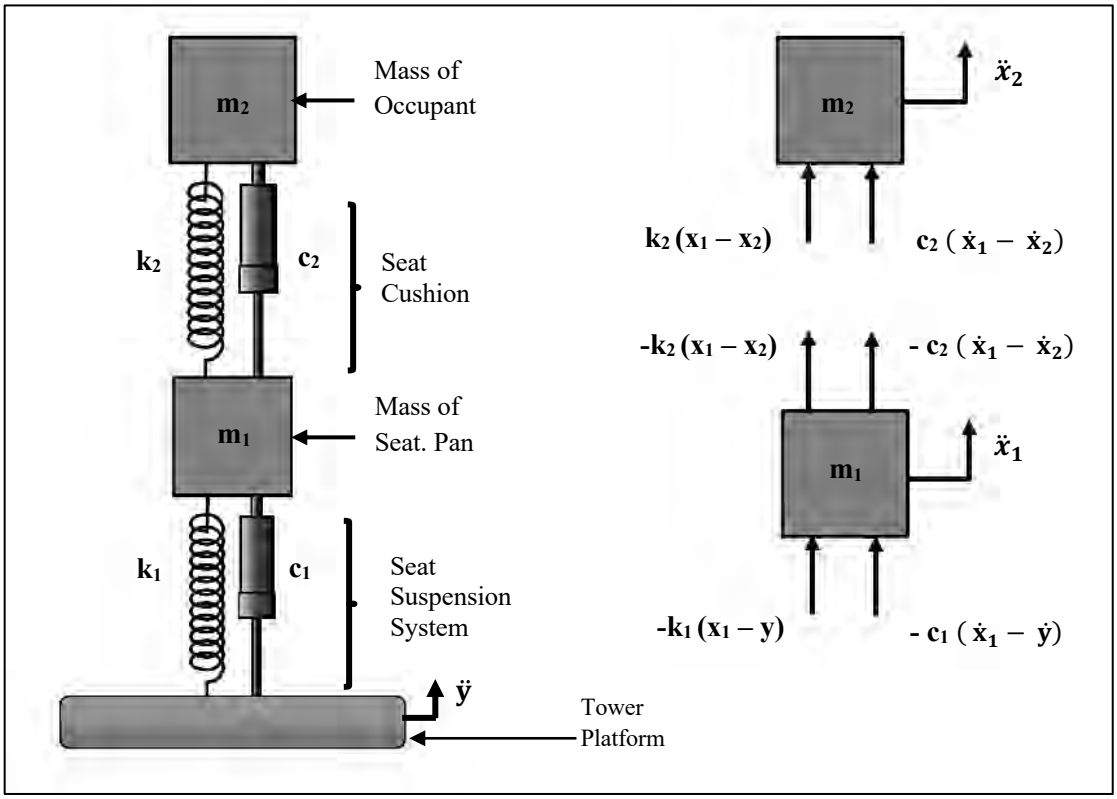

Figure 4-3: 2DOF System Exposed to a Base Excitation and Free Body Diagram

The right side of the figure shows the forces acting on the system based on the input acceleration. Those forces were used to develop the equations of motion, which were represented in the form of a mass matrix coupled by the stiffness and damping matrices, as detailed in [27]. Applying Newton's law, the sum of the forces for each mass was given by the following equations.

$$m_1\ddot{x}_1 + (c_1 + c_2)\dot{x}_1 - c_2\dot{x}_2 + (k_1 + k_2)x_1 - k_2x_2 = c_1\dot{y} + k_1y \tag{4-53}$$

$$m_2\ddot{x}_2 - c_2\dot{x}_1 + c_2\dot{x}_2 - k_2x_1 + k_2x_2 = 0 \tag{4-54}$$

The two equations were placed in matrix form to yield:

$$\begin{bmatrix} m_1 & 0 \\ 0 & m_2 \end{bmatrix}\begin{Bmatrix} \ddot{x}_1 \\ \ddot{x}_2 \end{Bmatrix} + \begin{bmatrix} c_1 + c_2 & -c_2 \\ -c_2 & c_2 \end{bmatrix}\begin{Bmatrix} \dot{x}_1 \\ \dot{x}_2 \end{Bmatrix} + \begin{bmatrix} k_1 + k_2 & -k_2 \\ -k_2 & k_2 \end{bmatrix}\begin{Bmatrix} x_1 \\ x_2 \end{Bmatrix} = \begin{Bmatrix} c_1\dot{y} + k_1y \\ 0 \end{Bmatrix} \tag{4-55}$$

Similar to the SDOF model, the procedure to implement the variable that represented the relative relationship between the masses and the base was employed. During testing, the velocity associated with the base excitation was unknown information. However, the acceleration of the base was measured with accelerometers. Therefore, the base acceleration and the masses were used to eliminate the term on the right-hand side in (4-53) [27]. In Table 4-3, the subscript 'i' was used to denote a variable associated with either mass 1 or mass 2. The relative terms, and the use of the base acceleration and masses to symbolize the input force, is shown in (4-56).

Table 4-3: Variables Used to Represent the Relative Relationships for 2DOF

2DOF Base Excitation Variables Relative Relationship	
Variable	Relative Relationship
z_i	x_i - y
$\dot{z}_i$	$\dot{x}_i - \dot{y}$
$\ddot{z}_i$	$\ddot{x}_i - \ddot{y}$
$\ddot{x}_i$	$\ddot{z}_i + \ddot{y}$

$$\begin{bmatrix} m_1 & 0 \\ 0 & m_2 \end{bmatrix}\begin{Bmatrix} \ddot{z}_1 \\ \ddot{z}_2 \end{Bmatrix} + \begin{bmatrix} c_1 + c_2 & -c_2 \\ -c_2 & c_2 \end{bmatrix}\begin{Bmatrix} \dot{z}_1 \\ \dot{z}_2 \end{Bmatrix} + \begin{bmatrix} k_1 + k_2 & -k_2 \\ -k_2 & k_2 \end{bmatrix}\begin{Bmatrix} z_1 \\ z_2 \end{Bmatrix} = \begin{Bmatrix} -m_1\ddot{y} \\ -m_2\ddot{y} \end{Bmatrix} \quad (4\text{-}56)$$

When the forces on the right-hand side of (4-56) are characterized in the form of $f_i = F_i e^{j\omega t}$, then the response for each mass involves the displacement vector as follows:

$$x_1(t) = \bar{X}_1 e^{j\omega t} \rightarrow \bar{X}_1 = X_1 e^{j\phi_1} \quad (4\text{-}57)_{23}$$

$$x_2(t) = \bar{X}_2 e^{j\omega t} \rightarrow \bar{X}_2 = X_2 e^{j\phi_2} \quad (4\text{-}58)_{23}$$

Considering the preceding equations, an alternate form of (4-56) can be developed, as shown below. In the following expression, Cramer's rule can be used to determine $\overline{X}_1$ and $\overline{X}_2$.

$$\begin{bmatrix} k_1 + k_2 - m_1\omega^2 + j(c_1 + c_2)\omega & -k_2 - jc_2\omega \\ -k_2 - jc_2\omega & k_2 - m_2\omega^2 + jc_2\omega \end{bmatrix}\begin{Bmatrix} \bar{X}_1 \\ \bar{X}_2 \end{Bmatrix} = \begin{Bmatrix} F_1 \\ F_2 \end{Bmatrix} \quad (4\text{-}59)_{23}$$

The matrices that were developed for the 2DOF model lend themselves to a modal analysis of the system. The first step in the modal analysis is usually to cast the solution in the form of (4-56) using the relative relationship variable, z, as the dependent variable. The process then involves establishing an eigenvalue problem based on the homogeneous form of the coupled mass, stiffness, and damping matrices. Subsequently, a modal coordinate is defined. The newly defined modal coordinate is used to establish proof of the orthogonality relationships and to decouple the mass and relative relationship matrices from the stiffness terms. An extensive modal analysis, outside of the process to determine the natural frequencies of the system, was not conducted on the test system. Therefore, a synopsis of the theory used to conduct an in-depth modal analysis is not covered in this report.

In this section the equations of motion for the SDOF and 2DOF models for a mass-spring-damper system were developed. The equations of motion were manipulated to be presented as differential equations, and the solutions to those equations yielded the expressions used to determine the response of the system. The details of the state space representation of the system and the Newmark-Beta method for direct numerical integration are covered shortly. However, before moving on to those topics, an examination of the benefit of using either the SDOF or the 2DOF models for the analytical representation of the seat is presented.

Using SDOF versus 2DOF Model for Seat System Numerical Analysis

The test seat was comprised of four fairly rigid components, including the reinforced plastic pedestal, the steel spring housing, the reinforced plastic seat frame, and the aluminum (and steel) dampers. The seat frame consisted of the seat section and the back rest section, which were bolted together. It was difficult to determine how the upholstered-covered cushion padding was attached to the seat, but the seat cushion appeared to be injection-molded foam that was bonded to the seat. The foam seemed to be molded to the shape of the seat frame and, possibly, attached with a form of adhesive. Also, it was difficult to determine the thickness of the foam on the seat section, as the underside of the reinforced plastic seat pan was curved inward to accommodate the spring housing. The top of each damper was bolted to the base of the seat section of the seat frame, and the bottom of the dampers were bolted to the pedestal. When observed during drop testing, the seat components moved as a single unit along a single vertical axis without any noticeable movement outside of that vertical plane. Thus, it seemed like a reasonable assessment to say that the seat (main components) was comprised of a rigid structure with minimal dynamic interaction between its components. The payload was also a rigid structure.

As described earlier, the payload was constructed from three rigid Polyvinyl Chloride (PVC) pipe sections that were fused together. The payload was strapped to the seat as outlined in chapter three. From the theoretical perspective, the seat-occupant system could be described as a 2DOF system, just as it was illustrated in Figure 4-3. In the practical setting of the laboratory though, there was minimal vertical movement between the payload and the surface of the seat cushion upon impact. Two factors could be

attributed to the nominal payload-seat-cushion interaction. First, the payload was strapped to the seat, as a human occupant would be, in such a way to avoid excessive vertical movement (bouncing) or the possibility of being thrown from the seat. Second, the seat cushion foam was rather stiff, so it was not easily deformable. In essence, the seat cushion had the properties of a fairly stiff translational component with spring-damper characteristics that resulted in relatively insignificant dynamic interaction between it and the payload, or the reinforced plastic seat pan. This observation was not to insinuate that the seat cushion had no effect on the response of the payload; rather, it was to highlight the point that, due to its design and material properties, the seat cushion (back section included) appeared to perform like three elements. It appeared to possess the potential energy storing capacity of a spring, and because it had some mass, it had the capability to store kinetic energy like a mass component as well. Also, it had some ability to dissipate energy, like a damper. Taking all the aspects of the seat system into consideration, it was fair to postulate that it could have been modeled either as a SDOF or a 2DOF system.

The SDOF model was conceivable because the payload and seat practically moved as one with very little independent movement between the payload and the surface of the seat cushion or the seat pan. The 2DOF model was a feasible approach also. Although, the mass of the cushion had to be included in the seat mass as well. In Chapter 6, the discussion focuses on comparing the results of using the two concepts in the numerical analysis. Presently, the numerical analysis, and how it was implemented, is covered.

4.2 Numerical Models for Evaluating the Shock Mitigation Seat

Before delving into the explanation of the process to create the numerical models, it seems suitable to state the assumptions that were made to reduce the complexities in the model. Also, the limitation that the drop tower was incapable of replicating the forces that were outside the vertical plane is addressed.

4.2.1 Assumptions and Restriction of the Numerical Models

First, it was assumed that there was negligible friction between the guide brackets of the platform and the guide rails. Lubricating grease was injected to the housing of the guide brackets to reduce the effects of friction and coulomb damping between the two surfaces.

The second assumption, which was better suited for the SDOF model, presumed that the occupant was securely fastened to the seat, and that there was minimal vertical movement between the seat cushion and the occupant. The ISO and NSWCCD-80 reference documents allowed for 25 mm (1 in) of free vertical movement between the seat cushion and occupant. However, as that vertical limitation was not a significant distance in comparison to the system in its entirety, the second assumption treated the payload and seat as one single entity for the SDOF model. Finally, there was the restriction associated with using the tower to simulate only the vertical dynamic motions of the wave slam environment.

In Section 2.1, it was noted that the environment on the deck of an HSC during a wave slam event was comprised of a series of dynamic events. The events included translational motion, which was characterized by the heave, surge, and sway of the vessel. Also, rotational motion, which was represented by the pitch, roll, and yaw of the craft. Consequently, seat occupants were subjected to motion loading forces outside of the vertical plane (heave), which included forces associated with angular and lateral acceleration. However, using a drop tower to simulate a wave slam did not replicate the effects of the rotational motion (pitch, roll, and yaw). Thus, while a computational model based on the mass-springs-damper concept was aptly suited to represent the dynamics of the drop tower-seat system, it inherited the system's limitation of not being fully capable of simulating the forces associated with angular and lateral acceleration. The aforementioned concern notwithstanding, some consolation was taken in the fact that the vertical acceleration component contributed to the shock pulse more than the other dynamic components of the wave slam. Also, the test seat was designed to mitigate shock in the vertical direction only. Therefore, a numerical model of the seat based on the mass-spring-damper concept did serve some utility. The system's state space representation was one of the two techniques used to develop the numerical model.

4.2.2 State Space Representation

The state space method is used to transform a second-order differential equation that represents a dynamic system into a set of first-order differential equations. In this technique, the system state variables are represented as state vectors that characterize the configuration of the system at an instance in time. In most cases, for a mass-spring-damper system, the state variables are position and velocity. The derived equations are customarily represented as shown in (4-60) and (4-61), where $\dot{z}$ is the time derivative state vector, z is a vector with the state variables (position and velocity), y is typically an output vector, u is an input control vector, and **A**, **B**, **C**, and **D** represent system matrices.

$$\dot{z} = \boldsymbol{A}z + \boldsymbol{B}u \tag{4-60}$$

$$y = \boldsymbol{C}z + \boldsymbol{D}u \tag{4-61}$$

The vectors and matrices in the equations comprise the state variables, system inputs, and the system outputs. Table 4-4 itemizes the general definition of each element when the expressions are used to represent a mass-spring-damper system. In the forthcoming section, the state space representation is applied to the SDOF model of the seat. The procedure begins by revisiting the equation of motion for the base excited system.

Table 4-4: Elements of the State Space Representation

State Space Variables	
Variable	Description
z	Vector of state variables (position, velocity)
$\dot{z}$	Time derivative of state vector
u	Input (control) vector
A	System matrix (usually holds ratios of mass, spring, and damping values)
B	Input matrix
C	Output matrix
D	Feedforward matrix (Zero matrix when feedforward is not applicable)
y	Output vector

State Representation for SDOF Seat Model

Using the relative relationships shown in Table 4-2, the equation of motion for the SDOF system can be expressed as shown in (4-62).

$$m(\ddot{z} + \ddot{y}) = c(\dot{z}) + k(z) \tag{4-62}$$

In the expression above, the variable $\ddot{y}$ represents the input acceleration. That acceleration was recorded by the lower accelerometer, located on the base of seat pedestal, when the pulse-shaping device contacted the sand. Dividing (4-62) by the mass, m, and solving for the input acceleration resulted in the following equation:

$$\ddot{z} + \frac{c}{m}(\dot{z}) + \frac{k}{m}(z) = -\ddot{y} \tag{4-63}$$

The equation of motion in (4-63) formed the basis for the SDOF numerical analysis and it had to be rewritten using the variables from the numerical analysis. However, before that path is explored, Table 4-5 is presented to correlate the variables used in the analysis to the actual test system.

Table 4-5: SDOF Variable Relative Relationship and Correlation to Test System

SDOF Test System State Space Variable Representation		
Variable	Relative Relationship	Description
x	$z + y + z_{spring}$	Payload/seat position
$\dot{x}$	$\dot{z} + \dot{y}$	Payload/seat velocity
$\ddot{x}$	$\ddot{z} + \ddot{y}_{accel}$	Payload/seat acceleration (measured by accelerometer)
y	$x - z - z_{spring}$	Platform position
$\dot{y}$	$\dot{x} - \dot{z}$	Platform velocity
$\ddot{y}_{accel}$	$\ddot{x} - \ddot{z}$	Platform acceleration (measured by accelerometer)
z	$x - y - z_{spring}$	Relative distance between the payload/seat and platform
z_{spring}	x - y - z	Seat spring height (pedestal to top surface of seat cushion)
z_{spring}	The uncompressed spring height (including the pedestal) when the seat was empty	

In Table 4-5, the 'x' variable corresponds to the accelerometer that was located in the payload (combined seat-occupant mass response), and the 'y' variable relates to the accelerometer that was located on the seat pedestal base (tower platform input). The relative variable, 'z', represents the distance between the accelerometer that was located on the payload, and the accelerometer that was on the base of the pedestal. The subscript, 'accel', is used to identify the base input acceleration of the platform, or information that was derived from it. The variable, 'z_{spring}', is used to denote the height of the seat spring. It was the uncompressed spring height when the seat was empty, and the system was at rest.

Figure 4-4 is a sketch of the seat and platform in the raised configuration, which is the suspended system prior to a drop test. The drawing depicts the laboratory coordinate system with the values of the elements in the relative relationship. The position (height) values when the system was suspended at rest before a drop test were used for the initial conditions in the numerical model. The accelerometer location that is shown on the surface of the seat cushion in the figure was actually located in the base of the payload. The location indicated in the sketch was the location of the accelerometer relative to the surface of the seat cushion.

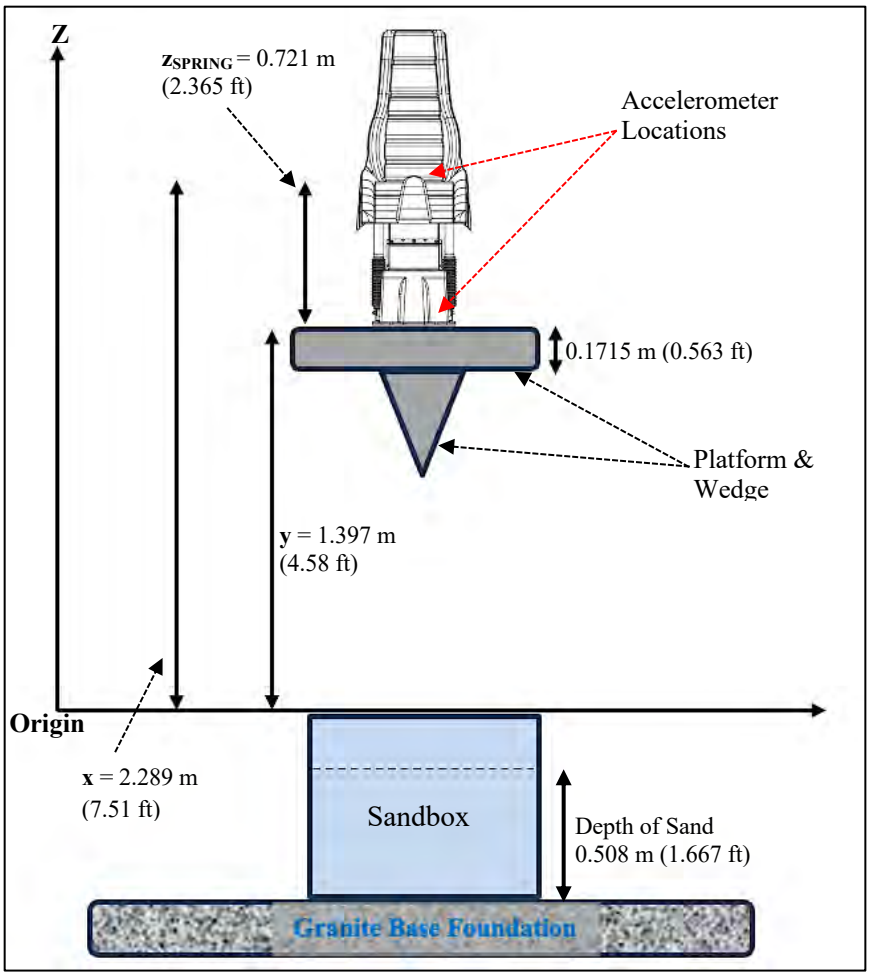

Figure 4-4: SDOF Test Coordinate System and Position Measurements

The upper and lower horizontal surfaces of the tower platform in Figure 4-4 were solid sheets of metal without exposed holes or gaps. Hence, during a drop it was likely that the platform possibly trapped air and created an aerodynamic damping effect. Thus, in the definition for the system damping, an additional damping term was included to accommodate for that effect. Also, although there was no explicit information regarding the seat spring profile, an unconfirmed source suggested that it was nonlinear. Consequently, the spring term was represented as a second-order polynomial to account for possible nonlinear behavior. Table 4-6 lists the definitions of the expressions used for the seat's damping and spring traits in the numerical model.

Table 4-6: Damping and Spring Definitions for SDOF Numerical Analysis

SDOF System Damping and Spring Definitions	
Expression	Definition
$\frac{c_1}{m}(\dot{z})$	Seat damping
$\frac{c_2}{m}(\dot{z}+\dot{y}_{accel})^2 sign(\dot{z}+\dot{y}_{accel})$	Other damping effects (air resistance)
$\frac{R}{m}(z)$	Polynomial for spring stiffness = $az + bz^2$ (restoring force)

The expression in (4-63) does not contain the system variables as they are defined in Table 4-6. Therefore, recalling Figure 4-2 and using the representative definitions from the numerical analysis, Figure 4-5 illustrates the free body diagram for the physical setup of the SDOF system.

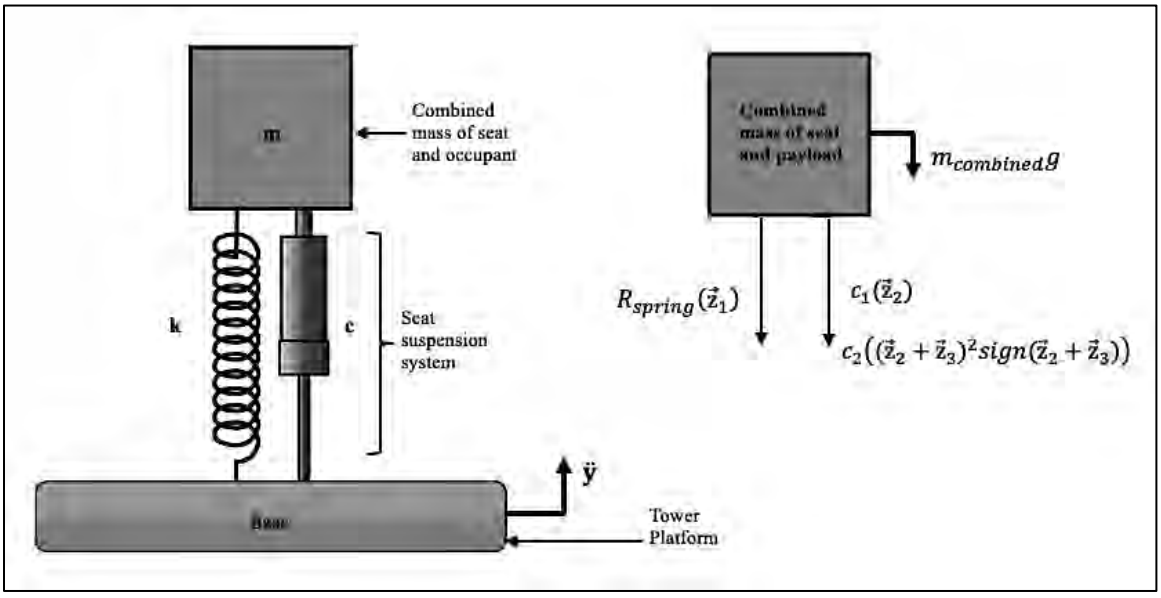

Figure 4-5: Free Body Diagram of SDOF Test System

The resulting equation of motion for the system that was used in the numerical model is expressed in (4-64).

$$\ddot{z} + \frac{c_1}{m}(\dot{z}) + \frac{c_2}{m}(\dot{z} + \dot{y}_{accel})^2 sign(\dot{z} + \dot{y}_{accel}) + \frac{R}{m}(z) = -\ddot{y}_{accel} - g \tag{4-64}$$

Keeping in mind that the state space representation equates the time derivative of the system variables (position and velocity) to the system's state and input matrices, the state space representation of the system had to take the form shown below.

$$\begin{bmatrix} z_1(t) \\ \dot{z}_2(t) \end{bmatrix} = \begin{bmatrix} 0 & 1 \\ \frac{-R}{m} & -\frac{(c_1 + c_2)}{m} \end{bmatrix} \begin{bmatrix} z_1(t) \\ z_2(t) \end{bmatrix} + \begin{bmatrix} 0 \\ \frac{1}{m} \end{bmatrix} \ddot{y}_{accel}(t) \tag{4-65}$$

$$x - y = \begin{bmatrix} 1 & 0 \end{bmatrix} \begin{bmatrix} z_1(t) \\ z_2(t) \end{bmatrix} \tag{4-66}$$

Where,

$z_1 = z$: Relative difference in position between the accelerometer location on the payload and the accelerometer location on the seat pedestal (platform) (x - y - z_{spring} in Figure 4-4).

$z_2 = \dot{z}$: Relative difference in velocity between the accelerometer location on the payload and the accelerometer location on the seat pedestal (platform).

In the numerical analysis, all the system state variables were combined into a matrix, the columns of which were equivalent to the vectors from (4-60). The definition of the state variable vectors as they related to the system are given in (4-67). The expression in (4-68) reflects how the state variables vector, the vectors of the system matrix, the vectors of the input matrix, and the input vector, which in this case was the base acceleration, were combined into one matrix. There are no second-order terms in (4-67), as is required by the state space representation.

$$\mathbf{z} = \begin{pmatrix} \vec{z}_1 \\ \vec{z}_2 \\ \vec{z}_3 \\ \vec{z}_4 \\ \vec{z}_5 \\ \vec{z}_6 \end{pmatrix} = \begin{pmatrix} \text{Relative position of payload to platform} \\ \text{Relative velocity of payload to platform} \\ \left.\begin{matrix} \text{Platform velocity} \\ \text{Platform position} \\ \text{Payload velocity} \\ \text{Payload position} \end{matrix}\right\} \text{Derived from accelerometers} \end{pmatrix} \tag{4-67}$$

$$\dot{\mathbf{Z}} = \frac{d}{dt}\begin{pmatrix} \vec{z}_1 \\ \vec{z}_2 \\ \vec{z}_3 \\ \vec{z}_4 \\ \vec{z}_5 \\ \vec{z}_6 \end{pmatrix} = \begin{pmatrix} \vec{z}_2 \\ -\frac{c_1}{m}\vec{z}_2 - \frac{c_2}{m}(\vec{z}_2 + \vec{z}_3)^2 \text{sign}(\vec{z}_2 + \vec{z}_3) - \frac{R(z_1)}{m} - g - \ddot{y}_{accel} \\ \ddot{y}_{accel}(t) \\ \vec{z}_3 \\ \ddot{x}_{accel}(t) \\ \vec{z}_5 \end{pmatrix} \tag{4-68}$$

Along with the time and the initial condition vectors, the second item of (4-68) was placed in a function that served as the input data for the Matlab® ODE45 (Runge-Kutta) integration process in the numerical analysis. The acceleration vectors from the payload and platform accelerometers were also included. They were used to derive the last four rows of (4-67). The platform acceleration time history was used to generate the input position and velocity vectors used in the expressions for the spring and damping forces. The payload acceleration time history was integrated to generate its position for comparison with the simulated response position. The simulated payload response acceleration that the numerical solver generated was the desired result to be compared with $\ddot{x}_{accel}$ and $\ddot{y}_{accel}$.

The state representation of the 2DOF model followed a similar procedure as the steps taken for the SDOF model. The next section begins with a look at the relative relationships based on the test coordinate system and then continues with introducing the 2DOF versions of (4-64), (4-67), and (4-68).

State Representation for 2DOF Seat Model

The difference in the equations of motion for the 2DOF model was the added variables for the mass of the seat and the spring and damping variables for the seat cushion. The variables used for the relative relationships and how each related to the test system setup are tabulated in Table 4-7.

Table 4-7: 2DOF Variable Relative Relationship and Correlation to Test System

2DOF Test System State Space Variable Representation		
Variable	Relative Relationship	Description
x	$z + y_{accel} + z_{spring}$	Seat pan position
$\dot{x}$	$\dot{z} + \dot{y}_{accel}$	Seat pan velocity
$\ddot{x}$	$\ddot{z} + \ddot{y}_{accel}$	Seat pan acceleration
z_{pay}	$x_{pay} - x - z_{cush}$	Relative position between the payload and seat pan
$\dot{z}_{pay}$	$\dot{x}_{pay} - \dot{x}$	Relative velocity between the payload and seat pan
$\ddot{z}_{pay}$	$\ddot{x}_{pay} - \ddot{x}$	Relative acceleration between the payload and seat
z	$x - y_{accel} - z_{spring}$	Relative distance between the seat and platform
z_{cush}	The uncompressed thickness of the seat cushion without a payload	

In the table, the ‘y’ variable still relates to the accelerometer located on the seat pedestal base (tower platform input). However, the ‘x’ variable now has two definitions. The ‘x’ variable with the subscript ‘pay’ corresponds to the accelerometer that was located on the payload, but the stand alone ‘x’ variable relates to a point that was located on the underside of the seat pan. Variables with the ‘cush’ subscript relate to the seat cushion. Figure 4-6 shows the coordinate system with the position values used to develop the relative relationship for the 2DOF model. In actuality, as seen in the figure, the locations designated for the payload and the seat pan were approximately 0.10 m (0.33 ft) apart. Comparable to the SDOF system representation in Figure 4-4, the accelerometer location that is shown on the surface of the seat cushion in Figure 4-6 was actually located in the base of the payload. The location indicated in the sketch was the location of the accelerometer relative to the surface of the seat cushion.

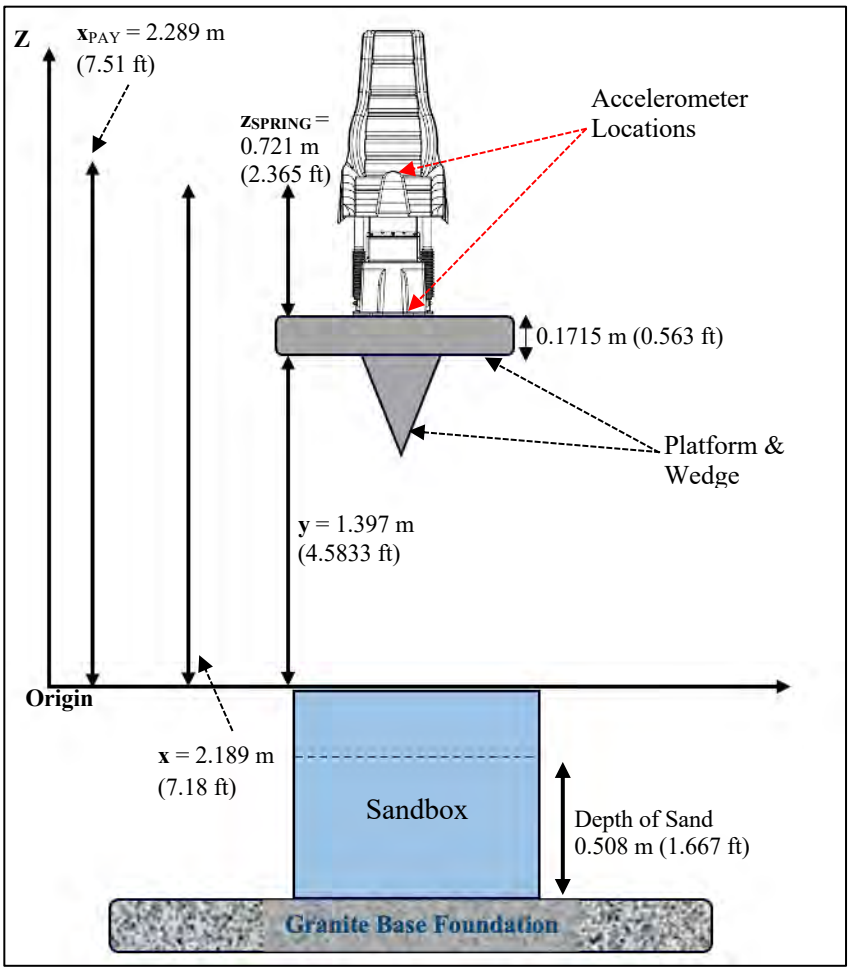

Figure 4-6: 2DOF Test Coordinate System and Position Measurements

Using the relative relationships from Table 4-7, retaining the definitions from Table 4-6, and returning to the 2DOF system in Figure 4-3, the free body diagram for the 2DOF system is displayed in Figure 4-7. In the figure, the forces acting on the seat were tallied, and the seat mass was designated as m_{seat}, which was the equivalent of m_1 in Figure 4-3. The forces acting on the payload were accounted for, and the payload mass was designated as m_{pay}, which was analogous to m_2 in Figure 4-3.

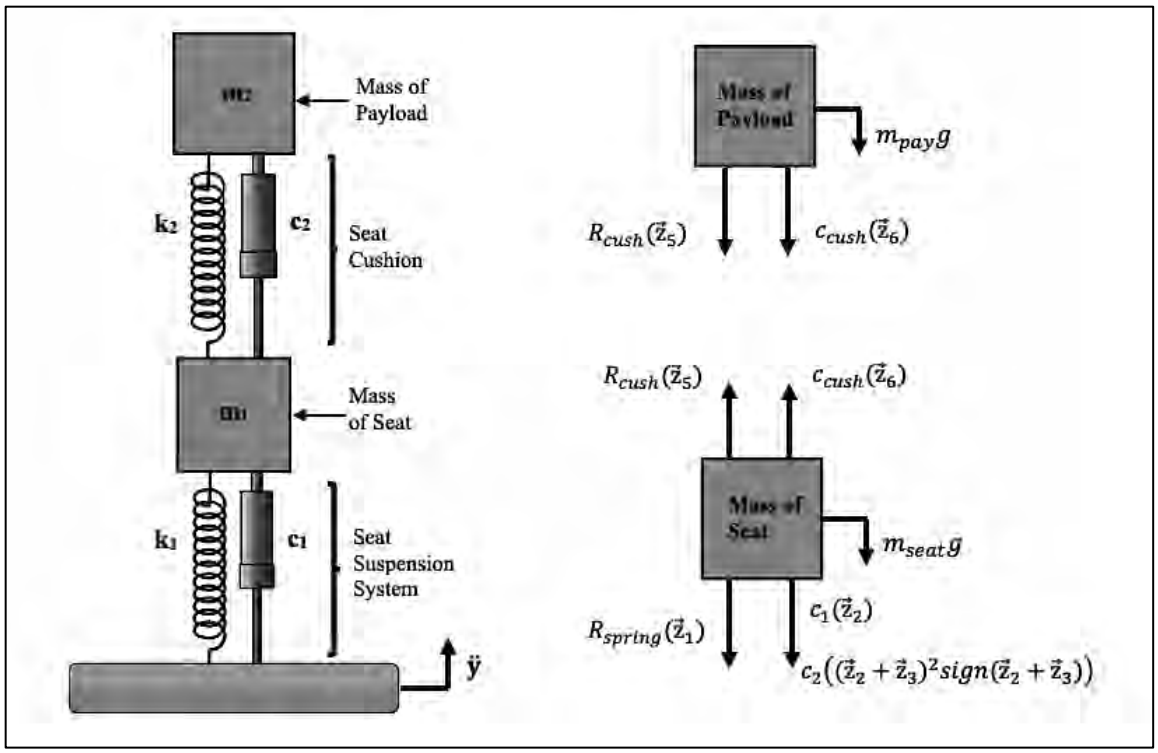

Figure 4-7: Free Body Diagram of 2DOF Test System

Adhering to the structure of (4-64), the equations of motion for the 2DOF model were represented for the seat and payload, respectively, as shown below.

$$\ddot{z} + \frac{c_1}{m_{seat}}(\dot{z}) + \frac{c_2}{m_{seat}}(\dot{z}+\dot{y}_{accel})^2 sign(\dot{z}+\dot{y}_{accel}) + \frac{R}{m_{seat}}(z) - \frac{R_{cush}}{m_{seat}}(z_{pay}) - \frac{c_{cush}}{m_{seat}}(\dot{z}_{pay}) = -\ddot{y}_{accel} - g \tag{4-69}$$

$$\ddot{z}_{pay} + \frac{R_{cush}}{m_{pay}}(z_{pay}) + \frac{c_{cush}}{m_{pay}}(\dot{z}_{pay}) = -\ddot{x} - g \tag{4-70}$$

In addition to the time and the initial condition vectors, the elements of (4-69) and (4-70) were placed in a function that served as the argument for the Matlab® ODE45 (Runge-Kutta) integration function

in the numerical analysis. The acceleration vectors from the payload and platform accelerometers were also included. The platform acceleration time history was used to generate the input position and velocity vectors used in the expressions for the spring and damping forces acting on the seat pan.

In a similar manner as with the SDOF model, the expressions in (4-69) and (4-70) had to be represented as either a vector or a matrix to create the state space representation for the 2DOF model. Subsequently, each system vector (or matrix) was combined as vectors of a consolidated matrix. The definition of each system vector is given in (4-71). Observe that (4-71) does not contain any elements greater than first-order terms. Items $\vec{z}_3$, $\vec{z}_4$, $\vec{z}_7$, and $\vec{z}_8$ (with the 'accel' term) were derived from the accelerometers and were analogous to the last four entries in (4-67). The expression in (4-72) combined the state variable vectors, the vectors of the system matrix (which now included terms representing the behavior of the seat cushion), the vectors of the input matrix, and the input vector. For the 2DOF model, the simulated payload and seat response accelerations were the sought-after products to be compared with the recorded empirical data.

$$\mathbf{z} = \begin{pmatrix} \vec{z}_1 \\ \vec{z}_2 \\ \vec{z}_3 \\ \vec{z}_4 \\ \vec{z}_5 \\ \vec{z}_6 \\ \vec{z}_7 \\ \vec{z}_8 \end{pmatrix} = \begin{pmatrix} \text{Relative position of seat to platform} \\ \text{Relative velocity of seat to platform} \\ \text{Platform velocity (accel)} \\ \text{Platform position (accel)} \\ \text{Amount cushion was stretched} \\ \text{Relative velocity of payload to seat} \\ \text{Payload velocity (accel)} \\ \text{Payload position (accel)} \end{pmatrix} \tag{4-71}$$

$$\dot{\mathbf{Z}} = \frac{\mathrm{d}}{\mathrm{dt}} \begin{pmatrix} \vec{z}_1 \\ \vec{z}_2 \\ \vec{z}_3 \\ \vec{z}_4 \\ \vec{z}_5 \\ \vec{z}_6 \\ \vec{z}_7 \\ \vec{z}_8 \end{pmatrix} = \tag{4-72}$$

$$\begin{pmatrix} \vec{z}_2 \\ -\frac{c_1}{m_{seat}}(\vec{z}_2) - \frac{c_2}{m_{seat}}(\vec{z}_2 + \vec{z}_3)^2 sign(\vec{z}_2 + \vec{z}_3) + \frac{R}{m_{seat}}(\vec{z}_1) - \frac{R_{cush}}{m_{seat}}(\vec{z}_5) - \frac{c_{cush}}{m_{seat}}(\vec{z}_6) - g - \ddot{y}_{accel}(t) \\ \ddot{y}_{accel}(t) \\ \vec{z}_3 \\ \vec{z}_6 \\ -\frac{R_{cush}(z_5)}{m_{pay}} - \frac{c_{cush}}{m_{pay}}\vec{z}_6 - g - (\ddot{x}) \\ \ddot{x}_{accel}(t) \\ \vec{z}_7 \end{pmatrix}$$

The state space method provided a way to reduce the equations of motion from second order to first order differential equations to decrease the level of complexity when the analysis of the system was conducted. However, that approach did not specify the numerical integration routine to be implemented. In the final section of this chapter, the Newmark-Beta (Newmark-β) method, which dictated the integration method, is covered.

The Newmark-β method uses an incremental formulation technique that provides a way to implement different intergration schemes based on the chosen values of the quadrature parameters. The method is a popular time integration algorithm used in structural analysis, and the objective here was to form a basis for comparison between the simulated responses of the state space and Newmark-β methods.

4.2.3 Newmark-Beta Method for Numerical Integration

The Newmark-Beta (Newmark-β) method is a family of time-stepping algorithms used to implement direct numerical integration methods to solve certain second order differential equations in the evaluation of the response of structural dynamic systems. The method uses a Taylor series expansion of the displacement and velocities to compute the state of the system at the next time step. In line with the development presented in [28], the method began with approximating the integral terms of the acceleration by numerical quadrature. The integral terms for velocity and displacement are given in (4.73) and (4.74) respectively, where $\tau \in [t_i, t_{i+1}]$, and Δt is the time step size.

$$\dot{x}_{i+1} \approx \dot{x}_i + \int_{t_i}^{t_{i+1}} \ddot{x}(\tau) d\tau \tag{4-73}$$

$$x_{i+1} \approx x_i + \Delta t \dot{x}_i + \int_{t_i}^{t_{i+1}} (t_{i+1} - \tau)\ \ddot{x}(\tau) d\tau \tag{4-74}$$

The integrals terms can be reconciled through numerical quadrature to yield the following expressions:

$$\int_{t_i}^{t_{i+1}} \ddot{x}(\tau) d\tau \approx (1-\gamma)\Delta t \ddot{x}_i + \gamma \Delta t\ \ddot{x}_{i+1} + r_{error} \tag{4-75}$$

$$\int_{t_i}^{t_{i+1}} (t_{i+1} - \tau)\ \ddot{x}(\tau) d\tau \approx \left(\frac{1}{2} - \beta\right)(\Delta t)^2 \ddot{x}_i + \beta(\Delta t)^2 \ddot{x}_{i+1} + r'_{error} \tag{4-76}$$

When (4-75) and (4-76) are substituted into (4-73) and (4-74) (and the higher orders error terms are dropped) the Newmark approximation formulas for velocity and displacement are derived, as shown below.

$$\dot{x}_{i+1} \approx \dot{x}_i + [(1-\gamma)\Delta t]\ \ddot{x}_i + (\gamma\ \Delta t)\ \ddot{x}_{i+1} \tag{4-77}$$

$$x_{i+1} \approx x_i + (\Delta t)\dot{x}_i + \left[\left(\frac{1}{2} - \beta\right)(\Delta t)^2\right]\ \ddot{x}_i + [\beta(\Delta t)^2]\ddot{x}_{i+1} \tag{4-78}$$

Before introducing the incremental time-stepping terms, a brief explanation of the constants γ and β is warranted. The constants γ and β are the quadrature parameters, and they can be tuned to obtain unconditionally stable, numerically dissipative algorithms with second order accuracy.

The quadrature parameters can take on a range of values that influence stability and accuracy of the method, based on whether the system is damped or undamped, and depending on the size of the time step. For a linear system, the method is stable if $2\beta \geq \gamma \geq 1/2$, regardless of the size of the time step.

In most cases, the selection of $\gamma = 1/2$ and a value of $\beta = 1/4$ makes the algorithm implicit and provides second order accuracy. These values are suitable from all aspects because they ensure unconditional stability with the highest accuracy. In this study, the acceleration within the time interval $[t_i, t_{i+1}]$ was presumed to be a constant average. That approach is known as constant average acceleration, where $\ddot{x}(\tau) = \frac{1}{2}(\ddot{x}_{i+1} + \ddot{x}_i)$. In this implicit approach, the state of the system is computed from information from the current state (i) as well as the future state ($i + 1$). Next, the time stepping algorithm is presented.

The time stepping algorithm for the method was formulated by solving for acceleration in (4-77) and velocity in (4-78) and then introducing the incremental terms for displacement, velocity, and acceleration. The resulting expressions are shown below.

$$\ddot{x}_{i+1} - \ddot{x}_i \approx \frac{1}{\beta(\Delta t)^2}(x_{i+1} - x_i) - \frac{1}{\beta(\Delta t)}\dot{x}_i - \frac{1}{2\beta}\ddot{x}_i \tag{4-79}$$

$$\dot{x}_{i+1} - \dot{x}_i \approx \frac{\gamma}{\beta(\Delta t)}(x_{i+1} - x_i) + \frac{\gamma}{\beta}\dot{x}_i + \Delta t\left(1 - \frac{\gamma}{2\beta}\right)\ddot{x}_i \tag{4-80}$$

The application of the Newmark-Beta method to the mass-spring-damper concept began with the discretization of the summation-of-the-forces equation. That modified version of (4-3) included the restoring load term, 'R', and the term for the external load, 'F', as follows:

$$\boldsymbol{M}\ddot{x}(t) + \boldsymbol{C}\dot{x}(t) + \boldsymbol{K}x(t) + \boldsymbol{R}(x(t), \dot{x}(t)) = \vec{F}_{ext}(t) \tag{4-81}_{29}$$

In (4-81), **M** was the mass matrix, **C** was the damping matrix, **K** was the stiffness matrix, **R**(x, ẋ) represented the restoring forces, and $\vec{F}_{ext}$ was the external dynamic load vector. The discretization process involved substituting (4-79) and (4-80) into (4-81) over the time step $i + 1$. In the interest of conciseness,

the left-hand sides of (4-79) and (4-80) were rewritten prior to insertion into (4-81). The expressions for the incremental terms in [(4-79) and (4-80)] were expressed as follows [29]:

$$\delta x_i = x_{i+1} - x_1 \tag{4-82a}$$

$$\delta \dot{x}_i = \dot{x}_{i+1} - \dot{x}_i \tag{4-82b}$$

$$\delta \ddot{x}_i = \ddot{x}_{i+1} - \ddot{x}_i \tag{4-82c}$$

Using the convention from (4-82a/b/c), (4-79) and (4-80) were rewritten as shown below [29].

$$\delta \ddot{x}_i \approx \frac{1}{\beta(\Delta t)^2}\,\delta x_i - \frac{1}{\beta(\Delta t)}\dot{x}_i - \frac{1}{2\beta}\ddot{x}_i \tag{4-83}$$

$$\delta \dot{x}_i \approx \frac{\gamma}{\beta(\Delta t)}\,\delta x_i - \frac{\gamma}{\beta}\dot{x}_i + \Delta t\left(1 - \frac{\gamma}{2\beta}\right)\ddot{x}_i \tag{4-84}$$

Now, returning to the discretization of (4-81) over the time step $i + 1$, that equation was restructured using the abridged incremental terms as illustrated below.

$$M\delta \ddot{x}_i + C\delta \dot{x}_i + K\delta x_i + \delta R_i = \delta F_i \tag{4-85}$$

Then, making the substitutions of (4-83) and (4-84) into (4-85) led to:

$$M\left(\frac{\delta x_i}{\beta(\Delta t)^2} - \frac{\dot{x}_i}{\beta(\Delta t)} - \frac{1}{2\beta}\ddot{x}_i\right) + C\left[\frac{\gamma}{\beta(\Delta t)}\,\delta x_i - \frac{\gamma}{\beta}\dot{x}_i + \Delta t\left(1 - \frac{\gamma}{2\beta}\right)\ddot{x}_i\right] + K\delta x_i + \delta R_i = \delta F_i \tag{4-86}$$

The next steps involved regrouping the terms in (4-86) and solving for the incremental displacements.

$$M\left(\frac{\delta x_i}{\beta(\Delta t)^2}\right) - M\left(\frac{\dot{x}_i}{\beta(\Delta t)}\right) - M\left(\frac{\ddot{x}_i}{2\beta}\right) + C\left(\frac{\gamma\delta x_i}{\beta(\Delta t)}\right) + C\left[-\frac{\gamma\dot{x}_i}{\beta} + \Delta t\left(1 - \frac{\gamma}{2\beta}\right)\ddot{x}_i\right] + K\delta x_i + \delta R_i = \delta F_i \tag{4-87}$$

$$M\left(\frac{\delta x_i}{\beta(\Delta t)^2}\right) + C\left(\frac{\gamma\delta x_i}{\beta(\Delta t)}\right) + K\delta x_i = \delta F_i - \delta R_i + M\left(\frac{\dot{x}_i}{\beta(\Delta t)}\right) + M\left(\frac{\ddot{x}_i}{2\beta}\right) - C\left[-\frac{\gamma\dot{x}_i}{\beta} + \Delta t\left(1 - \frac{\gamma}{2\beta}\right)\ddot{x}_i\right] \tag{4-88}$$

$$\left[\frac{M}{\beta(\Delta t)^2} + \frac{C\gamma}{\beta(\Delta t)} + K\right]\delta x_i = \delta F_i - \delta R_i + M\left(\frac{\dot{x}_i}{\beta(\Delta t)}\right) + M\left(\frac{\ddot{x}_i}{2\beta}\right) + \left[\frac{C\gamma}{\beta}\dot{x}_i - C\Delta t\left(1 - \frac{\gamma}{2\beta}\right)\ddot{x}_i\right] \tag{4-89}$$

$$\left[\frac{M}{\beta(\Delta t)^2} + \frac{C\gamma}{\beta(\Delta t)} + K\right]\delta x_i = \delta F_i - \delta R_i + \left[\frac{M}{2\beta} - C\Delta t\left(1 - \frac{\gamma}{2\beta}\right)\right]\ddot{x}_i + \left(\frac{M}{\beta(\Delta t)} + \frac{C\gamma}{\beta}\right)\dot{x}_i \tag{4-90}$$

Now, let $\beta = 1/4$ and $\gamma = 1/2$ in (4-90) to yield:

$$\left[\frac{4M}{(\Delta t)^2} + \frac{2C}{(\Delta t)} + K\right]\delta x_i = \delta F_i - \delta R_i + (2M)\ddot{x}_i + \left(\frac{4M}{(\Delta t)} + 2C\right)\dot{x}_i \tag{4-91}$$

The terms on either side of the equal sign in (4-91) were elements of the function that formed the input argument for the solver in the Matlab®. The difference between the left-hand side (LHS) and right-hand side (RHS) of (4-91) was known as the residual. The method iterated to converge on the dynamic equilibrium condition by finding displacement and velocity values that satisfied the balance in (4-91) at each time step. To derive the time stepping expressions for the direct integration method, first (4-78) had to be expanded and rewritten using (4-82a/c), which led to the expression below.

$$\delta x_i = \Delta t \dot{x}_i + \frac{(\Delta t)^2}{2} \ddot{x}_i + (\Delta t)^2 \beta \delta \ddot{x}_i \tag{4-92}$$

Then, for the time stepping expression in the analysis, (4-78) became the term shown below. The RHS of (4-92) was equivalent to all the terms on the RHS of (4-78) except for the variable x_i.

$$x_{i+1} \approx x_i + \delta x_i \tag{4-93}$$

The terms in (4-79) and (4-80) were manipulated by moving the current time step from the LHS to the RHS. Then, after some algebraic manipulation, the LHS of (4-92) was used to reduce the number of terms in each equation, which produced the following expressions:

$$\ddot{x}_{i+1} = \frac{1}{\beta(\Delta t)^2} \delta x_i - \frac{1}{\beta(\Delta t)} \dot{x}_i + \left(1 - \frac{1}{2\beta}\right) \ddot{x}_i \tag{4-94}$$

$$\dot{x}_{i+1} = \frac{\gamma}{\beta(\Delta t)} \delta x_i + \left(1 - \frac{\gamma}{\beta}\right) \dot{x}_i + \Delta t \left(1 - \frac{\gamma}{2\beta}\right) \ddot{x}_i \tag{4-95}$$

The expressions represented by (4-77), (4-78), (4-93), (4-94), and (4-95) were included in the iterative process of the numerical analysis and formed the basis for implementing the Newmark-β direct integration

method to perform the time-stepping simulation. The equations of motion for the SDOF model were based on the same principle of relative relationships that were exhibited in (4-62) and (4-64).

Focusing on the SDOF model for the time being, (4-81) was rewritten to accommodate for the relative relationship between the payload and the platform during base excitation. The resulting equation with the representative terms is shown in (4-96). In the numerical analysis, the element 'R', was used to incorporate the seat spring restoring and damping forces. Table 4-8 itemizes the definitions of the expressions for the damping, spring, and external forces.

$$m\ddot{z}(t) + c_1\dot{z}(t) + R\big(z(t)\,,\dot{z}(t)\big) = F_{ext}(t) \tag{4-96}$$

Table 4-8: Definitions of Forces for Numerical Analysis

Forces Defined in Numerical Analysis	
Expression	Definition
$c_1\,\dot{z}(t)$	Seat damping
$R\,\dot{z}(t)$	$c_2(\dot{z}+\dot{y}_{accel})^2 \text{sign}(\dot{z}+\dot{y}_{accel})$ [Other damping effects]
$R\,z(t)$	$k_1 z + k_2 z^2$ [Polynomial for spring stiffness]
$F_{ext}(t)$	$-m\dot{y}_{accel} - mg$

The items in Table 4-8 and the time step and the iteration expressions ((4-77), (4-78), (4-93), (4-94), and (4-95)) were the input arguments for the Matlab® solver. The $\dot{y}_{accel}$ variable was the input velocity derived from the accelerometer located on the platform. Subsequently, it was used to derive the platform displacement for implementation of the relative relationship terms.

In summary, the Newmark-β method sequentially updated the simulated displacement, velocity, and acceleration of the system based on the optimization of the elements of the equation of motion to achieve equilibrium between the LHS and RHS of (4-91).

4.3 Summary

This chapter provided an in-depth look at the mass-spring-damper concept used to form the mathematical basis for the analytical representation of the shock mitigation seat system. The single degree of freedom (SDOF) and the two degree of freedom (2DOF) models were examined. It was shown that, in correlation to a shock mitigation seat, the chief difference between the two models was that the SDOF model treated the seat and occupant as a single translational lumped-mass element, while the 2DOF model characterized the seat and occupant as separate entities with some dynamic interaction. The 2DOF model adopted the notion that the seat cushion functioned as an active translational spring-damper element.

The equations of motion, and the subsequent differential equations, were derived by applying Newton's law to the free body diagrams of the models. The idea of using an impact analysis was also broached. The impact analysis incorporated simplified versions of the equations based on the acceleration due to gravity and the drop height. The impact model only applied to SDOF systems, and several assumptions had to be made to implement the impact method. There was a brief discussion that addressed the relevance of representing the test seat as either a SDOF or a 2DOF model. The characteristics of the seat suggested that either approach was valid. The discussion remains open and is resolved when the numerical model is discussed in Chapter 6.

The inability of the drop tower to simulate the non-vertical motion associated with a wave slam was resolved because the tower aptly replicates the main component of the wave slam, which is the vertical pulse. Also, the test seat was designed to mitigate shock pulses in the vertical axis only, so the tower limitation did not undermine the analysis. The closing section of the chapter covered applying the state space representation to the system, and it introduced the Newmark-β time-stepping algorithm for direct integration. The equations and mathematical operations that formed the core for those techniques were explored, and the expressions that served as the input arguments for the numerical analysis were identified.

In the ensuing chapter, the findings of the experimental analysis are discussed. The main themes in the upcoming chapter are the repeatability of the function of the drop tower and a comparison of the seat

MR values for the three payload weights at the severity threshold levels. The overarching objective was to use all the available empirical and derived data to rate the seat for use in a specific class of HSC. Coverage on a statistical analysis that was conducted on the empirical data to determine the level of repeatability of the drop tower is presented. The impact method is explored to determine how velocity and energy values calculated using that approach compared to similar values derived using numerical integration of the acceleration time histories. The closing topic addresses the findings of a supplementary task that evaluated certain system characteristics using a limited analytical modal analysis.

Chapter 5. Laboratory Single Impact Testing of Shock Mitigation Seat

One area of emphasis during the experimental analysis was to implement the test procedure outlined earlier in Chapter 3. In particular, the intent was to execute the steps in Table E-1 in Appendix E. Albeit an idealized list, iterating through the items in the table was the precursor to establishing the repeatability of using a drop tower in a laboratory setting to simulate a wave slam event, which was an affirmed objective of the study. Of course, a statistical examination of the tower performance was necessary to actually quantify the repeatability of the method. The empirical data post processing tasks and the procedure to develop the mitigation ratios were conducted concurrently with the laboratory drop tests. A total of 114 tests were conducted, but not all of them were fully processed and used towards appraising the seat.

Some of the non-participating tests were used to evaluate certain aspects of the DAQ system and the software features. Other tests were used as system health checks to ensure that the tower was functioning as it should have been. The results from 80 of the tests were used as the data sets for the study. Some of those contributed to the mitigation ratio peak (MR_{PEAK}) calculations, while others were used to determine the mitigation ratio for the shock response spectrum (MR_{SRS}). Still, others were used to determine what test configuration was able to come close to simulating loads in the realm of those observed in at sea wave slam events.

This chapter covers the results of the experimental analysis as they pertain to achieving the stated objectives of the study. The calculated MR values are presented, and the rating of the seat based on those values and the associated severity threshold levels are provided. The results of using the impact method to determine how much energy was dissipated in the sand is also covered. Finally, the chapter will close with an overview of the system characteristics founded on a brief analytical modal analysis.

5.1 Repeatability of The Drop Tower Method

Earlier, the advantage(s) of using a drop tower to simulate a wave slam event for the laboratory testing of a shock mitigation seat were listed. The major advantage in that list was the fiscal aspect, which is the fact that the drop tower is a more financially attractive alternative to at sea testing. However, not least among the items on the list was the notion that a drop tower offered a level of predictability and repeatability (consistency). At sea testing requires pre-test planning for the appropriate weather and sea state conditions, and even then it is difficult to predict what amplitude of wave slams would be encountered. In short, at sea testing is not a controlled environment.

The drop tower, when set to a specific test configuration (payload mass, drop height, etc.) should deliver close to the same outcome with each drop. That is, it should be evident that a specific test procedure and test configuration should produce a specific corresponding result. Consequently, the drop tower method theoretically provided a controlled environment that ensured repeatability. The word 'repeatability' has been used on more than one occasion in reference to the drop tower in this report. However, the question arose about what repeatability was in the context of this study and how was it going to be quantified.

After some deliberation on first how to define repeatability and how to quantify it, the idea surfaced to isolate what the drop tower was intended to do. The key was to identify to what level it did what it was intended to do and how consistently it did it at that level.

The drop tower in this study was used to simulate a wave slam event by delivering a vertical acceleration pulse to the base of the seat system. Therefore, the function of the drop tower was to produce an acceleration pulse. The indication of the level to which it performed that function was the peak acceleration amplitude measured at the base of the seat during each drop. To quantify the repeatability of the tower, a statistical analysis was conducted on a subset of the peak amplitude acceleration values measured at the base of the seat pedestal (input acceleration).

5.1.1 Normal Distribution of Peak Input Accelerations

It has been established that the drop tower's primary purpose was to produce an acceleration pulse to the base of the seat. However, to compute its feature of repeatability meant establishing a trend in the data. Thus, applying a normal distribution to the data was an appropriate measure.

In the field of statistics, continuous data is any form of numerical (quantitative) data derived from the measurement of a variable. Normal (Gaussian) distributions can be used to characterize variables that have real values (continuous data), but whose distributions are unknown. Typically, measurable quantities that are expected to be the result of more than one independent process, including measurement error, have normal distributions. When the premise of the normal distribution was applied to the drop tower, the peak input acceleration pulse was treated as the measured variable (continuous data), and the test procedure served as the independent factor.

Fundamentally, for impact analysis of a mass-spring-damper system when all other factors are held constant, the factors that influence the peak acceleration are the drop height and the mass. However, the effect of the drop height and the mass on the peak acceleration is more prominent when the collisions are near elastic. There was some energy dissipation, due to the sand, during an impact using the drop tower, so the collision was not near elastic. Therefore, other elements of the system (other than the drop height and the mass) could have contributed to the occurrence of modulation in the peak input acceleration measurements. The driving element of the peak input acceleration was the pulse-shaping device attached to the underside of the tower platform.

From the test data, a set of 54 drop tests results were used to evaluate the repeatability of the drop tower method. The data set was divided into two subsets, which included a set of 27 test results using the wedge as the pulse-shaping device and a set of 27 test results using the five tines as the pulse-shaping device. Each of the two subsets consisted of nine drops at each of the three payload mass values. The steps outlined in Table E-1 were followed precisely for every drop test. The aim was to test to the severity threshold levels corresponding to HSC Classes 3 and 4, so the platform was raised to the maximum height

of 1.397 m (4.583 ft) above the top edge of the sandbox for every drop test. Therefore, for the 54 data points, the peak input acceleration was the dependent variable, the test procedure, the drop height, and the impact surface were the constant variables, and the pulse-shaping device and the payload mass were the independent variables. The findings revealed that the data for the wedge was more evenly distributed (a very slight negative skew) than the data for the tines. The data for the tines had a positive skew due to the fact that the mass of the distribution was concentrated on the left side of the figure with a longer right tail.

Wedge Input Acceleration Distribution

The highest measured peak input acceleration value when the wedge was used as the pulse-shaping device was 8.17517 g, the lowest measured value was 5.54966 g, and the mean peak acceleration value was 6.93156 g. The data point values were similar across all three masses. The payload mass did not seem to have a significant effect on the amplitude of the peak acceleration values, which was evident with the low standard deviation value of 0.64919. Interestingly, both the highest and the lowest measured peak acceleration input values occurred with the heaviest payload mass of 112.76 kg (248.6 lb). The second and third lowest values occurred with the 83.5 kg (184.0 lb) mass. The average measured peak acceleration pulse duration times across all of the 27 drop tests was 0.1223 seconds. Therefore, the acceleration pulse time duration satisfied the requirement for all levels of the severity threshold and based on the mean peak acceleration value of 6.93156 g, the wedge consistently performed at a severity threshold level between levels four and five. Consequently, the drop tower, when equipped with the wedge, could be used to test a shock mitigation seat that was intended for use in HSC Classes 3 and 4 at a severity threshold level of four.

Figure 5-1 portrays the normal distribution for the peak input acceleration values for the wedge. The distribution was fairly symmetric with a relatively inconsequential negative skew. Table 5-1 lists the statistical measures for the wedge data set. The table indicates that the data followed the 68-95-99.7 empirical rule well. The rule states that for a normal distribution, barring any overpowering effect of an external influence, 68%, 95%, and 99.7% of the measured values should fall within one, two, and three standard deviations of the mean, correspondingly. Figure 5-2 is a histogram that displays the occurrences

(frequency) with which specific 'bins' of peak input acceleration values occurred. Up next, is a review of the statistical analysis of the data from tests in which the five tines were the pulse-shaping device.

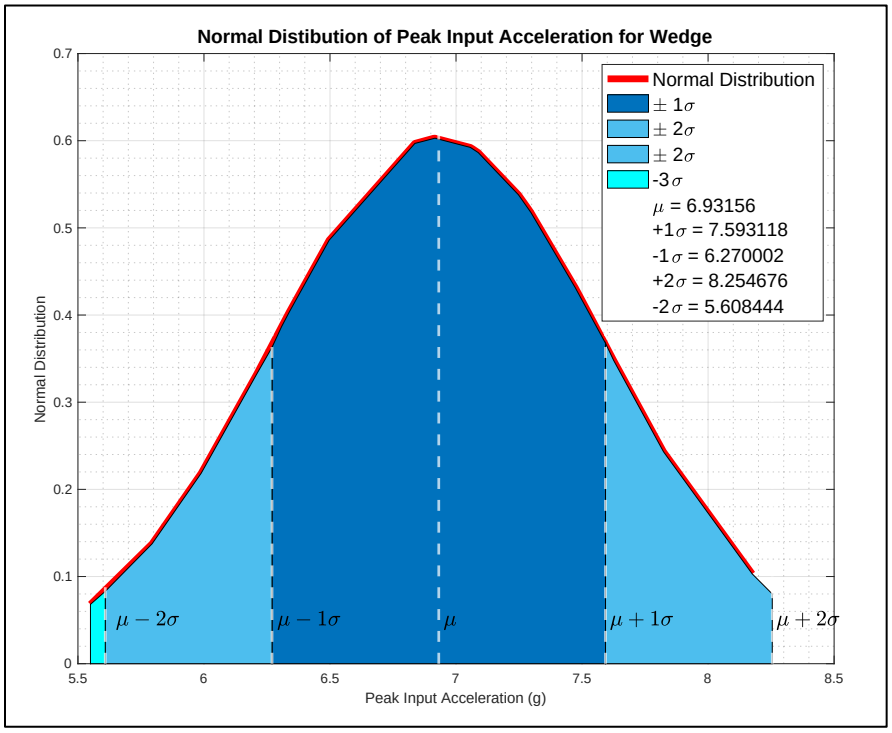

Figure 5-1: Normal Distribution of Peak Input Acceleration Values for Wedge

Table 5-1: Statistical Measures of the Peak Input Acceleration Values for the Wedge

Statistics for Peak Input Acceleration with Wedge	
Statistical Measure	Values
Mean $[\mu]$	6.93156 g
Median $[\nu]$	7.05701 g
Standard Deviation $[\sigma]$	0.64919
Skew	-0.31674
$[\mu - 1\sigma \leq \ddot{y} \leq \mu + 1\sigma]$	70.4% (Theoretical probability: 68.27%)
$[\mu - 2\sigma \leq \ddot{y} \leq \mu + 2\sigma]$	96.3% (Theoretical probability: 95.45%)
$[\mu - 3\sigma \leq \ddot{y} \leq \mu + 3\sigma]$	100% (Theoretical probability: 99.73%)

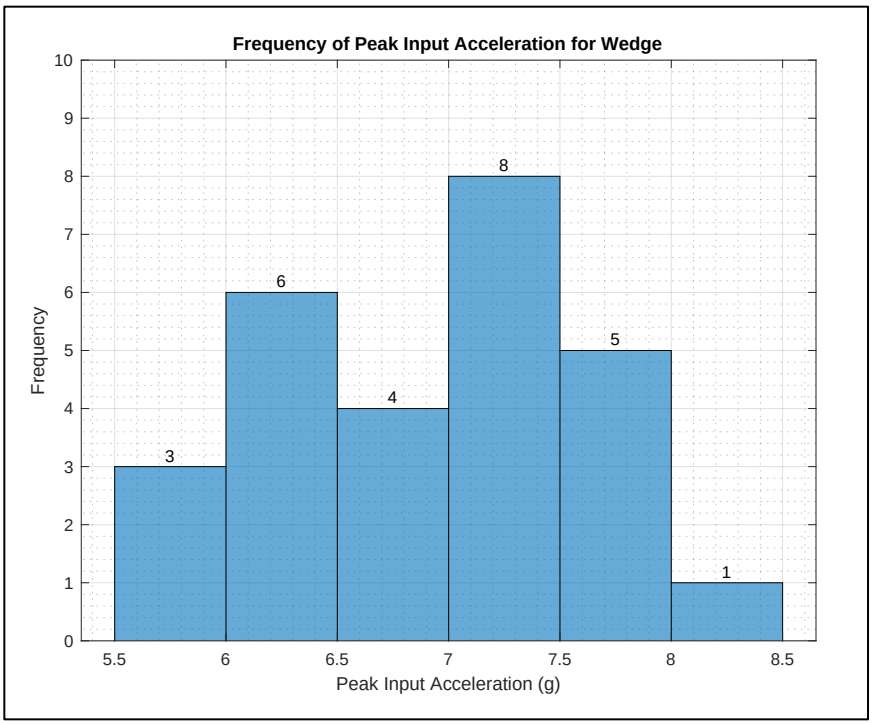

Figure 5-2: Frequency of Peak Input Acceleration Values for Wedge

Five Tines Input Acceleration Distribution

In general, the measured peak input acceleration values generated by the tines had higher amplitudes than those measured for the wedge. None of the peak acceleration values for the wedge were in excess of 8.2 g. In contrast, eight of the 27 measured peak input acceleration values for the tines were over 10 g with the highest value of 12.62 g and the second highest, at 12.38 g occurring during tests involving the 112.76 kg (248.6 lb) payload mass. Yet, similar to the wedge data values, the lowest amplitude peak acceleration value of 6.45 g also transpired during a test with the 112.76 kg (248.6 lb) mass. The mean peak acceleration value was 9.035 g. Again, as with the wedge, the payload mass did not seem to have any noteworthy effect on the amplitude of the peak acceleration values, except for the fact that the 49.6 kg (109.3 lb) payload had four instances of double-digit peak amplitude values, whereas the 83.5 kg (184.0 lb) and the 112.76 kg (248.6 lb) payloads had two each.

The standard deviation for the data set did exceed one with a value of 1.8096, which was an indication that the data points were spread further away from the mean value. In terms of meeting the severity threshold level based on the peak acceleration, ten of the values met the criteria for severity threshold level five, while eight of the values qualified for the highest level, six. The remainder of the values were applicable to severity threshold level four. The average acceleration pulse duration times across all of the 27 data points was lower than the average for the wedge at a time of 0.1101 seconds. Also, only one of the times that corresponded to the peak acceleration values above 10 g qualified for the minimum pulse duration time of 0.10 seconds recommended by the reference documents [6, 7].

The data suggested that while, on average, the five tines were able to produce higher input acceleration pulse amplitudes than the wedge, the time durations for those pulses were less than the time that was suggested by the ISO and NSWCCD documents. The reduced times did not come as a surprise though, as there was prior knowledge concerning the tradeoff between higher acceleration amplitudes and reduced pulse duration times when using the tines as the pulse-shaping device. Figure 5-3 portrays the normal distribution for the peak input acceleration values for the five tines. The distribution was not symmetric, as it contained a positive skew (right skewed). In addition, there were no data points beyond $\pm 2\sigma$. Table 5-2 lists the statistical measures for the five tines data set. The table indicates that the data deviated from the 68-95-99.7 empirical rule, with no data points beyond $\pm 2\sigma$, as illustrated in the figure for the distribution. Figure 5-4 is a histogram that displays the frequency with which specific ‘bins’ of peak input acceleration values occurred. The figure shows that 14 values occurred between 7 g and 9 g. and 25 values occurred above 7 g.

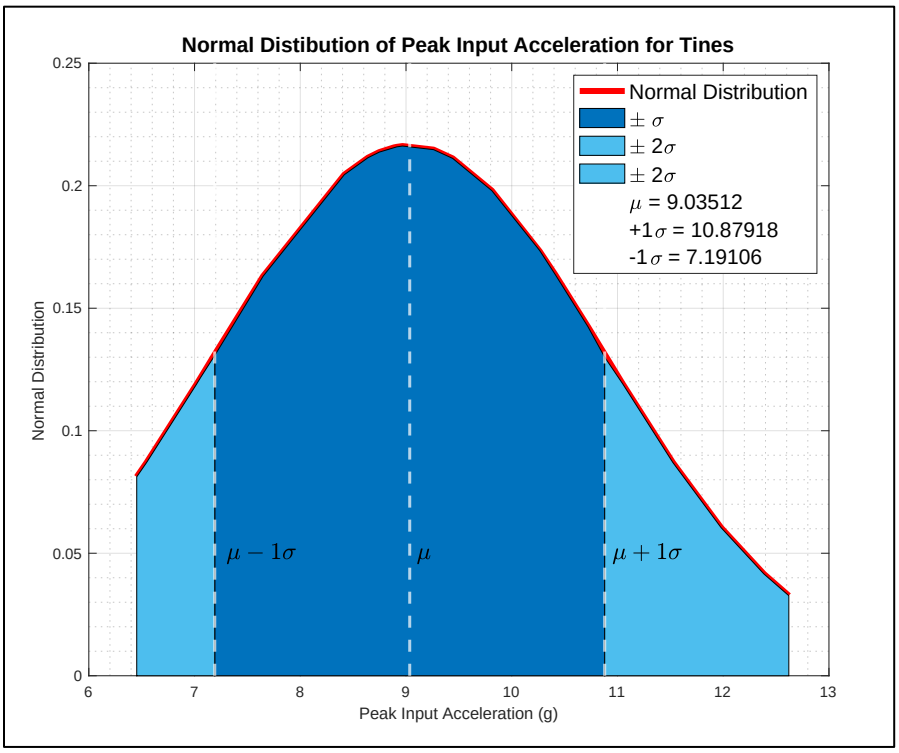

Figure 5-3: Normal Distribution of Peak Input Acceleration Values for Five Tines

Table 5-2: Statistical Measures of the Peak Input Acceleration Values for the Five Tines

Statistics for Peak Input Acceleration with Five Tines	
Statistical Measure	Values
Mean $[\mu]$	9.03512 g
Median $[\nu]$	8.88631 g
Standard Deviation $[\sigma]$	1.8096
Skew	0.41287
$[\mu - 1\sigma \leq \ddot{y} \leq \mu + 1\sigma]$	51.9% (Theoretical probability: 68.27%)
$[\mu - 2\sigma \leq \ddot{y} \leq \mu + 2\sigma]$	100% (Theoretical probability: 95.45%)
$[\mu - 3\sigma \leq \ddot{y} \leq \mu + 3\sigma]$	100% (Theoretical probability: 99.73%)

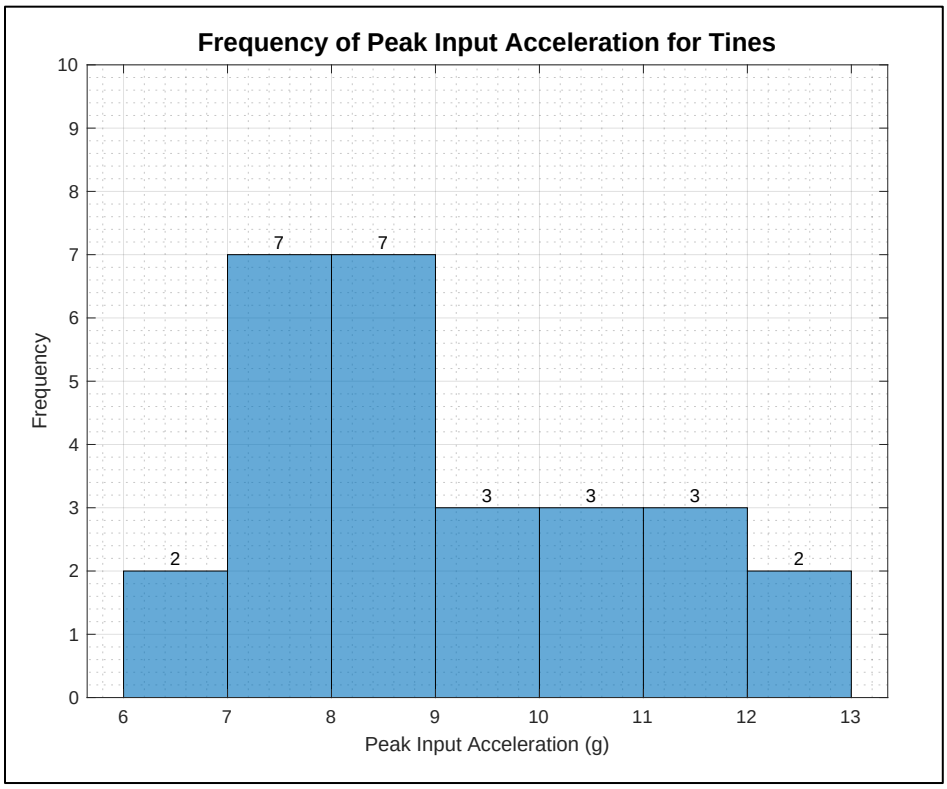

Figure 5-4: Frequency of Peak Input Acceleration Values for Five Tines

A few points of interest can be gleaned from a compilation of the findings. First, on average, using the tines resulted in higher peak input acceleration values than using the wedge. However, the tradeoff for the higher acceleration values was the reduced pulse duration times, which only impacted the tines' ability to meet the time requirement as per the reference documents and not necessarily the repeatability of the method. An additional outcome of the tests was that, although the standard deviation was low for the configuration with the tines, it was even lower when the wedge was used, suggesting that there was less spread in the data for the wedge. Finally, both approaches generated normal (or approximately normal) distributions.

The significance of the normal distributions for the drop tower method was that when the entire data set (54 data points) was considered, the greatest influence on the results was the pulse-shaping device, which was an internal system element. Therefore, there was no single external element that had a

substantially larger influence on the system than the rest of the inherent effects. Hence, it was reasonable to conclude that the drop tower method, when used to simulate a wave slam event, did offer an acceptable level of repeatability.

Tables 5-3 to 5-5 and Tables 5-6 to 5-8 itemize the peak input acceleration, pulse duration, and the correlated severity threshold level for each of the three payload masses for the 27-data-point wedge subset and the 27-data-point five tines subset, respectively. The entries in Tables 5-3 to 5-5 show that 23 of the 27 tests were rated at a severity threshold level of four. Hence, the data suggested that the drop tower was capable of consistently performing at a severity threshold level of four (HSC Class 3 and HSC Class 4-1). In addition, with the tines installed, it could test to severity threshold levels five and six (HSC Class 4-2 and HSC Class 4-3), albeit with a shortened pulse duration time. In the following section, the results that focused on the response of the seat are examined. The central topic in that discourse is the mitigation ratio (MR). Akin to this section, the segment categorizes the findings based on using the wedge and the tines as the pulse-shaping devices.

Table 5-3: Drop Tower Performance with the 49.6kg/109.3lb Payload w/Wedge

Tower Performance for 49.6 kg (109.3 lb) Payload w/Wedge		
Peak Input Acceleration (g)	Pulse Duration (s)	Severity Threshold Level
7.29697	0.1195	4
7.24763	0.1266	4
7.62569	0.1211	4
6.33931	0.1172	4
7.56260	0.1188	4
6.49677	0.1219	4
7.08821	0.1180	4
7.05701	0.1188	4
6.32639	0.1242	4

Table 5-4: Drop Tower Performance with the 83.5kg/184lb Payload w/Wedge

Tower Performance for 83.5 kg (184.0 lb) Payload w/Wedge		
Peak Input Acceleration (g)	Pulse Duration (s)	Severity Threshold Level
6.91030	0.1203	4
7.47309	0.1258	4
7.82320	0.1250	4
7.06630	0.1266	4
5.79417	0.1234	3
5.98898	0.1227	3
6.20921	0.1234	4
6.91643	0.1180	4
6.91631	0.1258	4

Table 5-5: Drop Tower Performance with the 112.76kg/248.6lb Payload w/Wedge

Tower Performance for 112.76 kg (248.6 lb) Payload w/Wedge		
Peak Input Acceleration (g)	Pulse Duration (s)	Severity Threshold Level
7.52305	0.1227	4
8.17517	0.1250	5
6.30829	0.1258	4
6.83688	0.1164	4
7.48170	0.1242	4
7.28415	0.1258	4
7.58978	0.1281	4
6.26494	0.1156	4
5.54966	0.1211	3

Table 5-6: Drop Tower Performance with the 49.6kg/109.3lb Payload w/Five Tines

Tower Performance for 49.6 kg (109.3 lb) Payload w/Five Tines		
Peak Input Acceleration (g)	Pulse Duration (s)	Severity Threshold Level
10.26415	0.0914	6
8.88631	0.0984	5
11.98011	0.0820	6
10.72098	0.0805	6
10.41249	0.0828	6
8.64026	0.1094	5
9.81150	0.0984	5
7.64891	0.1289	4
8.74702	0.1117	5

Table 5-7: Drop Tower Performance with the 83.5kg/184lb Payload w/Five Tines

Tower Performance for 83.5 kg (184 lb) Payload w/Five Tines		
Peak Input Acceleration (g)	Pulse Duration (s)	Severity Threshold Level
9.44145	0.1008	5
7.04463	0.1250	4
7.18417	0.1281	4
8.96689	0.1148	5
8.74767	0.0992	5
7.06172	0.1227	4
11.04693	0.0961	6
7.01719	0.1250	4
11.52376	0.0977	6

Table 5-8: Drop Tower Performance with the 112.76kg/248.6lb Payload w/Five Tines

Tower Performance for112.76 kg (248.6 lb) Payload w/Five Tines		
Peak Input Acceleration (g)	Pulse Duration (s)	Severity Threshold Level
7.03339	0.1242	4
6.54743	0.1383	4
8.91396	0.1227	5
12.38474	0.1008	6
7.17113	0.1336	4
6.45318	0.1313	4
8.41711	0.1188	5
9.26074	0.1141	5
12.62052	0.0961	6

5.2 Mitigation Ratio (MR)

The mitigation ratio was at the center of the experimental analysis of the seat. The response-input relationship (transmissibility) of that calculation provided a fundamental approach to discerning the performance of the seat. The acceleration time histories were used to calculate the MR_{PEAK}, and it was the ratio of the peak response acceleration amplitude of the payload to the peak input acceleration amplitude delivered to the base of the seat. The MR_{SRS}, on the other hand, was an indication of the seat's performance in the frequency domain. It was based on the responses of an array of linear SDOF systems to a base excitation. The MR_{SRS} was more useful as a range of values rather than a single value. The range corresponded to the frequency range for the response of the human body to rapidly applied accelerations. A total of 70 tests were used to generate the data for using the MR values to appraise the seat.

Each data point represented the MR value calculated for a designated payload mass with a specific damping setting for the seat. In accordance with the reference documents, three drop tests were conducted for each payload mass. Additionally, for each payload, tests were conducted with the seat damping set to either level one, three, or six. Using that cadence resulted in two subsets of 27 MR values each, one subset

for the wedge data and another for the tines data. The five-tines configuration was used for the 27-data-point tines subset. However, the remaining 16 MR values (to make up the 70 data point population) were a combination of two test setups, eight test with five tines and eight tests with three tines. The three tines produced even higher input acceleration pulse amplitudes than the five tines configuration produced. Before exploring the subject of the MR values, a minor but relevant detour into the topic of the filter cut-off frequency is necessary.

Data Filter Cut-Off Frequency

In the data processing section of Chapter 3, the topic of what filter cut-off frequency to use during post processing of the data was covered. There was a consensus among the guidance documents that collected data should be filtered before it was to be used in any analysis, including the calculation of the MR values. However, there was some ambiguity on what was considered an appropriate filter cut-off frequency. While most of the past studies that were cited in the NSWCCD reports focused on analysis of signals below 80 Hz (even below 20 Hz), the reports stated that the choice of the cut-off frequency should be based on the requirements of the associated research. In keeping with that trend of thought, the data was filtered to different cut-off frequencies to determine the value that was most appropriate for the needs of the study.

The data in question was the input data (measured by the accelerometer on the base of the seat pedestal [platform]) and the response data (measured by the accelerometer in the base of the payload). The compromise to be reconciled was to what frequency should the raw data have been filtered in order to discard the unwanted signal noise, but to still retain enough information to avoid excessively altering the shape of the acceleration pulse. The ‘butter’ function in Matlab® was used to implement a 4-pole Butterworth filter to compare the effects of using cut-off frequencies of 20 Hz, 80 Hz, 100 Hz, and 150 Hz. The test data for the comparison was the 49.6 kg (109.3 lb) payload with the seat damping level set to one at the maximum drop height of 1.397 m (4.583 ft).

Filtering down to any level below the sampling frequency offers the potential to alter the data in some way. However, the primary concern during this endeavor was to avoid filtering to a cut-off frequency

that would potentially change the amplitude of the acceleration pulse. Filtering to 20 Hz reduced the peak input acceleration amplitude by 1 g. At a cut-off frequency of 20 Hz, the plot was reduced to smooth lines that retained very little information from the original signal. At 150 Hz, the peak amplitude for the input acceleration was reduced by less than .5 g, and considerably more of the detailed characteristics of the signal was captured. As expected, filtering to frequencies of 80 Hz and 100 Hz resulted in outcomes somewhere in between the 20 Hz data and the 150 Hz data with 100 Hz having greater resolution than 80 Hz. The unfiltered payload response acceleration signal was less noisy in contrast to the platform input signal. Consequently, there was not much variation among the 80 Hz, 100 Hz, and the 150 Hz filtered payload response signals. Although the 20 Hz filtered payload response data did not capture some of the signal information, it still possessed a higher fidelity that the 20 Hz filtered platform input data.

Taking all the findings into consideration, the decision was made to filter the data using a cut-off frequency of 150 Hz. That frequency captured most of the payload response data without compromising too much of the platform input data. Figure 5-5 and Figure 5-6 depict the unfiltered platform input acceleration versus the filtered platform input acceleration for a cut-off frequency of 20 Hz and 150 Hz, respectively. Figure 5-7 and Figure 5-8 feature the unfiltered payload response acceleration versus the filtered payload response acceleration for a 20 Hz and 150 Hz cut-off frequency, respectively. The figures show that a substantial amount of information was removed when the data was filtered to 20 Hz. In contrast, the 150 Hz filter captured enough of the signal information to retain the shape of the curve. Coming up, is an examination of the MR values.

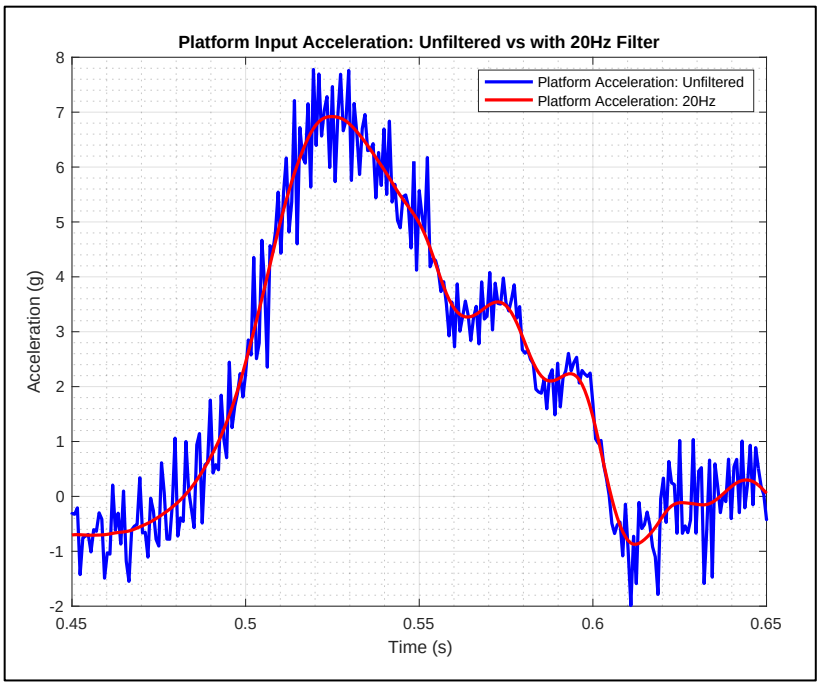

Figure 5-5: Unfiltered Platform Input Acceleration vs 20 Hz Filter

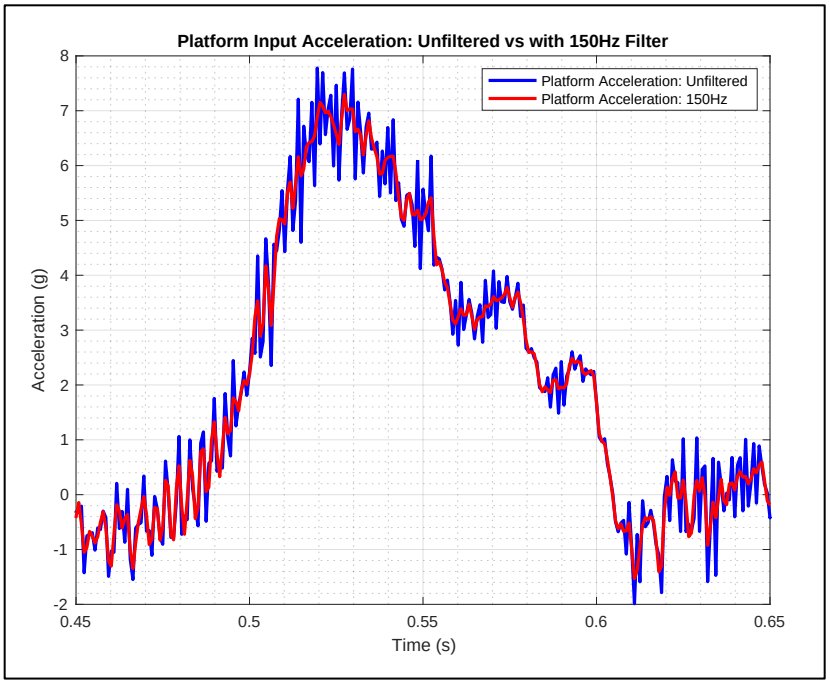

Figure 5-6: Unfiltered Platform Input Acceleration vs 150 Hz Filter

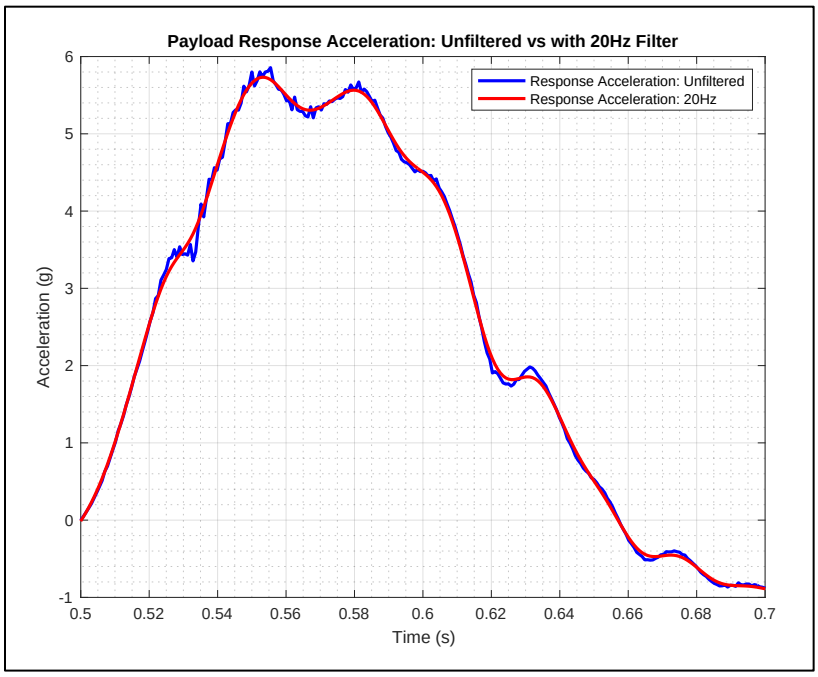

Figure 5-7: Unfiltered Payload Response Acceleration vs 20 Hz Filter

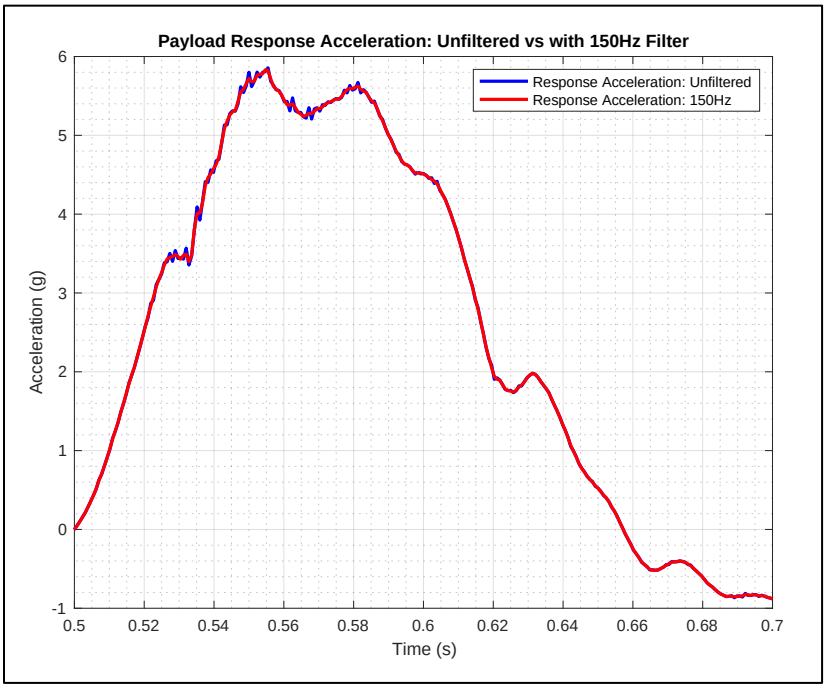

Figure 5-8: Unfiltered Payload Response Acceleration vs 150 Hz Filter

5.2.1 Mitigation Ratio Peak (MR_{PEAK})

As stated earlier, the MR_{PEAK} was exclusively concerned with the ratio of the maximum payload response acceleration to the maximum platform input acceleration (as expressed in (2-2)). As such, smaller MR values corresponded to more of the incoming acceleration pulse load being attenuated. The data was scrutinized to identify trends in the MR values and the peak response acceleration values that may have been linked to the payload mass and/or the seat damping level settings.

Wedge MR_{PEAK}

In an attempt to preserve the integrity of the results, and to establish a correlation with the evaluation of the tower, the same subset of 27 tests with the wedge that were used to evaluate the tower's repeatability, were also used to derive the MR values. The first feature of the data that was immediately noticeable was the consistency of the peak response of the seat regardless of the payload mass or the seat damping setting.

The NSWCCD reports cautioned against averaging the derived MR values for a subset of tests in the course of evaluating the performance of the seat. That proposal seemed rational, as each drop test was a unique entity, and the resulting input and response data were inherent to that test. Therefore, averages were not to be included in the tally used to assess the seat. Consequently, the references to statistical measures, such as the mean and the standard deviation, were used to detect trends in the empirical data, mainly to identify if the payload mass, or the seat damping setting, had any effect on the response of the seat. The statistical measures were not intended to convey the 'level' or 'quality' of seat's performance.

Across all three payload masses at each of the three damping levels (one, three, and six), the payload peak response acceleration (which was an indication of the seat's performance) remained within a very tight range of values irrespective of the peak platform input acceleration. The lowest payload peak response acceleration was 5.32168 g, which was measured during a test with the 112.76 kg (248.6 lb) payload with the seat damping level set to six. The platform input peak acceleration for that test was 6.26494 g. The MR_{PEAK} was 0.8494. Hence, the seat mitigated just over 15% of the incoming acceleration impulse load.

The highest payload peak response acceleration was 6.56259 g using the 83.5 kg (184.0 lb) payload, also at a damping level of six. The peak input acceleration for the platform for that drop was 6.9164 g. The resulting MR_{PEAK} was 0.9488, which was a 5% reduction in amplitude. The average payload peak response acceleration across all 27 tests was 5.66424 g, and there was very little spread in the data which was evident by the standard deviation value of 0.28659.

The average MR_{PEAK} value for each of the three payload categories was 0.7947 for the 49.6 kg (109.3 lb) payload, 0.8821 for the 83.5 kg (184.0 lb) payload, and 0.7957 for the 112.76 kg (248.6 lb) payload. The lowest MR_{PEAK} value was 0.6828 for the 112.76 kg (248.6 lb) payload with a seat damping setting of one. That equated to roughly a 32% attenuation of the incoming dynamic load. The highest and second highest MR_{PEAK} values belonged to the 83.5 kg (184.0 lb) payload with values of 0.9947 and 0.9944 respectively at a damping level of three. In fact, of the five MR values above 0.90, four came by way of the 83.5 kg (184.0 lb) payload with the fifth value calculated for the 112.76 kg (248.6 lb) payload. A review of all the wedge data disclosed that there was no definitive trend that could be identified. Stated differently, neither the payload mass, nor the seat damping level exerted more influence on the MR_{PEAK} values over the other. If any one factor was selected to have the strongest effect on the MR_{PEAK} values, it was the peak input acceleration.

The peak response acceleration of the seat was a more consistent variable than the peak input acceleration. Two of the three lowest peak input accelerations were for the 83.5 kg (184.0 lb) payload at 5.7942 g and 5.989 g. The third lowest peak input acceleration was measured for the 112.76 kg (248.6 lb) payload at 5.5497 g. Not surprisingly, those three values correspond to the three highest MR_{PEAK} values mentioned earlier. The next step was to discern what was to be inferred about the seat's performance from the aforementioned results.

The first step to getting an idea of how those results contributed to the appraisal of the seat was to express the seat's performance based in terms of the MR_{PEAK} values. The second was to assess the data for any trends that may have highlighted an apparent characteristic of the seat

Tables 5-9 to 5-11 list all the relevant data for the wedge subset for the three payload masses. An account of the items in the tables shows that, when the wedge was used as the pulse-shaping device, the tower was able to deliver a severity threshold level of four 23 out of 27 times. Of the remaining four tests, one was at a level five, and three were at a level three. The calculated MR_{PEAK} for the seat was less than unity (one) for every single test. The seat attenuated the incoming acceleration load at 10% or better (the best was 31.7%) for 22 of the 27 tests. The average percent mitigation was almost identical for the 49.6 kg (109.3 lb) and 112.76 kg (248.6 lb) payloads at 20.5% and 20.4%, respectively. It was 11.8% for the 83.5 kg (184 lb) payload. Therefore, it was declared with a certain level of confidence that the preliminary evaluation of the seat was that it was capable of diminishing incoming, vertical, dynamic loads within a range of 10% to 20% at a severity threshold level of four and below. Certainly, this assessment was only part of the overall seat evaluation, additional input (Tines data and MR_{SRS}) was still required to convey the complete story. One item to be resolved, though, was actually a hypothetical thought.

The difference in the lowest seat peak response, 5.3217 g, and the highest, 6.5626 g, was just over 1.2 g. In contrast, the difference between the highest and lowest peak input acceleration was just over 2.6 g. Thus, the seat responded in a somewhat similar manner despite the fluctuation in the peak input acceleration. Consequently, it seemed that the seat displayed a linear response within (or up to) a certain range of peak input acceleration values. That notion began as conjecture, but later seemed credible through a comparison of a five tines data set with a three tines data set.

Figure 5-9 is a bar graph showing the mean MR_{PEAK} values for each of the three payload masses. The mean MR_{PEAK} values were not intended to be used as a parameter to evaluate the seat but as a summarizing visual aid that complemented the data in the tables. Figure 5-10 shows selected tests from each payload category for the wedge with the associated MR_{PEAK} values. A review of the tines data follows, then a summary of the MR_{SRS} values is presented.

Table 5-9: Peak Response and MR_{PEAK} Values for 49.6 kg (109.3 lb) Payload w/Wedge

Response and MR_{PEAK} Values for 49.6 kg (109.3 lb) Payload w/Wedge						
Payload Mass (kg/lb)	Damp Level	Peak Input (g)	Severity Threshold Level	Peak Response (g)	MR_{PEAK}	Mitigation (%)
49.6/109.3	1	7.29697	4	5.83105	0.7991	20.1
49.6/109.3	1	7.24763	4	5.72962	0.7906	20.9
49.6/109.3	1	7.62569	4	5.57811	0.7315	26.9
49.6/109.3	3	6.33931	4	5.48141	0.8647	13.5
49.6/109.3	3	7.56260	4	5.37516	0.7108	28.9
49.6/109.3	3	6.49677	4	5.45071	0.8390	16.1
49.6/109.3	6	7.08821	4	5.40800	0.7630	23.7
49.6/109.3	6	7.05701	4	5.58778	0.7918	20.8
49.6/109.3	6	6.32639	4	5.45091	0.8616	13.8
Mean				5.54364	0.7947	20.5
Standard Deviation				0.1534	0.05412	5.10

Table 5-10: Peak Response and MR_{PEAK} Values for 83.5 kg (184.0 lb) Payload w/Wedge

Response and MR_{PEAK} Values for 83.5 kg (184 lb) Payload w/Wedge						
Payload Mass (kg/lb)	Damp Level	Peak Input (g)	Severity Threshold Level	Peak Response (g)	MR_{PEAK}	Mitigation (%)
83.5/184.0	1	6.91030	4	5.68732	0.8230	17.7
83.5/184.0	1	7.47309	4	5.78871	0.7746	22.5
83.5/184.0	1	7.82320	4	5.94973	0.7605	24.0
83.5/184.0	3	7.06630	4	5.81037	0.8223	17.8
83.5/184.0	3	5.79417	3	5.76149	0.9944	0.6
83.5/184.0	3	5.98898	3	5.95732	0.9947	0.5
83.5/184.0	6	6.20921	4	5.55941	0.8953	10.5
83.5/184.0	6	6.91643	4	6.56259	0.9488	5.1
83.5/184.0	6	6.91631	4	6.39849	0.9251	7.5
Mean				5.94172	0.8821	11.8
Standard Deviation				0.3314	0.0903	8.51

Table 5-11: Peak Response and MR_{PEAK} Values for 112.76 kg (248.6 lb) Payload w/Wedge

Response and MR_{PEAK} Values for 112.76 kg (248.6 lb) Payload w/Wedge						
Payload Mass (kg/lb)	Damp Level	Peak Input (g)	Severity Threshold Level	Peak Response (g)	MR_{PEAK}	Mitigation (%)
112.76/248.6	1	7.52305	4	5.67335	0.7541	24.6
112.76/248.6	1	8.17517	5	5.58166	0.6828	31.7
112.76/248.6	1	6.30829	4	5.54919	0.8797	12.0
112.76/248.6	3	6.83688	4	5.49285	0.8034	19.7
112.76/248.6	3	7.48170	4	5.51027	0.7365	26.4
112.76/248.6	3	7.28415	4	5.46454	0.7502	25.0
112.76/248.6	6	7.58978	4	5.61565	0.7399	26.0
112.76/248.6	6	6.26494	4	5.32168	0.8494	15.1
112.76/248.6	6	5.54966	3	5.35719	0.9653	3.5
Mean				5.50738	0.7957	20.4
Standard Deviation				0.1149	0.08799	8.30

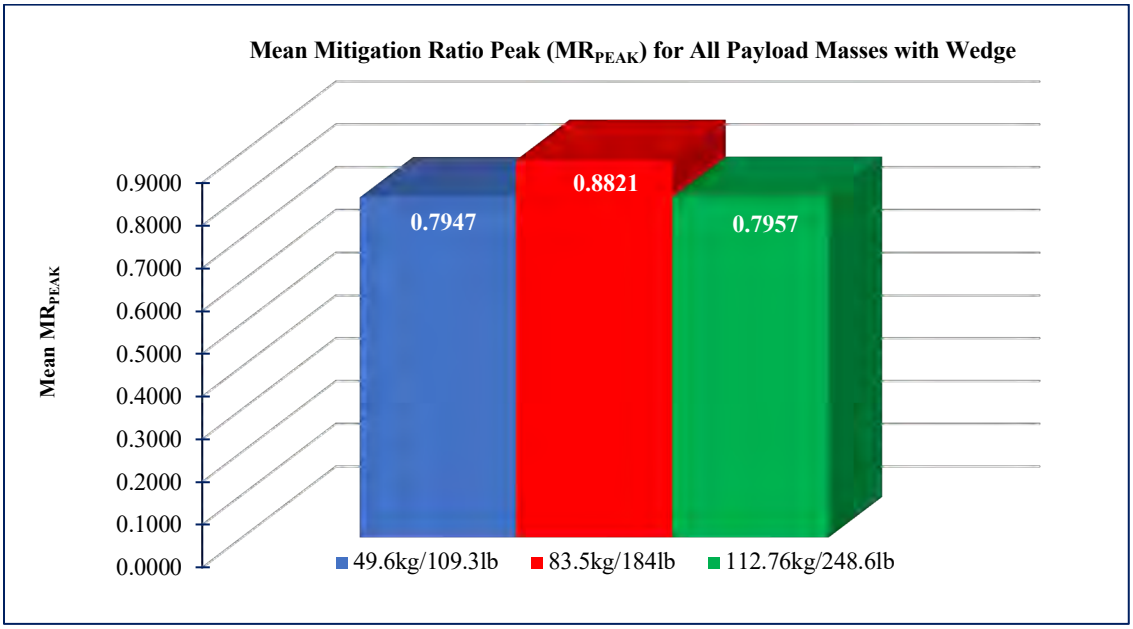

Figure 5-9: Mean MR_{PEAK} Value for All Three Payload Masses with Wedge

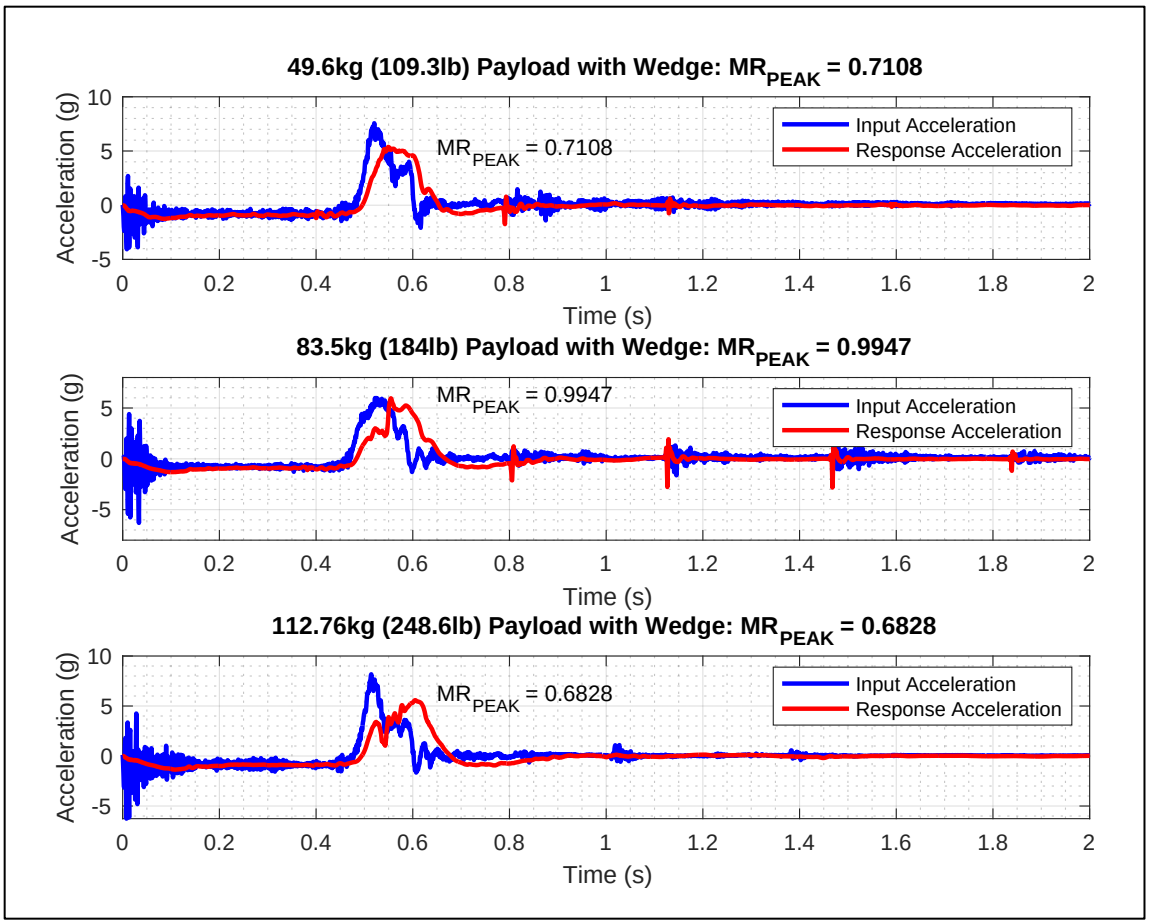

Figure 5-10: MR_{PEAK} Values for Selected Tests with the Wedge

Five Tines MR_{PEAK}

Two sets of test results were used as part of the tines data. The same tines subset of 27 tests that were used to evaluate the tower were used for the same reason as explained for the wedge data. That data set formed the basis for comparison with the wedge data. An additional set of 16 tests were conducted to ascertain whether there was any validity to the idea that the seat may have performed differently depending on the amplitude level of the input acceleration. The additional subset was comprised of eight tests with five tines and eight tests with three tines. The three tines delivered higher peak input accelerations, and so, those values served as the upper benchmark to test the assumption. There were higher amplitudes and more

variation in the peak response accelerations when the tines were used as the pulse-shaping device. Also, the MR_{PEAKS} values were lower overall.

In the 27-data-point subset for the five tines, there were eight instances in which the peak response accelerations were 7.00 g and above with three exceeding 8.00 g. In contrast, for the wedge, there were only two peak response values above 6.00 g and none at 7.00 g or above. As suspected, all but two of the response values above 7.00 g were linked to peak input accelerations above 10.00 g. However, there were some peak input accelerations that registered above 8.00 g that garnered peak responses only slightly above 5.00 g. Hence, there was more spread in the seat response data for the five tines. The highest recorded peak response acceleration was during a test for the 49.6 kg (109.3 lb) payload at a value of 8.65119 g with damping level three. That payload also had the second and third highest peak response values of 8.54494 g and 8.39750 g with damping levels of one and three respectively. Those values corresponded to peak input acceleration values of 10.721 g, 11.980 g, and 10.412 g, respectively. The lowest peak response occurred with the heaviest mass, as it did when the wedge was used.

The lowest peak response was 4.9405 g with the 112.76 kg (248.6 lb) payload. The damping setting for that test was level one. There were 10 instances in which the seat's peak response acceleration was measured at values between 5.00 g and 5.6 g, and six of those occurred with the 112.76 kg (248.6 lb) payload. The other four were measured during the tests with the 83.5 kg (184.0 lb) payload. The highest peak responses were measured during tests with the 49.6 kg (109.3 lb) payload, while the lowest peak responses were measured for the 112.76 kg (248.6 lb) payload. The values for the 83.5 kg (184.0 lb) payload were somewhere in the middle of the other two data sets. Unlike the results for the wedge, the five tines data displayed some correlation between the payload mass and the seat peak response acceleration. There was also a similar connection with the seat damping, but that relationship was more apparent when the MR_{PEAK} values were considered.

Dissimilar to the wedge MR_{PEAK} values, the lowest calculated MR_{PEAK} values were associated with the damping level setting of six for the five tines data. For each payload category, the lowest MR_{PEAK} value occurred when the seat damping level was set to six. The lowest calculated MR_{PEAK} value for the 49.6 kg

(109.3 lb) payload was 0.7039 with a damping level of six. For the 83.5 kg (184.0 lb) payload, the lowest MR_{PEAK} value was 0.6313, also at a damping level of six. Finally, a MR_{PEAK} value of 0.5006 was derived for the 112.76 kg (248.6 lb) payload with a damping level of six. Those values symbolized 30%, 37%, and 50% mitigation rates, respectively, for the seat. Interestingly, and exactly like the wedge data, the 112.76 kg (248.6 lb) payload had the lowest and the third highest MR_{PEAK} values of 0.5006 and 0.8014 respectively. The highest, 0.8069, and second highest, 0.8065, were calculated for the 49.6 kg (109.3 lb) payload. The lowest MR_{PEAK} value group average was 0.6621 for the 112.76 kg (248.6 lb). The average for the 49.6 kg (109.3 lb) payload was 0.7653, and the average was 0.7068 for the 83.5 kg (184.0 lb) payload. The average percent mitigation for the 49.6 kg (109.3 lb) payload was 23.9%. The average percent mitigation for the 83.5 kg (184.0 lb) and the 112.76 kg (248.6 lb) payloads were 28.3% and 31.8%, respectively. Therefore, based on the statistical measures, the seat seemed to attenuate more of the incoming dynamic load when the peak input accelerations were higher. There was a caveat associated with the lower MR_{PEAK} and higher percent mitigation values though.

Nine of the MR_{PEAK} values were calculated from data points for which the pulse duration times were under the suggested 0.10 seconds. Hence, those MR_{PEAK} values were considered invalid. Tables 5-12 to 5-14 itemize the data for the 27-data-point five tines subset. The data entries with the asterisk in the 'Severity Threshold Level' column did not meet the pulse duration time requirement. The mean percent mitigation ratios with the asterisk were calculated using the tests that did not meet the pulse duration requirement. However, those values were still similar to the mean percent mitigation ratios derived from using just the valid tests. That occurrence was an indication of the consistency of the seat's performance.

Table 5-12: Peak Response and MR_{PEAK} Values for 49.6 kg (109.3 lb) Payload w/Tines

Response and MR_{PEAK} Values for 49.6 kg (109.3 lb) Payload w/5 Tines						
Payload Mass (kg/lb)	Damp Level	Peak Input (g)	Severity Threshold Level	Peak Response (g)	MR_{PEAK}	Mitigation (%)
49.6/109.3	1	10.26415	6*	7.80640	0.7606	23.9*
49.6/109.3	1	8.88631	5*	7.02667	0.7907	20.9*
49.6/109.3	1	11.98011	6*	8.54494	0.7133	28.7*
49.6/109.3	3	10.72098	6*	8.65119	0.8069	19.3*
49.6/109.3	3	10.41249	6*	8.39750	0.8065	19.4*
49.6/109.3	3	8.64026	5	6.82095	0.7894	21.1
49.6/109.3	6	9.81150	5*	7.14225	0.7279	27.2*
49.6/109.3	6	7.64891	4	6.03401	0.7889	21.1
49.6/109.3	6	8.74702	5	6.15721	0.7039	29.6
Mean				7.3979	0.7563	23.9/23.5*
Standard Deviation				0.9993	0.0405	3.82

Table 5-13: Peak Response and MR_{PEAK} Values for 83.5 kg (184.0 lb) Payload w/Tines

Response and MR_{PEAK} Values for 83.5 kg (184 lb) Payload w/5 Tines						
Payload Mass (kg/lb)	Damp Level	Peak Input (g)	Severity Threshold Level	Peak Response (g)	MR_{PEAK}	Mitigation (%)
83.5/184.0	1	9.44145	5	6.55246	0.6940	30.6
83.5/184.0	1	7.04463	4	5.11805	0.7265	27.4
83.5/184.0	1	7.18417	4	5.45360	0.7591	24.1
83.5/184.0	3	8.96689	5	6.04264	0.6739	32.6
83.5/184.0	3	8.74767	5*	6.88862	0.7875	21.3*
83.5/184.0	3	7.06172	4	5.05855	0.7163	28.4
83.5/184.0	6	11.04693	6*	6.97427	0.6313	36.9*
83.5/184.0	6	7.01719	4	5.13314	0.7315	26.9
83.5/184.0	6	11.52376	6*	7.38319	0.6407	35.9*
Mean				6.06717	0.7068	28.3/29.3*
Standard Deviation				0.91054	0.0520	4.90

Table 5-14: Peak Response and MR_{PEAK} Values for 112.76 kg (248.6 lb) Payload w/Tines

Response and MR_{PEAK} Values for 112.76 kg (248.6 lb) Payload w/5 Tines						
Payload Mass (kg/lb)	Damp Level	Peak Input (g)	Severity Threshold Level	Peak Response (g)	MR_{PEAK}	Mitigation (%)
112.76/248.6	1	7.03339	4	5.63660	0.8014	19.9
112.76/248.6	1	6.54743	4	4.94052	0.7546	24.5
112.76/248.6	1	8.91396	5	5.40088	0.6059	39.4
112.76/248.6	3	12.38474	6	7.00096	0.5653	43.5
112.76/248.6	3	7.17113	4	5.35100	0.7462	25.4
112.76/248.6	3	6.45318	4	5.12033	0.7935	20.7
112.76/248.6	6	8.41711	5	5.25659	0.6245	37.6
112.76/248.6	6	9.26074	5	5.24768	0.5667	43.3
112.76/248.6	6	12.62052	6*	6.31721	0.5006	49.9*
Mean				5.5876	0.6621	31.8/33.8*
Standard Deviation				0.6600	0.1126	10.62

In spite of the data points that were discarded due to the shortened pulse duration, the data exhibited a link between the MR_{PEAK} value and the payload mass.

The MR_{PEAK} value decreased as the payload mass increased, so clearly there was a relationship between the seat performance and the mass when the tines were used as the pulse shaping device. With the drop tower, the acceleration during a drop was due to gravity, which was a constant value. Thus, the only way to increase the momentum going into the sandbox was to either increase the drop height or the mass (shown by the acceleration impulse expressed by (4-52)). The drop height was constant, so to explore that notion of increasing the energy during the impact, tests with five and three tines were conducted with only the 112.76 kg (248.6 lb) payload with a seat damping level of one. The intent was to observe how the seat responded with the configuration that delivered the highest possible peak input accelerations and the softest damping setting.

Three Tines versus Five Tines Input Acceleration

The tines were not only capable of generating the near half-sine pulse shape required for the analysis, but because of the smaller profile, that configuration created higher input acceleration pulses than the wedge, as less energy was lost to the sand. For the same reason, three tines produced even higher input acceleration pulses than the five tines. The only compromise was that the pulse durations were less than the recommended 0.10 seconds (more so with three tines than with five). That was the rationale for not using drop tests with three tines to evaluate the tower. Therefore, the data in the inquiry to follow was not used to assess the seat, it was used to decipher whether the seat displayed a different response above a certain peak input acceleration range.

In at sea trials, wave slams in excess of 20 g have been observed, so using tines was one way to determine if the tower could achieve peak input accelerations in the vicinity of those real-world values. The configuration for all 16 tests (eight with five tines, and eight with three tines) was the 112.76 kg (248.6 lb) payload with a seat damping level of one at the maximum height allowed by the tower.

Six of the highest peak input accelerations values were achieved with three tines. Those values ranged from 15.89 g to 17.81 g. The two lowest peak input acceleration values transpired with tests involving the five tines setup. The values for the two lowest peak accelerations were 7.582 g and 9.179 g. Of the tests conducted with the three tines, a single test fulfilled the 0.10 second pulse duration requirement. That was for a drop with a peak input acceleration of 11.613 g. The rest were within the 0.07 – 0.08 second range. For the five tines, the two lowest peak input values met the pulse duration criteria, with times of 0.13 seconds and 0.11 seconds, none of the other tests satisfied the pulse duration time requirement. Those pulse duration values were around 0.09 seconds. The peak response acceleration values were higher for the test with three tines as well.

The highest amplitude peak response acceleration was 10.16 g, which corresponded to the second highest peak input of 17.507 g for a test with three tines. There were no peak response accelerations above 7.37 g for the five tine tests, and in fact, the two lowest response acceleration values were recorded for the five tines setup with values of 5.44 g and 5.67 g. Those two values were linked to the two lowest peak input

acceleration values. On the other hand, there were no response values lower than 6.9 g for the three tines data set, which seemed in line with the hypothesis. Not unexpected at all, were the lower figures for the MR_{PEAK} values.

Recall for the 27-point wedge and five tines data subsets, the lowest MR_{PEAK} values were calculated for the highest peak input accelerations. Consequently, it came as no surprise that the three tine/five tine data subset would produce the lowest average MR_{PEAK} values, as that data set had the highest measured peak input accelerations. The lowest MR_{PEAK} value was 0.50437 for the five tines data set. However, the highest MR_{PEAK} value was also calculated for the five tines data set. That value was 0.7175. Two of the three highest MR_{PEAK} values aligned with the two lowest peak input accelerations, which agreed with comparison between the wedge and five tines results. There were no MR_{PEAK} values above 0.634 for the three tines data, and the set contained the third lowest MR_{PEAK} value of 0.51626. Overall, the MR_{PEAK} values were lower for the entire subset. The group average MR_{PEAK} values were 0.56525 and 0.56337 for the three tines and five tines, respectively. Therefore, on average, the seat diminished up to 43% of the incoming acceleration pulse.

From an overview of the outcome, the peak response acceleration values for the five tines were lower to match the lower input accelerations. The peak response acceleration values were higher for the three tines tests because the peak input accelerations were higher, yet the group average MR_{PEAK} value was only 0.19% larger than the mean MR_{PEAK} value for the five tines tests. Also, there was more consistency in the peak response acceleration values when the peak input accelerations values were below approximately 8.00 g, as witnessed with the wedge data. Therefore, it could be construed that the seat had a fairly linear response when the input acceleration values were low (below 8.00 g) and a more adaptive response when the input acceleration values were higher (above 8.00 g). The lower calculated MR_{PEAK} values associated with the higher input accelerations for the 16-point data set, also corroborated the hypothesis.

At this point, the intermediate assessment of the seat was that it was officially capable of attenuating up to 30% of an incoming, vertically applied, dynamic load at a severity threshold level of four and below. Including the three tines and five tines data for which the pulse duration criteria was not attained, the seat

was unofficially capable of mitigating up to 40% of the incoming acceleration pulse at a severity threshold level of six and below. Figure 5-11 illustrates the average MR_{PEAK} for the 27-data-point data sets for the wedge and the five tines. The error bars represent the ±1 standard deviation error for each payload based on the combined mean MR_{PEAK} value for that payload across both the wedge and the five tines data set. The number in the column represents the individual MR_{PEAK} value for the payload. The 49.6 kg (109.3 lb) payload had the lowest standard deviation (0.021) from its combined mean MR_{PEAK} value (0.78) across the 18 data points (nine wedge plus nine five-tines). The 83.5 kg (184.0 lb) payload had the highest deviation (0.124) from its combined mean (0.79). The values for the 112.76 kg (248.6 lb) payload were 0.09 for the standard deviation and a combined mean MR_{PEAK} of 0.73. The graph for the standard error of the MR_{PEAK} values is given in Appendix A. Figure 5-12 shows selected tests for two of the payload categories for the five tines and one for the three tines with the associated MR_{PEAK} values. Notice that the test with the three tines achieved a peak input acceleration of 17 g. Up next is coverage of the MR_{SRS} analysis.

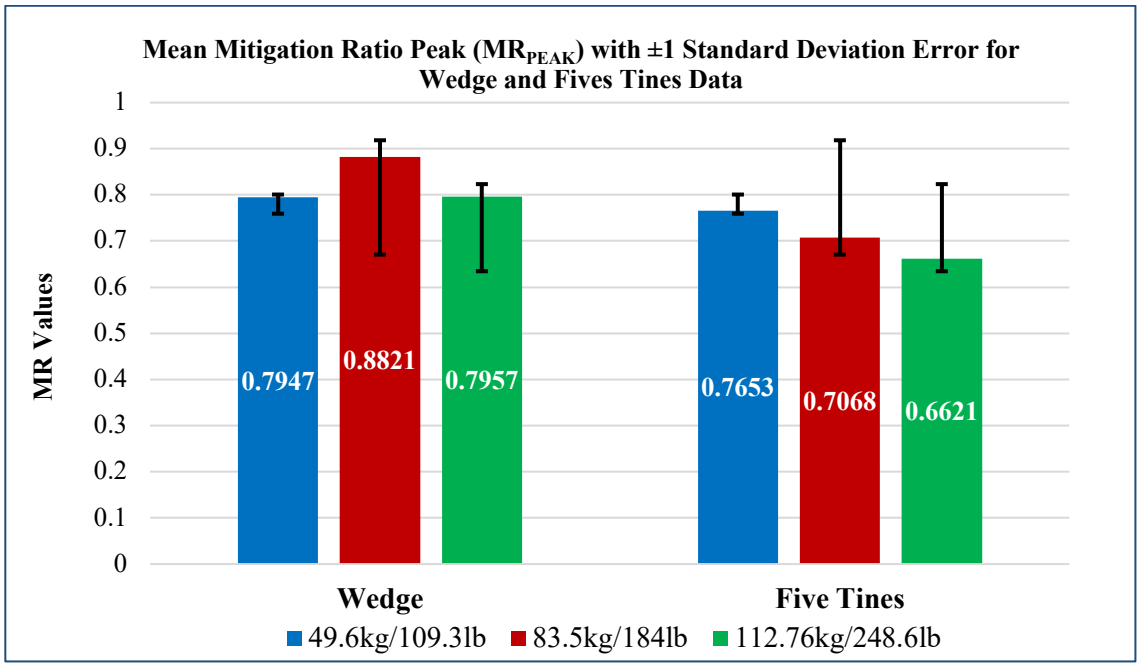

Figure 5-11: Mean MR_{PEAK} and Standard Deviation Error for Wedge and Five Tines per Payload

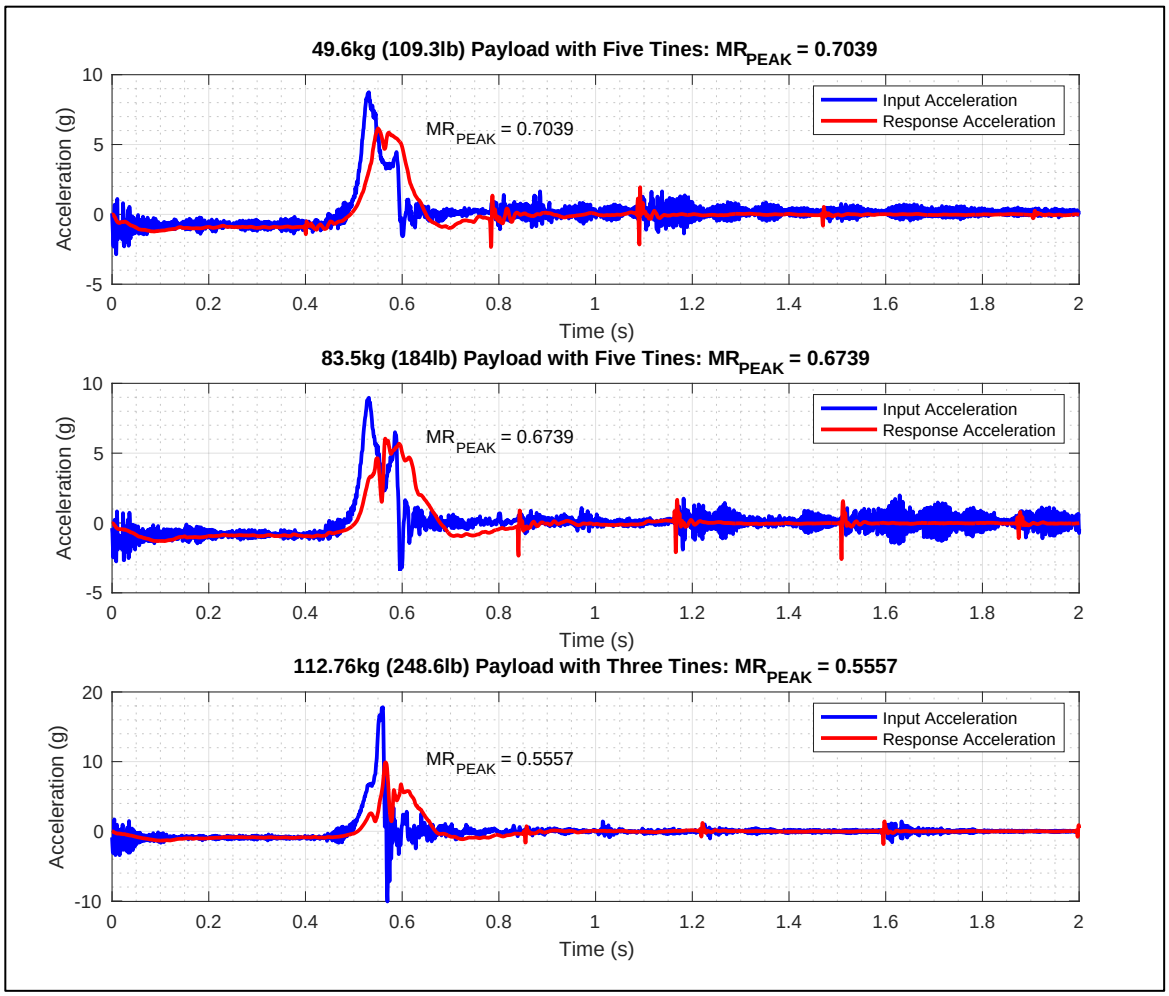

Figure 5-12: MR_{PEAK} Values for Selected Tests with Five and Three Tines

5.2.2 Mitigation Ratio Shock Response Spectrum (MR_{SRS})

Whereas the MR_{PEAK} was a glimpse of how the seat responded at a snapshot in time, the mitigation ratio shock response spectrum (MR_{SRS}) offered insight to the seat's performance over a range of frequencies. The SRS was a representation of the maximum responses of an array of linear SDOF systems to a base excitation such as a shock or an acceleration pulse. Subsequently, the variations in the maximum responses of the systems in the array were plotted against the natural frequency of each system. The advantage of the MR_{SRS} over the MR_{PEAK} was that the MR_{SRS} pointed to two pieces of information, including

the maximum response as well as the frequency at which the maximum response occurred. In this analysis, the frequency range of interest was 4 Hz to 10 Hz, as that range coincided with the frequency range of the response of the human body to rapidly applied accelerations pulses (some reference documents state the range could go up to 12 Hz).

The procedure to calculate the SRS usually begins with selecting the quality factor, Q. The quality factor is equivalent to the inverse of two times the damping ratio. However, as was previously noted, there was no damping (or stiffness) information available for the test seat. Thus, a decision was made to select a Q value of 10. Most reference texts state that using a value of 10 for the quality factor is a common practice when conducting a SRS analysis. The use of 10 for the Q value meant that the effective damping ratio across the array of SDOF systems was 0.05 (5%) for this analysis. The equations expressed in (5-1) and (5-2) describe the relationship of Q with regard to the equation of motion for a SDOF system exposed to base excitation and the system properties, respectively.

$$\ddot{z} + \frac{\omega_n}{Q}\,\dot{z} + \omega_n^2\, z = -\ddot{y} \tag{5-1}$$

$$Q = \frac{\sqrt{km}}{c} = \frac{1}{2\xi} \tag{5-2}$$

If an assumed value of around 28000 N/m was used for the seat's spring stiffness, and a lumped mass of the 112.76 kg (248.6 lb) payload plus the mass of the seat (41.80 kg (92.15 lb)), the damping coefficient was approximately 212 N*s/m, based on (5-2). Later, when the modal analysis is covered, it is shown that a credible approximation of the system damping was within a range of up to 10 times that value. The calculation of the MR_{SRS} was a bit different from the derivation of the MR_{PEAK}. Two data sets were used to generate the SRS values. First, a set of 10 tests were conducted using the same test configuration that was used for the eight-data-point five tines test, which was the 112.76 kg (248.6 lb) payload with a seat damping level of one at the maximum height allowed by the tower. The strategy was to visualize how the

system responded in the frequency domain with those higher amplitude peak input accelerations. The SRS values for the 10-data-point subset for the five tines were measured using the SRS module of the DAQ system. The damping ratio was set to 0.05 to ensure a Q value of 10. The frequency range was set from 1 Hz to 5000 Hz with the reference frequency set equal to the sampling frequency at 500 Hz. The resolution was set to $1/24^{th}$ octave. A different approach was used for the wedge data.

An interesting idea on how to approach the SRS analysis of the wedge data presented itself. Recall that some of the highest MR_{PEAK} values occurred during drop tests involving the wedge, but it was known that those figures represented the ratio of instantaneous maximums. Thus, those extremes may not have necessarily depicted a complete picture of the seat's dynamic response. Therefore, a decision was made to post process the time histories associated with the higher wedge MR_{PEAK} values to determine if the SRS values provided more insight into the seat's performance. The time histories were not processed using the DAQ system software. Instead, they were processed in Matlab® using a modified version of the Smallwood algorithm from [30]. The Smallwood method implements a filtering mechanism using the impulse invariant technique to convert the time transfer function to an equivalent digital filter [31-33].

Wedge MR_{SRS}

In the last two sections the MR data was presented as discrete numerical values that coincided with distinct instances in time. However, in light of what has been discussed so far, the analysis was better served when the MR_{SRS} was derived over a range of frequencies and graphically represented.

In order to avoid inundating the section with images for each of the 27 test runs, but still adhering to the objective, four time histories from the wedge data set are presented in this section. The time histories were those associated with the largest MR_{PEAK} value for the 49.6 kg (109.3 lb) payload, the largest and second largest for the 83.5 kg (184.0 lb) payload, and the largest from the 112.76 kg (248.6 lb) payload. Those figures were 0.8647, 0.9947, 0.9944, and 0.9653, respectively. If the seat was evaluated based on those numbers alone, its performance would be considered poor. However, with the positive SRS (SRSP), the aim was to view the MR values in the frequency range noted earlier (4 Hz to 10 Hz). The SRSP was calculated because it provided insight into the highest positive response during base excitation of a linear

array of SDOF systems with similar properties as the test system. A look at the SRSP graphs for the four tests revealed that the peak response acceleration and the MR_{SRS} values were lower across the entire frequency range of interest and became increasingly lower as the frequency approached 10 Hz.

For all four data sets, the peak input SRSP occurred during the range of interest. With the exception of 49.6 kg (109.3 lb) payload, the lowest calculated MR_{SRS} values also occurred in that range. The response SRSP values were higher than the input SRSP values below 4 Hz. The minimum response SRSP values occurred at around 8 Hz and generally began to increase towards the input SRSP values in the vicinity of 9 Hz to 10 Hz. The data for the 49.6 kg (109.3 lb) payload was the only set in which the lowest MR_{SRS} value did not occur within the frequency range of interest. However, its MR_{SRS} value was the only one that remained less than one after 10 Hz (except for a small peak at around 25 Hz). The MR_{SRS} values for the 83.5 kg (184.0 lb) payload climbed above one at around 15 Hz and remained above one until the end of the record. The 112.76 kg (248.6 lb) payload displayed a similar trend as the 83.5 kg (184.0 lb) payload, but the MR_{SRS} value trended below one at around 50 Hz.

To reiterate the point made in Chapter 2, the SRS was a spectral portrayal of the response of a hypothetical SDOF system that had one or more resonances in the frequency range of interest. In this regard, it offered insight into the behavior of a system similar to the test system in the frequency spectrum. Figures 5-13 to 5-16 illustrate that, in the frequency range of interest, the MR_{SRS} value was less than one. The response in the frequency range was of more interest in an SRS analysis, but for reference Table 5-15 lists the maximum and minimum calculated MR_{SRS} values in the range of interest. Three of the four values were lower than the values depicted by the corresponding MR_{PEAK}. The difference in the values in the table supported the fact that, by itself, the MR_{PEAK} did not convey a complete representation of the system's dynamic behavior. In the ensuing section, an account of the MR_{SRS} for the five tines is given.

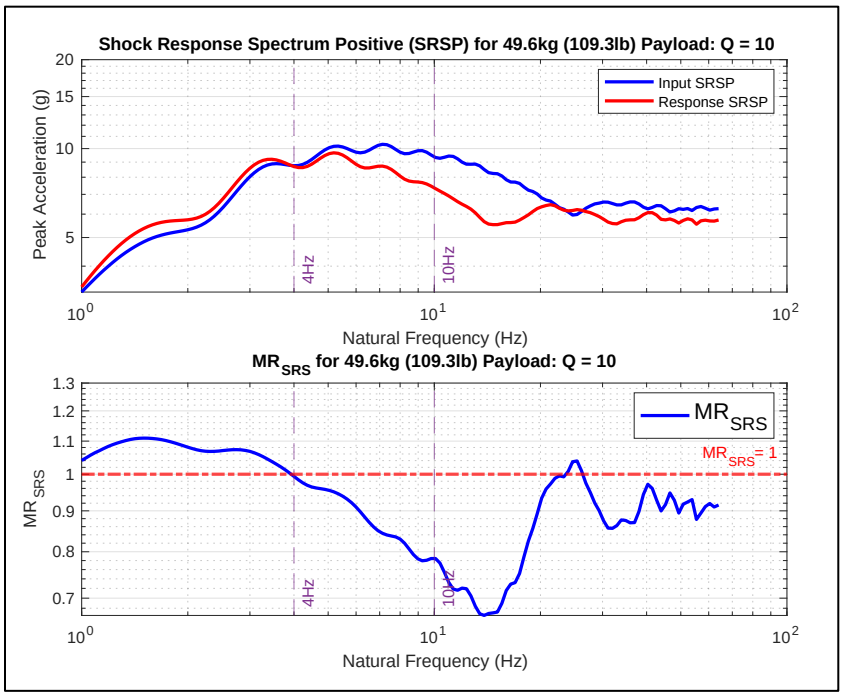

Figure 5-13: SRSP and MR_{SRS} for 49.6kg/109.3lb Payload w/Wedge: Q = 10

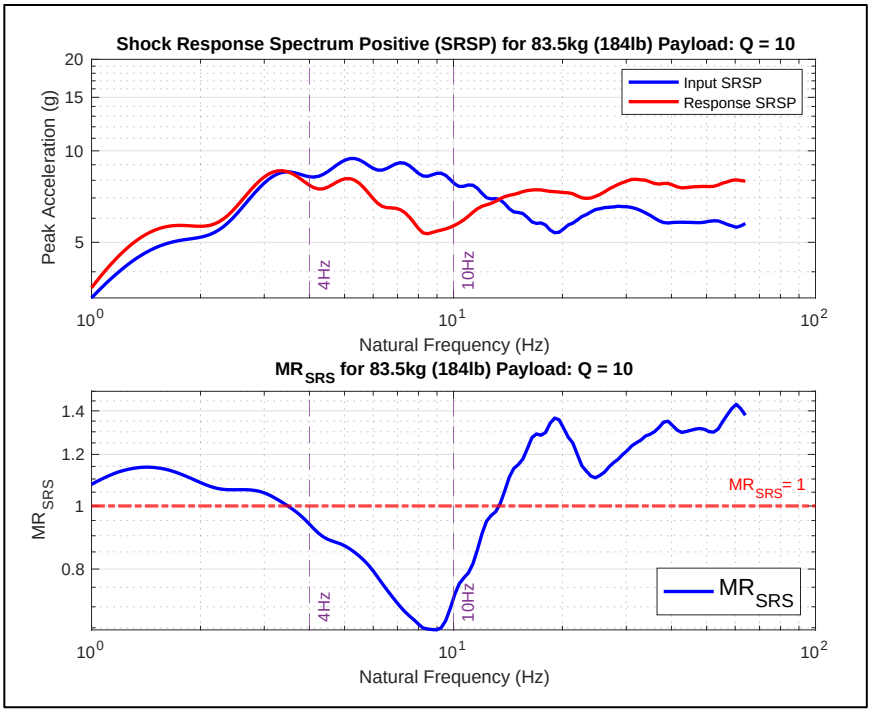

Figure 5-14: SRSP and MR_{SRS} for 83.5kg/184lb Payload w/Wedge (1): Q = 10

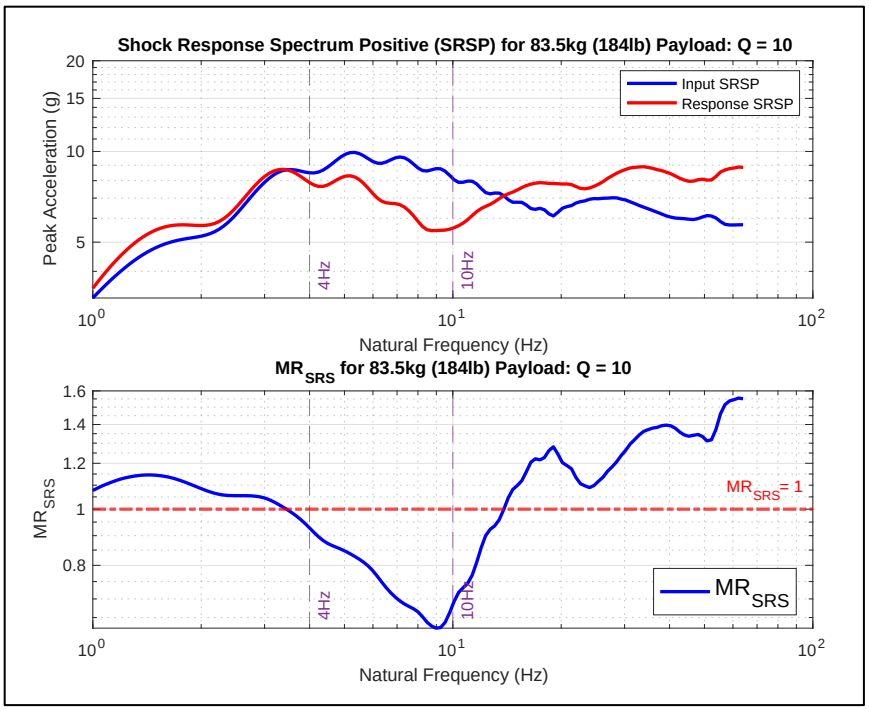

Figure 5-15: SRSP and MR_{SRS} for 83.5kg/184l Payload w/Wedge (2): Q = 10

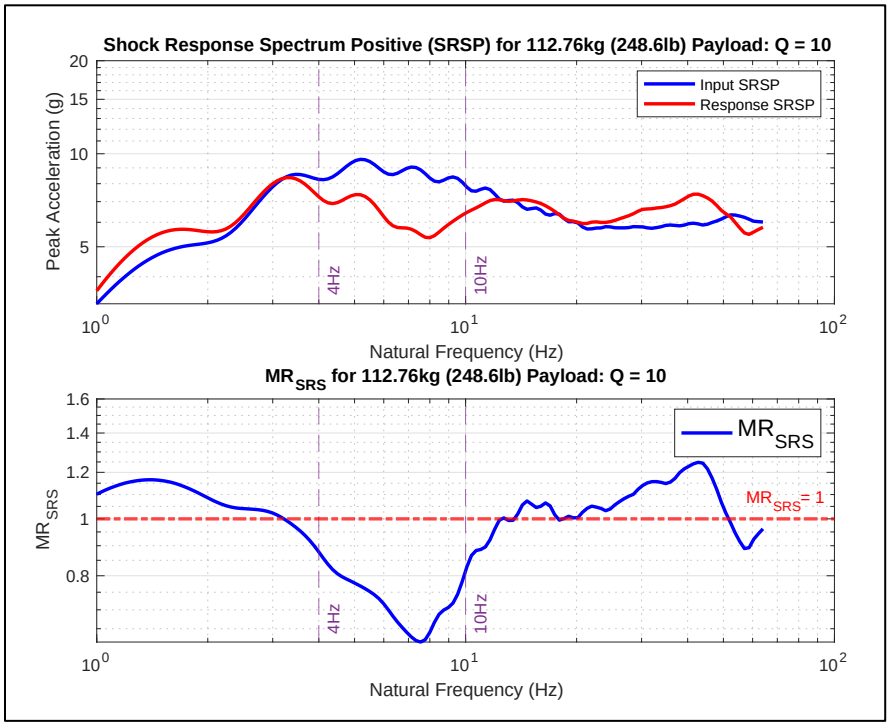

Figure 5-16: SRSP and MR_{SRS} for 112.76kg/248.6lb Payload w/Wedge: Q = 10

Table 5-15: MR_{PEAK} and MR_{SRS} Values for the Four Selected Wedge Data Sets

MR Values for Selected Wedge Data Sets			
Payload Mass	MR_{PEAK}	Maximum MR_{SRS} in Range of Interest	Minimum MR_{SRS} in Range of Interest
49.6 kg (109.3 lb)	0.8647	0.9937	0.7795
83.5 kg (184.0 lb)	0.9947	0.9375	0.6452
83.5 kg (184.0 lb)	0.9944	0.9280	0.6232
112.76 kg (248.6 lb)	0.9653	0.8783	0.6170

Five Tines MR_{SRS}

The findings from four of the 10 tests with the five tines are covered in this section. The four tests corresponded to the four highest peak input accelerations. With a similar train of thought as described for the wedge, the goal was to get an idea of the seat's response during the higher input acceleration levels. All the tests were conducted with the 112.76 kg (248.6 lb) payload with a seat damping level of one, so the distinction was really to determine if the adaptive characteristic (possible nonlinear behavior) that was observed for the time history data set, would be discerned in the frequency domain.

The most noticeable and distinctive feature of the tines data set was the presence of a peak in the input SRSP. Most of the SRSP data sets for the wedge were fairly rounded plots that trended at or below 10 g across the entire record. Each of the selected input records in the tines data set had a peak with an amplitude of between 20 g and 40 g that occurred within the range of 400 Hz and 700 Hz. In the entire data set, there was no test in which the peak input acceleration exceeded 14.75 g in the time domain. However, in the frequency domain the input SRSP for each test equaled or surpassed 20 g. Occurrences of higher amplitudes in a SRS analysis is typically considered to be associated with amplification due to the resonance.

The input acceleration was measured by the lower accelerometer, which was located on the base of the seat pedestal. The point of attachment of the seat pedestal to the platform was a considerably rigid interface, and the platform was a significantly heavier piece of hardware than the seat. Thus, it was possible that the resonance was attributed to the seat pedestal. Whereas the peak was prominent in every input SRSP,

it was not present in every response SRSP, and for the responses in which it did occur, it was not as conspicuous as the corresponding input SRSP.

Of the 10 data sets, four of the response SRSP plots displayed the peak. For each of the four data sets, the peak amplitude was just above 10 g. Also, the peak occurred over a shorter frequency range of between approximately 350 Hz and 550 Hz. Although the peak occurred in tests that were linked to higher input acceleration values in the time domain, it was not apparent why it was only visible in some of the response SRSP data corresponding to those higher input tests. One assumption was that the payload structure (PVC tubing filled with lead ballasts) had a very narrow resonance range. However, while the system dynamics in that high frequency range warranted being mentioned, its existence was irrelevant because the MR_{SRS} values were under one in the frequency range of interest.

The MR_{SRS} values were below one in the frequency range of interest for all the tests. Like the wedge data sets, the MR_{SRS} values were above one from 1 Hz to just before 4 Hz, at which point the values dipped below one. However, in contrast to the wedge data sets, the MR_{SRS} values remained below one for the entirety of each series history. Figures 5-17 to 5-20 show that, in the frequency range of interest, the seat had MR_{SRS} values that were less than one. Also, notice the peak in the response in Figure 5-20. Table 5-16 lists the calculated MR_{SRS} values in the range of interest for the four selected data sets for the 112.76 kg (248.6 lb) payload. Additionally, in the interest of forming a comparison, two tests from the 27-data-point five tines tests were post processed to calculate the SRSP. One test was for the 49.6 kg (109.3 lb) payload, and the other was for the 83.5 kg (184.0 lb) payload.

The relationship between the MR values for the tines was different from what was witnessed with the wedge values. The MR_{PEAK} values fell between the maximum and minimum MR_{SRS} values in the range of interest for the 49.6 kg (109.3 lb) and 83.5 kg (184.0 lb) payloads. However, for the four selected data sets for the 112.76 kg (248.6 lb) payload, the MR_{PEAK} values were actually lower than the minimum MR_{SRS} values. That activity was consistent with the occurrence of the lower MR_{PEAK} values that were observed in all the tines data sets.

The numbers showed that for high amplitude input accelerations with the tines, the MR_{PEAK} values were typically low. However, for those same high amplitude input accelerations, the minimum MR_{SRS} values, in the frequency range of interest, were higher than the MR_{PEAK} values. Therefore, while the numbers indicated that the seat did mitigate the incoming dynamic load (especially in the frequency range of interest), the possible adaptive characteristic of the seat was not as readily apparent in the frequency domain as it was in the time domain. Next, before the focus shifts to the seat rating, a look at the cumulative distribution function (CDF) for the MR_{PEAK} values is given.

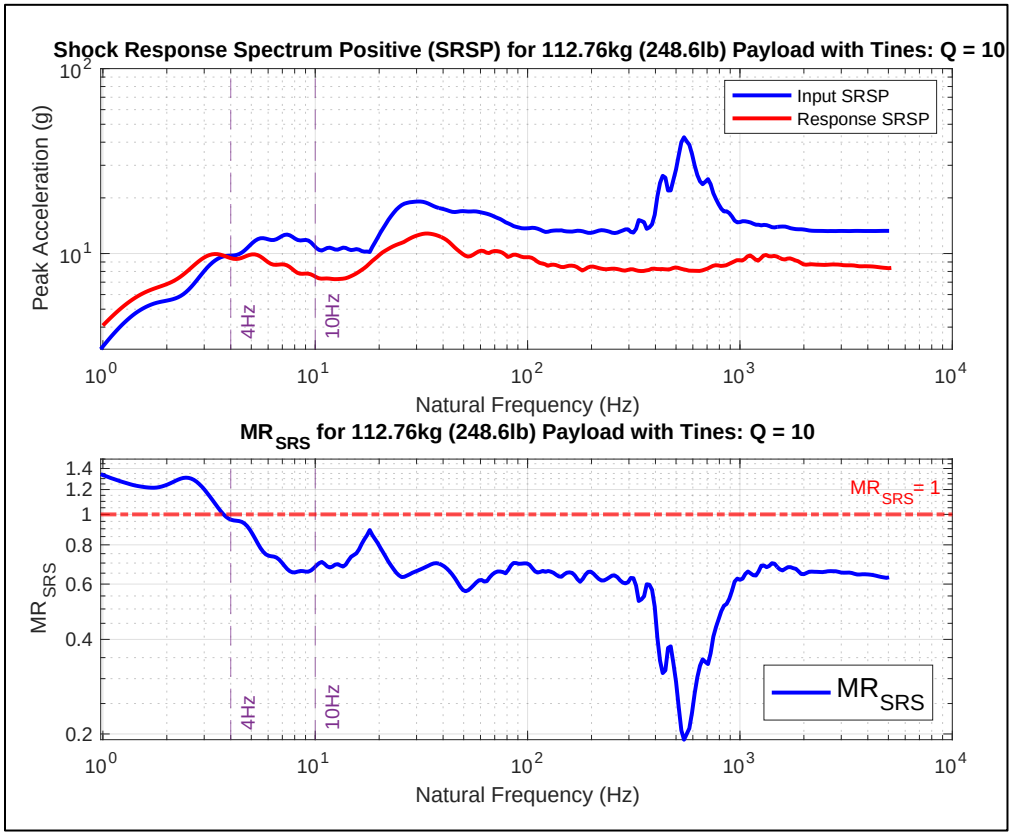

Figure 5-17: SRSP and MR_{SRS} for 112.76kg /248.6lb Payload w/5 Tines (1): Q = 10

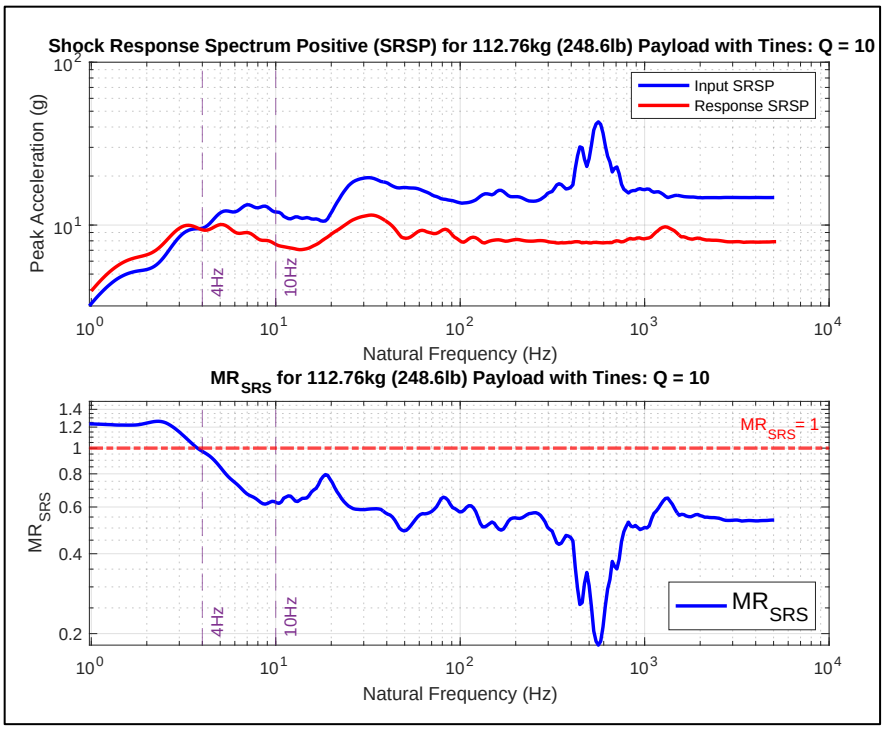

Figure 5-18: SRSP and MR_{SRS} for 112.76kg/248.6lb Payload w/5 Tines (2): Q = 10

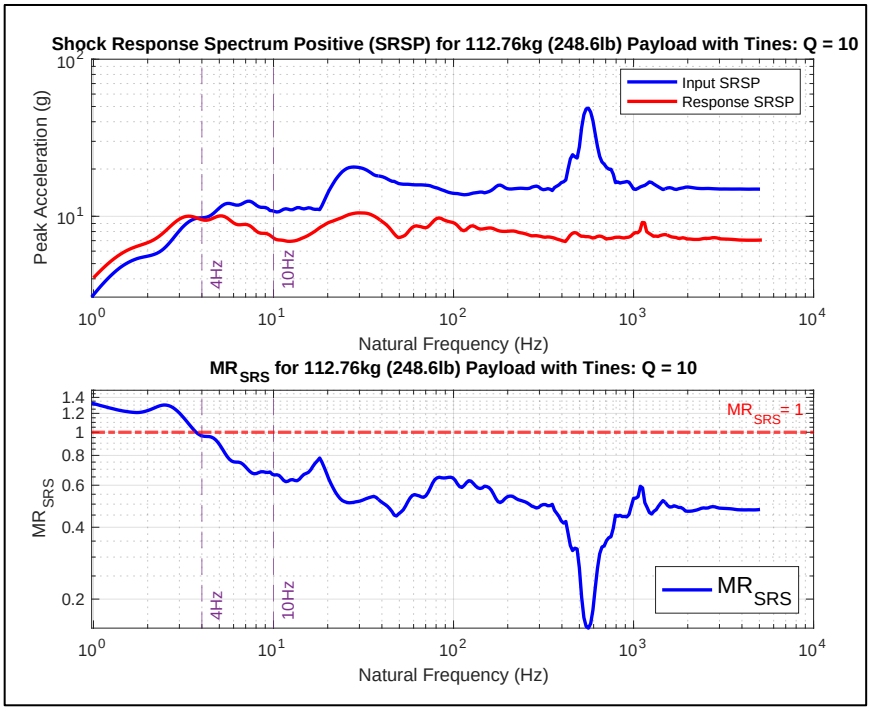

Figure 5-19: SRSP and MR_{SRS} for 112.76kg/248.6lb Payload w/5 Tines (3): Q = 10

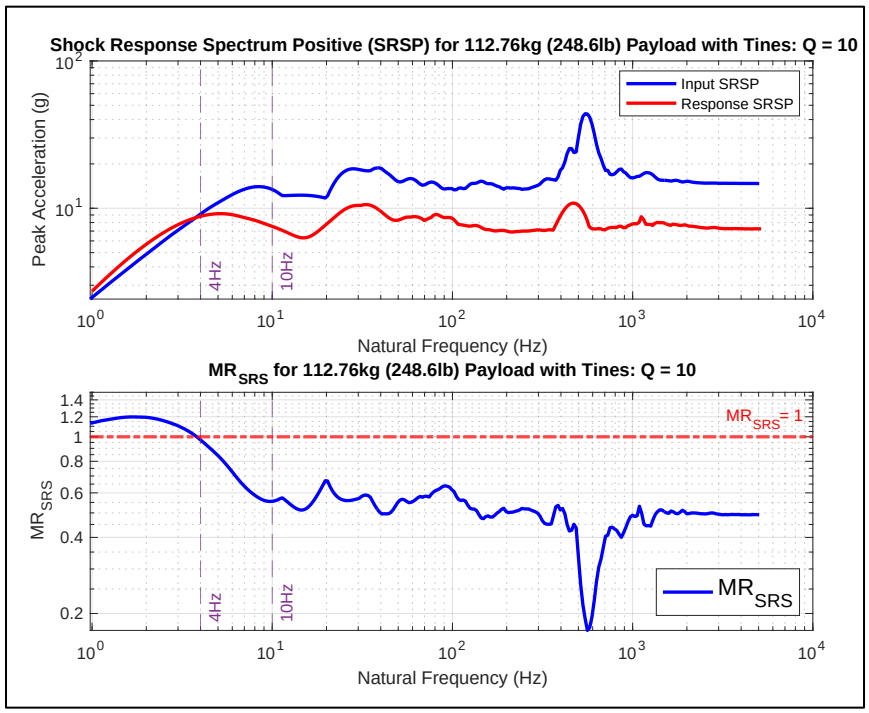

Figure 5-20: SRSP and MR_{SRS} for 112.76kg/248.6lb Payload w/5 Tines (4): Q = 10

Table 5-16: MR_{PEAK} and MR_{SRS} Values for Six Selected Tine Data Sets

MR Values for Selected Tines Data Set			
Payload Mass	MR_{PEAK}	Maximum MR_{SRS} in Range of Interest	Minimum MR_{SRS} in Range of Interest
49.6 kg (109.3 lb)	0.8069	0.9762	0.7306
83.5 kg (184.0 lb)	0.7875	0.9243	0.6309
112.76 kg (248.6 lb) Test 4	0.6366	0.9611	0.6539
112.76 kg (248.6 lb) Test 5	0.5371	0.9702	0.6152
112.76 kg (248.6 lb) Test 7	0.4815	0.9651	0.6621
112.76 kg (248.6 lb) Test 8	0.5010	0.8783	0.5550

Cumulative Distribution Function (CDF)

The cumulative distribution function (CDF) is a statistical probability measure that a random variable element, '*n*', of a data set, will assume a value less than or equal to '*n*' when evaluated at the function. The CDF has a range from zero to one for all values of '*n*'. When applied to the MR_{PEAK} data sets,

the CDF showed the percentage of MR_{PEAK} values less than one. The CDF was applied to the MR_{PEAK} for the wedge and the times data sets. The CDF provided a graphical representation of how the range of MR_{PEAK} values correlated to the maximum value of one and to what direction the data sets were trending.

In Figure 5-21, the values on the x axis represent the range of MR_{PEAK} values and the y axis is the CDF, which was adjusted to display the distribution scale in percentages. The graph shows that the MR_{PEAK} values for the tines data set were less than the wedge values 32% of the time. The mean MR_{PEAK} value for the entire data set (wedge and tines) was 0.77. The distribution shows that 80% of the MR_{PEAK} values for the tines were at or below the mean value. In contrast, only 28% of the wedge values were at or below the mean. The CDF was not intended to qualify one pulse-shaping device over another; instead, the trend that it exhibited offered an alternate perspective of the data. The data showed that in general, the tines delivered higher input acceleration values than the wedge, but the associated MR_{PEAK} values were lower. Thus, what the CDF in Figure 5-21 does is provide another way to substantiate or refute the inference that the seat may have had a nonlinear response above a certain input acceleration range.

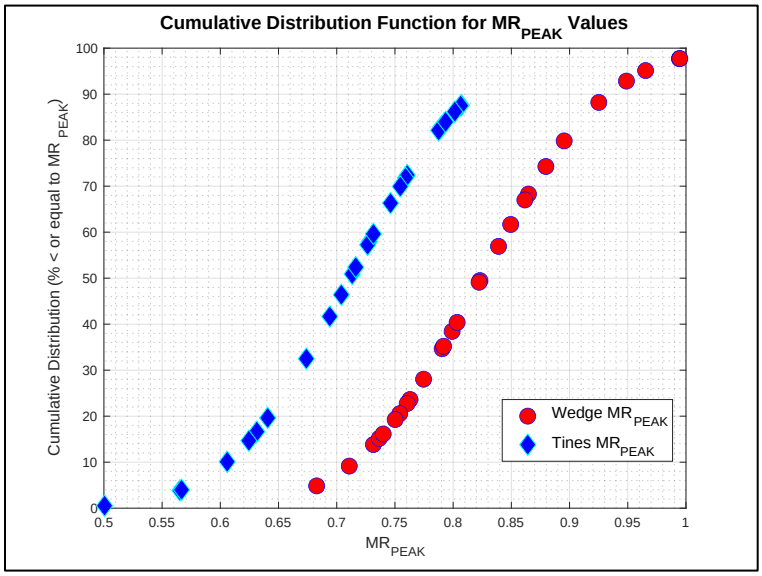

Figure 5-21: Cumulative Distribution Function for MR_{PEAK} Values

5.3 Rating of the Test Seat

One of the topics discussed thus far represented the columns under the 'Severity Threshold' heading in Table 3-5. Specifically, the capability of the tower to repeatedly deliver input accelerations of a certain amplitude to the base of the seat. The other topic centered on the MR values. The MR_{PEAK} and MR_{SRS} were numbers affiliated with the seat. The goal now is to incorporate all the findings into a cohesive paradigm that offers insight into the operating envelope of the seat.

The tower with the wedge as the pulse-shaping device was capable of delivering peak input accelerations between 7 g and 8 g. The pulse durations associated with those input accelerations were above the recommended duration of 0.10 seconds. Based on those numbers, the tower easily achieved a severity threshold level of four for 23 of the 27 tests. When the tines were installed, there was an increase in the input acceleration values, but the pulse duration times were reduced. Using five tines resulted in nine instances of severity threshold level four, 10 counts of level five, and eight counts of level six. Of the level four instances, all met the pulse duration time requirement. Seven of the 10 instances of level five, and one instance of the level six qualified for the time criteria. If strict adherence to the guidance proposed in the reference documents was upheld, then the 70% rate of qualification for the time requirement at level five seemed like ample evidence to declare that, when fitted with five tines, the tower operated at a severity threshold level of five. However, for argument's sake, say that in the dynamic environment on the deck of a HSC, 0.02 seconds is considered an imperceptible amount of time to a seat occupant. That would mean that the reduced pulse duration times did not disqualify the tower, as all of them were at or within that value of the recommended time minimum. In any case, that perspective was secondary, as the study endeavored to uphold the recommended time parameter. The MR value, on the other hand, was a very steady indicator.

Pulse duration time discrepancy aside, the calculated MR_{PEAK} and MR_{SRS} values were below one for every single data set. Across the entire wedge data set the seat attenuated 14% to 29% of the incoming acceleration pulse for the 49.6 kg (109.3 lb) payload, 0.5% to 24% for the 83.5 kg (184.0 lb) payload, and 3% to 32% for the 112.76 kg (248.6 lb) payload. The four MR_{PEAK} values over 0.9 for the 83.5 kg (184.0

lb) payload, contributed to the lower range for that mass category. For the tines data that did qualify, the mitigation rate was 21% to 29% for the 49.6 kg (109.3 lb) payload, 24% to 31% for the 83.5 kg (184.0 lb) payload, and 19% to 42% for the 112.76 kg (248.6 lb) payload. The midpoint of the lowest range (0.5% to 24%) to the midpoint of the highest range (20% to 42%) seemed like a reasonable window to assign to the seat's attenuation capability.

Therefore, taking everything onto consideration, the seat mitigated between 10% to 30% of the incoming acceleration pulse when it was tested to a severity threshold of level five with all three payload categories. However, the tower did not meet the pulse time duration target for all of the level five tests. Also, there was no information in the reference documents on how numbers that fell between the severity threshold level benchmarks should be accounted for. Consequently, the conservative evaluation of the tower was that it was fully capable of testing to a severity threshold level of four. The more aggressive assessment was that the tower had the potential to test to a severity threshold level of five 70% of the time. For reference, Table 3-4 is repeated here as Table 5-17. The new table contains the same information as previously listed but with some additional information.

The last row of the table, assigned to level four, signified where the tower system stood within the recommended severity threshold level criteria. The added rows, between levels four and five, depicted where the average values for the tower data ranked depending on whether the wedge or the five tines was used as the pulse-shaping device. The average for the tines data was only calculated for the tests that satisfied the time duration conditions. Severity threshold levels were not assigned, as the values fell between the established severity threshold levels.

Based on the columns under the 'HSC Class' heading, the seat was rated for use in vessels ranging from HSC Class 3 to HSC Class 4-3 for operating conditions that matched severity threshold level four. If the craft would be expected to operate in environments with conditions above those stipulated by level four, then retesting the seat at a higher severity threshold level would be required. In the upcoming section, a look into the impact method is presented. The impact method was not intended to be the anchor of the

analytical effort; it was just another investigative approach that was used to help garner an additional understanding of the dynamics of the tower-seat system.

Table 5-17: Severity Threshold Level, HSC Class Rating, and Wedge and Tine Data Standing

Seat Rating Based on Severity Threshold and HSC Class								
	Severity Threshold				HSC Class			
Level	Peak Input Acceleration (g)	Impact Duration (s)	Recommended Drop Height (ft)	(m)	Class 4 Military 4-3	4-2	4-1	Class 3 SAR
6	10.19	0.10	6.78	2.07	Required	Not Required	Not Required	Not Required
5	8.15	0.10	4.34	1.32	Required	Required	Not Required	Not Required
Tines	8.11	0.12	4.583	1.397				
Wedge	6.93	0.12	4.583	1.397				
4	6.12	0.10	2.44	0.74	Required	Required	Required	Required

5.4 Impact Method

The impact method used the concept of equating kinetic energy to potential energy based on relative velocity, acceleration due to gravity, and drop height. The primary purpose of implementing the impact method was to determine the amount of energy that was dissipated into the sand during a drop test. Of course, a numerical integration of the acceleration time history would have provided that answer, but using the method was a good exercise in verifying classical calculations with the computer-generated results. The prerequisites for implementing the method were listed in Chapter 4, but one of them was not applicable to this analysis, another fell in a gray area, and an assumption was made about a third based on what was the desired outcome and the physical setup of the system.

Two of the three items in question were the requirements that the seat remained attached to the impact surface and that no energy was dissipated during the impact. Based on the test setup, the condition

that no energy was spent could not be attained. The fact that the seat remained attached to the platform and the wedge (or tines) remained in contact with the sand after the impact was conceded as the provision that the seat remained attached to the impact surface. However, the whole purpose of the task was to determine the energy consumed in the sand. Thus, the work around was to perform impact method calculations for the velocity just above the surface of the sand and conduct a numerical integration procedure for the velocity during the impact. The third item required that the system had a linear response. However, the thought was that the desired outcome of the impact analysis was to determine the energy expended in the sand. Hence, the location of interest was the bottom edge of the pulse-shaping device (wedge or tines), which was below the spring unit. Consequently, the relative velocity at the edge of the pulse-shaping device (just above the sand, and just before it came to a stop in the sand) was of concern, not necessarily the impact velocities at the accelerometer locations (those velocities were available through the numerical integration). Therefore, the condition that the system have a linear response did not need to be satisfied.

To apply the method, the plan was to calculate the relative velocity based on the vertical Z axis with the top edge of the sandbox as the zero location. The direction pointing upward away from the top edge of the sandbox was the positive Z direction. The drop height (h) during a drop was constant. That is, the tower platform was raised to the same height for each drop. However, the distance traveled relative to the top edge of the sandbox was different at the two accelerometer locations. There was about a 0.721 m (2.365 ft) vertical distance between the higher accelerometer located in the base of the payload and the lower one located on the platform (base of seat pedestal). Hence, the potential energy (and the subsequent velocity) at the payload location was slightly higher than at the base of the seat.

The first reference location for the height required to calculate the energy expended in the sand was the bottom edge of the suspended wedge (or tines) to the surface of the sand. The second height was that height plus the depth of the wedge in the sand. The final position of the bottom edge of the platform (in relation to the top edge of the sandbox) was recorded after each drop. In addition, the length of the wedge and the tines were known values. Therefore, all the values required for (4-41) were either known or could

have been calculated. For convenience, (4-40), (4-41), and Figure 4-4 are shown below as (5-3), (5-4) , and Figure 5-22.

$$\frac{1}{2}m\dot{x}^2 = mgh \tag{5-3}$$

$$\dot{x} = \sqrt{2gh} \tag{5-4}$$

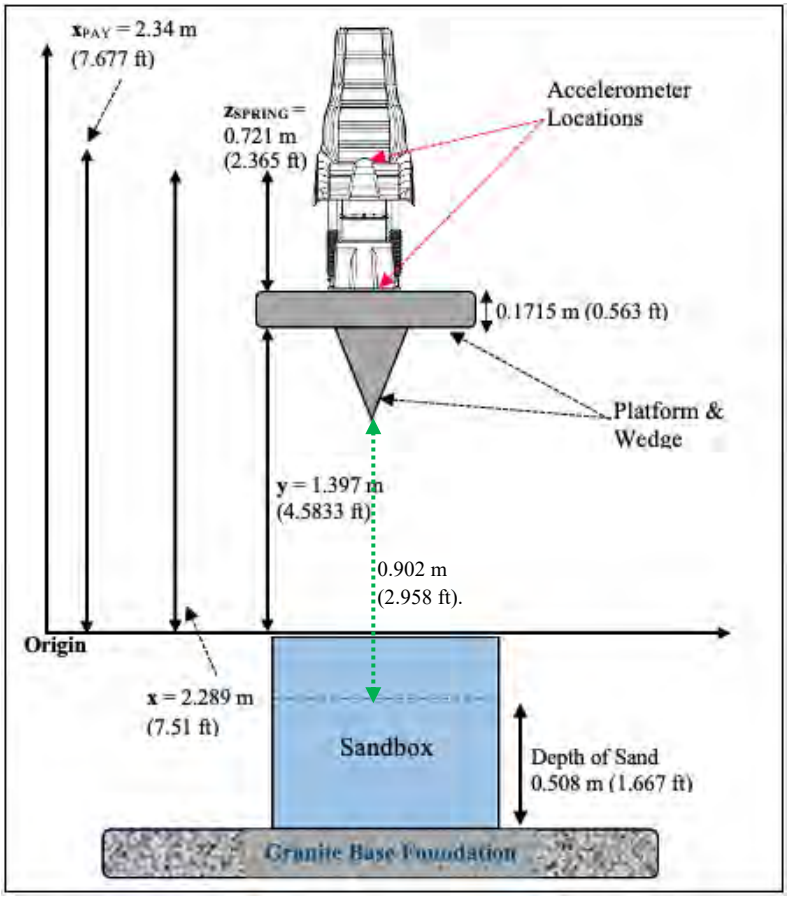

Figure 5-22: Distance Between the Wedge and Sand Surface for Impact Method

Adhering to the plan to calculate the relative velocity just before impact with the sand, the bottom edge of the wedge when the platform was suspended to the surface of the sand was considered the drop height (h). The bottom edge of the wedge (or tines) was the impact point because from the bottom edge of the wedge to the surface of the sand was an easier location to access (and measure) than any other two points that were collinearly located on the same vertical Z axis. Also, using that approach made it easier to determine how much of the wedge was buried in the sand. Referring to the green dashed arrow in Figure 5-22 when the platform was suspended at maximum height, the distance from the bottom edge of the wedge to the surface of the sand was approximately 0.902 m (2.958 ft). That distance served to calculate the first velocity at the surface of the sand.

The height for the second velocity calculation was the first distance plus the distance the wedge was submerged into the sand. That distance was the longitudinal length of the wedge minus two distances. The longitudinal length of the wedge was the side opposite the hypotenuse of the triangle formed by half the wedge. One of the two distances was the distance between the top edge of the sandbox and the bottom edge of the platform after a drop. The other distance was the distance from the top edge of the sandbox to the surface of the sand. That final number was the approximate amount the wedge was buried in the sand.

Theoretically, those velocities could be used to determine the kinetic energy (KE) at the bottom edge of the wedge just before entering the sand, and the KE just before the wedge came to a complete stop, by using the left-hand side of (5-3). That was, of course, neglecting friction and coulomb damping within the sand. However, since the final velocity of the system was zero, those velocities were considered the maximum velocity at those specific locations along that vertical axis. The expression in (5-4) was the method used to determine the velocities. The relative velocity calculated by using the edge of the wedge was different from those calculated at the accelerometer locations. That was because the total distance from the bottom edge of the wedge to the surface of the sand (0.902 m/2.958 ft) was a shorter distance than the total relative distances available for travel at either accelerometer location. In turn, that corresponded to less potential energy at the top of the drop height for the wedge location.

The impact method was concerned with maximums, so to use that approach to determine the energy lost to the sand, the primary value of interest was the maximum velocity. At the end of a drop, the system came to rest, so the practical velocity (and energy) at that point was zero. That is, all the energy entering the sand was dispelled in the sand. However, if the velocity just before the pulse-shaping device came to a stop was considered, then that energy would be considered the maximum energy based on the equivalent potential energy. The numerical analogy of that concept was the area under the acceleration pulse curve.

To determine the maximum velocity during a drop, a numerical integration was carried out on the area under the acceleration pulse curve using Matlab®. The impact method and the numerical integration was applied to the same six tests, which was one for each mass category from the wedge data set and one for each mass category from the tines data set.

The velocity and subsequent energy values that were derived using (5-4) and (5-3) were not directly comparable to the numerically integrated values. The impact method produced maximum relative velocities *prior* to and *during* impact based on the location at the bottom edge of the wedge. At the accelerometer locations, the impact method produced velocities based on potential energy due to height locations *prior* to impact. In contrast, the numerical integration generated total velocities *during* impact based on the area under the acceleration pulse at the two accelerometer locations. Nonetheless, the impact method served as an analytical tool to provide a rough estimate of the system velocities and the energy exchange between the pulse-shaping devices and the sand.

Impact Method :Velocity

Using the distance identified in Figure 5-22, and the expression in (5-4), the average relative velocity at the bottom edge of the wedge, just before entering the sand, was 4.2061 m/s (13.80 ft/s). When the tines were installed, the distance to the surface of the sand was slightly longer at 0.9081 m (2.979 ft). The calculated relative velocity at the base of the tines just prior to colliding with the sand was 4.2202 m/s (13.85 ft/s). Those values equated to the relative velocity at those specific locations at the point in time just as the pulse-shaping devices entered the sand. Just before the end of its travel through the sand, the pulse-shaping devices traversed a total distance of approximately 1.34 m (4.396 ft). As the system came to a stop

at the end of a drop, the velocities based on that drop height were considered the maximum velocity the system achieved as the pulse-shaping devices traveled through the sand. The average velocity at that point for the wedge was 5.133 m/s (16.841 ft/s) and 5.153 m/s (16.906 ft/s) for the tines.

As expected, the maximum relative velocities at the accelerometer locations were larger than at the edge of the pulse-shaping devices, and the values for the payload location were higher than those calculated for the platform, which correlated to the difference in height at those locations. The small differences in the values across the tests were based on the final resting location of the bottom edge of the platform relative to the top edge of the sandbox. Depending on the test, that distance ranged from 0.0381 m (0.125 ft) to 0.0601 m (0.1972 ft), which contributed to trivial variations in the actual drop height used in (5-4).

Across the wedge and tines data, the maximum relative velocity at the accelerometer in the base of the payload had an average of 6.633 m/s (21.762 ft/s), and the maximum average at the accelerometer located on the platform was 5.465 m/s (17.931 ft/s).

Impact Method: Energy

The left-hand side (LHS) of (5-3) was used to calculate the total energy consumed in the sand. The total energy just at the surface of the sand when the wedge was installed was 3464.8 J (3.284 Btu) for the 49.6 kg (109.3 lb) payload, 3764.7 J (3.568 Btu) for the 83.5 kg (184.0 lb) payload, and 4023.5 J (3.814 Btu) for the 112.76 kg (248.6 lb) payload. The values were slightly less for the tines. For the 49.6 kg (109.3 lb) payload the value was 3450.1 J (3.27 Btu). The value for the 83.5 kg (184.0 lb) payload was 3751.9 J (3.556 Btu) and 4012.5 J (3.803 Btu) for the 112.76 kg (248.6 lb) payload. In accordance with the theoretical impact concept, the values near the end of travel through the sand were higher.

For the wedge, the values were 5172.3 J (4.90 Btu) for the 49.6 kg (109.3 lb) payload, 5577.5 J (5.29 Btu) for the 83.5 kg (184.0 lb) payload, and 6006.3 J (5.69 Btu) for the 112.76 kg (248.6 lb) payload. The values for the tines tests were 5091.8 J (4.826 Btu) for the 49.6 kg (109.3 lb) payload, 5589.83 J (5.298 Btu) for the 83.5 kg (184.0 lb) payload, and 6050.98 J (5.735 Btu) for the 112.76 kg (248.6 lb) payload. The calculated energy values just before the system came to a stop were idealized values that did not account for friction, damping, and other physical phenomenon that occurred in the sand. Considering that the system

came to a complete stop after achieving those values, then it was plausible that the amount of energy lost to the sand was the difference in the surface values and the final values.

The location of interest for the energy calculation was the bottom edge of the pulse-shaping devices. That meant that the mass of the entire system was above the location of interest. Thus, the mass that was used in (5-3) was the total combined mass of the payload, seat, tower platform, and the pulse-shaping device. For the wedge the total combined mass across the three payloads ranged from 391.70 kg to 454.86 kg (863.55 lb to 1002.79 lb), and for the tines the range was 387.44 kg to 450.6 kg (854.15 lb to 993.40 lb). To put the energy values into perspective, the kinetic energy of a 1 kg (2.20462 lb) mass traveling at 1.41 m/s (4.63 ft/s) is approximately one joule (0.001 Btu). Hence, for a system on the order of 400 times heavier, moving at about four times the velocity, the values derived by the impact method seemed reasonable.

Numerical Integration: Velocity

The maximum velocities generated by the numerical integration were lower in value than the relative maximum values calculated using the impact method. The maximum velocities generated by the numerical integration were the maximum velocities during the impact. The area under the acceleration pulse signified the total velocity relative to the accelerometer locations as the pulse-shaping device moved through the sand. The relationship between the velocity values at the accelerometer locations was the same as with the relative velocity values calculated by the impact method, in that the total values at the payload were marginally higher than those at the platform location during impact. For the tests for which the wedge was installed, the average across the three payloads at the payload location was 5.296 m/s (17.375 ft/s). The average at the platform location was 4.523 m/s (14.839 ft/s). The values for the tines were similar with averages of 5.218 m/s (17.119 ft/s) and 4.522 m/s (14.836 ft/s) at the payload and platform locations, respectively.

Numerical Integration: Energy

The bottom edge of the wedge (or tines) ‘carried’ the entire mass of the system above its location. That was the reason for using the entire mass of the system in the LHS of (5-3) to calculate the energy. However, the velocities computed with the numerical integration approach corresponded to the

accelerometer locations, and those locations only 'carried' partial amounts of the system's mass. Thus, to adjust for the mass accordingly, only the payload mass was used in (5-3) to compute the energy corresponding to the payload accelerometer location. The combined mass of the payload and the seat was used in (5-3) for energy calculations that were associated with the accelerometer location on the platform.

At the payload location, for the 49.6 kg (109.3 lb) payload mass, the computed energy was 655.50 J (0.623 Btu). The 83.5 kg (184.0 lb) payload and the 112.76 kg (248.6 lb) payloads registered 1175.08 J (1.114 Btu) and 1677.68 J (1.590 Btu), respectively. The values with the tines were 602.44 J (0.571 Btu) for the 49.6 kg (109.3 lb) payload mass, 1216.6 J (1.15 Btu) for the 83.5 kg (184.0 lb) payload, and 1599.6 J (1.516 Btu) for the 112.76 kg (248.6 lb) payload.

In comparison, the energy values formulated for the platform accelerometer location were a bit higher except for the 83.5 kg (184.0 lb) payload for the tines and the 112.76 (248.6 lb) payload for the wedge. For the wedge, the value for the 49.6 kg (109.3 lb) payload mass was 944.81 J (0.896 Btu), 1301.59 J (1.234 Btu) for the 83.5 kg (184.0 lb) payload, and 1547.54 J (1.467 Btu) for the 112.76 kg (248.6 lb) payload. The values for the tines were 940.73 J (0.892 Btu), 1212.36 J (1.149 Btu), and 1660.41 J (1.574 Btu), for the 49.6 kg (109.3 lb), 83.5 kg (184.0 lb), and 112.76 kg (248.6 lb) payloads, respectively. Those values were lower than the values derived using the impact method, but they accounted for forces such as friction and damping in the system, and so were deemed to be more accurate.

Overall, the velocity values generated by the impact method were within reasonable agreement with the numerical integration approach while the energy numbers displayed some discrepancy. The average velocity just before the pulse-shaping device entered the sand was determined to be 4.213 m/s (13.822 ft/s) across both devices and all three payloads. Just prior to when the system came to a stop in the sand, the average velocity at the edge of the pulse-shaping device was 5.143 m/s (16.873 ft/s) across both devices at all three payloads categories. The average relative velocities for the accelerometer locations were higher using the impact method at 5.47 m/s (17.946 ft/s) and 6.63 m/s (21.752 ft/s) for the platform and payload locations, respectively. Those values were in comparison to the total velocities during the impact

computed using numerical integration at 4.523 m/s (14.839 ft/s) and 5.26 m/s (17.257 ft/s) for the platform and payload locations, respectively.

The impact method was used to calculate the velocity during free fall, prior to the pulse-shaping device impacting the sand; whereas the integration technique only considered the area under the acceleration pulse, which coincided with the time during the collision. Also, from a practical perspective, the impact method did not account for friction and coulomb damping in the system. Hence, the disagreement between the methods due to the marginally higher relative velocity values for the impact method was an artifact of simulating an idealized system. The disparity in the derived energy values came down to what total mass was used in the equation.

To calculate the energy at the bottom edge of the pulse-shaping device, the entire mass of the system had to be accounted for. At the accelerometer locations though, only the mass 'at' or 'above' that specific location was used. The outcome was higher energy values based on the relative velocity at the bottom edge of the pulse-shaping device, than those generated at the accelerometer locations. It seemed reasonable that towards the end of its movement, a system with a mass of that size would be capable of generating an energy output within the realm of the values that were derived. The discrepancy between the products of the two methods aside, the numerical integration was based on measured accelerometer data, so the values derived from that process were accepted as having greater merit.

Table 5-18 itemizes the velocity values for both methods. Table 5-19 lists the energy numbers for the impact method, and Table 5-20 notes the energy values for the numerical integration. The mean values for the energy by way of the numerical integration were not computed because of the variation in the numbers from payload to payload. In the next section, the topic covers a synopsis of some of the fundamental modal properties of the tower-seat system.

Table 5-18: Velocity Values for Impact Method vs Numerical Integration

Impact Method and Numerical Integration Velocities				
Impact Method				
Device	Payload Mass (kg)	Total Mass (kg)	Velocity @ Sand Surface (m/s)	Velocity @ Sand Bottom (m/s)
Wedge	49.6	391.7	4.2061	5.1390
	83.5	425.6	4.2061	5.1196
	112.76	454.86	4.2061	5.1390
Five Tines	49.6	387.4356	4.2202	5.1269
	83.5	421.3356	4.2202	5.1511
	112.76	450.5956	4.2202	5.1824
Mean Value			4.2131	5.1430
Numerical Integration				
Device	Payload Mass (kg)	Total Mass (kg)	Platform Impact Velocity (m/s)	Payload Impact Velocity (m/s)
Wedge	49.6	391.7	4.5444	5.1411
	83.5	425.6	4.5562	5.3053
	112.76	454.86	4.4735	5.4550
Five Tines	49.6	387.4356	4.5346	4.9287
	83.5	421.3356	4.3973	5.3982
	112.76	450.5956	4.6338	5.3265
Mean Value			4.5232	5.2591

Table 5-19: Energy Values for Impact Method

Impact Method Energy Values					
Device	Payload Mass (kg)	Total Mass (kg)	Energy @ Sand Surface (J)	Energy @ Sand Bottom (J)	Energy Difference (J)
Wedge	49.6	391.7	3464.82	5172.26	1707.44
	83.5	425.6	3764.67	5577.50	1812.83
	112.76	454.86	4023.51	6006.27	1982.76
Five Tines	49.6	387.4356	3450.09	5091.83	1641.74
	83.5	421.3356	3751.96	5589.83	1837.87
	112.76	450.5956	4012.52	6050.97	2038.45
Mean Value			3744.60	5581.44	1836.84

Table 5-20: Energy Values for Numerical Integration

Numerical Integration Energy Values					
Device	Payload Mass (kg)	Payload & Seat Mass (kg)	Payload Impact Energy (J)	Platform Impact Energy (J)	Energy Difference (J)
Wedge	49.6	91.5	655.50	944.813	289.313
	83.5	125.4	1175.08	1301.59	126.51
	112.76	154.66	1677.68	1547.54	-130.14
Five Tines	49.6	91.5	602.44	940.73	338.29
	83.5	125.4	1216.60	1212.36	-4.24
	112.76	154.66	1599.60	1660.41	60.81

5.5 Analytical Modal Analysis

The primary purpose of the analytical modal analysis effort was to determine the natural frequency of the tower-seat system. An accurate experimental modal analysis of a system the size of the one in question would have involved the use of supplementary hardware such as an impact hammer or a shaker table. Also, for a more comprehensive evaluation of the system's modal properties additional, strategically placed, accelerometers and possibly a force transducer may have been required. In contrast, the analytical modal analysis relied on techniques that involved mathematical manipulation of the measured acceleration signals, such as conducting a fast Fourier transform (FFT). A fundamental query that this analysis sought to resolve was whether the seat-occupant dynamic was aptly represented by a SDOF system. The hope was that the outcome of the modal analysis would have brought the study one step closer to resolving that inquiry. The first step in the process was to begin with some of the classic equations outlined in Chapter 4. However, an essential system characteristic that was required for an analytical modal analysis had to be determined.

No documentation or any form of information regarding the profile of the seat spring was available. Consequently, to determine the profile of the spring, a force versus displacement experiment had to be conducted. With the use of a laser, the displacement of the seat was measured from a fixed position on the

underside of the seat to a fixed position on the platform. Measurements were taken as individual 13.61 kg (30 lb) steel plates were added to the empty seat one at a time. A total of 20 plates (272.16 kg/600 lb) was placed in the seat. The total displacement of the spring under that weight was 0.095 m (0.312 ft), and the associated total force was 2668.93 N (600 lbf). The force versus displacement plot was linear for the measured data, but a polynomial regression fit was applied to the data to determine if there was any credence to the nonlinearity supposition.

Using the 'Curve Fitter' application in Matlab®, three expressions were developed for the force versus displacement plot. A polynomial fit up to the third degree was applied to the data, and according to the sum of squares due to error (SSE) and the R-square statistic, the third-degree polynomial was the best fit. Indeed, a number of regression models could be applied to tightly spaced data that has a general linear trend to produce a 'good' fit. However, considering that the calculated MR_{PEAK} values for the higher peak input acceleration (resulting in higher applied forces) were lower than the MR_{PEAK} values associated with the lower peak input accelerations, it was not a flagrant assumption to state that the seat had an adaptive response. The supposition was that the seat may have had a linear response within a certain input acceleration range and a nonlinear response outside of that range. Also, dynamics outside of the range included compression and tension. Table 5-21 lists the polynomials, the coefficient values, the SSE, and the R-square for the three fits. Figure 5-23 is a graph depicting the linear fit along the data points, and Figure 5-24 is a graph displaying the third order polynomial fit over the data points.

Table 5-21: Polynomial Coefficients and Fit Statistics for Force vs Displacement Data

Regression Fits for Force vs Displacement Data Points						
Polynomial Form	p1 (N/m)	p2 (N/m)	p3 (N/m)	p4 (N/m)	SSE	R-square
$p1x + p2$	27862	50.1821			1.1228e+04	0.99918
$p1x^2 + p2x + p3$	-2.421e+04	30136	17.1287		4.3567e+03	0.99968
$p1x^3 + p2x^2 + p3x + p4$	7.7615e+04	-3.516e+04	3.053e+04	14.51	4.3126e+03	0.99969

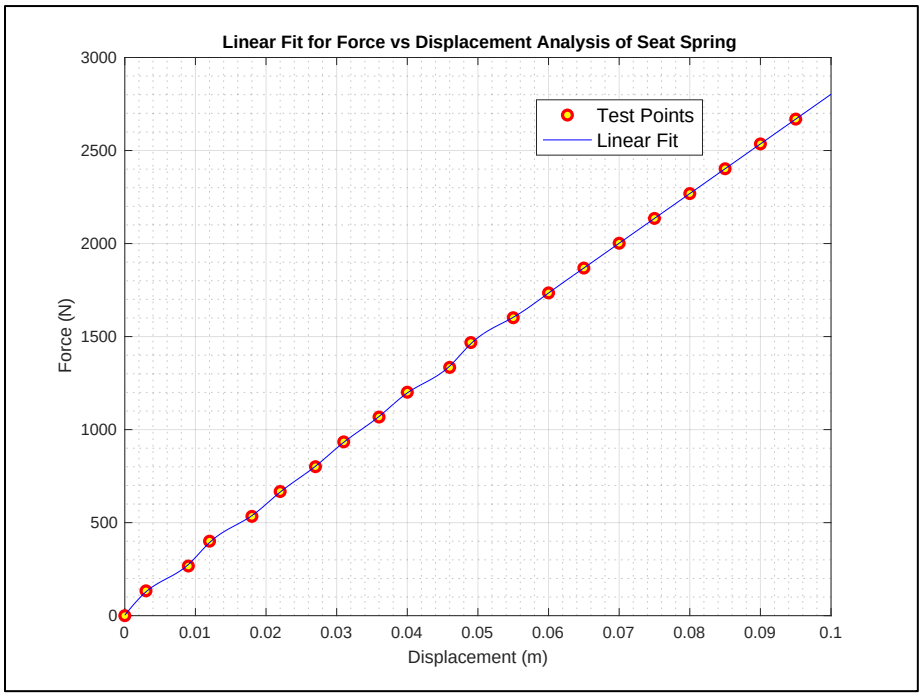

Figure 5-23: Linear Fit for Force vs Displacement Data Points

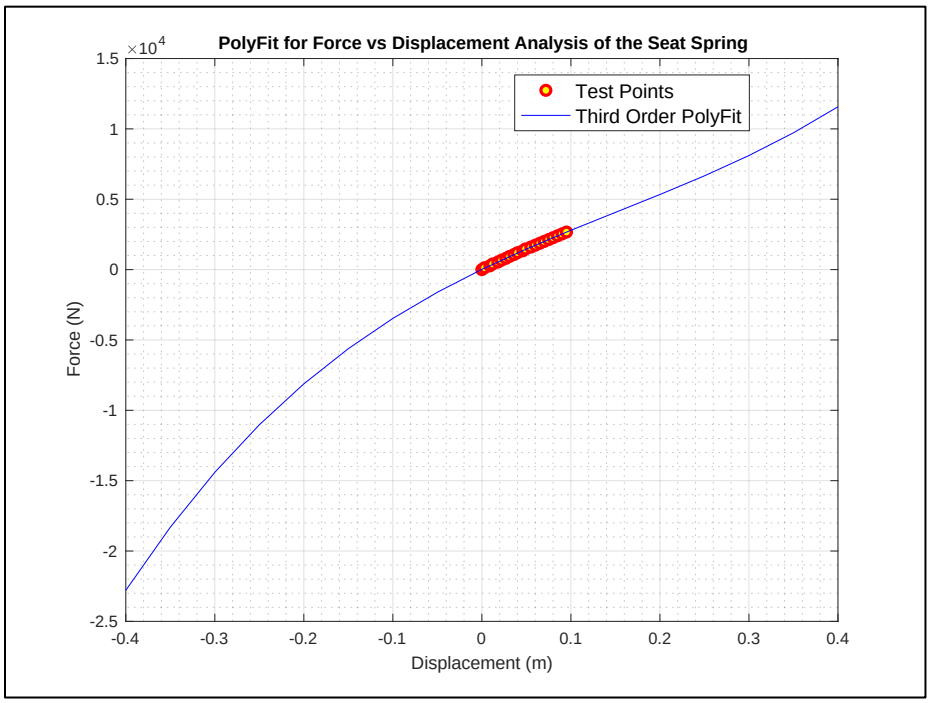

Figure 5-24: Third Order Polyfit for Force vs Displacement Data Points

Once what seemed like plausible values for the spring constant were developed, the second task was to discern the damping coefficient by way of the damping ratio. Based on an examination of the acceleration time histories at the two accelerometer locations, the location at the base of the payload was about one-half critical damping, and the response of the system at the platform location was even less damped. The platform location was not influenced by the seat dampers, so it was a logical outcome that the behavior at that location would equate to a more active response.

A first approximation based on the behavior of the acceleration plots was that the payload location had a damping ratio of roughly $\xi = 0.5$, and the platform location value was about $\xi = 0.10$. Those numbers were speculations, and values by way of an experimental analysis were required, so the acceleration time histories were used to calculate the logarithmic decrement, and thereafter the logarithmic decrement was used determine the damping ratio.

To compute the logarithmic decrement successive peaks after the initial excitation peak had to be identified in the time history. For most of the time histories for the platform location, successive peaks were clearly distinguishable, but the time histories for the payload location presented a challenge. The acceleration time histories for the payload location contained almost no oscillations after the initial impact, and routinely returned to a steady state without any significant fluctuation about zero. As a result, those histories could not be used to calculate the logarithmic decrement. Therefore, the decision was made to adopt a damping ratio value of 0.5 for the payload location. It was understood that the damping ratio at the payload location was the more vital of the two values in terms of performing a complete modal analysis, but a starting value was required, and the assigned value seemed like a reasonable starting point. The thought was that the value could be adjusted later based on the critical damping value. In the interest of verifying the assumed damping ratio at the platform location, three acceleration time histories, one for each payload mass, were used to derive the logarithmic decrement. Figure 5-25 is an image of one of the acceleration time histories that was used to determine the logarithmic decrement. Notice the absence of oscillations in the plot of the payload response (red line).

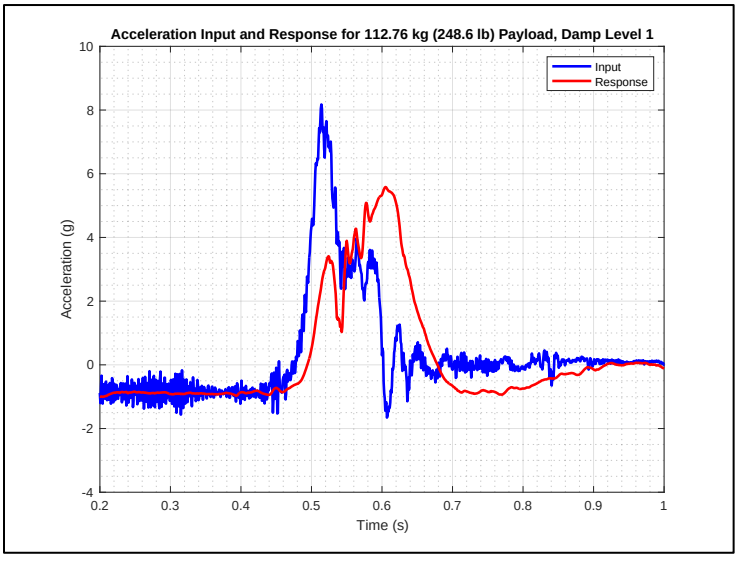

Figure 5-25: Example of Acceleration Time History to Determine Logarithmic Decrement

The logarithmic decrement values were used in (4-27) to calculate the damping ratios. The three derived damping ratio values were 0.01 for the test with the 49.6 kg (109.3 lb) payload, 0.07 for the 83.5 kg (184.0 lb) payload, and 0.09 for the 112.76 kg (248.6 lb) payload. The value for the 49.6 kg (109.3 lb) payload was an order smaller than the initial guess for the damping ratio, but the other two values were close enough to the initial guess of 0.10. With the spring constants developed from the fit of the force versus displacement data points and the derived damping ratio values, all the elements necessary to calculate the approximate natural frequency and approximate damping coefficient were available. The subsequent derivation of the natural frequency, though, had to be based on whether the system was modeled as a single degree of freedom (SDOF) or two degree of freedom (2DOF) system (both undamped and damped).

Single Degree of Freedom (SDOF) without Damping

In the SDOF concept, the occupant and seat were considered a lumped mass, so the derivation of the approximate undamped natural frequency was a matter of modifying the LHS of (4-6). The expression presented in (5-5) below was the form applicable to this analysis.

$$\omega_n = \sqrt{\frac{k_{seat}}{m_{payload} + m_{seat}}} \tag{5-5}$$

The values for the spring constant (k_{seat}) were the p1, p2, and p3, coeffcients for the linear, second order, and third order equations, respectively, in Table 5-21. Based on twice the square root of the product of the spring constant and the sum of the payload and seat masses, the critical damping was 4344 N-s/m (24.55 lbf-s/in) at the higher end. Therefore, when the initial estimate of 0.5 for the damping ratio at the payload location (payload-seat interface) was considered, the approximate damping coefficient was 2150 N-s/m (12.28 lbf-s/in). The expression for the critical damping coefficient is given in (5-6), and the relationship between the damping coefficient, the critical damping coefficient, and the damping ratio is shown in (5-7) below.

$$C_c = 2\sqrt{km} \tag{5-6}$$

$$\xi = \frac{C}{C_c} \tag{5-7}$$

The average approximated undamped natural frequency was 2.85 Hz for the 49.6 kg (109.3 lb) payload mass, for the 83.5 kg (184.0 lb) payload it was 2.45 Hz, and it was 2.25 Hz for the 112.76 kg (248.6 lb) payload. The critical damping values based on the spring constants, and the lumped masses ranged from 3191.61 N-s/m for the 49.6 kg (109.3 lb) payload to 4344.52 for the 112.76 kg (248.6 lb) payload.

The approximated damping coefficient values derived via the logarithmic decrement were low in comparison to the values derived using the critical damping numbers. On the lower end the value was 31.92 N-s/m (0.18 lbf-s/in) for the 49.6 kg (109.3 lb) payload and 391.01 N-s/m (2.23 lbf-s/in) at the higher range for the 112.76 kg (248.6 lb) payload.

For the most part, the critical damping values seemed credible because they were based on experimentally collected data and actual system properties. The approximated damping coefficient values were derived via the logarithmic decrement established from the acceleration time histories on the platform, which was not a particularly damped location. Consequently, the system damping had to be somewhere between those two benchmark values. Using the 0.5 damping ratio estimate with the critical damping numbers, the system damping coefficient values ranged from 1595.80 N-s/m (9.11 lbf-s/in) to 2172.26 N-s/m (12.40 lbf-s/in). The natural frequency and critical damping values were based on actual system properties, and since the seat-payload subsystem was not a highly excitable system, those values were considered feasible. Thus, the approximated damping coefficient based on the critical damping value was acceptable. Later, during the numerical analysis, the plan was to adjust that value as necessary based on the simulated response of the numerical model.

Table 5-22 itemizes the values for the approximated natural frequency without damping. The approximated damping coefficient values for each payload at the three spring constants and the damping

ratios are listed in Table 5-23 along with the estimated damped natural frequencies. In the analysis of the damped natural frequency, the damping coefficients based on half the critical damping coefficient for each payload were retained.

Table 5-22: Modal Properties for SDOF System without Damping

SDOF Modal Properties without Damping		
Seat & Payload Mass (kg)	Spring Constant (N/m)	Frequency (Hz)
m	k	f_n
91.5	27862	2.779
125.4		2.373
154.66		2.137
91.5	30136	2.890
125.4		2.468
154.66		2.222
91.5	30530	2.909
125.4		2.484
154.66		2.237

Single Degree of Freedom (SDOF) with Damping

When the damping is included in the analytical derivation of the natural frequency, the expression represented in (5-5) has an added term under the radical. The expression for the SDOF natural frequency when the damping is considered is shown below.

$$\omega_n = \sqrt{\frac{k_{seat}}{m_{payload} + m_{seat}} - \left(\frac{c}{2(m_{payload} + m_{seat})}\right)^2} \tag{5-8}$$

The natural frequency values for the SDOF system when damping was taken into consideration are listed in Table 5-23. The damping values used in (5-8) were based on half the critical damping value at each payload mass. The natural frequency values when damping was included were lower, which is in accordance with the expected behavior of an undamped system versus a damped system. The table itemizes the approximated damping coefficient values for each payload at the three spring constants. The variable 'α' in the table represents the natural log of the ratio of the magnitude to two successive peaks in the response time history. As shown next, deriving the natural frequency of the 2DOF system introduced two additional values that had to be estimated.

Table 5-23: Modal Properties for SDOF System with Damping

SDOF Modal Properties with Damping						
Seat & Payload Mass (kg)	Spring Constant (N/m)	Frequency (Hz)	Critical Damping (N*s/m)	Damping Coefficient (N*s/m)	Damping Coefficient (N*s/m)	Damping Ratio ξ
m	k	f_n	$C_c = 2\sqrt{km}$	$\xi 2\sqrt{km}$	$0.5\ C_c$	$\frac{\alpha}{\sqrt{(2\pi)^2 + \alpha^2}}$
91.5	27862	2.40	3191.61	31.9160574	1595.803	0.01
125.4		2.05	3736.90	261.5831198	1868.451	0.07
154.66		1.85	4150.35	373.5314757	2075.175	0.09
91.5	30136	2.50	3319.30	33.19295347	1659.648	0.01
125.4		2.14	3886.41	272.0485245	1943.204	0.07
154.66		1.93	4316.40	388.4757048	2158.198	0.09
91.5	30530	2.52	3340.92	33.40923226	1670.462	0.01
125.4		2.15	3911.73	273.8211394	1955.865	0.07
154.66		1.94	4344.52	391.0069364	2172.261	0.09

Two Degree of Freedom (2DOF) without Damping

The 2DOF concept treated the seat cushion as an active translational element with spring-like and damping capabilities. However, no information was available for the seat cushion properties. An attempt to conduct a force versus displacement analysis on the cushion proved to be impractical, as there was no way to compress the cushion without compressing the main spring as well. Without any information for the attributes of the cushion, estimates were made based on the characteristics of polyurethane foam.

To assign the estimated values to the seat cushion properties, a few considerations came to mind. First, the payload response acceleration time history from Figure 5-25 depicted a rather damped level of activity, and that response was measured just above the seat cushion. Next, the force versus displacement analysis of the spring revealed that not only was the spring constant a high value, but the spring also had a relatively linear response up to 2669 N (600 lbf). That effect was captured in the payload response

acceleration. Finally, the approximated damping coefficient derived from the critical damping value was based on assuming a damping ratio of 0.5, which appeared like a fair appraisal of the seat damping. Hence, it seemed like assigning the cushion property values within the range of the main suspension system was a good a starting point. The properties of interest for the 2DOF system were the approximate fundamental and second natural frequency values, and the process begun by developing the characteristic equation.

The development of the expression for the characteristic equation originated by setting the determinant of the 2DOF equation of motion matrix equal to zero. The natural frequencies (and damping ratios) were determined from the roots of the characteristic equation. The expression for the equation of motion in matrix form is presented below in (5-9).

$$\begin{bmatrix} m_1 & 0 \\ 0 & m_2 \end{bmatrix} \begin{Bmatrix} \ddot{z}_1 \\ \ddot{z}_2 \end{Bmatrix} + \begin{bmatrix} c_1 + c_2 & -c_2 \\ -c_2 & c_2 \end{bmatrix} \begin{Bmatrix} \dot{z}_1 \\ \dot{z}_2 \end{Bmatrix} + \begin{bmatrix} k_1 + k_2 & -k_2 \\ -k_2 & k_2 \end{bmatrix} \begin{Bmatrix} z_1 \\ z_2 \end{Bmatrix} = 0 \tag{5-9}$$

The natural frequencies of the system were determined by solving the frequency equation, which took the following form:

$$|-\omega^2[m] + [k]| = 0 \tag{5-10}$$

Restructuring the mass and stiffness matrices from (5-9) in the form of (5-10) led to:

$$\begin{bmatrix} k_1 + k_2 - \omega^2 m_1 & -k_2 \\ -k_2 & k_2 - \omega^2 m_2 \end{bmatrix} \begin{Bmatrix} z_1 \\ z_2 \end{Bmatrix} = 0 \tag{5-11}$$

Next, the terms in (5-11) were rewritten to solve for z_1 and z_2 beginning with the first row as follows:

$$(k_1 + k_2 - \omega^2 m_1) z_1 - k_2 z_2 = 0 \tag{5-12}$$

Therefore, the expression for z_2 was:

$$z_2 = \frac{1}{k_2}(k_1 + k_2 - \omega^2 m_1) z_1 \tag{5-13}$$

The second row gave:

$$-k_2 z_1 + (k_2 - \omega^2 m_2) z_2 = 0 \tag{5-14}$$

Substituting the term for z_2 into (5-14) and rearranging led to:

$$[(k_1 + k_2 - \omega^2 m_1)(k_2 - \omega^2 m_2) - k_2^2] \frac{z_1}{k_2} = 0 \tag{5-15}$$

The term in the brackets in (5-15) is the determinant of the matrix from (5-11), and it is equal to zero. Neglecting z_1 for the moment, the characteristic equation was derived by multiplying out the determinant, which gave way to the quadratic equation shown below.

$$m_1 m_2 (\omega^2)^2 + [-m_1 k_2 - m_2(k_1 + k_2)]\omega^2 + k_1 k_2 = 0 \tag{5-16}$$

In (5-16), for the masses, the subscripts '1' and '2' correspond to the seat and the payload, respectively, and for the spring constants, the subscript '1' refers to the seat spring, and '2' relates to the cushion spring.

The eigenvalues of (5-16) were the natural frequencies of the system. The eigenfrequencies represented the approximate range of values for the roots of (5-16). The assigned value for the seat cushion

spring value was 20000 N/m (114.20 lbf/in), which was based on the high end of the published range of spring values for polyurethane foams. The seat spring constant was held at 27862 N/m (159.1 lbf/in).

The approximated fundamental frequency values were very similar to the natural frequencies derived for the SDOF system. The values ranged from roughly 1.59 Hz on the lower end (112.76 kg/248.6 lb) to 2.36 Hz on the upper end (49.6 kg/109.3 lb). The fundamental frequency for the 49.6 kg (109.3 lb) payload was 2.36 Hz and the second natural frequency was 8.57 Hz. The fundamental and second natural frequencies for the 83.5 kg (184.0 lb) payload were 1.84 Hz and 8.45 Hz, respectively. For the 112.76 kg (248.6 lb) payload, the values were 1.59 Hz for the fundamental frequency and 8.42 Hz for the second natural frequency. As mentioned earlier, these values were derived based on the approximation at the higher end of the published spring values for polyurethane foam and possibly reflect an over estimation. Table 5-24 summarizes the approximated natural frequency values for the 2DOF system. Next, the damping is accounted for in the 2DOF system. Terms representing the damping of the seat and the seat cushion are added to (5-11) to resolve the natural frequency values.

Table 5-24: Natural Frequencies for 2DOF System without Damping

2DOF Seat Natural Frequencies without Damping		
Seat/ Payload Mass [kg]	Fundamental Frequency [Hz]	Second Natural Frequency [Hz]
m	f_1	f_2
17.6/49.6	2.36	8.57
17.6/83.5	1.84	8.45
17.6/112.76	1.59	8.42

Two Degree of Freedom (2DOF) with Damping

The spring constants used in the undamped approach were maintained for the analysis with damping included. The seat damping was assigned the values of 1600 N-s/m (9.14 lbf-s/in), 1900 N-s/m (10.85 lbf-s/in), and 2100 N-s/m (12.00 lbf-s/in) based on the average of half the critical damping coefficient value at each payload mass. The supposed seat cushion damping value was set to 2000 N-s/m (11.42 lbf-s/in) (based on damping values for polyurethane foam). The equation to represent the natural frequency of the 2DOF system when damping is accounted for is shown in (5-17) below.

$$\begin{bmatrix} k_1 + k_2 - \omega^2 m_1 + i(c_1 + c_2)\omega & -k_2 - ic_2\omega \\ -k_2 - ic_2\omega & k_2 - \omega^2 m_2 + ic_2\omega \end{bmatrix} \begin{Bmatrix} z_1 \\ z_2 \end{Bmatrix} = 0 \tag{5-17}$$

In a similar manner as with (5-16), the eigenvalues of the determinant of the matrix in (5-17) can be determined to derive the natural frequency values. An alternate form of (5-17) is presented in (5-18) below.

$$det\left[\begin{bmatrix} m_1 & 0 \\ 0 & m_2 \end{bmatrix}\omega^2 - \begin{bmatrix} k_1 + k_2 & -k_2 \\ -k_2 & k_2 \end{bmatrix} + i\begin{bmatrix} c_1 + c_2 & -c_2 \\ -c_2 & c_2 \end{bmatrix}\omega\right] = 0 \tag{5-18}$$

The values were derived using the Matlab® function ‘damp’, and they were lower than the undamped values, as expected. The fundamental frequency for the 49.6 kg (109.3 lb) payload was 1.94 Hz. The fundamental frequencies for the 83.5 kg (184.0 lb) and the 112.76 kg (248.6 lb) payloads were 1.88 Hz and 1.61 Hz, respectively. The values for the second natural frequency were 2.48 Hz, 1.96 Hz, and 1.91 Hz for the 49.6 kg (109.3 lb), 83.5 kg (184.0 lb), and 112.76 kg (248.6 lb) payloads respectively. That result seemed rational based on the fact that the seat cushion adds an extra element of damping that is not accounted for in the undamped system. Table 5-25 lists the damped fundamental and second frequencies and the numerically derived damping ratio and pole values. In the next section, a look at an alternate option

to determine the natural frequency of the system is presented. The next approach eliminates the need to designate the system type because it involves applying an FFT to the acceleration time histories.

Table 5-25: Natural Frequencies for 2DOF System with Damping

2DOF Modal Properties with Damping					
Seat/Payload Mass [kg]	Fundamental Frequency [Hz]	Second Natural Frequency [Hz	Damping Coefficient [N*s/m]	Fundamental & Second Damping Ratio	Fundamental and Second Poles
m	f_1	f_2	0.5 C_c	ξ	P
17.6/49.6	1.94	2.48	1600	1.0/0.552	-12.2+0i -8.6 – 12.99i
17.6/83.5	1.88	1.96	1900	0.4854/1.0	-5.73+10.31i -12.3+0i
17.6/112.76	1.61	1.91	2100	0.442/1.0	-4.46+9.1i -11.98+0i

Fast Fourier Transform (FFT)

The Fourier transform is a well-known algorithm that converts a signal from the time domain to the frequency domain. The Fast Fourier transform (FFT) generates a discrete Fourier of the signal based on a complex function of frequency. The benefit of using the FFT for this analysis was that the acceleration time histories could be used without concern for designating the system as a SDOF or a 2DOF system. In a sense, this approach was considered a way to assess the veracity of the natural frequency values derived earlier. To determine the natural frequency values, the acceleration time histories from six tests were processed, one from each payload category for the wedge and one from each payload category for the five tines. After each signal was processed and converted from the time domain to the frequency domain, the natural frequency was identified by the peaks in the FFT of the response acceleration. The FFTs were generated using the 'fft' function in Matlab®.

Two features about the FFT-generated natural frequency values stood out. First, the values were lower than those derived using the standard equations used for the SDOF and the damped 2DOF models. Second, the value and the FFT plot were the same regardless of the mass of the payload. The highest magnitude peak for the response signal occurred at a frequency of 0.625 Hz, which represented the fundamental frequency. The next highest peak, the second natural frequency, occurred at about 1.563 Hz for the 49.6 kg (109.3 lb) and the 83.5 kg (184.0 lb) payloads and around 1.402 Hz for the 112.76 kg (248.6 lb) payload. The undamped fundamental frequency values for the SDOF and 2DOF models were on the order of three to four times the FFT-generated fundamental frequency. The same order of magnitude existed between the undamped second natural frequency of the 2DOF approach and the FFT-generated second natural frequency. Keeping in mind that the spring constant was experimentally derived, and the damping coefficient was an estimate based on an assumed damping ratio and the critical damping, the SDOF and 2DOF values did have an inherent error factor. In contrast, the only input to the FFT algorithm was the measured accelerometer data, so the argument for the legitimacy of the natural frequency was in favor of the FFT method. Figure 5-26 illustrates the FFT graph for one of the acceleration time histories, all of which were practically identical.

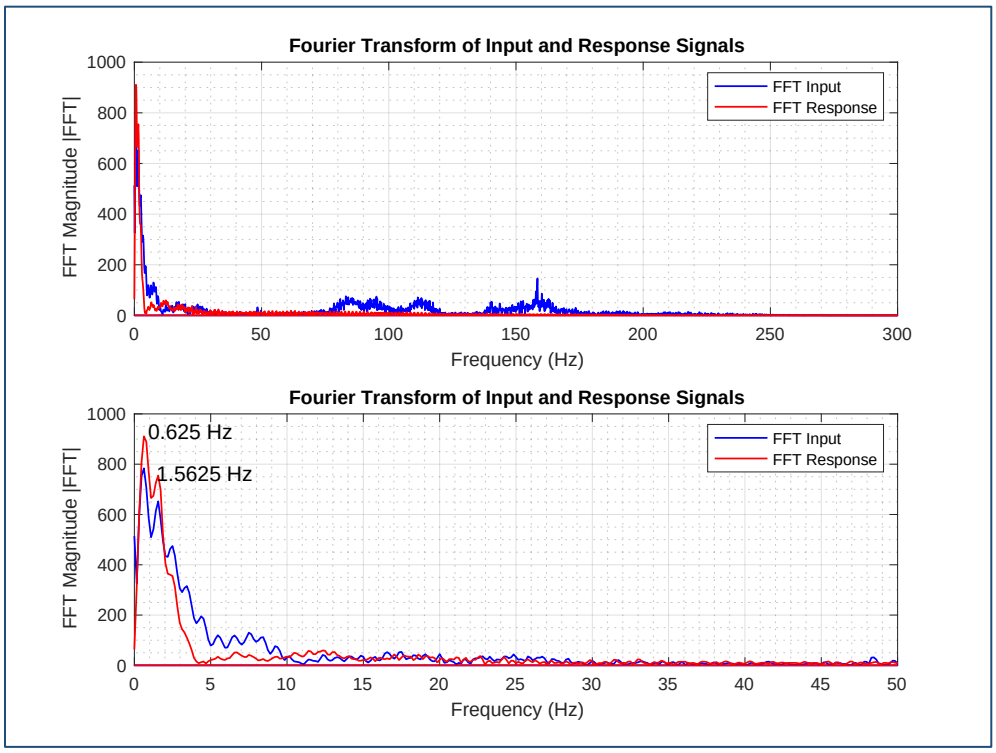

Figure 5-26: Fast Fourier Transform of Input and Response Signals

5.6 Summary

In this chapter, the discussion focused on the main components of the experimental analysis. The highlights of the account were the drop tower's repeatability, and the seat's performance and rating. Those two topics formed the basis for one of the two primary objectives of the study. A supplementary narrative addressed exploring the impact method as an approximate assessment of the system's dynamics. The final discussion was an overview of a general analytical modal analysis of the system.

One of the goals of this work is to demonstrate that the drop tower was capable of simulating the vertical acceleration pulse associated with a wave slam event. Undoubtedly, the drop tower was capable of delivering a vertical, rapidly applied acceleration pulse to the base of the seat. What remained unclear at

the beginning was how was the trait of repeatability going to be identified in the tower's function. The answer was to conduct a statistical analysis on what the tower was designed to do.

A normal distribution was applied to the peak input acceleration values for a subset of drop tests. Half of the data points were from tests conducted with the wedge as the pulse-shaping device, and the other half were from tests performed with five tines as the pulse-shaping device. The data for the tines contained a slight right skew, but overall, the distribution for each data set fell within the one, two, and three standard deviations of the mean according to the 68-95-99.7 rule of a normal distribution. In general, the input accelerations had higher amplitudes when the tines were installed with a mean value of 9.04 g, compared to a mean of 6.93 g when the wedge was used. The conclusion was that the tower was capable of consistently operating at a severity threshold level of four and could perform at level five 70% of the time. The tower demonstrated a level of repeatability because there was no single external element that had a markedly larger influence on the system than the rest of the inherent effects. The mitigation ratio (MR) values also displayed some correlation to the pulse-shaping device.

The MR values were calculated for the same subset of tests that was used for the statistical analysis of the tower. A surplus set of tests were processed to provide additional data points that were used to identify a particular aspect of the seat's response.

For the entire data set, there was not a single calculated MR_{PEAK} value that exceeded one. When the wedge was used as the pulse-shaping device, the seat exhibited a fairly consistent peak response acceleration. The mean response acceleration was 5.66 g with a very low standard deviation of 0.2866 across all the payload masses. The mean MR_{PEAK} value for the wedge data was 0.7947, 0.8821, and 0.7957 for the 49.6 kg (109.3 lb), 83.5 kg (184.0 lb), and 112.76 kg (248.6 lb) payload masses, respectively. There was more spread in the tines data, but the MR_{PEAK} values were lower.

The seat displayed higher response accelerations when the five tines were installed. It had a response of 8.65 g for one of the tests. The mean response acceleration was 6.35 g, but the standard deviation was higher across all the payload masses at 1.1216. The mean MR_{PEAK} values were lower for the tines data with the mean for the 49.6 kg (109.3 lb) payload at 0.7653, and 0.7068 for the 83.5 kg (184.0 lb)

payload. The mean for the 112.76 kg (248.6 lb) payload was 0.6621. As the MR_{PEAK} values were lower when the input accelerations were higher, the belief was that the seat possessed an adaptive characteristic in its performance. Some credence was added to that notion when the MR values for the extra data set were processed.

A set of tests were conducted using three tines (instead of five) and the 112.76 kg (248.6 lb) payload. The three tines (with that payload) delivered even higher peak input accelerations than the five-tines configuration. The mean input acceleration value for the three tines was 15.55 g with a recorded high of 17.88 g. The peak seat response at that amplitude was 10.16 g. The mean MR_{PEAK} value for the entire data set was 0.5653, which was lower than the 27-data-point sets for the wedge and the five tines. Therefore, it appeared that the seat performed better at higher incoming dynamic loads. The emphasis of the MR_{SRS} values was the frequency range within 4 Hz to 10 Hz.

The MR_{SRS} values for that range were all below one. The highest value was 0.9370 with the 49.6 kg (109.3 lb) payload and the lowest was 0.5550, which was for the 112.76 kg (248.6 lb) payload. Ultimately, based on the findings, the seat was rated for use in vessels ranging from HSC Class 3 to HSC Class 4-3 for operating conditions that matched a severity threshold level of four. The impact method was investigated to ascertain its utility in serving as a way to modestly approximate the dynamics of the system.

Using the concept of equating kinetic energy to potential energy, the impact method was used to calculate relative velocities of the system at specific heights, which were in turn used to determine the approximate amount of energy that was lost to the sand at the end of a drop test. The approximated values from the method were compared with those derived from numerical integration of the area under the acceleration time history pulse.

The mean approximated relative velocities values calculated using the impact method were 5.47 m/s (17.95 ft/s) and 6.63 m/s (21.75 ft/s) at the input (base of seat pedestal/platform) and payload accelerometer locations, respectively. Those values were associated with those locations before the pulse-shaping device entered the sand. For the numerical integration, the mean values at those locations were calculated as the pulse-shaping device traveled through the sand. The mean velocity was 4.52 m/s (14.83

ft/s) for the input location and 5.26 m/s (17.26 ft/s) for the payload location. Those velocities corresponded to the area under the acceleration time history pulse.

Using the impact method, the energy for a point located on the bottom edge of the wedge (or tines) ranged from 5172 J to 6050 J (4.90 Btu to 5.73 Btu) across the three payload masses. Those values were based on that location just before it came to a stop in the sand. The mean value for the difference in the energy at the surface of the sand to the energy just before the pulse-shaping device came to a stop was 1836 J (1.74 Btu). The energy numbers computed using the numerical integration approach were lower with a range of 602 J to 1677 J (0.57 Btu to 1.59 Btu). The impact method did not account for phenomenon such as friction or damping, whereas the numerical integration technique was derived from measured accelerometer data, so the consensus was that the numerical integration values held more worth. Coverage of a modal analysis of the system closed off the chapter.

A limited analytical modal analysis was performed in order to determine the natural frequency of the system. The system was evaluated as a SDOF and a 2DOF system with and without damping. A fast Fourier transform (FFT) was applied to a few selected acceleration time histories as an alternate approach to approximating the natural frequency.

The SDOF approach relied on the classical equation involving the system stiffness and the mass, as shown in (5-5). The expression in (5-8) took damping into consideration. Using three experimentally derived spring constants and the combined lumped mass of the payload and the seat, the approximate natural frequency values without damping ranged from 2.14 Hz for the 112.76 kg (248.6 lb) payload to 2.91 Hz for the 49.6 kg (109.3 lb) payload. When the payload mass was 83.5 kg (184.0 lb), the natural frequency was roughly 2.45 Hz. The values when damping was included ranged from 1.85 Hz to 2.52 Hz depending on the spring constant. The expression in (5-16) was used to calculate the values for the 2DOF model without damping. The values ranged from 1.59 Hz to 2.36 Hz for the fundamental frequency and 8.42 Hz to 8.57 Hz for the second natural frequency. The lower values were calculated for the 112.76 kg (248.6 lb) payload, and the higher values were linked to the 49.6 kg (109.3 lb) payload. The fundamental frequencies when damping was accounted for were lower with values of 1.94 Hz for the 49.6 kg (109.3 lb) payload and

1.88 Hz and 1.61 Hz for the 83.5 kg (184.0 lb) and the 112.76 kg (248.6 lb) payloads, respectively. The peaks in the FFT graph occurred at lower frequency values than either of the other two sets of values.

The highest peak in the FFT graph for the response acceleration signal was at 0.625 Hz, which corresponded to the natural frequency. The other prominent peak was at 1.5625 Hz (1.402 Hz for the heaviest payload mass), signifying the second natural frequency. As the spring constant was experimentally derived, and the damping coefficient was an estimate based on the speculated damping ratio and the critical damping, the SDOF and 2DOF values were considered to contain an intrinsic error. The FFT algorithm was applied to measured accelerometer data, so the values derived from that method may have been more valid.

Up next, the discussion transitions to the numerical model of the seat. That account centers on the comparison between the experimental response acceleration of the seat and the simulated response acceleration generated by the SDOF and 2DOF models. Also, a subject of interest that is presented is the presence of a product of the tower dynamics that was evident in the acceleration time histories.

Chapter 6. Simulated Response of Numerical Models for Shock Mitigation Seat

In this chapter the emphasis is placed on the simulated payload response generated by the numerical models. Specifically, how closely the simulated payload response acceleration compared to the response acceleration measured at the base of the payload. In the spirit of resolving the question regarding whether the seat was best modeled as a single degree of freedom (SDOF) or a two degree of freedom (2DOF) system, the numerical model was approached from the perspective of those two concepts. However, each approach came with a potential drawback.

In the SDOF concept, the payload and the seat were considered to be a single translational element that stored the kinetic energy of the system. However, the disadvantage of following that path was that it introduced the risk of not fully capturing the dynamic interaction between the payload and the seat. In the 2DOF concept, the payload and the section of the seat beneath the seat cushion, which is commonly referred to as the seat pan, were deemed to be two separate mass elements capable of storing kinetic energy. Additionally, in the 2DOF model, the seat cushion could have been modeled to either have the potential energy storing capacity of a spring, the energy dissipating capability of a damper, or both. The cushion material was assumed to be polyurethane foam, which has both spring and damping capabilities. Consequently, the seat cushion was model as both a spring and a damper. The 2DOF concept meant introducing more uncertainty into the analysis. Specifically, the added error associated with estimating the seat cushion properties. Nonetheless, based on the test setup, an argument could have been made to support both models.

The discussion ahead covers how each model was implemented, the comparison of the simulated response acceleration with the payload response acceleration, and the presence of an unexpected signal artifact in the acceleration time histories.

6.1 Single Degree of Freedom (SDOF) Numerical Model

In the laboratory coordinate system, the vertical axis, collinear with the height of the tower, was considered the Z axis as depicted in Figure 4-4. The positive Z direction pointed towards the top of the tower in the direction of the hoist and the negative z direction pointed towards the bottom of the tower in the direction of the sandbox. Any point on the horizontal plane parallel to and intersecting with the top edge of the sandbox was considered the zero height on the Z axis. The components of the physical system that were represented in some way in the numerical analysis from the top down (hoist to sandbox) were the payload, the seat, the suspension system (spring and dampers), the seat pedestal, and the tower platform. An accelerometer was attached to the payload in a location that represented the base of the spinal column of a hypothetical seat occupant, and another was located on the base of the seat pedestal. At the end of a drop, as the pulse-shaping device came to a stop in the sand, most of the dynamic load (minus the energy lost to the sand) from the acceleration pulse entered the base of the seat through the platform. Hence, the system was defined as being exposed to a base excitation. The elements of the numerical model had designations based on the interaction between the seat and platform, as well as the position of the accelerometers.

In the numerical model, each variable was matched to the single degree of freedom (SDOF) representation of the system as pictured in Figure 4-5. The mass was defined as the combined mass of the payload and the section of the seat above the suspension system, and the spring stiffness and damping coefficient values were matched to the suspension system of the seat. The signal measured by the accelerometer positioned on the base of the pedestal was defined as the input to the system. In a similar manner, the signal measured by the accelerometer in the payload was assigned as the response of the system. That was the signal with which the output of the numerical model was compared to.

To establish a comparison between two techniques, the SDOF numerical model was implemented using the state space representation and the Newmark-Beta method (Newmark-β) as described in Chapter 4. The purpose of the comparison was to assess which method produced a simulated response that formed

a closer fit with the experimental data. Figure 6-1 illustrates the tower-seat system identifying the vertical axis and the designations of the system elements in the numerical model. In the upcoming subsection, the results from the state space version of the SDOF model is presented.

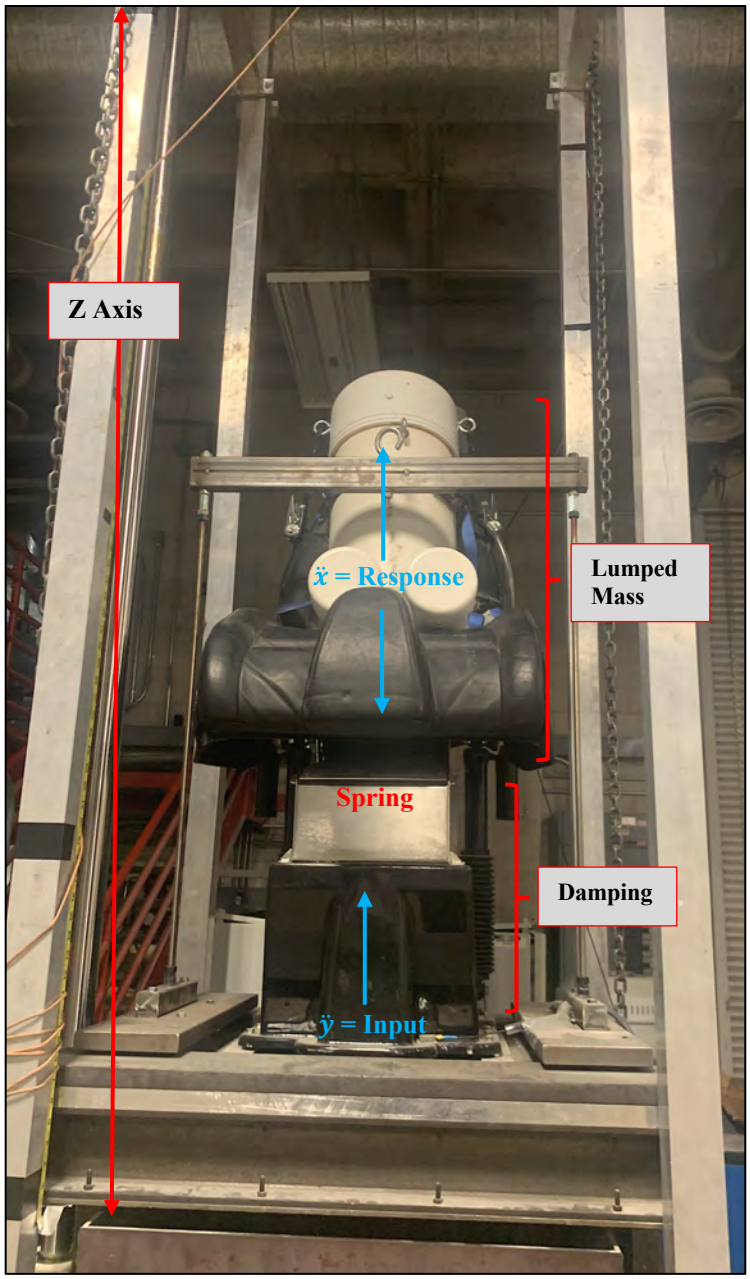

Figure 6-1: Designation of System Elements for SDOF Numerical Model

6.1.1 SDOF Simulated Response Using State Space Model

Recall from Chapter 4 that the state space method was used to transform the second-order differential equation that represented a dynamic system into a set of first-order differential equations. Therefore, all the entries of the state matrix were either the position or the velocity of the payload (response) or the platform (input). The system variables represented in the numerical model were the lumped mass of the payload and the seat, the expression defining the spring stiffness, and the expression for the damping coefficients. The arguments for the integration algorithm (Runge-Kutta) were the aforementioned variables, as well as the input acceleration time histories and the initial conditions.

The input acceleration time history was used to generate the input position and velocity for the spring and damping forces. The initial condition for the input position, was the distance from the top edge of the sandbox 'up' (positive Z direction) to the input accelerometer on the platform. For the payload (response), the initial position condition was the input initial condition plus the distance from the input accelerometer to the response accelerometer, minus the distance the spring was compressed by the payload. The initial spring compression was essentially a function of the mass of the payload, the acceleration due to gravity, and the spring stiffness constant. An entry from (4-68) is shown here as (6-1). That expression was one element of the function that served as the argument for the integration algorithm. Before viewing some of the graphs of the simulated response produced by the numerical model, an explanation on the selection of the seat damping coefficient is necessary.

$$-\frac{c_1}{m}(\dot{z}) - \frac{c_2}{m}(\dot{z} + \dot{y}_{accel})^2 sign(\dot{z} + \dot{y}_{accel}) - \frac{R}{m}(z) - g - \ddot{y}_{accel} \tag{6-1}$$

In Chapter 5, it was mentioned that the force versus displacement data points from the experimental spring analysis were fitted to a linear, second, and third order polynomial regression fits. The outcome was that although the R-squared values for the fits were close, the third order polynomial fit had the highest R-squared value. Consequently, the numerical model was executed using the spring constant from the linear

fit, which was 27862 N/m (159.1 lbf/in), as well as the value from the third order polynomial fit, 30530 N/m (174.33 lbf/in), to determine which value yielded the better results. As there was no information for the damping coefficient, a nonlinear least-squares fit was used to define a second order polynomial for the damping. The Matlab function 'lsqnonlin' was used to generate two values for the damping expression. The time acceleration histories from three tests were used as the input. The lower and upper bounds for the starting points for the fit were 0 N-s/m and 5000 N-s/m (28.55 lbf-s/in), respectively. The upper bound was based on a value just over the maximum critical damping listed in Table 5-22 for the 112.76 kg (248.6 lb) payload. The fit returned coefficients of 1900 N-s/m (10.85 lbf-s/in) and 100 N-s/m (0.57 lbf-s/in) for c1 and c2 in (6-1), respectively. Those were the starting points for the damping values, and they were adjusted (up from 1900 and down from 100) until the simulated response acceleration matched the experimental response acceleration as closely as possible.

The graphs showed that the simulated response acceleration from the numerical model exhibited a strong alignment with the experimental response acceleration measured by the accelerometer in the base of the payload. What was also evident in each graph was the presence of a periodically spaced pulse in most of the time histories. Those spikes were the result of a component of the tower that was not captured by the equations of motion. Figures 6-2 to 6-4 display the simulated response versus the experimental response accelerations for each payload category for the wedge. The '(W)' in the title signifies a test conducted with the wedge. Figure 6-5 is a graph for the position for one test with the 49.6 kg (109.3 lb) payload with the wedge. Figures 6-6 to 6-7 show the simulated response versus the experimental response accelerations for each payload category for the five tines. The '(T)' in the title denotes a test conducted with the five tines. Figure 6-9 is a graph for the position for one test with the 83.5 kg (184 lb) payload with the five tines. In the graphs, the light blue line represents the base input acceleration, the dark blue line is the experimental payload response acceleration, and the red line is the simulated payload response acceleration. Additional graphs can be viewed in Appendix B.

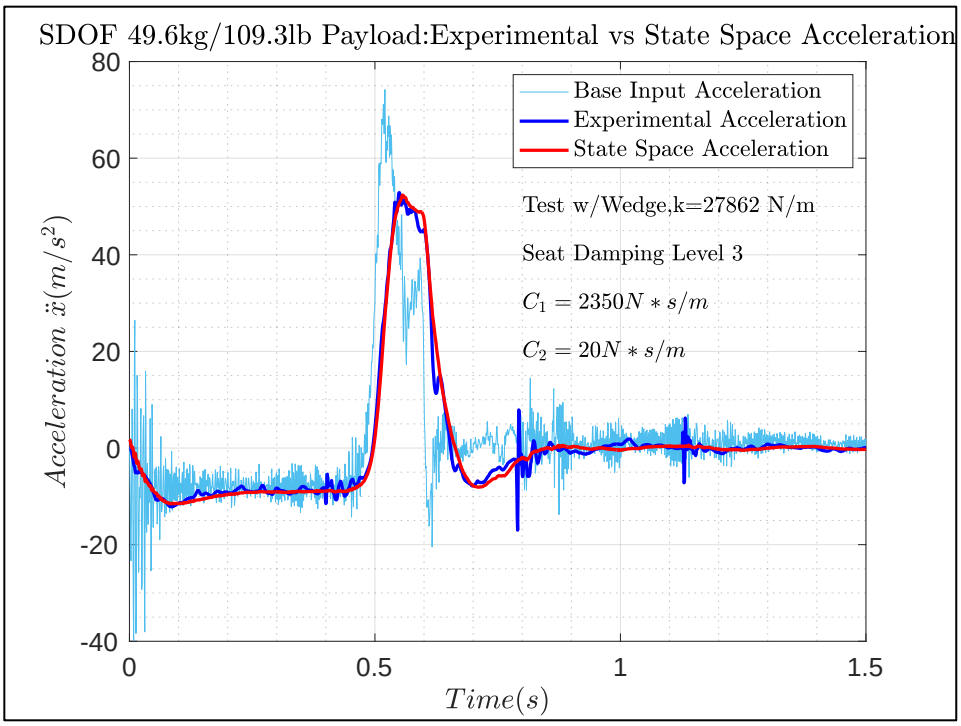

Figure 6-2: SDOF 49.6kg/109.3lb Payload (W): Experimental vs State Space Acceleration

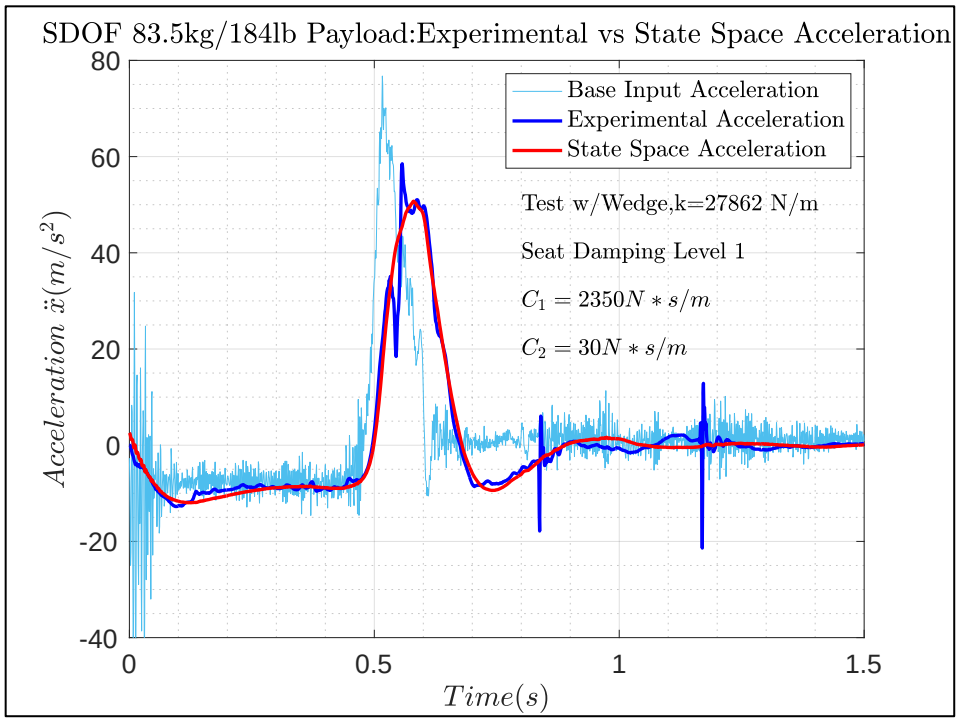

Figure 6-3: SDOF 83.5kg/184lb Payload (W): Experimental vs State Space Acceleration

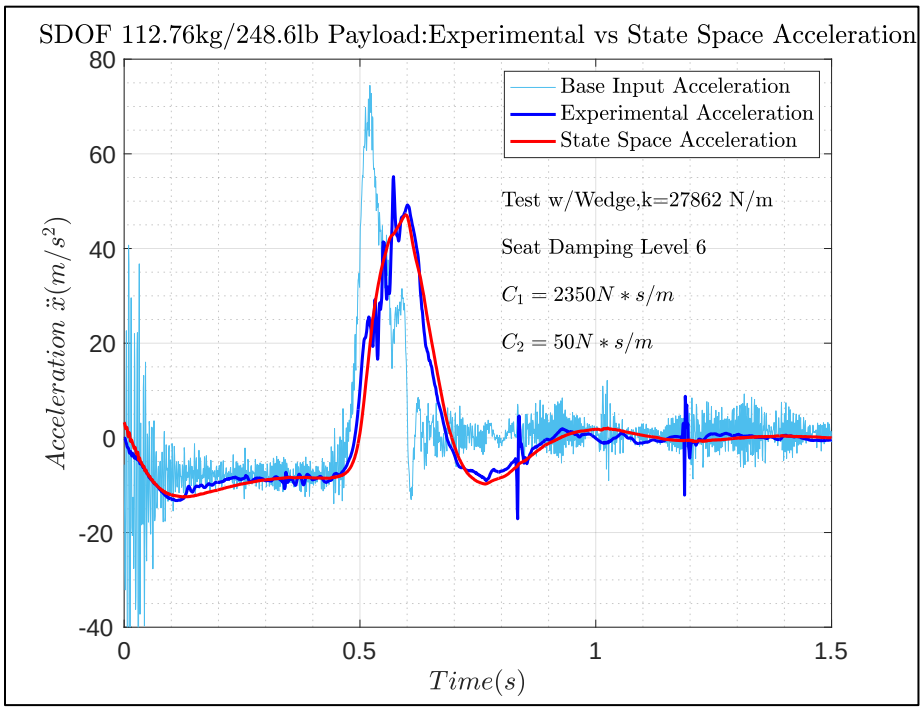

Figure 6-4: SDOF 112.76kg/248.6lb Payload (W): Experimental vs State Space Acceleration

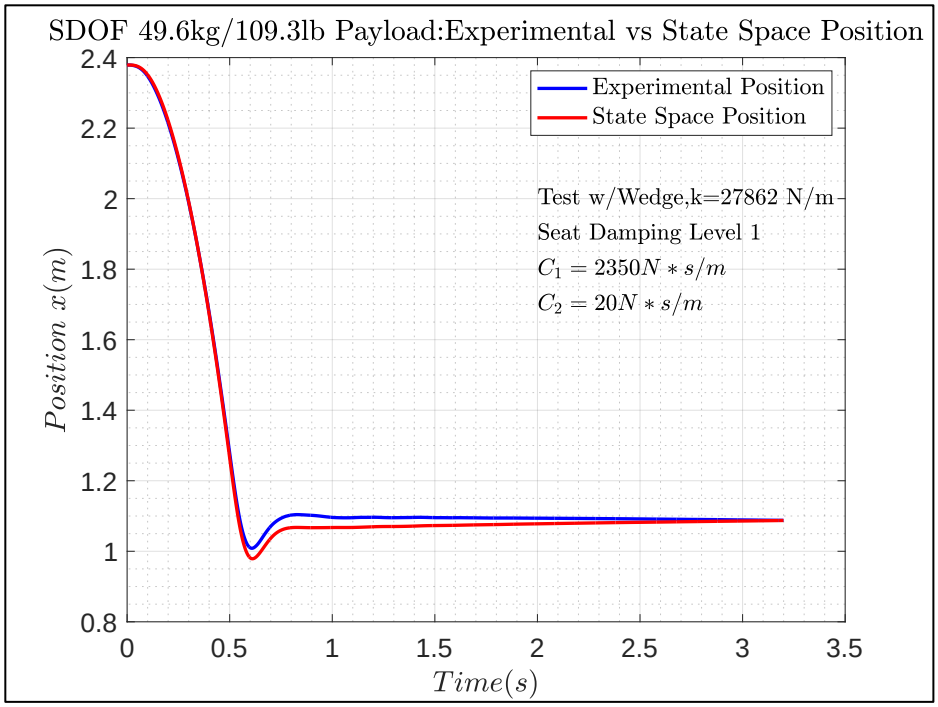

Figure 6-5: SDOF 49.6kg/109.3lb Payload (W): Experimental vs State Space Position

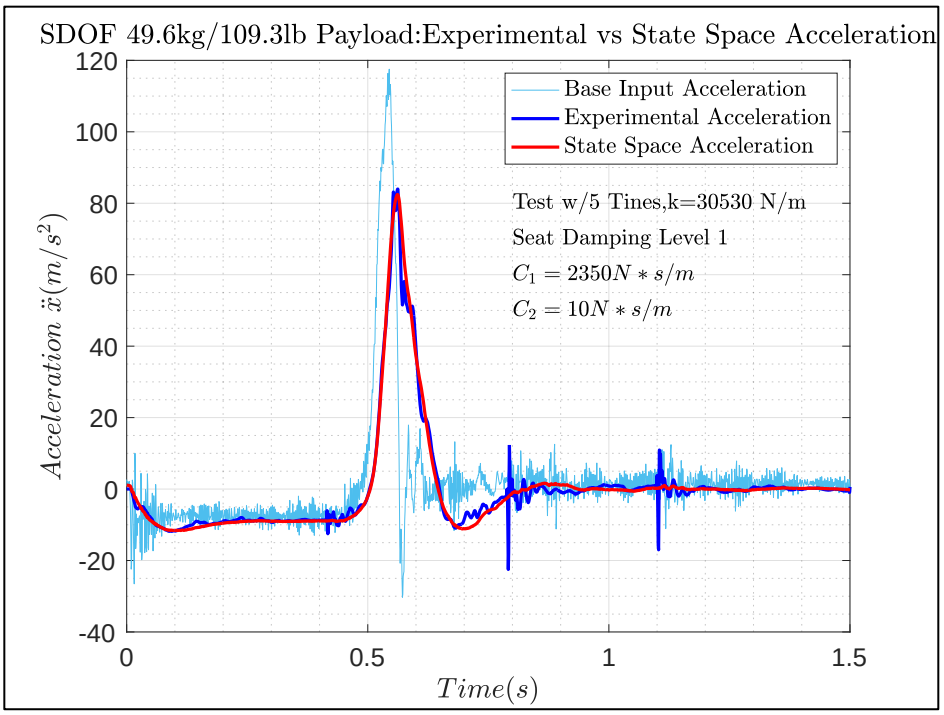

Figure 6-6: SDOF 49.6kg/109.3lb Payload (T): Experimental vs State Space Acceleration

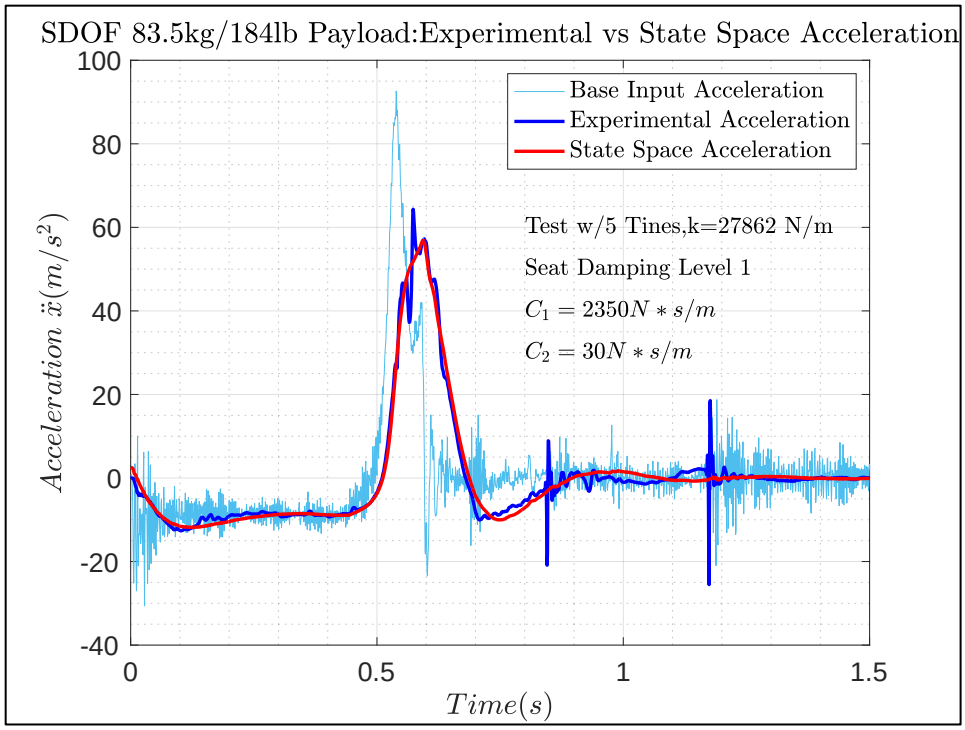

Figure 6-7: SDOF 83.5kg/184lb Payload (T): Experimental vs State Space Acceleration

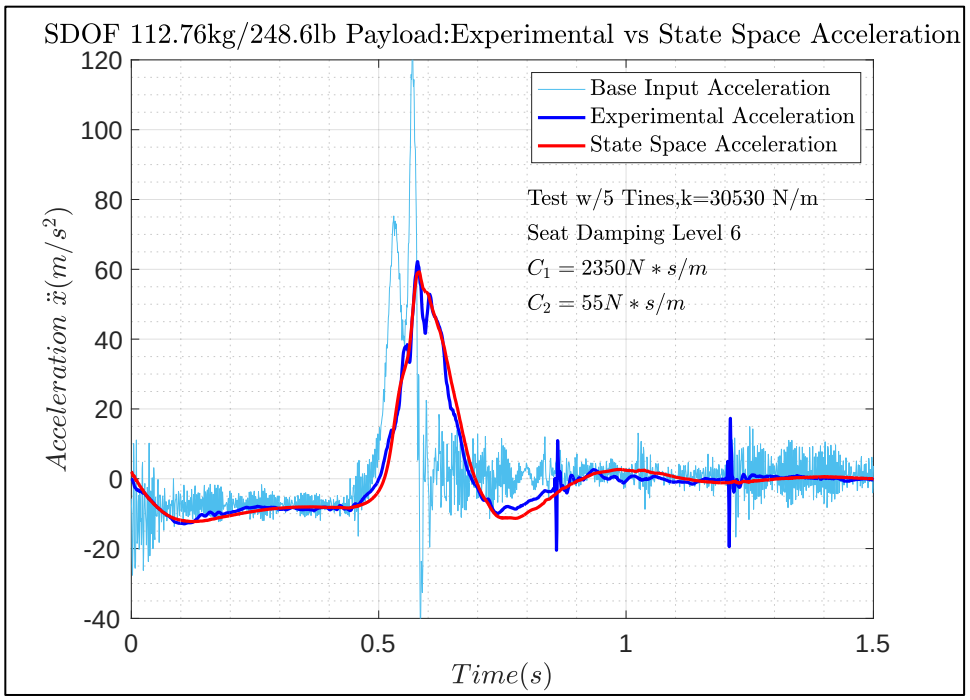

Figure 6-8: SDOF 112.76kg/248.6lb Payload (T): Experimental vs State Space Acceleration

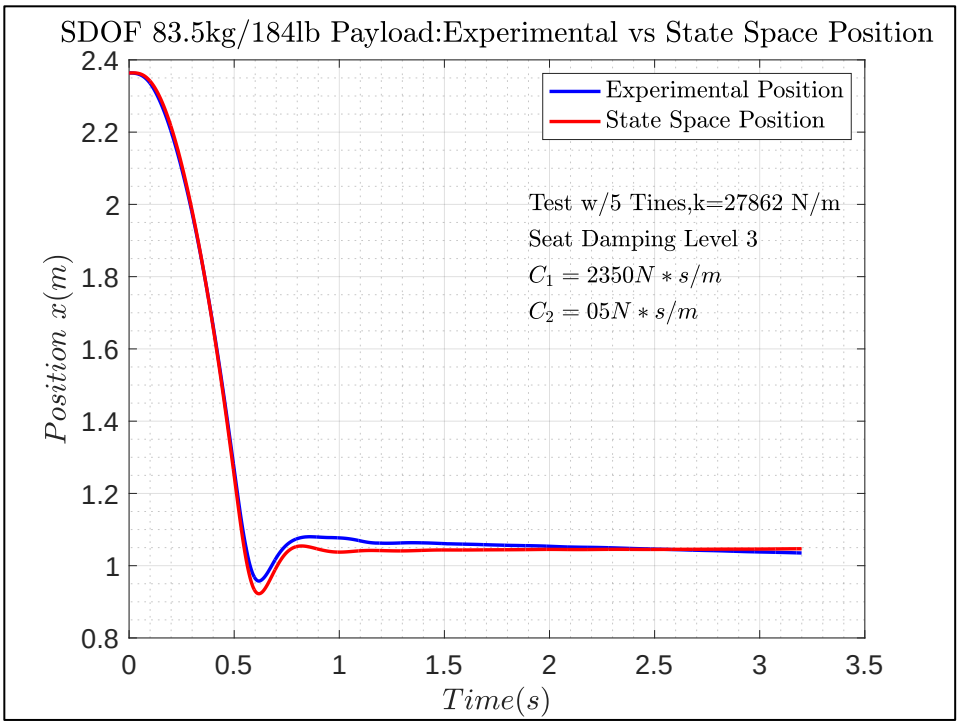

Figure 6-9: SDOF 83.5kg/184lb Payload (T): Experimental vs State Space Position

Before addressing the spikes in the experimental acceleration time history, the findings from the state-space-based numerical analysis are examined. The preceding figures illustrate a close match between the experimental and simulated response acceleration (and position) data, but beyond the images, the numerical analysis revealed some points of interest.

SDOF State Space Acceleration

The first noticeable item of interest was the variation of the values for the damping coefficient. It was stated earlier that the starting point for c1 and c2 was 1900 N-s/m (10.85 lbf-s/in) and 100 N-s/m (0.57 lbf-s/in), respectively. The outcome showed that c1 affected the damping associated with the peak acceleration pulse. The value for c1 ranged from 2100 N-s/m (11.99 lbf-s/in) to 2500 N-s/m (14.28 lbf-s/in) with the value of 2350 N-s/m (13.42 lbf-s/in) serving as a good compromise. The higher end of the range impacted the tests for which the seat damping was set to levels one and three, and the lower end of the range influenced the tests for which the seat damping level was set to six. Revisiting the subject of the damping ratio that was covered in chapter five, it seemed that the estimate of 0.50 for the damping ratio was not too far outside the range of possible values. Using the critical damping values from Table 5-23 and the values from the numerical model, the approximate range for the damping ratio for the system was 0.576 to 0.658. The value for c2 affected the depth of the negative dip in the acceleration time history that typically occurred after the main pulse.

The original value for c2 was 100 N-s/m (0.57 lbf-s/in), but the alignment between the experimental and simulated data improved when that value was reduced. The depth of the dip below zero after the main pulse for the simulated response was shallower when c2 ranged from 10 N-s/m (0.057 lbf-s/in) to 50 N-s/m (0.29 lbf-s/in). For the five tines data set with the 112.76 kg (248.6 lb) payload, the value reached as high as 55 N-s/m (0.31 lbf-s/in). When c1 moved towards the higher end, c2 had to be adjusted downward or the spring constant value had to be decreased. For the spring constants that were derived from the regression fit, the lower value of 27862 N/m (159.1 lbf/in) from the linear fit fared slightly better for the tests for which the wedge was installed or the lower amplitude test for the five tines. The third order value of 30530 N/m (174.33 lbf/in) produced better alignment with the higher amplitude empirical tines data. The mean absolute

percent error values were very high, but that was attributed to the spikes and the noise in the experimental data.

Although the experimental data was filtered down to 150 Hz from 500 Hz, the signal still contained a certain level of noise, especially in comparison to the output of a numerical model. Hence, the large values for the mean absolute percent error. Once the value for c1 that appeared to result in the closest match between the simulated and experimental acceleration data was established, it was kept constant for all of the runs. Thus, the variation in the percent error was influenced more by the value of the spring constant.

The percent error values were high across all three payloads for both spring constants. Although, the values tended to be marginally lower when the larger spring constant was used. The 83.5 kg (184 lb) payload recorded the lowest error value at around 44% for the higher spring constant for the wedge simulation data. The highest error value was up to 475.6% for the 49.6 kg (109.3 lb) payload with the lower spring constant value for the tines simulation output data. The 112.76 kg (248.6 lb) payload yielded the lowest average error value for the wedge data with the larger spring constant value.

Figure 6-10 illustrates the presence of noise in the 150 Hz filtered experimental input and response acceleration signals. In the figure, the light blue line represented the 150 Hz filtered base input acceleration, the dark blue line was the 150 Hz filtered experimental payload response acceleration, and the red line was the simulated payload response acceleration. Table 6-1 lists the mean absolute percent errors for the simulated acceleration for each payload for the wedge and the tines.

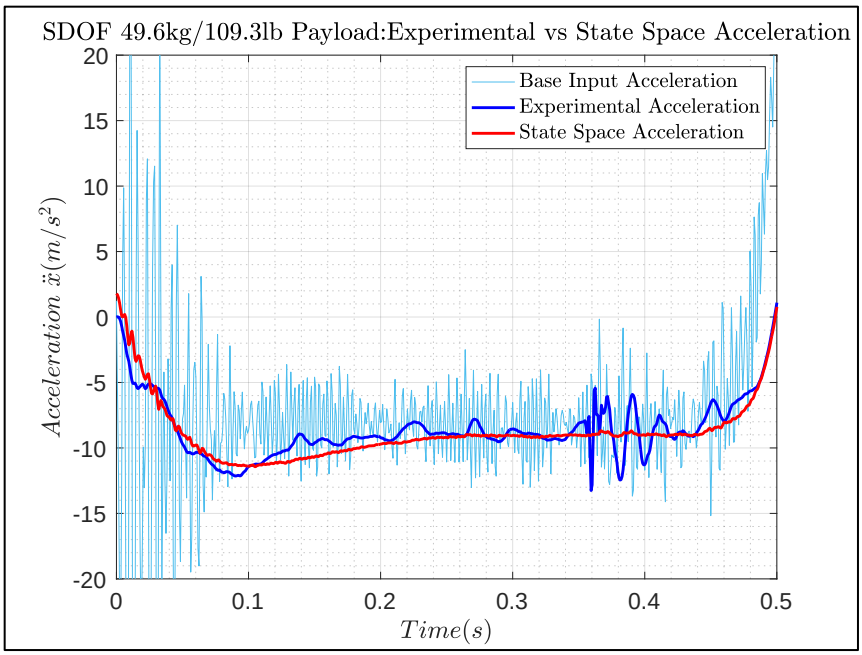

Figure 6-10: Presence of Noise in 150 Hz Filtered Experimental Data

Table 6-1: Mean Absolute Percent Error for SDOF State Space Acceleration

Mean Absolute Percent Error for SDOF State Space Acceleration						
	Wedge					
Seat Damp Level	49.6kg/109.3lb 2350/20 (N-s/m)		83.5kg/184lb 2350/30 (N-s/m)		112.76kg/248.6lb 2350/40 (N-s/m)	
	27862 k (N/m)	30530 k (N/m)	27862 k (N/m)	30530 k (N/m)	27862 k (N/m)	30530 k (N/m)
1	86%	56%	159%	99%	83%	51%
3	188%	130%	154%	44%	83%	45%
6	92%	65%	104%	60%	65%	51%
	Five Tines					
	49.6kg/109.3lb 2350/10 (N-s/m)		83.5kg/184lb 2350/30 (N-s/m)		112.76kg/248.6lb 2350/55 (N-s/m)	
	27862 k (N/m)	30530 k (N/m)	27862 k (N/m)	30530 k (N/m)	27862 k (N/m)	30530 k (N/m)
1	288.65%	186%	147%	137%	230.6%	152%
3	113.1%	72%	75%	67%	141.4%	96%
6	475.6%	305%	60%	55%	121.2%	82%

In general, the combination of values that generated the closest fit of the wedge data for all three payloads was 27862 N/m (159.1 lbf/in) for the spring constant, 2350 N-s/m (13.42 lbf-s/in) for c1, and the range of 20 N-s/m (0.11 lbf-s/in) to 40 N-s/m (0.23 lbf-s/in) for c2. For the tines, the spring constant of 30530 N/m (174.33 lbf/in) worked better for the 49.6 kg (109.3 lb) and 112.76 kg (248.6 lb) payloads, but the value of 27862 N/m (159.1 lbf/in) offered closer alignment for the 83.5 kg (184 lb) payload data, despite what the percent error suggested. The value for c1 for the tines was equivalent to the value used for the wedge at 2350 N-s/m (13.42 lbf-s/in), and the range for c2 was 10 N-s/m (0.057 lbf-s/in) to 55 N-s/m (0.31 lbf-s/in). Table 6-2 itemizes the range of spring stiffness and damping values that seemed to generate the best fit of the simulated response acceleration with the experimental response acceleration data for the selected tests. The entries for c2 in Table 6-2 suggest that there was a direct correlation between an increase in the payload mass and an increase in the second order damping value. The numerical model position data was influenced by the spring constant. However, it also appeared to be sensitive to adjustments in the c2 damping value as well.

Table 6-2: Spring and Damping Values for SDOF State Space Acceleration

Spring Stiffness and Damping Values for SDOF State Space Acceleration									
	Wedge								
Seat Damp Level	49.6kg/109.3lb			83.5kg/184lb			112.76kg/248.6lb		
	k (N/m)	c_1 (Ns/m)	c_2 (Ns/m)	k (N/m)	c_1 (Ns/m)	c_2 (Ns/m)	k (N/m)	c_1 (Ns/m)	c_2 (Ns/m)
1	27682	2350	20	27682	2350	30	27682	2350	40
3	27682	2350	20	27682	2350	30	27682	2350	40
6	27682	2350	20	27682	2350	30	27682	2350	50
	Five Tines								
	49.6kg/109.3lb			83.5kg/184lb			112.76kg/248.6lb		
	k (N/m)	c_1 (Ns/m)	c_2 (Ns/m)	k (N/m)	c_1 (Ns/m)	c_2 (Ns/m)	k (N/m)	c_1 (Ns/m)	c_2 (Ns/m)
1	30530	2350	10	27682	2350	30	30530	2350	55
3	30530	2350	10	27682	2350	30	30530	2350	55
6	30530	2350	10	27682	2350	30	30530	2350	55

SDOF State Space Position

The trend of the position plot corresponds to the height of the payload from its suspended position before a drop to its position at rest after a drop. For each test, the starting position of the accelerometer located in the base of the payload was approximately 2.29 m (7.51 ft) above the top edge of the sandbox. At the end of a test, the accelerometer was usually about 1.0 m (3.28 ft) above the top edge of the sandbox (see Figure 4-4). Most of the graphs for the response position showed that the simulated data aligned with the experimental position data for the payload.

For the 49.6 kg (109.3 lb) payload, the numerical position data looked promising for all three of the seat damping levels with the lower spring constant for the wedge. In contrast, for the 112.76 kg (248.6 lb) payload, the higher spring constant value worked better with the wedge simulated data. The higher spring constant resulted in a closer alignment with the experimental data for seat damping levels one and six with the 83.5 kg (184 lb) payload. The values for c2 ranged from zero on the lower end for the 112.76 kg (248.6 lb) payload to 35 N-s/m (0.20 lbf-s/in) on the high end for the 83.5 kg (184 lb) payload. For the

83.5 kg (184 lb) payload, the alignment was good for seat damping levels one and three for the wedge data, but fine tuning for seat damping level six was a challenge. The adjustments would either cause the model and experimental data to cross just after the 1.5 second mark or diverge just at the one second time frame. For the tines data, the lower spring constant generated better agreement for all the tests, except for the seat damping levels three and six for the 49.6 kg (109.3 lb) payload.

The alignment of the numerical position with the experimental position was generally better with the tines data set. The 83.5 kg (184 lb) and 112.76 kg (248.6 lb) payloads data matched well with the tines data with the lower spring constant value. The values for c2 ranged from zero on the low end for the 49.6 kg (109.3 lb) payload to 50 N-s/m (0.29 lbf-s/in) on the high end for the 83.5 kg (184 lb) payload. Unlike the acceleration data, there was no distinct relationship between the second order damping values and the increase in payload mass. The mean absolute percent error values for the simulated position data were considerably low compared to the acceleration results.

The position graphs displayed a close agreement between the experimental position and the numerical model position output. The lowest error was 1.23% for the 83.5 kg (184 lb) payload with the tines data with the lower spring constant value and a seat damping setting of three. The largest error was 4.98%, which occurred with the 112.76 kg (248.6 lb) payload with the higher spring constant value and also at the seat damping level of three. Table 6-3 lists the mean absolute percent error with accompanying spring and c2 values for the simulated position. The entries in Table 6-3 are affiliated with the variable values that provided the closest alignment between the experimental and numerical data.

Overall, the results from the state space numerical analysis were favorable. However, the relatively close match between the experimental and simulated acceleration and position data aside, the spikes in the experimental acceleration time histories were reminiscent of a feature in the tower design.

Table 6-3: Mean Absolute Percent Error for SDOF State Space Position

Mean Absolute Percent Error for SDOF State Space Position									
				Wedge					
Seat	49.6kg/109.3lb			83.5kg/184lb			112.76kg/248.6lb		
Damp Level	k (N/m)	c_2 (Ns/m)	Error (%)	k (N/m)	c_2 (Ns/m)	Error (%)	k (N/m)	c_2 (Ns/m)	Error (%)
1	27862	20	1.42	30530	30	2.77	30530	10	1.8
3	27862	20	1.41	27862	35	1.39	30530	10	4.98
6	27862	20	3.92	30530	30	3.68	30530	00	1.76
				Five Tines					
	49.6kg/109.3lb			83.5kg/184lb			112.76kg/248.6lb		
	k (N/m)	c_2 (Ns/m)	Error (%)	k (N/m)	c_2 (Ns/m)	Error (%)	k (N/m)	c_2 (Ns/m)	Error (%)
1	27862	00	2.83	27682	30	2.07	27862	20	3.08
3	30530	00	1.39	27682	05	1.23	27862	20	4.09
6	30530	00	3.04	27682	50	3.81	27862	15	1.32

Experimental Acceleration Time History Spikes

In Chapter 3, during the description of the drop tower, it was mentioned that a horizontal bar with a hook (hoist frame) was the attachment point for the cable from the hoist. That bar was supported by two semi-rigid metal rods that were bolted to the platform. The issue was that those two rods were not sufficiently rigid. Upon impact, due to the incoming dynamic load to the platform, those rods pitched back and forth in a periodic manner which caused the horizontal bar to strike the mid-torso section of the payload. The first impact to the payload occurred during the acceleration pulse with typically two additional impacts occurring mere fractions of a second thereafter. The results were those clearly identifiable (almost evenly spaced in time) spikes in the experimental response acceleration time histories.

There was no value in replicating that phenomenon in a numerical analysis, but its occurrence may serve to inform possible modifications to the tower moving forward. Figure 6-11 shows the horizontal bar supported by the two rods, and Figure 6-12 depicts the spikes in the experimental response acceleration. Notice that the spikes are almost evenly spaced in time, which indicates the periodic nature of the pitching motion of the rods. The Newmark-Beta (Newmark-β) numerical version of the SDOF model is covered next.

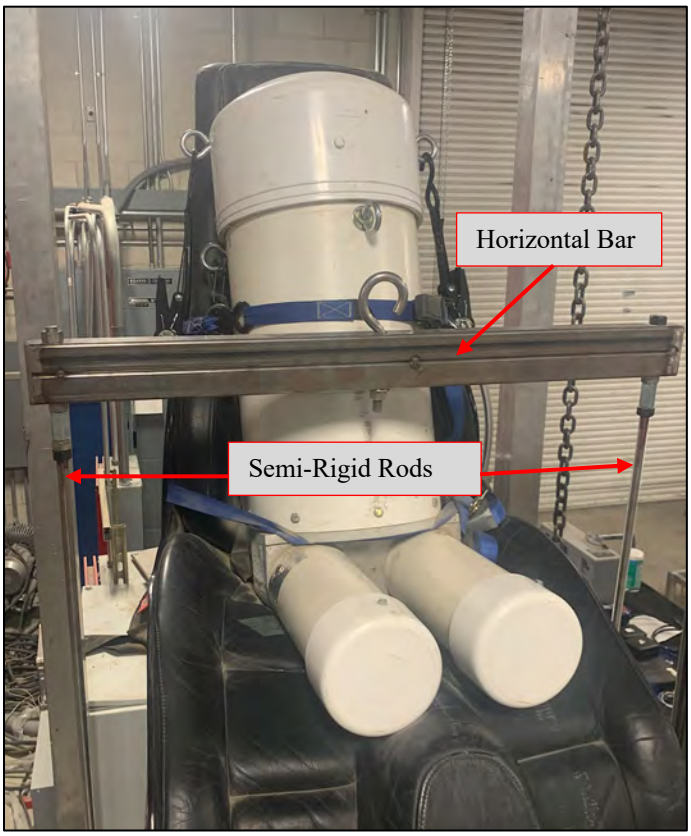

Figure 6-11: Horizontal Bar Positioned Mid-Torso of the Payload

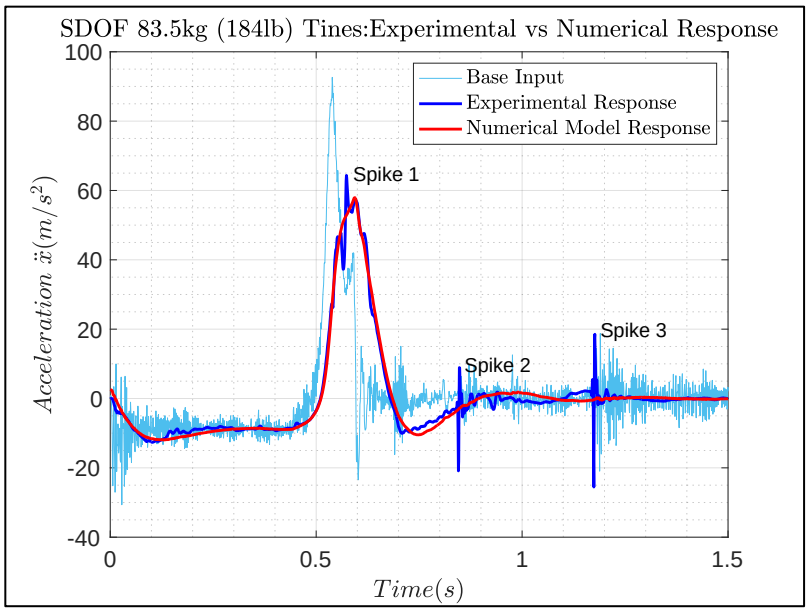

Figure 6-12: Graph Identifying Spikes in the Experimental Acceleration Time History

6.1.2 SDOF Simulated Response Using Newmark-Beta Model

The Newmark-Beta (Newmark-β) method presented an alternate approach to the numerical analysis. Referring to the discussion in Chapter 4, it was based on a time-stepping algorithm that implemented direct numerical integration to solve the differential equations used to represent structural dynamic systems. The method used a Taylor series expansion of the displacement and velocities to compute the state of the system at the next time step. In turn, those displacement and velocity values were used for the spring and damping forces to determine the equilibrium between the LHS and RHS in the equation for the residual (4-91). Similar to the state space method, the entries to the algorithm were enclosed in a function.

The system variables represented in the function were the mass of the payload plus the mass of the seat and the equations representing the spring stiffness and the damping coefficients. The arguments for the solver algorithm were the function that contained the aforementioned variables, as well as the input acceleration time histories and the initial conditions. The Matlab® solver was embedded in the time stepping algorithm. The spring and damping coefficients from the state space analysis were implemented in the Newmark-β method. The quadrature values were set to $\gamma = 1/2$ and $\beta = 1/4$ for second order accuracy and unconditional stability.

To keep the comparison of the methods fair, simulated responses were generated for the same set of selected tests that were used for the state space method. The outcome indicated that the methods produced relatively similar results. The differences were minor, and probably attributed to the inner workings of the Matlab® numerical solvers. Figures 6-13 to 6-15 display the simulated response versus the experimental response accelerations for each payload category for the wedge. The '(W)' in the title signifies a test conducted with the wedge. Figure 6-16 is a graph for the position for one test with the 112.76 kg (248.6 lb) payload with the wedge. Figures 6-17 to 6-19 show the simulated response versus the experimental response accelerations for each payload category for the five tines. The '(T)' in the title implies a test conducted with the five tines. Figure 6-20 is a graph for the position for one test with the 112.76 kg (248.6 lb) payload with

the five tines. In all the graphs, the light blue line represents the 150 Hz filtered base input acceleration, the dark blue line is the 150 Hz filtered experimental payload response acceleration, and the red line is the simulated payload response acceleration. Additional graphs can be viewed in Appendix B.

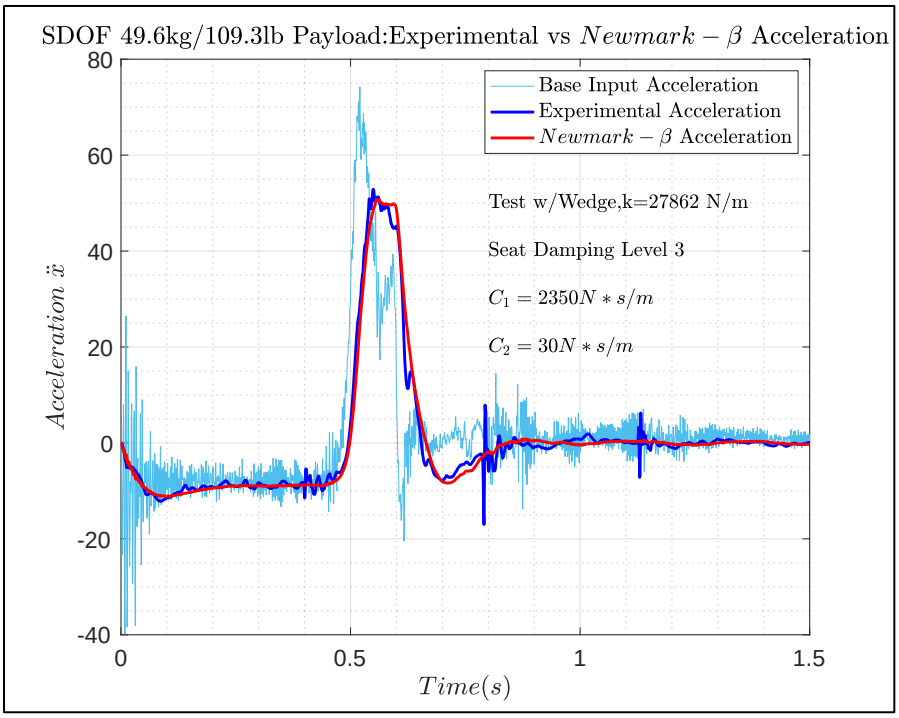

Figure 6-13: SDOF 49.6kg/109.3lb Payload (W): Experimental vs Newmark-ß Acceleration

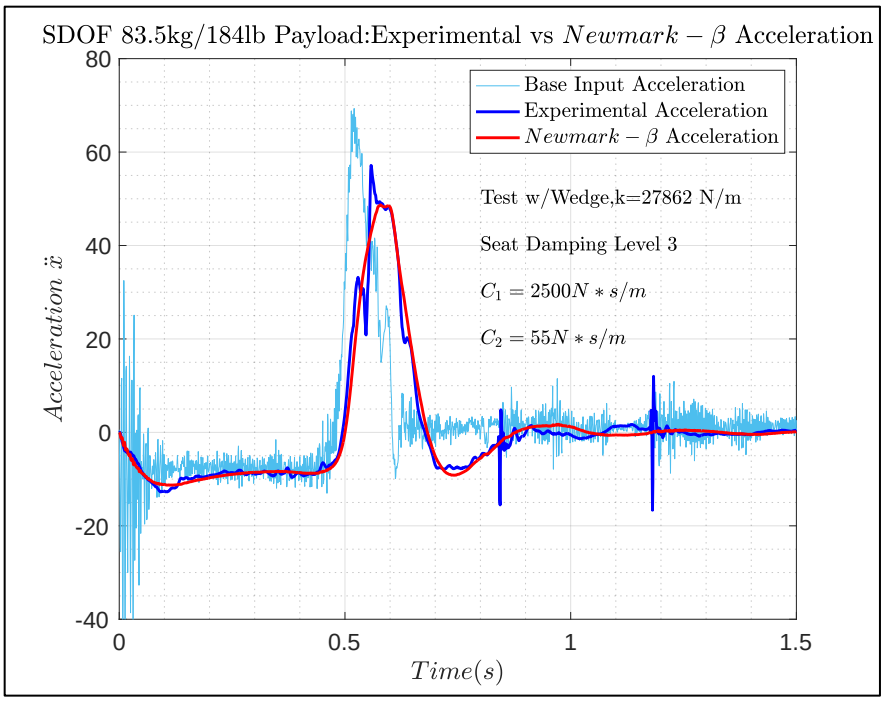

Figure 6-14: SDOF 83.5kg/184lb Payload (W): Experimental vs Newmark-ß Acceleration

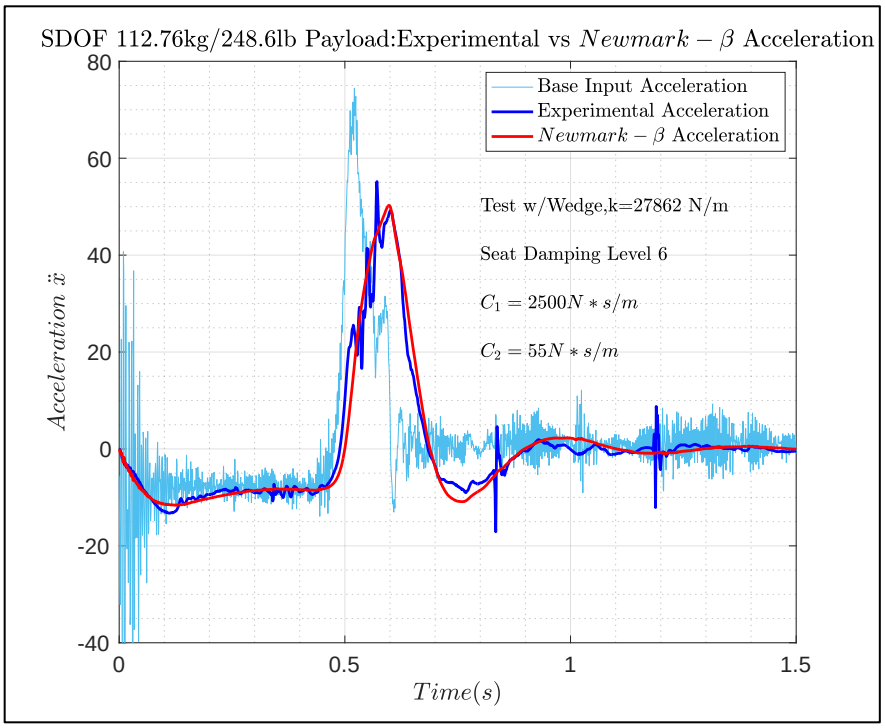

Figure 6-15: SDOF 112.76kg/248.6lb Payload (W): Experimental vs Newmark-ß Acceleration

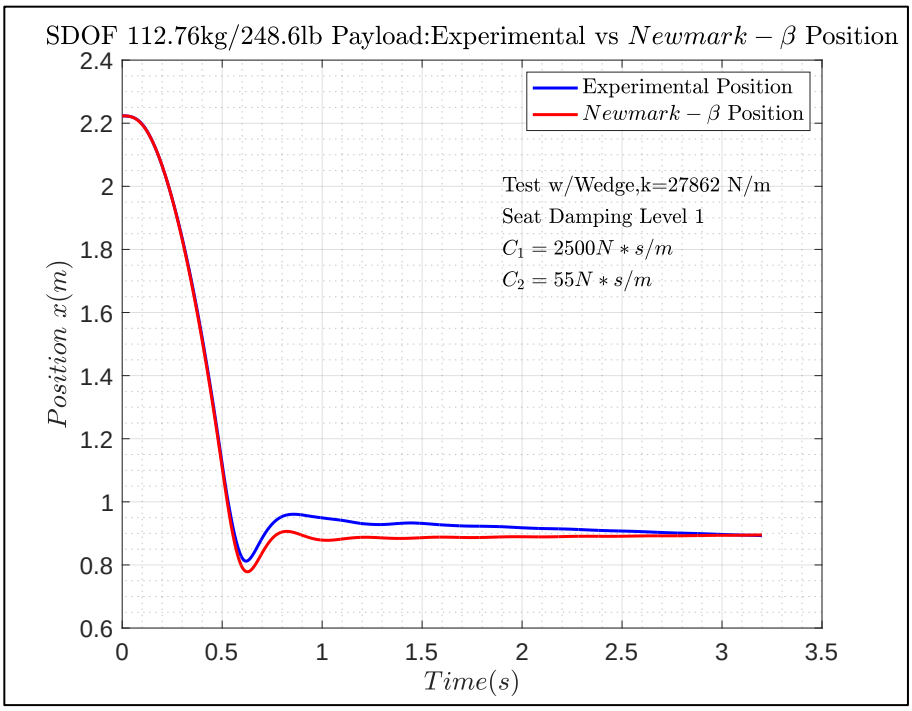

Figure 6-16: SDOF 112.76kg/248.6lb Payload (W): Experimental vs Newmark-ß Position

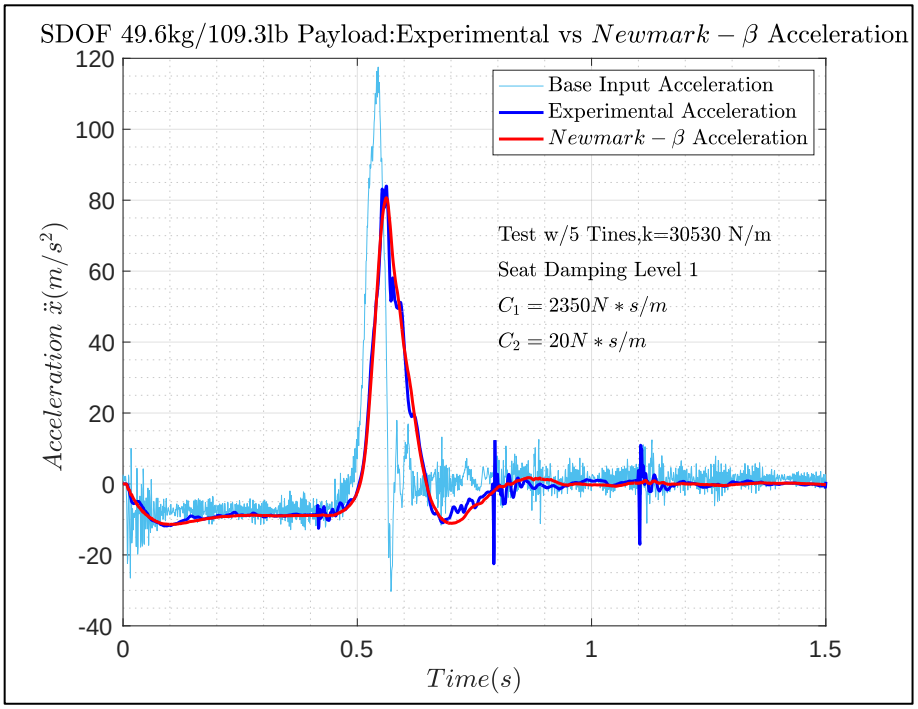

Figure 6-17: SDOF 49.6kg/109.3lb Payload (T): Experimental vs Newmark-ß Acceleration

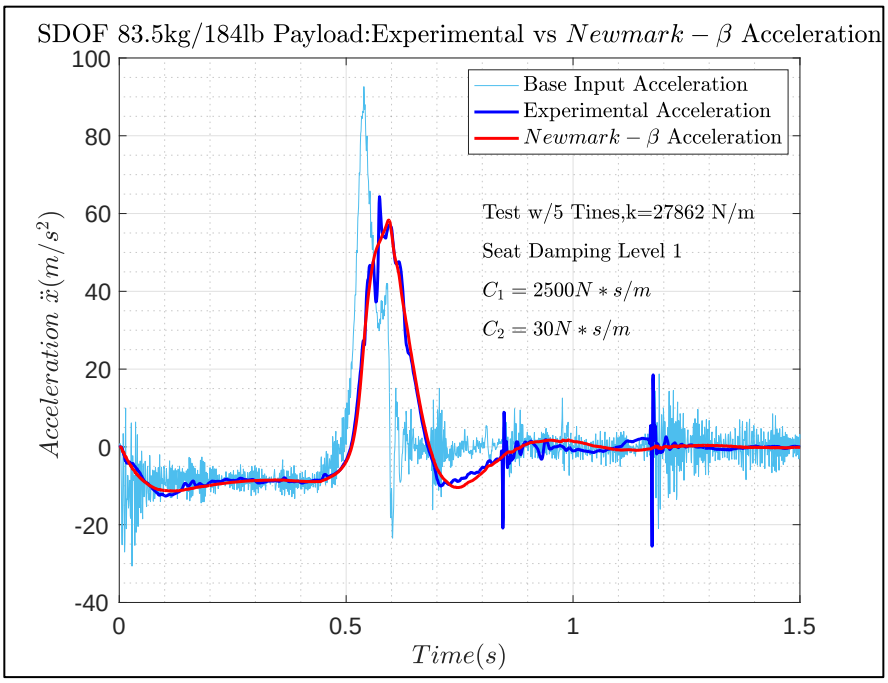

Figure 6-18: SDOF 83.5kg/184lb Payload (T): Experimental vs Newmark-ß Acceleration

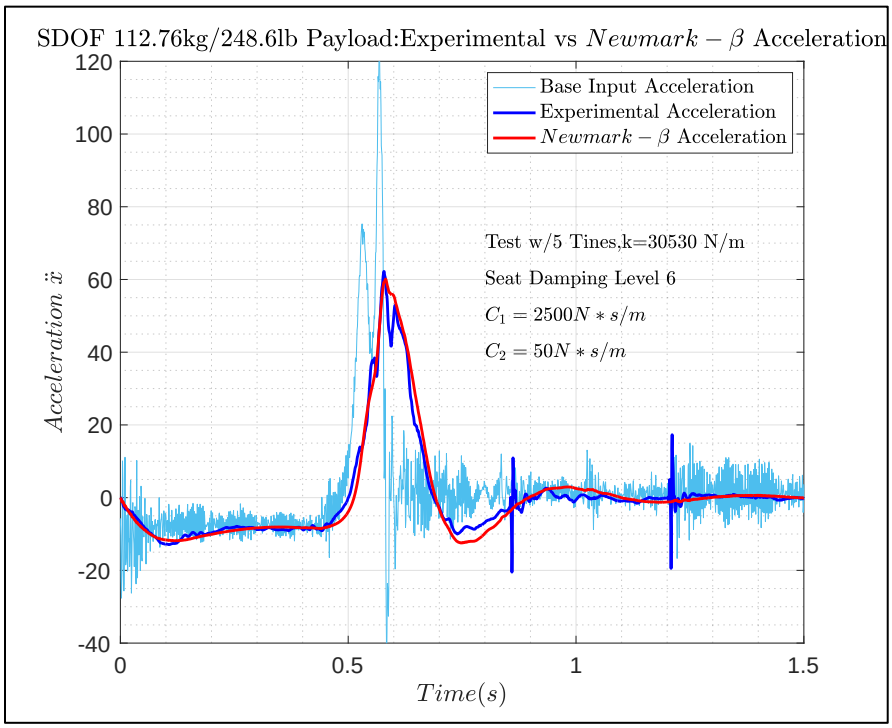

Figure 6-19: SDOF 112.76kg/248.6lb Payload (T): Experimental vs Newmark-ß Acceleration

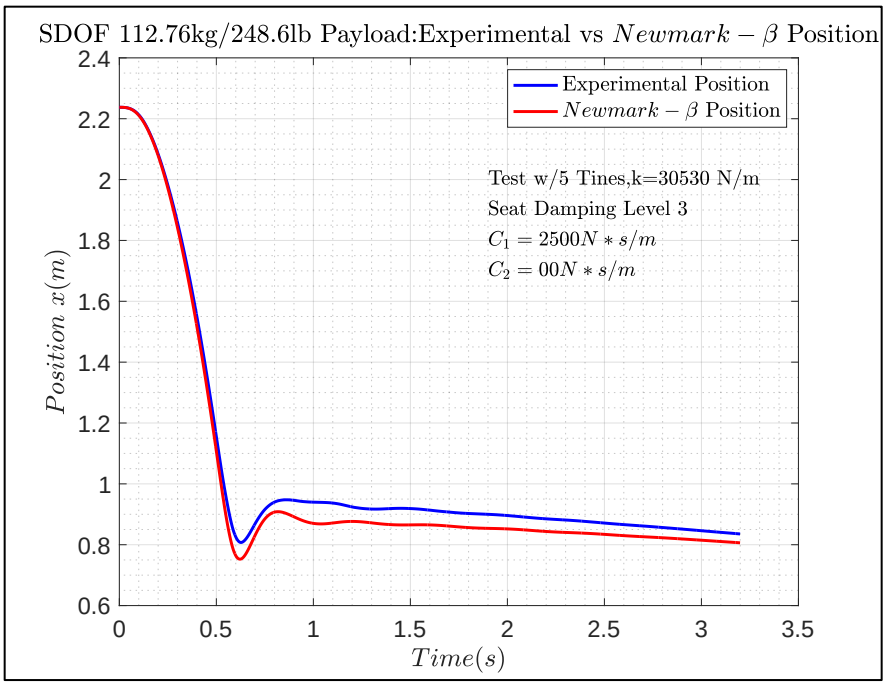

Figure 6-20: SDOF 112.76kg/248.6lb Payload (T): Experimental vs Newmark-ß Position

SDOF Newmark-Beta Acceleration

The match between the simulated acceleration and the experimental acceleration response data was satisfactory across all three payload categories. There were very minor differences between the state space and Newmark-β simulated acceleration data. The subtle differences between the two results were probably attributed to the fact that the Newmark-β method defined the time stepping algorithm; whereas in the state space model the time step was inherent to the built-in Matlab® solver. The combination of parameters that worked well for the state space method was more suited to the 49.6 kg (109.3 lb) payload with the wedge installed.

A spring constant of 27862 N/m (159.1 lbf/in) with a value of 2350 N-s/m (13.42 lbf-s/in) for c1, and a setting of 30 N-s/m (0.17 lbf-s/in) for c2 worked well for the 49.6 kg (109.3 lb) payload with the wedge at all three seat damping levels. To form a fit with the -1 g dip after the main acceleration pulse, the damping had to be increased for the 83.5 kg (184 lb) and 112.76 kg (248.6 lb) payloads with the wedge

data. The combination that seemed to work best for the two higher payloads was 2500 N-s/m (14.28 lbf-s/in) for c1 and a value of 55 N-s/m (0.31 lbf-s/in) for c2 at all three of the seat damping levels. For the tines, the curves exhibited a closer alignment when the larger spring constant was used with the 49.6 kg (109.3 lb) and the 112.76 kg (248.6 lb) payloads.

Along with the higher spring constant of 30530 N/m (174.33 lbf/in), the standard value of 2350 N-s/m (13.42 lbf-s/in) for c1 and the setting of 20 N-s/m (0.11 lbf-s/in) for c2, worked well for the 49.6 kg (109.3 lb) payload with the tines data. For the 112.76 kg (248.6 lb) payload, the model output fared better when the damping was increased to the higher values of 2500 N-s/m (14.28 lbf-s/in) and 50 N-s/m (0.29 lbf-s/in) in conjunction with the higher spring constant. To create a better match with the 83.5 kg (184 lb) payload for the tines data, the lower spring constant value, along with the higher value of 2500 N-s/m (14.28 lbf-s/in) for c1, appeared to be the best approach. Although the graphs for some of the simulated acceleration data from both methods appeared indistinguishable, the mean absolute percent error was actually lower for the Newmark-β method.

The highest recorded error was approximately 75% for the 49.6 kg (109.3 lb) payload with the lower spring constant value for the tines data. The lowest error occurred with the 83.5 kg (184 lb) payload for the higher spring constant, also with the tines. That value was 11.7%. Table 6-4 list the range of spring and damping values that seemed to return the best agreement of the simulated response acceleration with the experimental response acceleration data using the Newmark-β method. Notice the similar correlation between an increase in the payload mass and an increase in the second order damping value in Table 6-4, just as in Table 6-2. The mean absolute percent error numbers for the acceleration output are tabulated in Table 6-5. The error values for acceleration using the Newmark-β method were considerably lower than those associated with the state space analysis acceleration figures. However, higher percent error values for position were derived for the Newmark-β analysis.

Table 6-4: Spring Stiffness and Damping Values for SDOF Newmark-ß Acceleration

Spring Stiffness and Damping Values for SDOF Newmark-ß Acceleration									
	Wedge								
Seat Damp Level	49.6kg/109.3lb			83.5kg/184lb			112.76kg/248.6lb		
	k (N/m)	c_1 (Ns/m)	c_2 (Ns/m)	k (N/m)	c_1 (Ns/m)	c_2 (Ns/m)	k (N/m)	c_1 (Ns/m)	c_2 (Ns/m)
1	27682	2350	30	27682	2500	55	27682	2500	55
3	27682	2350	30	27682	2500	55	27682	2500	55
6	27682	2350	30	27682	2500	55	27682	2350	55
	Five Tines								
	49.6kg/109.3lb			83.5kg/184lb			112.76kg/248.6lb		
	k (N/m)	c_1 (Ns/m)	c_2 (Ns/m)	k (N/m)	c_1 (Ns/m)	c_2 (Ns/m)	k (N/m)	c_1 (Ns/m)	c_2 (Ns/m)
1	30530	2350	20	27682	2500	30	30530	2500	50
3	30530	2350	20	27682	2500	30	30530	2500	50
6	30530	2350	20	27682	2500	30	30530	2500	50

Table 6-5: Mean Absolute Percent Error for SDOF Newmark-ß Acceleration

Mean Absolute Percent Error for SDOF Newmark-ß Acceleration						
	Wedge					
Seat Damp Level	49.6kg/109.3lb 2350/30 (N-s/m)		83.5kg/184lb 2500/55 (N-s/m)		112.76kg/248.6lb 2500/55 (N-s/m)	
	27862 k (N/m)	30530 k (N/m)	27862 k (N/m)	30530 k (N/m)	27862 k (N/m)	30530 k (N/m)
1	19.9%	17%	40%	29.9%	37%	31.7%
3	68.1%	61.5%	28%	20.3%	41%	32.1%
6	31%	28.3%	73%	46.7%	33%	27.5%
	Five Tines					
	49.6kg/109.3lb 2350/20 (N-s/m)		83.5kg/184lb 2500/30 (N-s/m)		112.76kg/248.6lb 2500/50 (N-s/m)	
	27862 k (N/m)	30530 k (N/m)	27862 k (N/m)	30530 k (N/m)	27862 k (N/m)	30530 k (N/m)
1	20.6%	18%	19%	11.7%	47.7%	42%
3	30%	24%	19%	20.6%	69.6%	53%
6	75.4%	62%	36%	34.3%	72.1%	54%

SDOF Newmark-Beta Position

In keeping with the trend exhibited in the state space model, the mean absolute percent error values for position were lower than the percent error values for acceleration with the Newmark-β model as well. Although the error values for position were low, the numbers were generally a bit larger than the error values calculated for position when the state space method was implemented.

The position data from the model seemed less susceptible to manipulation of the damping values than the position values generated by the state space analysis. For each payload category, a c2 value of zero was used at some point in the analysis. However, a c2 value of zero did not produce significantly better results than a value of 30 N-s/m (0.17 lbf-s/in). In fact, values of 30 N-s/m (0.17 lbf-s/in) and 55 N-s/m (0.31 lbf-s/in) were the only two other values assigned to c2 other than zero. The lower spring value yielded plots that were more aligned with the experimental data for the 49.6 kg (109.3 lb) payload with the tines and for the 112.76 kg (248.6 lb) with the wedge data. The higher spring constant worked better for every other simulation.

The smallest error value was 2.7% for the 83.5 kg (184 lb) payload with the higher spring constant for the wedge data. The highest value was 6.6% for the 112.76 kg (248.6 lb) payload for the tines data set, also with the higher spring constant. The lowest and the highest errors both occurred with a c2 value of zero. The mean absolute percent error values in Table 6-6 were linked to the combination of model properties that provided the closest alignment between the experimental and numerical position data.

The graphs for both the state space and the Newmark-β numerical models exhibited rather agreeable alignments between the simulated and experimental acceleration response data, albeit with large mean absolute percent error values. However, it was understood that the noise in the experimental data, as well as the acceleration spikes, contributed to the large percent error values. The subsequent course of action after examining the findings of the SDOF numerical model was to ascertain if the seat was adequately exemplified by the SDOF concept.

Table 6-6: Mean Absolute Percent Error for SDOF Newmark-ß Position

Mean Absolute Percent Error for SDOF Newmark-ß Position									
	Wedge								
Seat	49.6kg/109.3lb			83.5kg/184lb			112.76kg/248.6lb		
Damp Level	k (N/m)	c_2 (Ns/m)	Error (%)	k (N/m)	c_2 (Ns/m)	Error (%)	k (N/m)	c_2 (Ns/m)	Error (%)
1	30530	00	3.88	30530	00	3.47	27862	55	2.84
3	30530	00	5.08	30530	00	4.3	27862	55	2.84
6	30530	00	5.47	30530	00	2.73	27682	55	3.08
	Five Tines								
	49.6kg/109.3lb			83.5kg/184lb			112.76kg/248.6lb		
	k (N/m)	c_2 (Ns/m)	Error (%)	k (N/m)	c_2 (Ns/m)	Error (%)	k (N/m)	c_2 (Ns/m)	Error (%)
1	27862	00	6.19	30530	30	5.57	30530	00	2.85
3	27862	00	3.68	30530	30	4.97	30530	00	4.31
6	27862	00	4.83	30530	30	2.88	30530	00	6.64

Reviewing recorded footage of the drop tests revealed that there was very little vertical (Z axis) separation between the payload and the seat cushion during an impact. The accelerometers located in the payload and on the base of the seat pedestal were single axis sensors that measured acceleration in the vertical direction only. Consequently, data was not collected for the system's dynamic response in the X-Y plane. The X-Y plane was parallel to the horizontal plane that intersected the top edge of the sandbox. In addition to showing that the vertical interaction was minimal, there was no visual indication in the recorded footage that the payload and the seat moved as individual entities in the X-Y plane. Indeed, the only way to detect the dynamic interaction in the X-Y plane would have been to install additional accelerometers with the capability to measure acceleration in the X-Y plane. However, surplus accelerometers were not available, so the proposition that there was only marginal dynamic interaction in the vertical X-Y axis was speculation. However, a few things were certain.

First, the dominant dynamic component of a wave slam event is the vertical component. Thus, the other forces were not of primary interest for the study. Second, the main area of concern in an analysis of a shock mitigation seat is the dynamic load experienced by the seat occupant. What was observed from the results of the SDOF numerical model was that the simulated data was in close agreement with the data

measured by the accelerometer in the payload. That data was reminiscent of the dynamic load that was experienced by the seat occupant. Also, the lack of accelerometer data in the X-Y plane did not detract from the veracity of the simulated response. Finally, the test seat was designed to mitigate acceleration pulses in the vertical direction only. Hence, the assessment at the halfway mark in the study was that the dynamic response of the seat was adequately characterized by the SDOF numerical analysis. In the next section, the focus shifts to the two degree of freedom (2DOF) numerical model for which, as is discussed, there was no equivalent experimental data for comparison with the simulated seat response data.

6.2 Two Degree of Freedom (2DOF) Numerical Model

The main premise with the two degree of freedom (2DOF) perspective was that the payload and the seat were two distinct system components that dynamically interacted. In the context of this study, the seat cushion was a spring-damper element, so the 'seat' was the component of the system below the seat cushion (or to the rear of the cushion when the backrest was considered) but above the main suspension system unit (leaf spring, twin dampers, and pedestal). That section of the seat was commonly referred to as the seat pan. Figure 6-21 provides a visual indication of the side panel of the seat pan and the upright back panel. In the image, the section beneath the upholstery is not shown because it was difficult to access that surface without removing and causing damage to the cushion and upholstery.

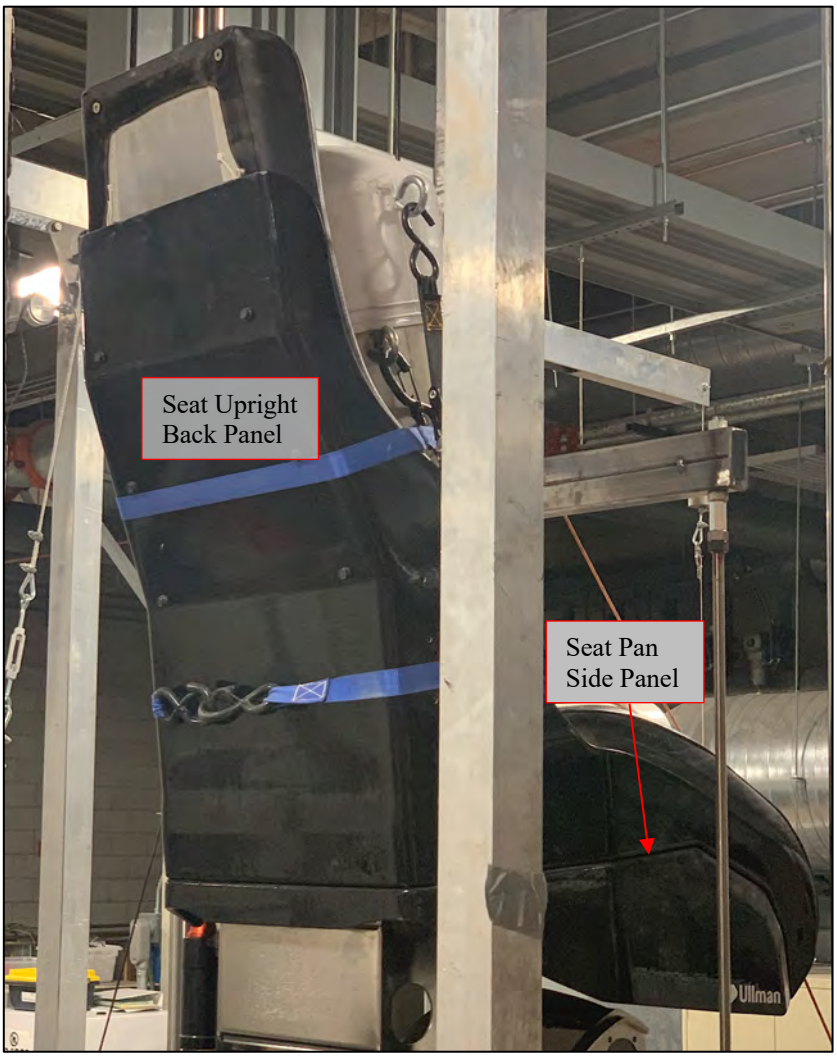

Figure 6-21: Seat Pan Side Panel and Upright Back Panel

The laboratory coordinate system for the 2DOF model was the same as that for the SDOF model. The only difference was the addition of the height assigned to a location on the underside of the seat pan.

In the 2DOF numerical model, the signal measured by the accelerometer positioned on the base of the pedestal was still defined as the input to the system. The signal measured by the accelerometer in the payload was assigned as the response of the payload. However, as a third accelerometer was not available to measure the response of the seat.

The response location of the seat was defined as a location on the underside of the seat pan but above the seat suspension system. Thus, in theory, the distance between the payload response and the seat response was the thickness of the seat cushion. Unfortunately, the section of the seat cushion beneath the upholstery surface but above the seat pan was inaccessible, so the thickness of the cushion was estimated based on the side profile of the seat pan. The disadvantage of not having a third accelerometer in that location was that there was no experimental response data to be compared with the numerical response data at that location. Therefore, the numerically simulated response data for that location approximated what the system's response would look like at a location beneath the padding of the seat cushion on the lower surface of the seat pan. In the 2DOF model, two additional items were added to the list of system elements that were represented in the numerical model.

In the numerical model, the variables were matched to the 2DOF elements of Figure 4-7. The mass of the seat pan was defined as 'mass one', and the seat spring and dampers were designated as 'spring one' and 'damper one.' The spring-damper properties of the seat cushion were defined as 'spring two' and 'damper two.' 'Mass two' was assigned to the mass of the payload. In this model, the elements that engaged in dynamic interaction were the payload, the seat cushion, the seat pan, and the main suspension system. The state space representation with the ODE45 solver (Runge-Kutta) was the only method used to implement the 2DOF numerical model. Figure 6-22 shows the tower-seat system identifying the designations of the system elements in the 2DOF numerical model. The location that the seat mass element was assigned to is not visible in Figure 6-22, but it was estimated to be on the underside of the seat pan below the lower surface of the seat cushion.

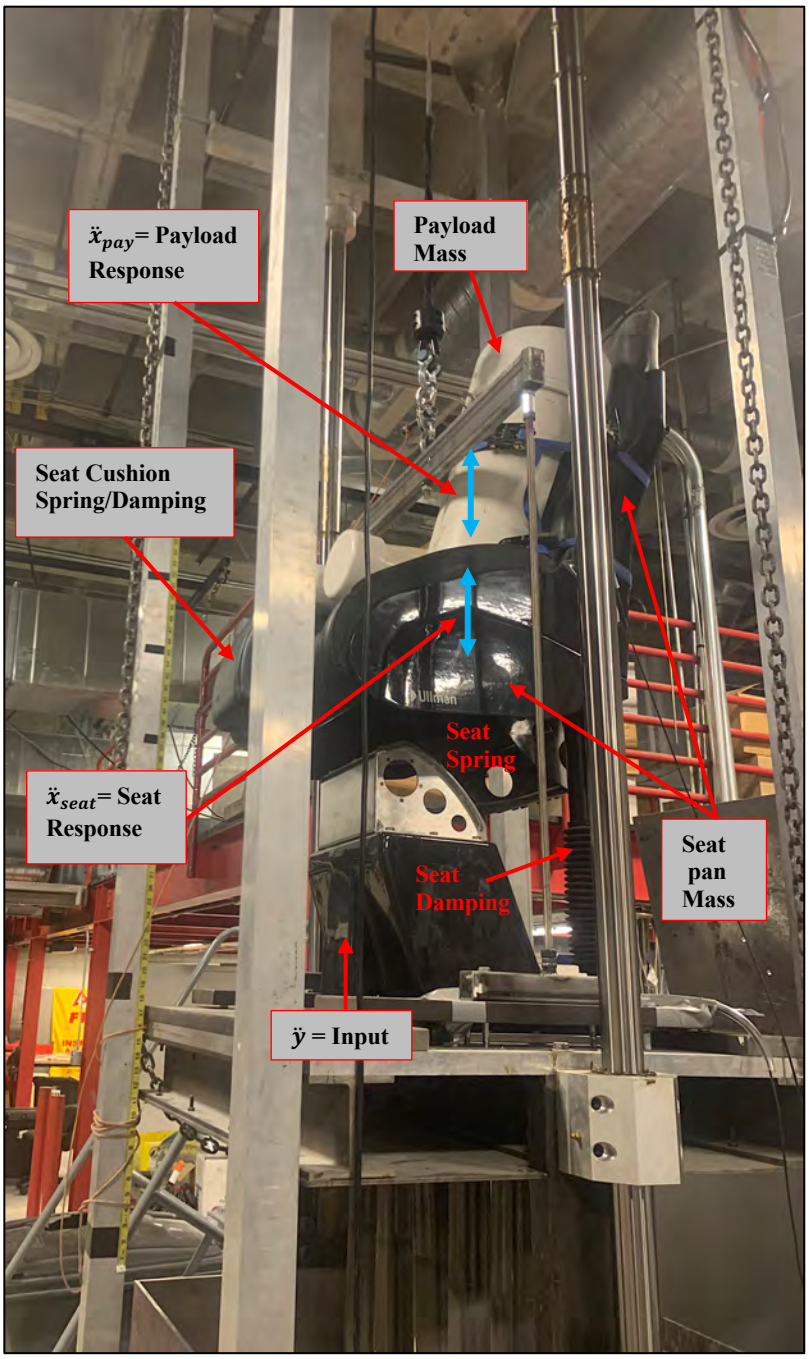

Figure 6-22: Designation of System Elements for 2DOF Numerical Model

6.2.1 2DOF Simulated Response Using State Space Model

The input to the 2DOF state space numerical model included the same variables as the SDOF model with certain additions. The values for the variables that defined the payload mass, the seat spring polynomial coefficients, and the seat damping coefficients remained the same. The added variables represented the mass of the seat pan, and the expressions that defined the estimated spring constant and damping coefficient for the seat cushion.

The mass of the seat pan was estimated to be the total mass of the seat minus the mass of the padding and upholstery, the spring housing, the dampers, and the pedestal. The seat pan was estimated to be approximately 17.6 kg (38.8 lb). The expression for the seat cushion spring was a function of the payload mass and the acceleration due to gravity. The idea of implementing the damping for the seat cushion as a nonlinear expression, similar to the damping for the SDOF analysis, was explored. However, the higher order term had no effect on the simulated response, so the expression was reduced to an integer that represented the seat cushion damping coefficient. There was no information about the type of foam used for the seat cushion, nor any precedent for the properties (stiffness, nor damping values), so estimates were developed based on the published properties of polyurethane foam.

The damping ratio for polyurethane foams can range from 0.05 to 0.15, and can go as high as 0.5, depending on the type of foam (open cell, closed cell, etc.). The spring characteristics of foam fall within a wide scope as well. The values for the spring constant of foams can range from 5000 N/m to about 21900 N/m (28.55 lbf/in to 125.05 lbf/in), again, depending on the type of product. Using the higher end of those ranges with (4-5) resulted in a damping coefficient of approximately 1570 N-s/m (8.97 lbf-s/in) with the 112.76 kg (248.6 lb) payload. The value of 1570 N-s/m (8.97 lbf-s/in) was used as the starting point for the damping value, and it was adjusted to match fractional values of the seat's main damping value. The methodology for developing the spring constant for the seat cushion was to use a fraction of the seat's main spring constant value in the expression for the seat cushion spring. That approach resulted in values assigned

to the seat cushion that were within the range of the spring constant for polyurethane foam and just over half the value of c1 for an initial damping value.

A value that equated of up to half the value of the seat's main spring constant was used as one of the inputs to the expression for the seat cushion spring. Values of half, three quarter, and up to two times the value of the first order term for the seat's main damping value were used as the seat cushion damping coefficient to evaluate which values provided the closest agreement with the experimental data. The range of 0.10 to 0.50 of the seat spring value as an input to the seat cushion stiffness term was applied for the entire analysis, and the value for the seat cushion damping coefficient ranged between 2.3e3 N-s/m to 5.5e3 N-s/m (13.13 lbf-s/in to 31.41 lbf-s/in). What became evident during the analysis was that the closer the seat cushion spring and damping values were to the seat's main spring and damping values, the more the simulated response of both the payload and the seat matched the simulated response of the SDOF numerical model. The damping values drove that occurrence more so than the spring values did.

When c1 and c2 were set to 2350 N-s/m and 10 N-s/m, respectively, and the seat cushion damping, C_C, was set to 1.0e4 or higher, the simulated response for the seat matched the experimental payload data well and closely resembled the simulated payload response of the SDOF model. At the same settings, the simulated response for the payload matched the experimental data closely also, except for the segment of time during the 1 g free fall leading to the peak acceleration amplitude. When the seat cushion modal properties were scaled to those large values, either extremely stiff or significantly damped, that was the theoretical equivalent of reducing the 2DOF model to the SDOF model. Essentially, that was reducing the seat cushion and the seat into one element. The upcoming graphs show that the simulated response acceleration of the seat formed a reasonably acceptable fit with the experimental payload response acceleration data. In contrast, the simulated payload response acceleration did not closely match the experimental payload response acceleration data.

The location in the physical set up that represented the position of the seat element of the 2DOF system was based on a point on the seat pan, which was about 0.127 m (0.417 ft) vertically below the accelerometer located in the base of the payload. However, the reinforced plastic seat pan was between the

incoming dynamic load and the upper section of the seat, so the seat cushion was on the opposite side of the seat pan from the incoming acceleration pulse. Thus, the damping effect of the seat cushion on the underside of the seat pan may have been reduced. The simulated response of the seat exhibited slightly higher amplitudes than the simulated payload response for most of the simulations. The equation of motion for the seat pan (mass one) included the seat cushion damping terms, and it seemed that those values were the dominant terms in the equation. That idea was corroborated by the effect that the adjustment of those terms had on the simulated responses. All the terms in the equation for the payload were based on the approximations of the seat cushion properties, so the simulated response for the payload (mass two) was inherently more prone to uncertainties linked to the estimated seat cushion property values.

Figures 6-23 to 6-26 show the simulated response versus the experimental response accelerations for the payload and the seat pan for selected tests for each payload category for the wedge. Figure 6-24 shows the response for the 49.6 kg (109.3 lb) payload when the seat cushion spring and damping values were made significantly large enough to reduce the 2DOF model to the SDOF model. The '(W)' in the title signifies a test conducted with the wedge. Figure 6-27 is a graph for the position for one test with the 49.6 kg (109.3 lb) payload with the wedge. Figures 6-28 to 6-31 depict the simulated response versus the experimental response accelerations for the payload and the seat pan for selected tests for each payload category for the five tines. The '(T)' in the title indicates a test conducted with the five tines. Figure 6-29 shows the response for the 49.6 kg (109.3 lb) payload when the seat cushion spring and damping values were made significantly large enough to reduce the 2DOF model to the SDOF model. Figure 6-32 is a graph for the position for one test with the 83.5 kg (184 lb) payload with the five tines. A subscript of 'c' in the graphs signifies values for the seat cushion, and a subscript of 's' is used to denote the main spring. The terms 'c1' and 'c2' represents the damping for the main suspension system. In the graphs, the light blue line represents the base input acceleration, the gold line is the experimental payload response acceleration, the dark blue line is the simulated payload response acceleration, and the red line is the simulated seat acceleration. Additional graphs can be viewed in Appendix C.

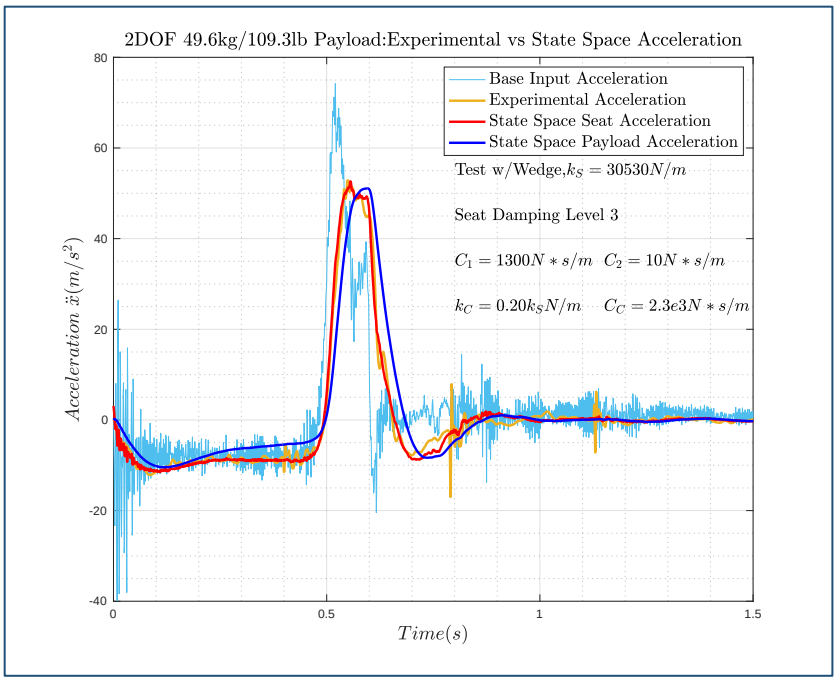

Figure 6-23:2DOF 49.6kg/109.3lb Payload (W): Experimental vs State Space Acceleration

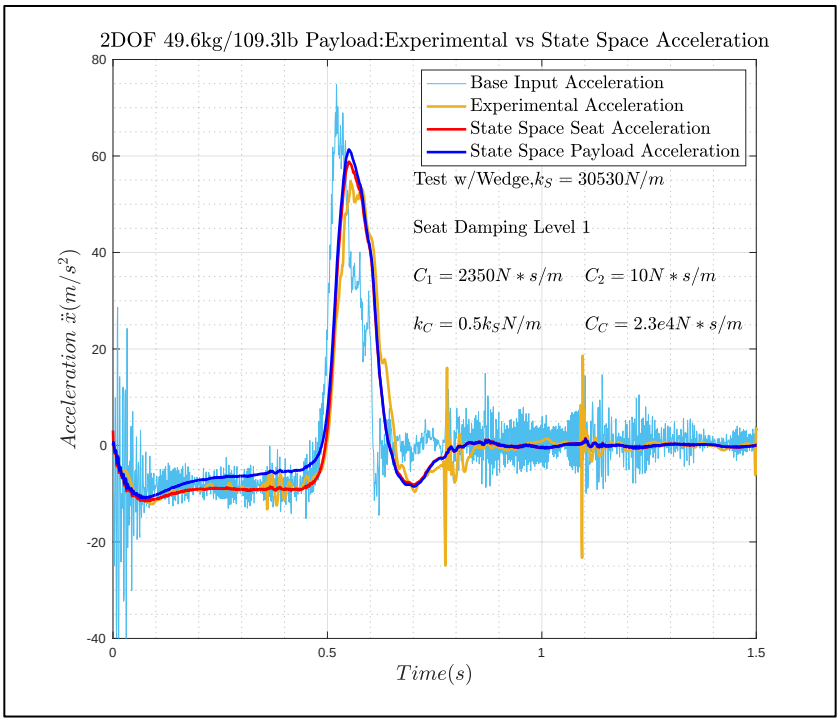

Figure 6-24: 2DOF 49.6kg/109.3lb Payload (W): Experimental vs State Space Acceleration

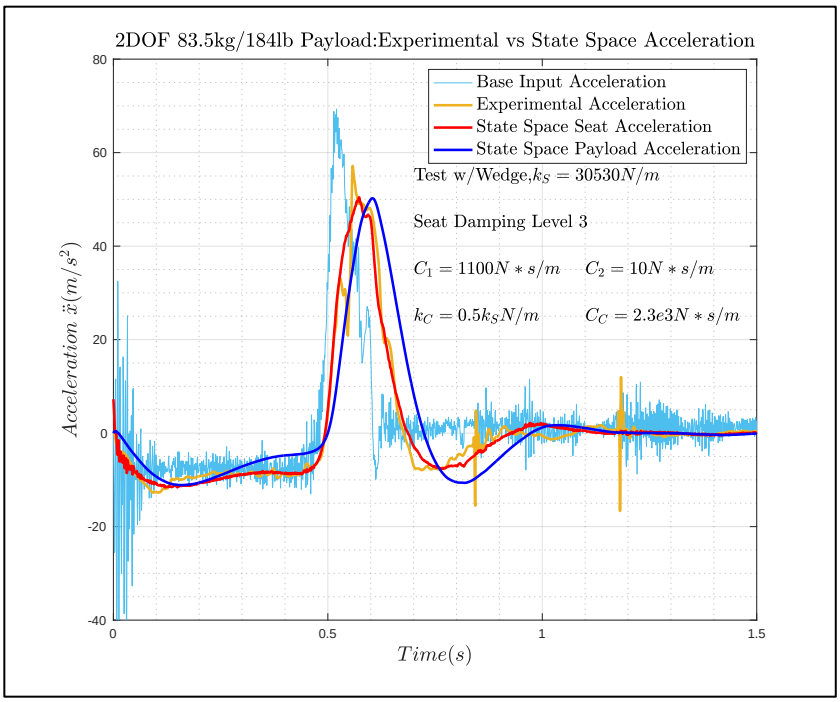

Figure 6-25: 2DOF 83.5kg/184lb Payload (W): Experimental vs State Space Acceleration

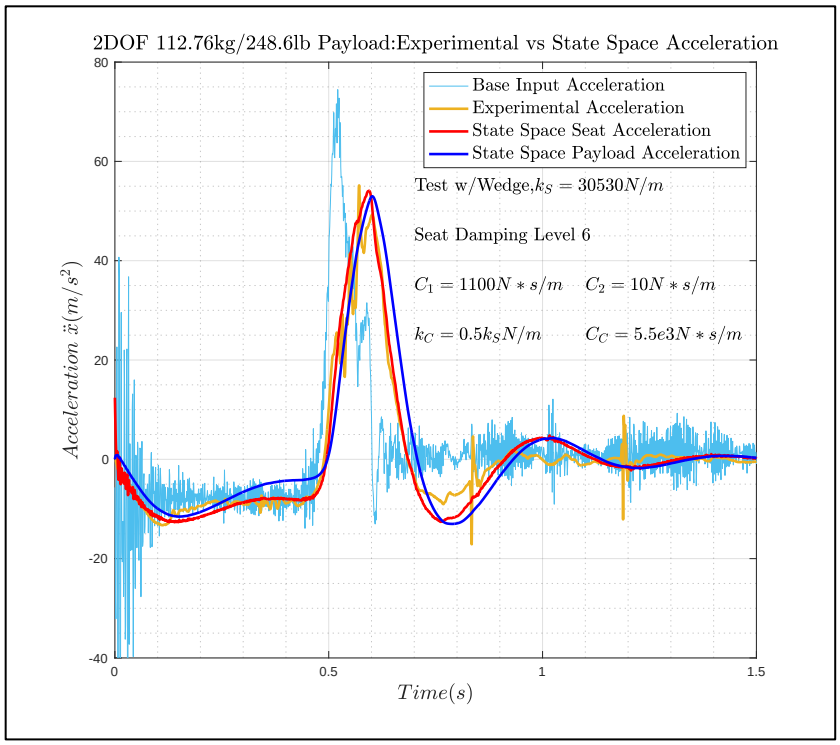

Figure 6-26: 2DOF 112.76kg/248.6lb Payload (W): Experimental vs State Space Acceleration

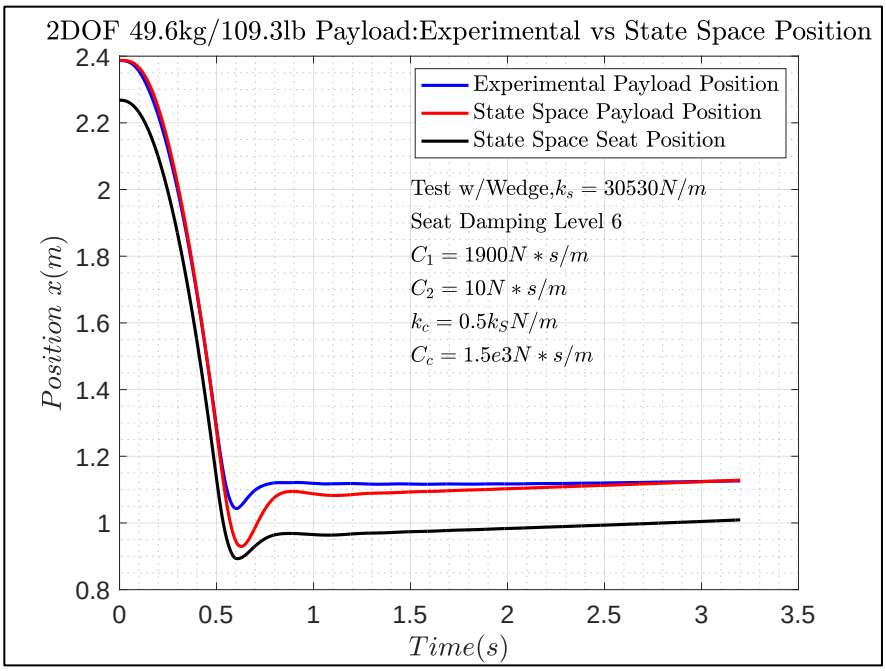

Figure 6-27: 2DOF 49.6kg/109.3lb Payload (W): Experimental vs State Space Position

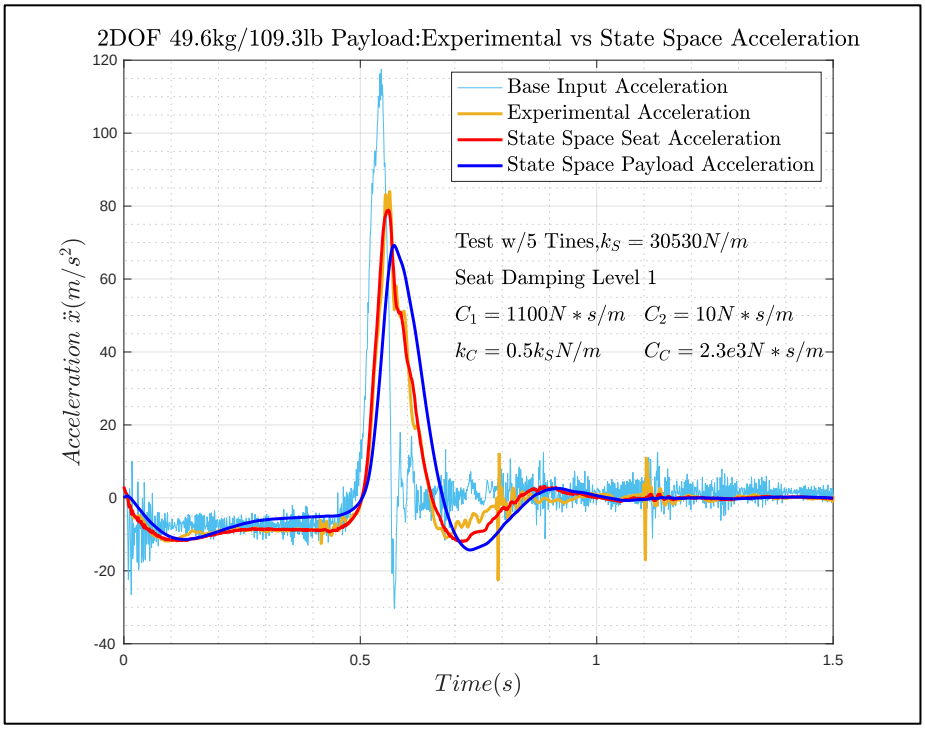

Figure 6-28: 2DOF 49.6kg/109.3lb Payload (T): Experimental vs State Space Acceleration

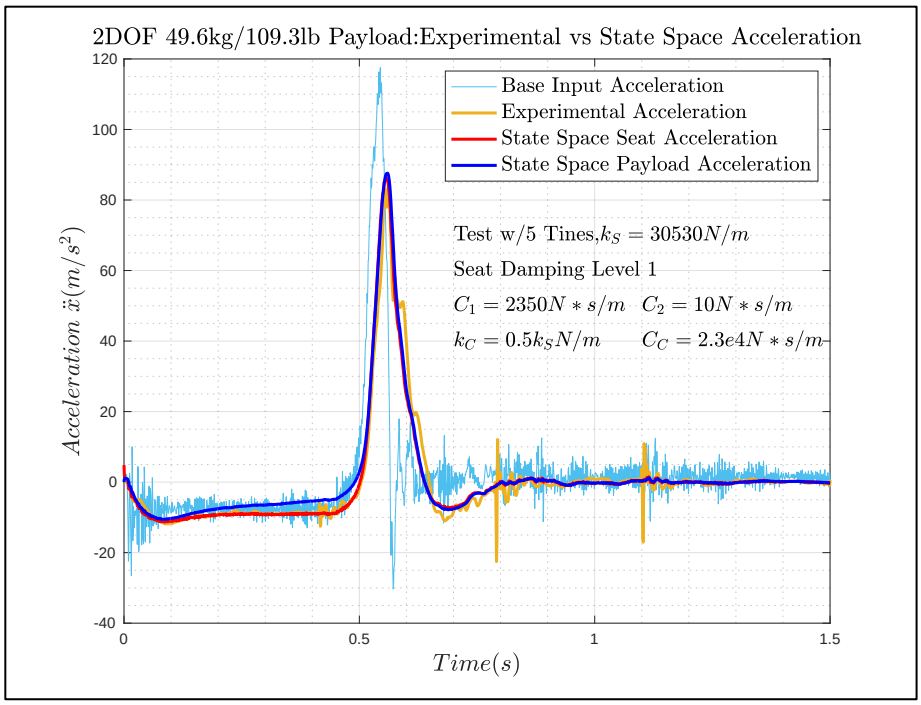

Figure 6-29: 2DOF 49.6kg/109.3lb Payload (T): Experimental vs State Space Acceleration

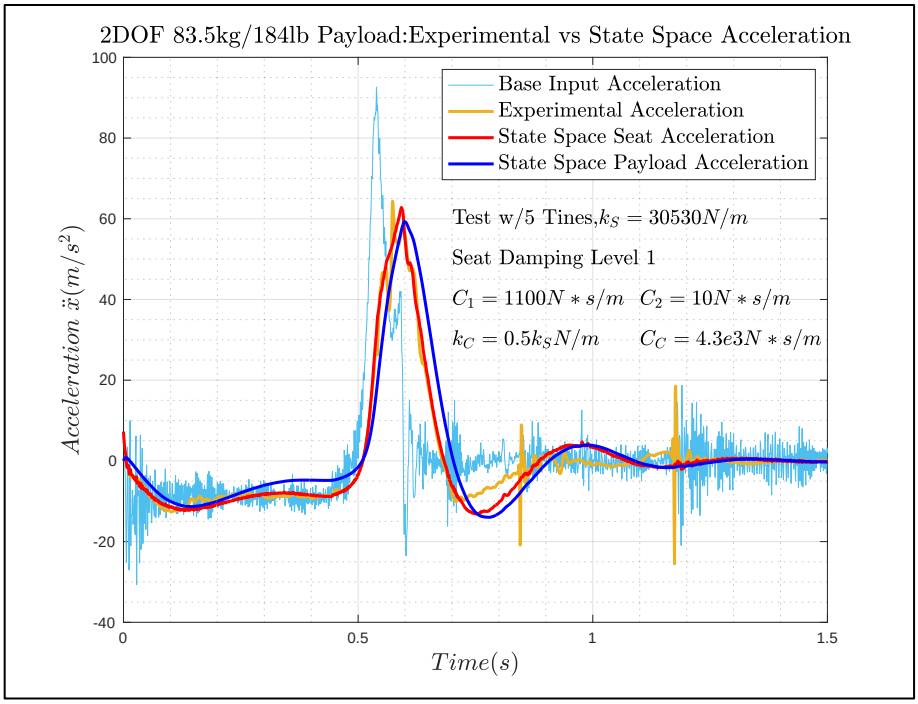

Figure 6-30: 2DOF 83.5kg/184lb Payload (T): Experimental vs State Space Acceleration

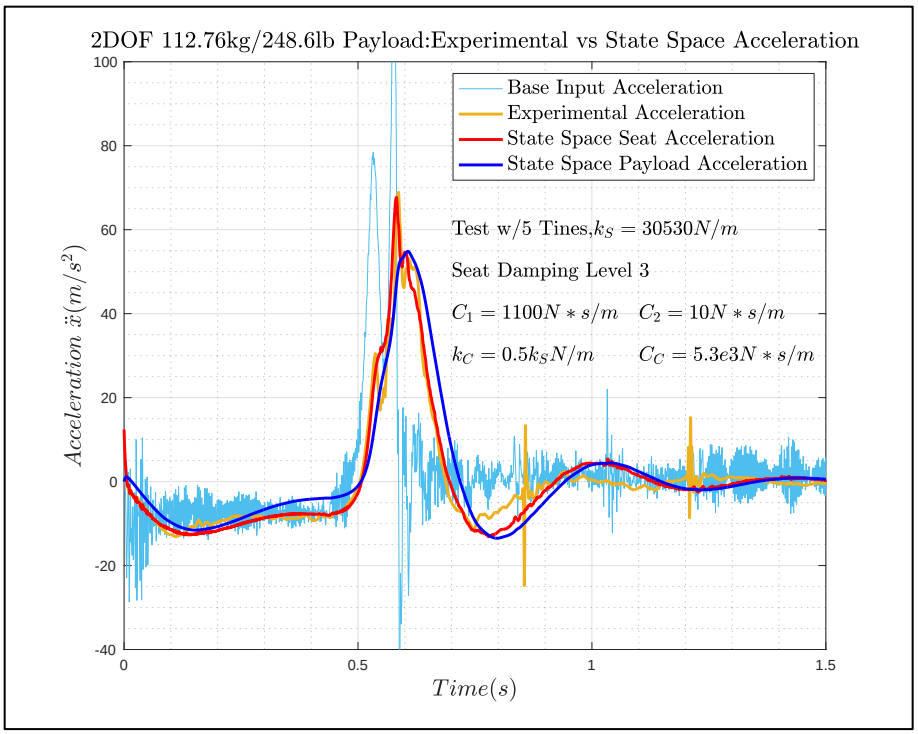

Figure 6-31: 2DOF 112.76kg/248.6lb Payload (T): Experimental vs State Space Acceleration

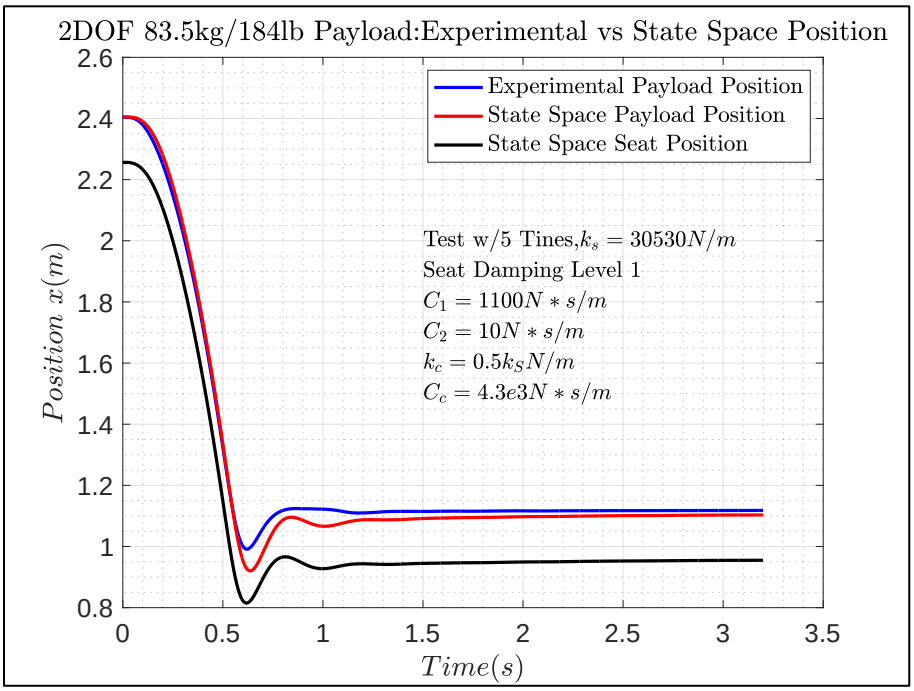

Figure 6-32: 2DOF 83.5kg/184lb Payload (T): Experimental vs State Space Position

2DOF State Space Acceleration

For all the tests, the simulated seat pan acceleration graphs visually matched the experimental payload response data. Unfortunately, an actual accelerometer was not located on the seat pan, so the graphs did not display an equivalent seat pan experimental data time history for comparison with the simulated seat pan acceleration. Although the simulated payload acceleration exhibited the general trend of the experimental data, the curves did not match as well, which was most likely related to the fact that the approximated spring and damping terms were the only terms in the equation of motion for the payload (mass two). One aspect of the 2DOF model that was promising was the time offset between the simulated payload and seat pan curves. In the physical system, the seat pan was situated closer to the incoming acceleration pulse, and so it experienced the dynamic load before the payload. That marginal delay that was expected from the seat pan to the payload was illustrated in the acceleration pulses in the graphs. For the wedge data, the higher main spring constant and lower seat damping values offered the best combination.

At all the payload categories, a seat spring constant value of 30530 N/m (174.33 lbf/in) and a combination of 1100-1300 N-s/m (6.28-7.42 lbf-s/in) and 10 N-s/m (0.057 lbf-s/in) for c1 and c2, respectively generated the best simulated response for the seat. For the most part, a seat cushion spring constant of 0.10 - 0.50 K_S (seat main spring) and a seat cushion damping coefficient between 2300 N-s/m (13.13 lbf-s/in) and 5500 N-s/m (31.41 lbf-s/in) seemed the be the most effective range to produce an acceptable outcome for the simulated payload acceleration data. Throughout the analysis for the acceleration, the seat cushion damping values displayed more influence over the simulated data than the seat's main damping values.

The seat's main damping values remained in the aforementioned range across the payload data sets, but the seat cushion damping was increased as the payload mass increased. The values of 2300 N-s/m (13.13 lbf-s/in), 4000 N-s/m (22.84 lbf-s/in) and 5300 N-s/m (30.26 lbf-s/in) for the seat cushion damping seemed to be the choice selections for the 49.6 kg (109.3 lb), 83.5 kg (184 lb), and the 112.76 kg (248.6 lb) payloads, respectively. The seat cushion damping increase was commensurate with the payload increase because the goal was to iterate through the estimated values that yielded the closest agreement to the empirical data.

Consequently, the heavier masses atop the seat cushion required a higher level of damping to keep the simulated data as faithful as possible to the experimental data. The same was true for the tines data set.

All the values that worked well for the wedge data set, were applicable to the tines data as well, including the increase in seat cushion damping to match the payload mass increase. For the 112.76 kg (248.6 lb) payload, the seat cushion damping was raised to 5500 N-s/m (31.41 lbf-s/in) to produce closer alignment between the simulated data and the experimental data. The mean absolute percent error values were high for each data set.

Although the simulated seat response acceleration data formed closer alignments with the experimental payload response data, the two data sets were not directly comparable. The experimental payload response data was collected by the accelerometer in the base of the payload, and the simulated seat acceleration data was based on a location on the seat pan that was not outfitted with an accelerometer. Therefore, the more accurate basis for comparison was between the simulated payload acceleration and the experimental payload acceleration. The error values were high for the same reason as with the SDOF analysis. Also, in a similar trend to the SDOF analysis, the error values were lower when the higher seat spring constant was used.

The highest percent error was 2614% for the 83.5 kg (184 lb) payload with the wedge, and the lowest was 75.58%, which was calculated for the 49.6 kg (109.3 lb) also with the wedge. Table 6-7 lists the spring and damping values for the seat (K_S, C_1, C_2) and the seat cushion (0.10 - 0.5 K_S , C_C). Table 6-8 tabulates the mean absolute percent error for the simulated payload acceleration. The mean absolute percent error for the simulated seat acceleration is provided in Appendix E. The next topic in the discussion covers the simulated position data.

Table 6-7: Spring Stiffness and Damping Values for 2DOF State Space Acceleration

Spring Stiffness and Damping Values for 2DOF State Space Acceleration									
Wedge: k_S = Seat spring, Cushion spring = 0.10 - 0.50 k_S									
Seat	49.6kg/109.3lb			83.5kg/184lb			112.76kg/248.6lb		
Damp Level	k_S (N/m)	c_1/c_2 (Ns/m)	c_C (Ns/m)	k_S (N/m)	c_1/c_2 (Ns/m)	c_C (Ns/m)	k_S (N/m)	c_1/c_2 (Ns/m)	c_C (Ns/m)
1	30530	1100/10	2.3e3	30530	1100/10	4.0e3	30530	1100/10	5.3e3
3	30530	1300/10	2.3e3	30530	1300/10	4.0e3	30530	1300/10	5.3e3
6	30530	1300/10	2.3e3	30530	1300/10	4.0e3	30530	1300/10	5.3e3
Five Tines: K_S = Seat spring, Cushion spring = 0.10 - 0.5 K_S									
	49.6kg/109.3lb			83.5kg/184lb			112.76kg/248.6lb		
	k_S (N/m)	c_1/c_2 (Ns/m)	c_C (Ns/m)	k_S (N/m)	c_1/c_2 (Ns/m)	c_C (Ns/m)	k_S (N/m)	c_1/c_2 (Ns/m)	c_C (Ns/m)
1	30530	1100/10	2.5e3	30530	1100/10	4.3e3	30530	1100/10	5.5e3
3	30530	1300/10	2.5e3	30530	1300/10	4.3e3	30530	1300/10	5.5e3
6	30530	1300/10	2.5e3	30530	1300/10	4.3e3	30530	1300/10	5.5e3

Table 6-8: Mean Absolute Percent Error for 2DOF State Space Payload Acceleration

Mean Absolute Percent Error for 2DOF State Space Payload Acceleration						
Wedge: k_S = Seat spring, Cushion spring = 0.10 - 0.5 k_S						
Seat	49.6kg/109.3lb		83.5kg/184lb		112.76kg/248.6lb	
Damp	1100/10 (N-s/m)		1300/10 (N-s/m)		1300/10 (N-s/m)	
Level	k_S (N/m)	k_S (N/m	k_S (N/m)	k_S (N/m)	k_S (N/m)	k_S (N/m)
	27862	30530	27862	30530	27862	30530
1	79.87%	75.58%	154.48%	142.19%	99.2%	88.16%
3	90.55%	82.19%	129.36%	122.6%	154.59%	133.27%
6	79.19%	77.21%	2614%	2480%	101.52%	88.22%
Five Tines: k_S = Seat spring, Cushion spring = 0.10 - 0.5 k_S						
	49.6kg/109.3lb		83.5kg/184lb		112.76kg/248.6lb	
	1100/10 (N-s/m)		1300/10 (N-s/m)		1300/10 (N-s/m)	
	k_S (N/m)	k_S (N/m)	k_S (N/m)	k_S (N/m)	k_S (N/m)	k_S (N/m)
	27862	30530	27862	30530	27862	30530
1	154.58%	119.1%	330.95%	235.24%	127.37%	106.28%
3	136.94%	113.88%	93.45%	80.36%	369.64%	348.0%
6	91.94%	83.06%	93.4%	87.42%	1822%	1679%

2DOF State Space Position

The distance between the accelerometer in the base of the payload and the point on the seat pan associated with the seat mass in the numerical model was approximately 0.10 m (0.33 ft). In the laboratory coordinate system that point was vertically below the payload. The anticipated trend of the position plots was for the position time histories of the experimental payload and the simulated payload to match and for the seat position time history to trend 'below' those two data sets. The position graphs showed just that. All three data sets began at the respective initial positions went through a period of free fall and leveled off just above 1 m (3.28 ft) for the experimental and simulated payload, and just under 1 m (3.28 ft) for the simulated seat position. The seat's main spring constant setting displayed more influence on the simulated position data than it did on the simulated acceleration data.

The mean absolute percent error values derived for the simulated position were much lower than the error values calculated for the simulated acceleration. For both the wedge and tines data set, the higher spring setting resulted in lower mean absolute percentage errors for the 49.6 kg (109.3 lb) and 83.5 kg (184 lb) payloads. However, the 112.76 kg (248.6 lb) payload fared better with the lower spring setting for both data sets. The seat damping value was only changed a single time to produce the desired effect on the position. The values for c1 and c2 were raised to 2350 N-s/m (13.42 lbf-s/in) and 10 N-s/m (0.057 lbf-s/in), respectively, just for the 49.6 kg (109.3 lb) payload with the wedge data. The lowest percent error occurred for the 49.6 kg (109.3 lb) payload with a value of 1.85% for a damping value of 1900 N-s/m (10.85 lbf-s/in) for c1. The highest error was also for the 49.6 kg (109.3 lb) payload at a value of 5.69% with the tines data. Table 6-9 itemizes the mean absolute percent error values for the simulated payload position. The error values for the simulated seat position were not derived as there was no basis for comparison with the experimental payload position.

Table 6-9: Mean Absolute Percent Error for 2DOF State Space Payload Position

Mean Absolute Percent Error for 2DOF State Space Payload Position									
Wedge: k_S = Seat spring, Cushion spring = 0.10 - 0.5 k_S									
Seat Damp Level	49.6kg/109.3lb			83.5kg/184lb			112.76kg/248.6lb		
	k_S (N/m)	c_1/c_2 (Ns/m)	Error (%)	k_S (N/m)	c_1/c_2 (Ns/m)	Error (%)	k_S (N/m)	c_1/c_2 (Ns/m)	Error (%)
1	27862	2350/10	4.25	30530	1100/10	4.54	30530	1100/10	3.67
3	30530	2350/10	2.02	30530	1100/10	2.58	27862	1100/10	2.48
6	30530	1900/10	1.85	30530	1100/10	2.84	27682	1100/10	3.09
Five Tines: k_S = Seat spring, Cushion spring = 0.10 - 0.5 k_S									
	49.6kg/109.3lb			83.5kg/184lb			112.76kg/248.6lb		
	k_S (N/m)	c_1/c_2 (Ns/m)	Error (%)	k_S (N/m)	c_1/c_2 (Ns/m)	Error (%)	k_S (N/m)	c_1/c_2 (Ns/m)	Error (%)
1	27862	1100/10	3.99	30530	1100/10	2.06	30530	1100/10	4.62
3	30530	1100/10	2.85	30530	1100/10	2.17	27862	1100/00	5.16
6	30530	1100/10	5.69	30530	1100/10	2.54	27862	1100/00	4.29

Considering that additional estimated values for some of the system properties were incorporated into the 2DOF numerical model, the simulated response acceleration data still exhibited satisfactory alignment with the experimental data. The simulated acceleration for the seat emerged as the model element that more closely matched the experimental payload data. The simulated payload data displayed a marginal time delay with the simulated seat acceleration, as it should have based on its location. However, the model required an increased level of damping for the simulated payload data to match the experimental payload data. The accelerometer that measured the experimental payload response was in a location that may have been prone to a higher level of damping.

The payload accelerometer was affixed in a cavity at the base of a Polyvinyl Chloride (PVC) tube that was filled with lead ballasts, which was positioned on top of a surface fabricated from a foam padding. From the accelerometer's viewpoint, it 'saw' a rigid surface in the positive Z direction and a relatively firm foam surface in the negative Z direction. In a practical sense, that location was sufficiently damped. Therefore, the extra damping that had to be applied to the payload element in the numerical model may have been warranted. The intention of the 2DOF analysis, though, was to determine if it provided more insight into the dynamic interaction between the seat and an occupant, than the SDOF approach. However,

to ascertain if the 2DOF model revealed any new information about the system, a brief review of the findings of the SDOF approach is in order.

When the process to develop the SDOF analysis was initiated, there was no prior knowledge of the modal properties of the seat, specifically the characteristics of the seat spring and the damping coefficient associated with the seat twin dampers. During the process of implementing and executing the SDOF numerical model, a few discoveries about the system properties and response were made. The first piece of information that the SDOF model revealed was the seat spring constant. Primarily, the range within which the value of the spring constant fell for the seat to sufficiently mitigate the incoming acceleration pulse. A spring constant range of approximately 27000 N/m (154.17 lbf/in) to 30500 N/m (174.16 lbf/in) provided sufficient stiffness to render adequate simulated system responses for all three payload categories across both the wedge and the tines data set. Another system property that was obscured by uncertainty, but which was exposed during the SDOF analysis, was the system damping coefficient value.

Recall that the seat was equipped with what was termed as adjustable damping with levels ranging from one (soft) to six (stiff), but no actual values were provided for those levels by the seat manufacturer. In the SDOF model, the seat damping was expressed as a second order term. The simulated system response acceleration graphs showed that the first order term could be modified to regulate the peak of the main acceleration pulse, while the second order term had some influence on the slope of the negative 1 g downtrend that occurred after the main pulse. The value that seemed to work well for the first order term, defined as c1, was 2350 N-s/m (13.42 lbf-s/in), and the range that was most effective for the second order term, c2, was 10 N-s/m to 50 N-s/m (0.057 lbf-s/in to 0.29 lbf-s/in). There was no indication of a correlation between the seat damping level and the approximated damping terms, but the second order term did increase as the payload mass increased. Overall, the SDOF numerical model produced simulated responses that were well matched with the experimental data, and the method helped to yield estimated system properties. In fact, those same system properties were applied in the 2DOF model.

The new information that the 2DOF numerical model exposed was associated with the seat cushion. Particularly, the 2DOF model showed that the seat cushion probably had damping values similar to the

seat's main damping values. Seat cushion damping coefficient values up to 2500 N-s/m (14.27 lbf-s/in) worked well for the 49.6 kg (lb) (109.3 lb) payload, and values at or above 4.0e3 N-s/m (22.84 lbf-s/in) were effective for the two higher payload masses. Again, there was no information from the manufacturer regarding the seat cushion properties, and while the 2DOF analysis resulted in a somewhat broad range of values for the seat cushion damping, it was information that was not uncovered by the SDOF analysis. Hence, the seat could be represented as a 2DOF model with the understanding that the accuracy of the simulated payload response (or the seat response) of the 2DOF model was more sensitive to adjustments in the approximated seat cushion damping values. Approaching the analysis of the seat from both the SDOF and 2DOF perspectives was advantageous because, in tandem, they offered a holistic characterization of the system that was not achieved during the experimental laboratory testing. Once the evaluation of the 2DOF analysis was complete, the aim was to take a step back and assess how the findings of the numerical analysis was integrated into the big picture.

One of the two inquires that fueled the primary objectives of this study was the plausibility of using the mass-spring-damper concept as the basis for an analytical representation of the seat-occupant system. Subsequently, that approach served as the foundation for the numerical model. The results that are presented in this chapter served as an indication that a numerical model formulated on the basis of representing the seat as a mass-spring-damper concept (SDOF and 2DOF), wholly and sufficiently characterized the dynamic response of the seat. The supplementary benefit of the numerical model was that through the close agreement between the simulated response acceleration and the experimental response acceleration, a certain level of validity was added to the empirical data. After an examination of the outcome of the numerical analysis, the comprehensive outlook was that the second fundamental objective of the study was fulfilled.

6.3 Summary

The focal point of this chapter is the numerical model of the shock mitigation seat. Upholding the targeted objectives of the study, the model was developed using the single degree of freedom (SDOF) and the two degree of freedom (2DOF) concepts. The SDOF analysis was conducted using two different techniques. The 2DOF model relied on one of those methods to conduct the analysis.

The SDOF model defined the mass of the seat and the occupant as a lumped mass. The analysis was implemented using the state space representation of the system (with Runge-Kutta solver), as well as with the Newmark-Beta (Newmark-ß) method for direct numerical integration. In the process of developing the SDOF model, approximate values that depicted the seat suspension stiffness and damping attributes were resolved. An estimated spring constant range of 27000 N/m (154.17 lbf/in) to 30500 N/m (174.16 lbf/in) and damping coefficient values of 2350 N-s/m (13.42 lbf-s/in) and 10 N-s/m to 50 N-s/m (0.057 lbf-s/in to 0.29 lbf-s/in), seemed to be the most effective measures for the model. The simulated response acceleration (and position) of the state space numerical model matched well with the experimental response acceleration (and position). The results supported the notion that the seat could be modeled as a SDOF system. The data generated by the Newmark-ß analysis was just as encouraging.

The simulated response acceleration and position data from the Newmark-ß method also displayed good alignment with the experimental response acceleration and position data. Also, the graphs generated by the Newmark-ß method were tantamount to the state space graphs. That was further evidence that supported the hypothesis that the behavior of the seat could be replicated by the SDOF concept. The SDOF analysis divulged unknown information about the seat's main suspension system, but during the course of conducting the 2DOF analysis, information related to dynamic behavior of the seat cushion was unveiled.

Like the properties of the seat's main suspension system, there was no available information regarding the dynamic traits of the seat cushion. Using published values for the stiffness and damping qualities of polyurethane foam, the starting value in the expression for the seat cushion spring profile was half the value of the seat's main spring constant. The highest published damping ratio for polyurethane

foam with the 112.76 kg (248.6 lb) payload was used to calculate the starting seat cushion damping coefficient. The eventual damping values for the 2DOF analysis were up to 2500 N-s/m (14.27 lbf-s/in) for the 49.6 kg (lb) (109.3 lb) payload and values at or above 4.0e3 N-s/m (22.84 lbf-s/in) for the two heavier payloads. The 2DOF simulated response acceleration and position data were acceptable considering the model contained additional information based on estimated seat cushion modal properties.

In the 2DOF model, the simulated response acceleration data for the seat displayed a higher level of congruency with the experimental payload response acceleration data than the simulated response of the payload did. However, a direct correlation between the simulated seat response and the experimental payload response could not be established because the model element representing the seat was defined at a point located vertically below the actual payload position. The simulated response for the payload improved when the approximated seat cushion damping was increased to a significantly large number. The graphs for the 2DOF model displayed the response delay between the seat location (mass one) and the payload location (mass two), which was in accordance with the physical setup of the test system.

Overall, the numerical analysis produced good results, especially when the two approaches, both the SDOF and 2DOF concepts, were viewed as two components of a consolidated technique. Together, the two methods suitably characterized the dynamic behavior of the seat and cultivated information about the system that was not exposed during the laboratory testing. Ultimately, the prevailing standpoint was that the numerical analysis satisfied the second of the two main objectives of the study. In the penultimate chapter, a recap of the history of the main topic and the motivation behind the study is presented. Also, an account of the results, and how they helped achieve the main objectives of the study are given. The chapter closes with a brief discussion on how this study contributed to the current compendium of knowledge on shock mitigation seat analysis.

Chapter 7. Conclusion

The priority of this venture was to cultivate an analytical approach that was conducive to evaluating the shock mitigating capabilities of the seat. Also, the aim was to use the approach to enable identifying the seat's operational envelope prior to installation in an HSC. In this chapter, a summary of the activities that supported this effort and how each contributed to achieving the objectives of the study is given.

7.1 Summary

Shock mitigation seats, sometimes referred to a suspension seats, were installed in HSC to diminish the rate of injury to on-board personnel from the mechanical shock due to wave slams. A wave slam is the violent impact between a waterborne craft and an incoming wave, and the shock created by the impact is the predominant cause of musculoskeletal injuries sustained by HSC operators and passengers. Shock mitigation seats can be divided into three categories, including active, adaptive, and passive systems.

Active seats require an external power source to 'actively' mitigate incoming shock loads. Adaptive seats do not require external power, but the stiffness (or damping) of the system can be adjusted depending on the operational environment. Passive seats are the simplest of the three concepts and do not require any external power, nor are there any means to adjust the stiffness of the system. Of the three seat types, passive seats are the most widely used seats in HSC. However, in some environments, these systems have been observed to amplify rather than attenuate shock loads. Also, because the characteristics of shock loads vary at sea, it became a challenge for potential seat clientele to select seats for a specific type of operating environment or a range of environments. Thus, an evolving area of interest was the development of a procedure to appraise passive seats for use across a range of operational environments prior to installation in a HSC. The concern was that although in the Community of Practice (CoP) studies on seats were being conducted, a universally accepted measurement system to classify, or rate, shock mitigation seats has not been established thus far.

Hence, the goal of this work is to develop a repeatable laboratory test procedure for shock mitigation seats to quantify their performance capabilities. In addition, a numerical model of the seat was developed to validate the empirical results, as well as to provide insight into the dynamic behavior of the seat. At the center of the laboratory test procedure was the drop tower, and the analytical representation of the seat as a mass-spring-damper system formed the basis for the numerical model.

The steps of the laboratory test procedure, including the use of a drop tower, and the premise of modeling the seat as a mass-spring-damper system were based on recommendations outlined in an International Organization for Standardization (ISO) document and the Naval Surface Warfare Center Carderock Division (NSWCCD) reference reports [2, 6, 7]. With the use of sand as the impact surface, the drop tower was used to simulate the rapidly applied shock associated with a wave slam to the base of the seat. The mass-spring-damper concept served as the analytical representation of the seat-occupant subsystem in the [HSC]-[seat-occupant]-[wave] global system in the numerical model. The function of the tower and the technique that was utilized in the numerical analysis formed the foundation for the two primary objectives of the study.

One of the two main objectives of this work was to ascertain if a single impact drop tower was a plausible method to simulate the rapidly applied vertical shock that was associated with the wave slam events experienced by an HSC. Particularly, what was to be examined was to what magnitude would the drop tower deliver the input shock and with what level of consistency could the magnitude be achieved. The other principal goal was to determine if the mass-spring-damper concept could appropriately characterize the dynamics of a shock mitigation seat. Through the implementation of the laboratory test procedure, the calculation of the seat mitigation ratio (MR), and the development of the single degree of freedom (SDOF) and the two degree of freedom (2DOF) numerical models, both objectives were realized.

To quantify the tower's aspect of repeatability, a normal distribution was applied to the peak input acceleration values achieved during the drop tests. The data points were from tests conducted with the wedge and the five tines as the pulse-shaping devices. The data for the wedge had a minor negative skew, and the tines data contained a slight positive skew, but overall, the distribution for each data set fell within

the one, two, and three standard deviations of the mean according to the 68-95-99.7 rule of a normal distribution. The distribution for the wedge data was 70.4%, 96.3%, and 100%. For the five tines data set, the spread was narrower with numbers of 51.9% and 100%. In general, the input accelerations had higher amplitudes when the tines were installed with a mean value of 9.04 g, compared to a mean of 6.93 g when the wedge was used. The conclusion was that the tower was capable of consistently operating at a severity threshold level of four.

According to the reference documents, a severity threshold rating of four meant that the tower in its configuration at the time was able to consistently deliver peak acceleration pulses of 6.12 g. A severity threshold level of five (8.15 g) could be achieved 70% of the time. The tower demonstrated a level of repeatability because there was no single external entity that had a distinctly larger influence on the system than the rest of the innate system elements. The data from the drop tests served as the information that was used to calculate the seat MR values.

Based on the transmissibility of the system (output to input ratio), the MR value was a numerical indication of the seat's shock mitigating capabilities. An MR value of less than one was required for a shock mitigation seat to be considered as fulfilling its function. The MR_{PEAK} value was the ratio of the peak response and input accelerations in the time domain measured during a drop test. The MR_{SRS} was the shock response spectrum history in the frequency domain, and it was calculated for the frequency range between 4 Hz and 10 Hz.

The mean MR_{PEAK} value for the wedge data was 0.7947, 0.8821, and 0.7957 for the 49.6 kg (109.3 lb), 83.5 kg (184.0 lb), and 112.76 kg (248.6 lb) payload masses, respectively. On average for the wedge data set, the seat attenuated 14% to 29% of the incoming acceleration pulse for the 49.6 kg (109.3 lb) payload, 0.5% to 24% for the 83.5 kg (184.0 lb) payload, and 3% to 32% for the 112.76 kg (248.6 lb) payload. For the tines, the mean MR_{PEAK} value for the 49.6 kg (109.3 lb) payload was 0.7653 and 0.7068 for the 83.5 kg (184.0 lb) payload. The mean for the 112.76 kg (248.6 lb) payload was 0.6621. The percent mitigation rate was 21% to 29% for the 49.6 kg (109.3 lb) payload, 24% to 31% for the 83.5 kg (184.0 lb) payload, and 19% to 42% for the 112.76 kg (248.6 lb) payload for the tines data set. A set of selected tests

were conducted to determine the MR_{SRS}, all of which displayed values below one between 4 Hz and 10 Hz. The seat was rated for use in vessels ranging from HSC Class 3 to HSC Class 4-3 for operating conditions in which the maximum expected acceleration inputs matched a severity threshold level four. The drop tests, in conjunction with the MR values, offered a way to evaluate the seat's function, but the numerical analysis provided insight into the dynamic response of the seat.

Information regarding the attributes of the seat suspension system was not available. Consequently, a desired outcome of the numerical analysis was the opportunity to decipher the spring stiffness and damping coefficient values for the seat. The SDOF model defined the mass of the seat and the occupant as a lumped mass. The analysis was implemented using the state space representation of the system (with a Runge-Kutta solver), as well as the Newmark-Beta (Newmark-ß) time stepping algorithm for direct numerical integration. The state space approach eliminated the second order equation of motion that represented the system and only depended on position and velocity terms. The Newmark-ß method was used to implement direct numerical integration to solve the equations of motion. The first products to emerge from the development of the SDOF numerical analysis were the approximate values for the seat spring stiffness and the damping coefficient.

An estimated spring constant range was 27000 N/m (154.17 lbf/in) to 30500 N/m (174.16 lbf/in). The damping was expressed as a second order term with coefficients c1 and c2, which were approximated to be 2350 N-s/m (13.42 lbf-s/in) and 10 N-s/m to 50 N-s/m (0.057 lbf-s/in to 0.29 lbf-s/in), respectively. A combination of those values, with either of the spring constant values, was effective in generating good alignment between the model's simulated response acceleration and position and the experimental payload response acceleration and position. The results of the Newmark-ß analysis were also in alignment with the experimental data.

The simulated response data produced by the Newmark-ß model was very close to the results of the state space model. In fact, when the graphs used to plot the simulated response for a specific data set (payload mass and pulse-shaping device combination) from both methods were placed side by side, they were practically identical. Two points could be highlighted about the SDOF analysis. First, both methods

generated good, completely accepted results. Second, the analysis disclosed unknown information about the seat's main suspension system. Together, those two outcomes engendered the accomplishment of a core objective of the study, and the seat could be characterized by a numerical model grounded in the SDOF concept. However, to support a comprehensive approach, the 2DOF analysis was conducted to complete the investigation. The SDOF analysis revealed unknown information about the seat's main suspension system, but information related to the dynamic behavior of the seat cushion was disclosed during the 2DOF analysis.

The 2DOF numerical analysis defined the payload and the seat as two separate system mass elements with the seat cushion acting as the energy storing spring and the energy dissipating damper between them. Hence, the added variables to the analysis represented the mass of the seat pan (the seat pan was mass one and the payload was designated as mass two), and the expressions that defined the estimated spring constant and damping coefficient for the seat cushion. Though, in the same manner as with the seat's main suspension system, the dynamic properties of the seat cushion were unknown.

The values for the seat's main spring stiffness and damping coefficients that were created for the SDOF analysis were used in the 2DOF model. To formulate values for the seat cushion, the published values for the stiffness and damping ratio of polyurethane foam was used with the 112.76 kg (248.6 lb) payload in the equation used to calculate the damping coefficient. The approximated damping values for the seat cushion in the 2DOF analysis was up to 2500 N-s/m (14.27 lbf-s/in) for the 49.6 kg (lb) (109.3 lb) payload, and values at or above 4.e3 N-s/m (22.84 lbf-s/in) for the two heavier payloads. The expression for the seat cushion spring contained a term that was set at up to half the value of the seat's main spring constant.

The simulated response acceleration data for the seat was in greater agreement with the experimental payload response acceleration data than the simulated response of the payload. The seat cushion spring term did not display a significant amount of influence on the shape of the simulated response acceleration data, but the seat cushion damping value did. An indication that it was a dominant term in the

2DOF system's equations of motion. The simulated response for both the seat and the payload improved when the estimated seat cushion damping was increased to a significantly large number.

When the seat cushion damping was set to 1.0e4 or higher, and c1 and c2 were set to 2350 N-s/m and 10 N-s/m, respectively, the simulated response acceleration for the seat and the payload matched the experimental data almost seamlessly. At those values, the 2DOF simulated response accelerations appeared identical to the SDOF model simulated response acceleration data. In agreement with the physical set up, the plots of the 2DOF simulated response acceleration data displayed the response delay between the seat location and the payload location. Although the simulated acceleration data for the seat agreed with the experimental data for the payload, the caveat was that because an accelerometer was not located on the seat pan, there was no experimental seat acceleration data for direct comparison with the simulated seat acceleration data.

Individually, each numerical analysis produced good results, and either method could have been used to validate the empirical data. However, the 2DOF model would require a higher level of tuning for the seat cushion property values. Together, the two methods aptly characterized the seat and fostered information about the system that was not uncovered during the laboratory testing. Therefore, the outcome of the numerical analysis satisfied the second of the two primary objectives of the study. The overarching purpose of any study is to add to the existing canon of the associated topic, so now the subject will transition to a summary of what was achieved with this work beyond the fundamental objectives.

Prior research in this area has been conducted, but as alluded to earlier, there was no consistent approach to the analysis of shock mitigation seats in the literature. A survey of the literature revealed that past studies performed on shock mitigation seats entailed different aspects of the analysis conducted in this work. However, the focus of those efforts always seemed to be restricted to one aspect of the analysis.

The efforts of some studies were concentrated on developing the experimental testing procedure without incorporating a numerical analysis. As a side note, there was no evidence in the reviewed literature of any experimental procedures using tines as the pulse-shaping device. Other work placed the emphasis on applying numerical methods to conduct a modal analysis of the seat. Also, there has been research aimed

at creating numerical models of shock mitigation seats that did not involve performing any laboratory tests on the seat, so those efforts did not contain an experimental component. Those studies relied on data garnered from unrelated experimental investigations or at sea test data. The common theme in the CoP is that there is no undertaking aimed at developing a combined approach to evaluate and rate seats, which is what this work strove to accomplish.

It has been stated in the industry that an established shock mitigation seat assessment protocol would be of value to HSC patrons. Therefore, this study aimed to develop a comprehensive approach that integrated experimental and numerical analysis modules targeted towards a complete appraisal of the seat. The products of the individual tasks were the rating of the seat for use in a specific class of HSC and an insight into the dynamic behavior of the seat. Hopefully, the outcome of the project is the development of a consolidated method to evaluate shock mitigation seats that adds to the literature. The succeeding, and final, chapter addresses prospective future work.

Chapter 8. Future Work

The goal of this chapter is to look at some of the procedures that could be added to the current method that would help inform future work.

Experimental Analysis

One hardware modification that would have to be implemented, would be to stabilize the horizontal bar that was used to attach the hook for the hoist. As noted, the horizontal bar was supported by two semi-rigid rods, which resulted in the bar striking the payload during a drop test. Replacing those rods with more rigid elements could prevent the bar from striking the payload during testing.

The consensus among HSC operators is that, while the vertical force associated with heave is the force responsible for most of the injuries due to wave slam events, the forces associated with the rotational motions (pitch, roll, and yaw) still pose the risk of injury to on-board personnel. Thus, although the drop tower was effective at simulating the vertical component of a wave slam, it was not designed to replicate the rotational motions experienced by an HSC. Consequently, one area of analysis that could be explored in future work is the capability to replicate dynamic motion outside the vertical axis. One option could be to use a shaker table that could be programmed to replicate dynamic motion outside of the vertical plane. That added test component would facilitate conducting analyses on seats designed to mitigate acceleration pulses in more than one degree of freedom. Another area of investigation that could be broadened would be the experimental modal analysis.

An in-depth experimental modal analysis may require mounting the seat on a vibration table. However, a less involved and more economical approach could be to use a modal hammer. With the addition of more strategically placed accelerometers and a modal hammer, a more detailed picture of the seat's modes of vibration could be determined. Knowledge of the seat's modes of vibration could help to determine how the seat design could be improved to attenuate whole body vibrations (WBV) within the response frequency range of the human body. The final element that could be included in future experimental work would be classified as a nice-to-have hardware component.

An anthropomorphic test device (ATD) is a ‘humanlike’ test instrument that simulates human response to impacts and rapid accelerations. ATDs are fitted with sensors in certain sections of the body form to measure the applied forces from different directions during impact. Also, accelerometers could be attached to the ATD to collect additional measurements. The drawback with an ATD is that the mass is usually fixed, so while extra weight could be added to replicate heavier seat occupants, the ATD cannot be made lighter to simulate lighter seat occupants. The benefit with using an ATD is because of its ‘humanlike’ form, the dynamic interaction between it and the seat may more closely represent the interaction between the seat and a human occupant, as opposed to an inert payload. An advancement for the numerical analysis would be to use accelerometer data from at sea trials for the input acceleration to the numerical model.

Numerical Analysis

Some of the peak acceleration amplitudes that are experienced at sea can reach levels that the drop tower was incapable of achieving. Hence, using data collected from at sea trials as the input to the numerical model would assist in determining how the seat would respond to higher magnitude wave slams. Also, it would provide insight into how the seat would perform during successive wave slams. Finally, developing a computational model of the seat in finite element and Multiphysics software applications, such as FEMAP® and LS-DYNA®, would be a good way to gain a three-dimensional perspective of the dynamics of the system.

Incorporating the aforementioned procedures and elements into the existing protocol would improve the present methodology.

Appendix A. Graphs for Mitigation Ratio (MR_{PEAK} and MR_{SRS})

The blue line represents the platform input acceleration, and the red line signifies the payload response acceleration.

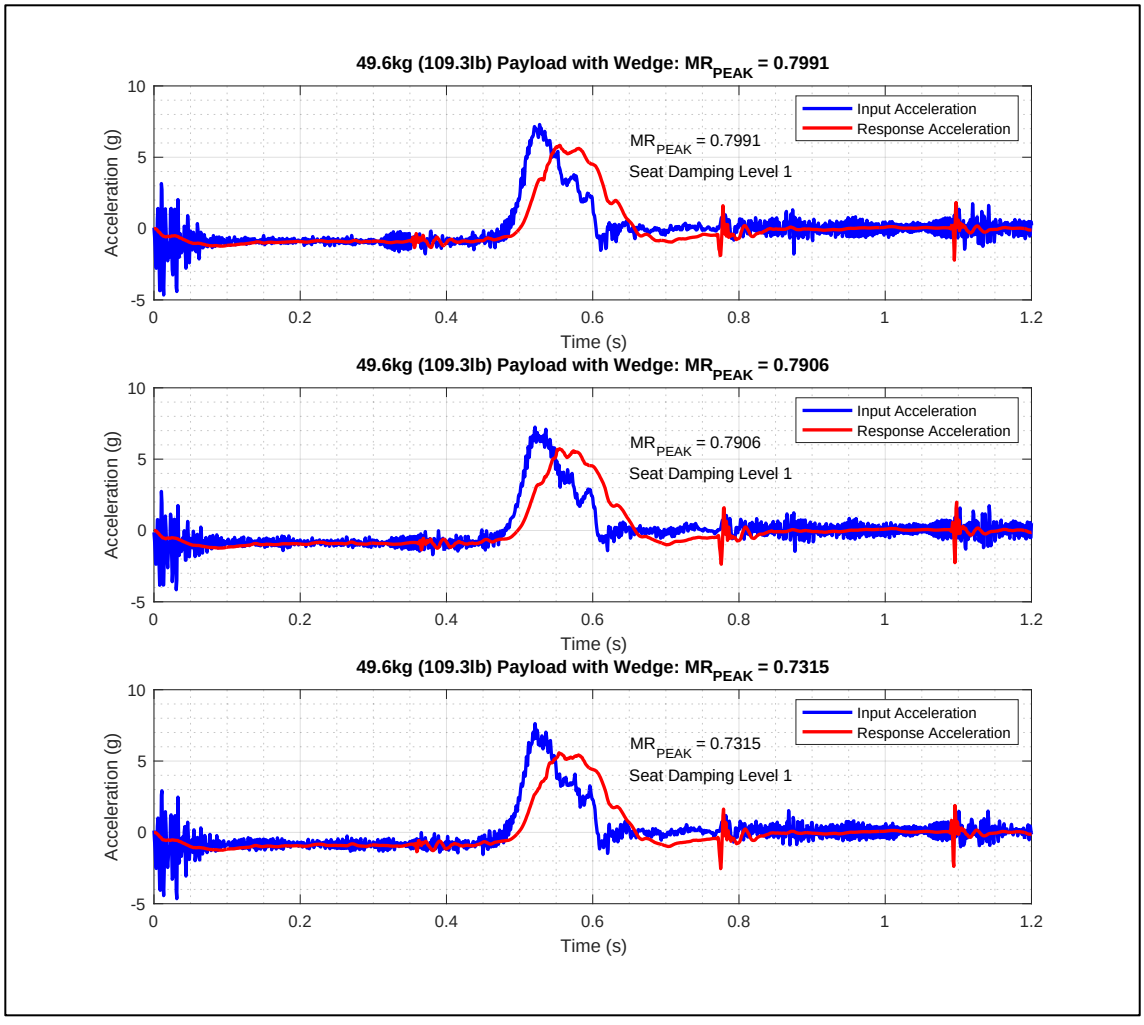

Figure A - 1: MR_{PEAK} for 49.6kg (109.3lb) Payload w/Wedge Seat Damping 1

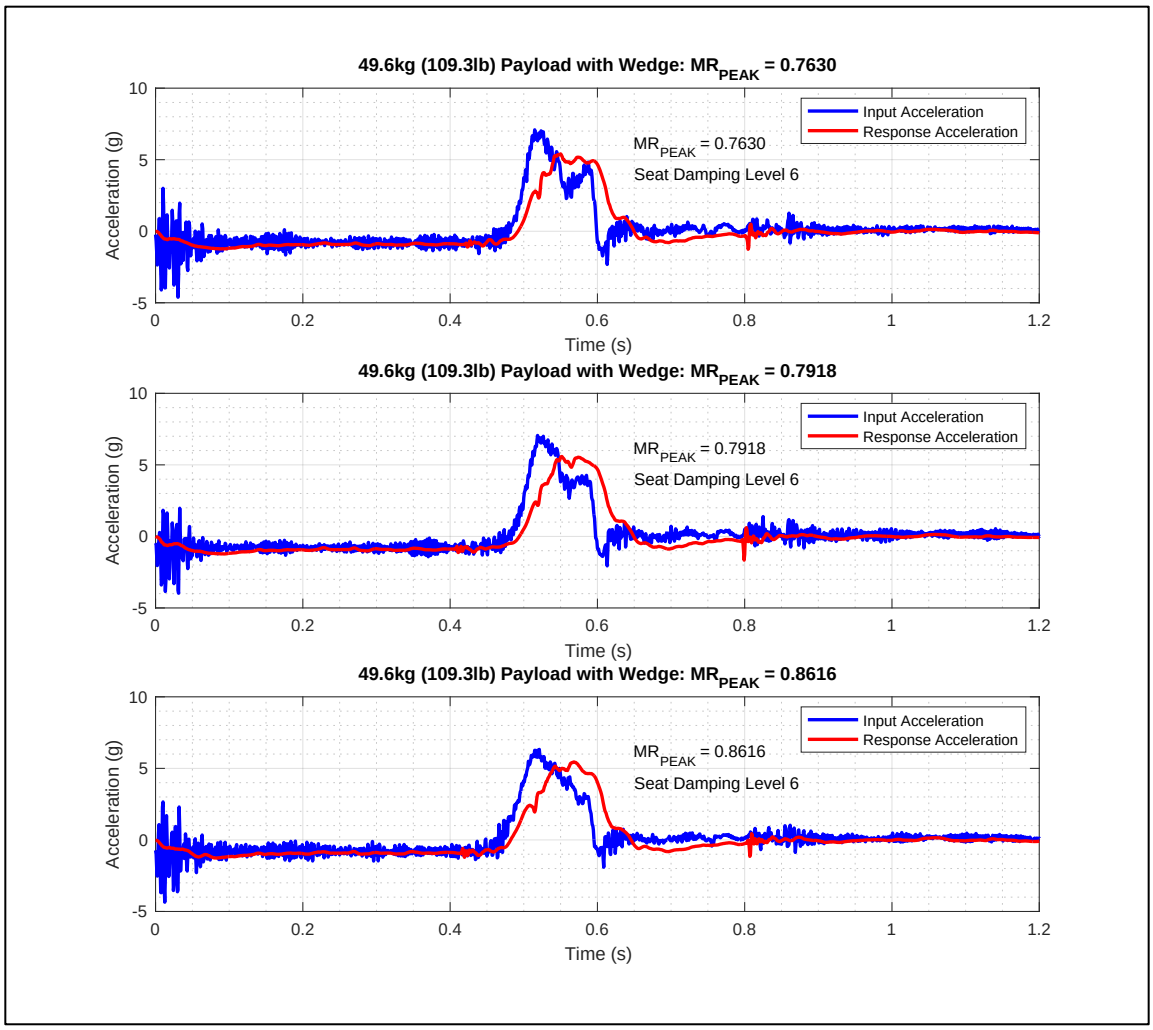

Figure A - 2: MR_{PEAK} for 49.6kg (109.3lb) Payload w/Wedge Seat Damping 6

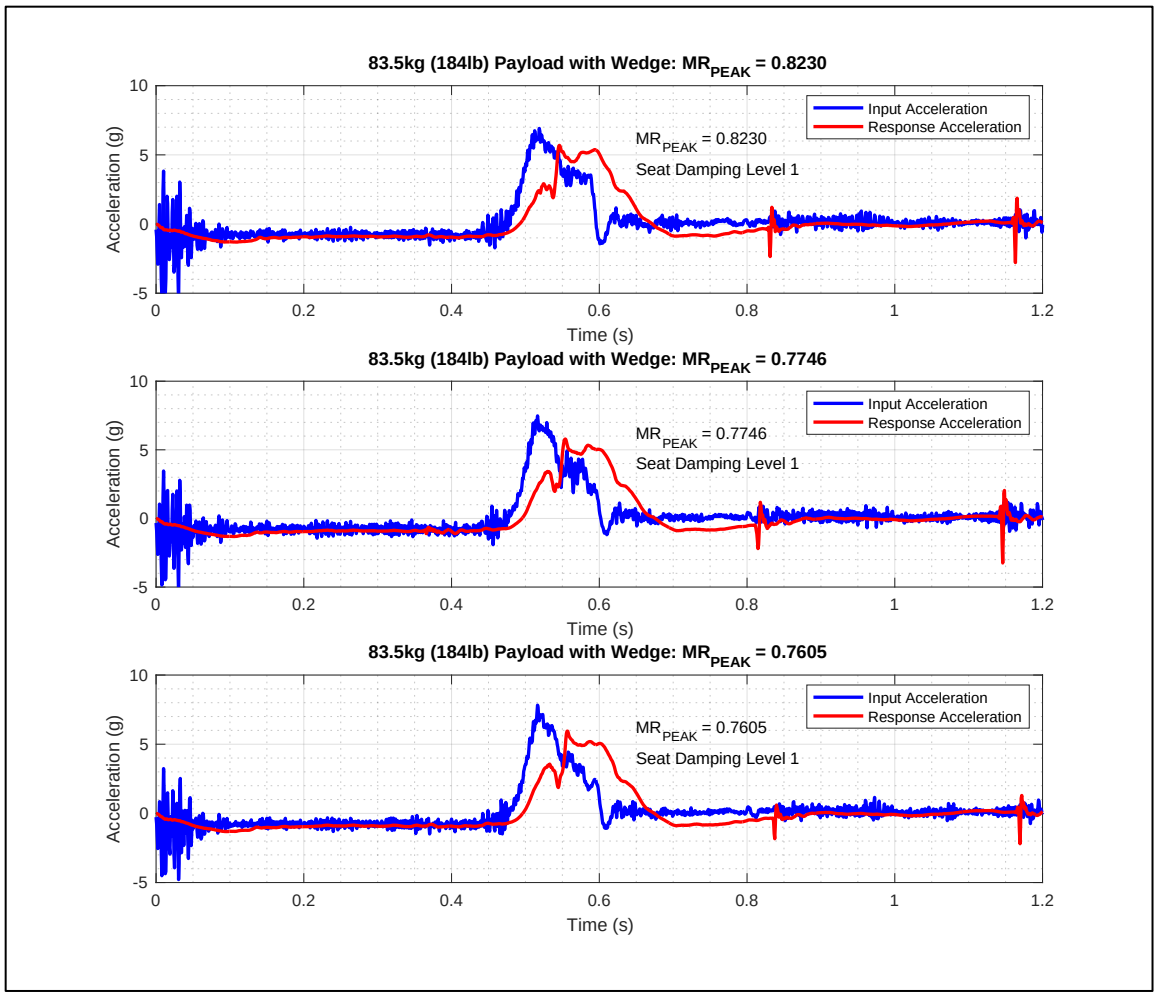

Figure A - 3: MR_{PEAK} for 83.5kg (184lb) Payload w/Wedge Seat Damping 1

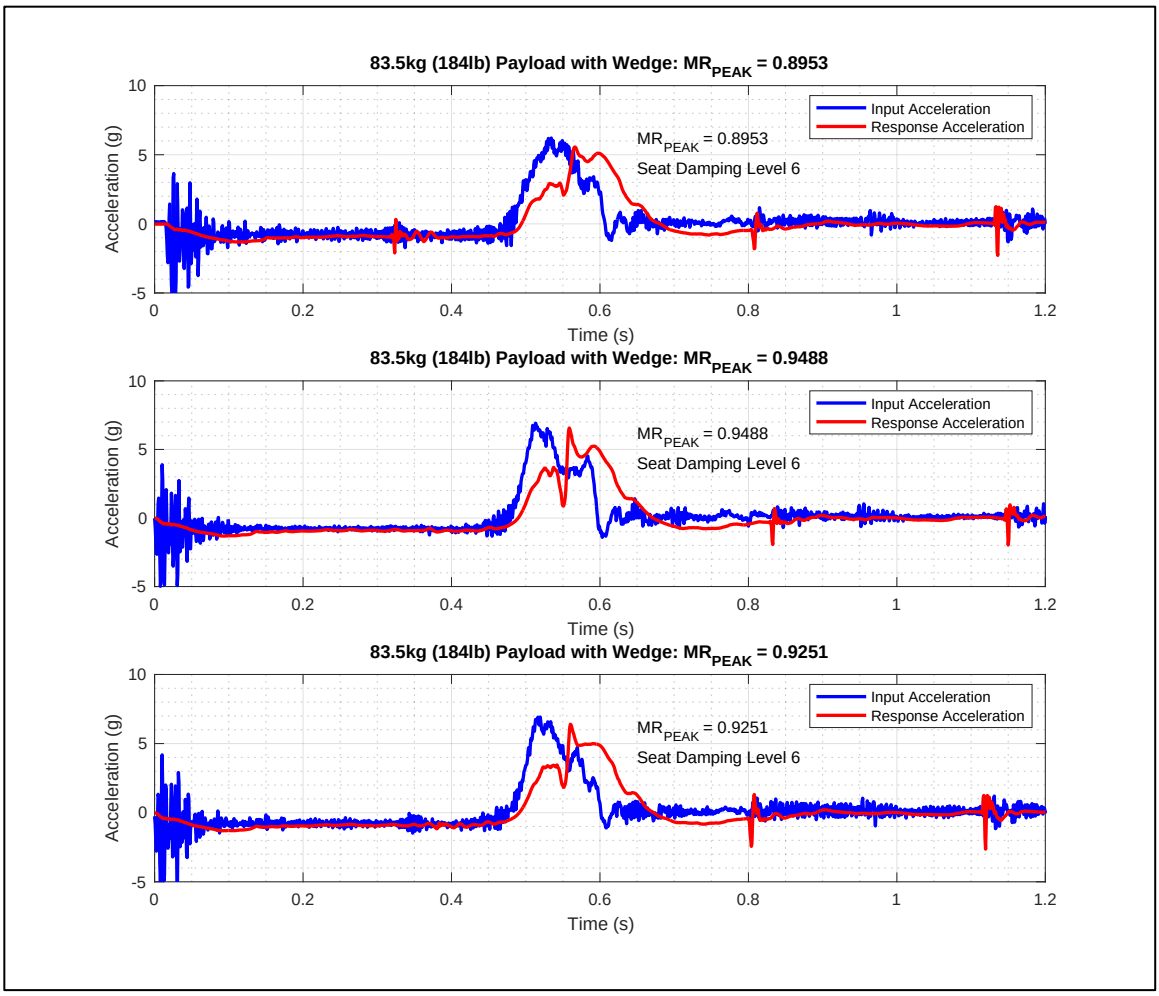

Figure A - 4: MR_{PEAK} for 83.5kg (184lb) Payload w/Wedge Seat Damping 6

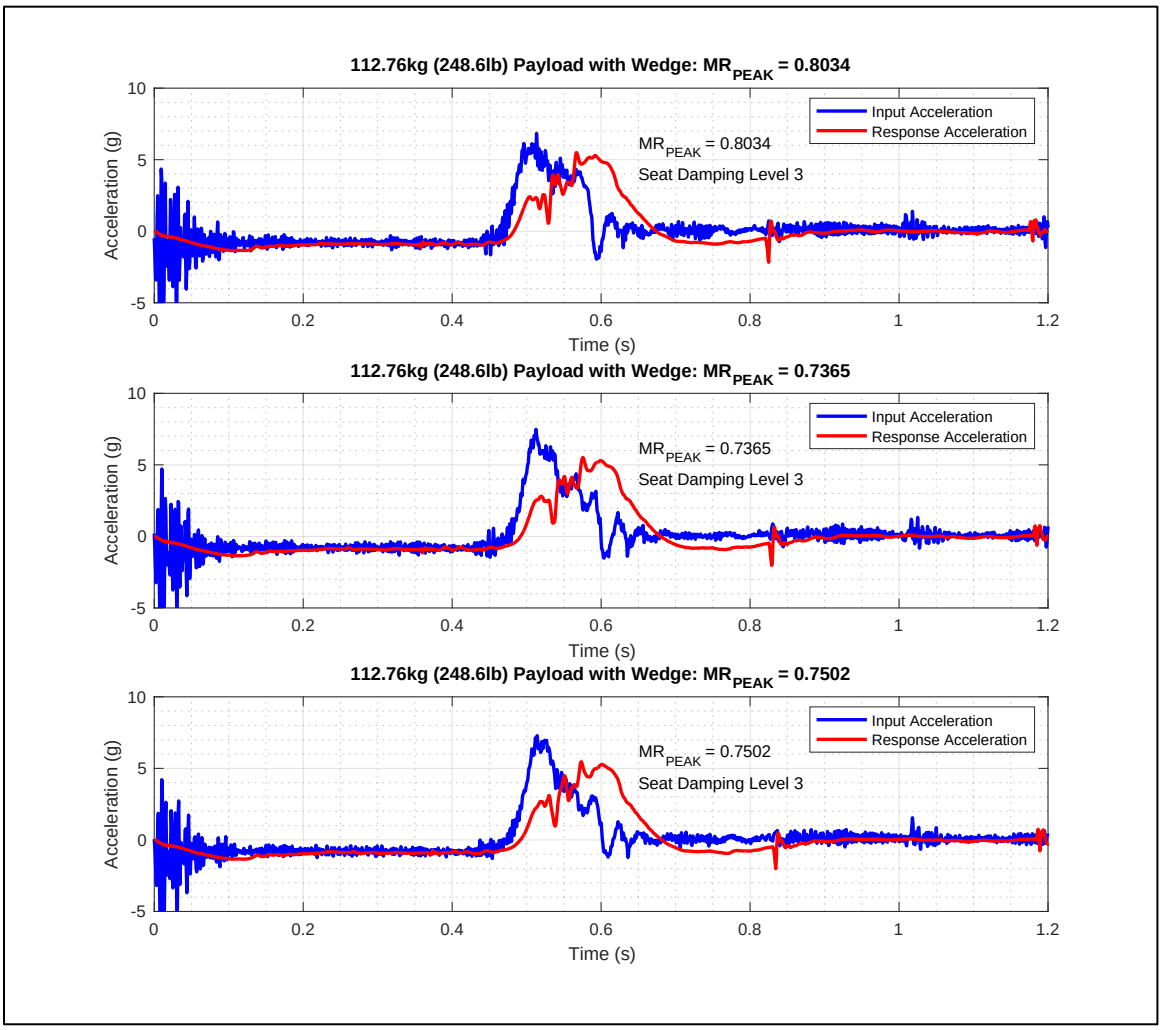

Figure A - 5: MR_{PEAK} for 112.76kg (248.6lb) Payload w/Wedge Seat Damping 3

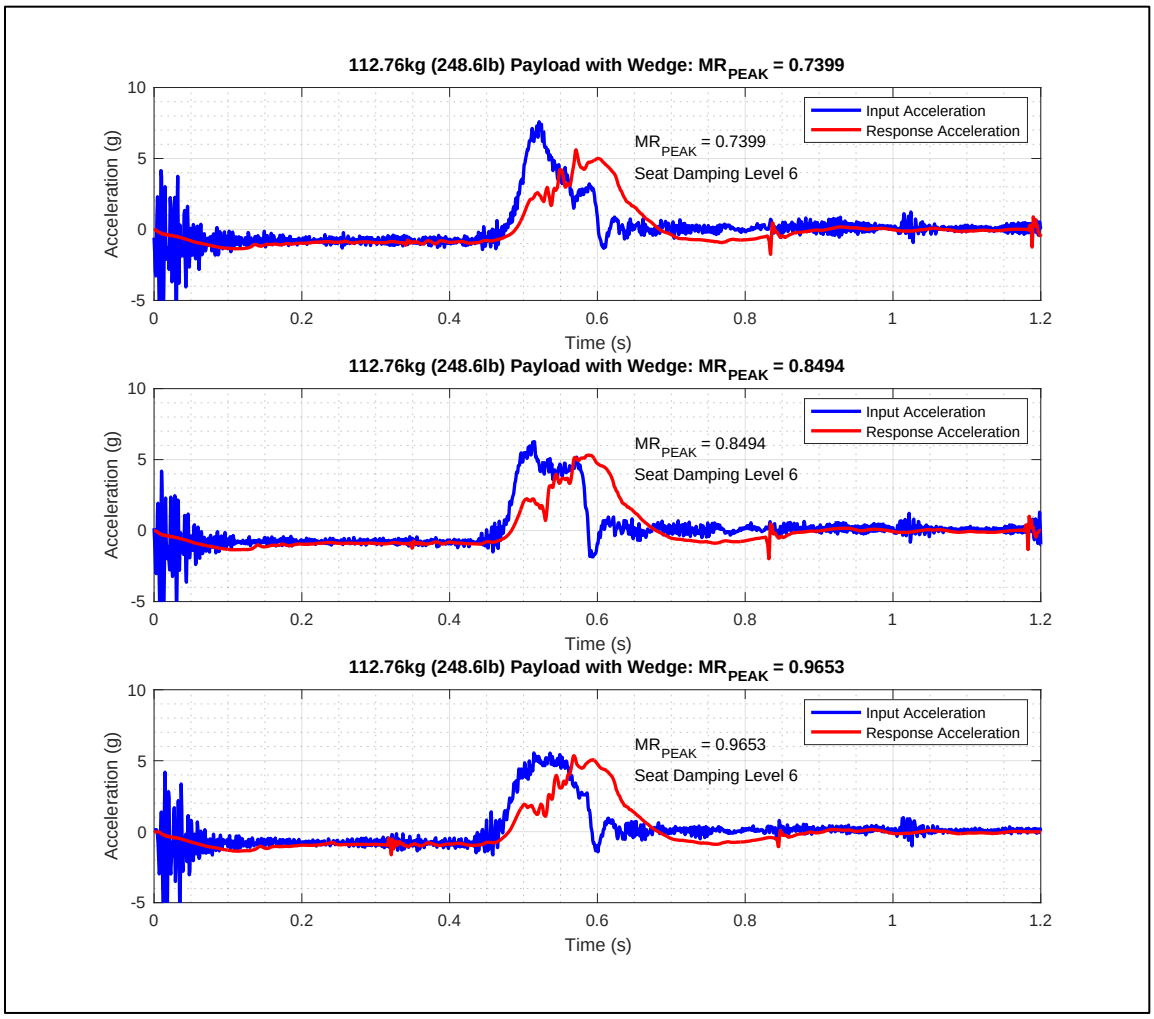

Figure A - 6: MR_{PEAK} for 112.76kg (248.6lb) Payload w/Wedge Seat Damping 6

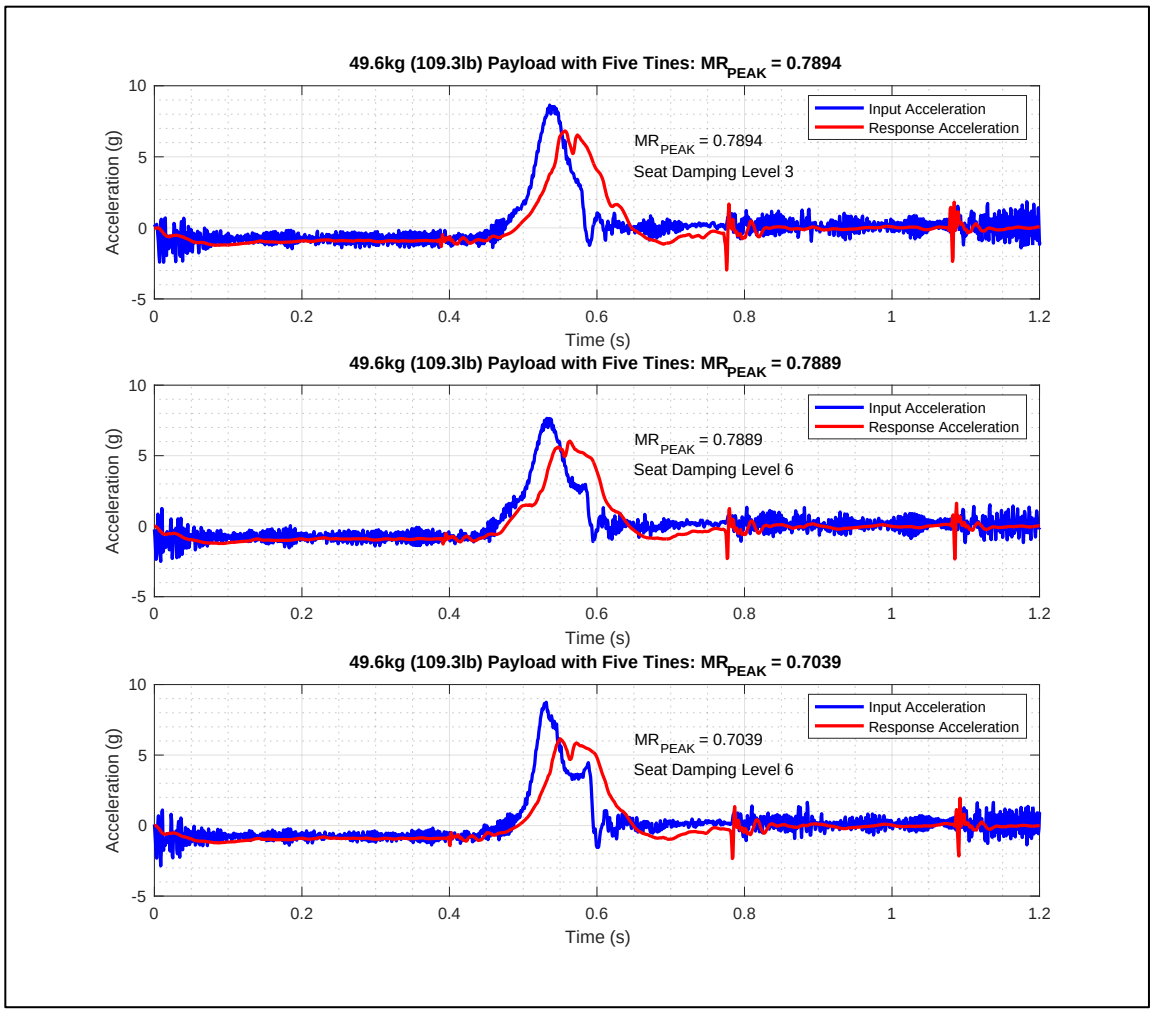

Figure A - 7: MR_{PEAK} for 49.6kg (109.3lb) Payload w/Tines Seat Damping 3 and 6

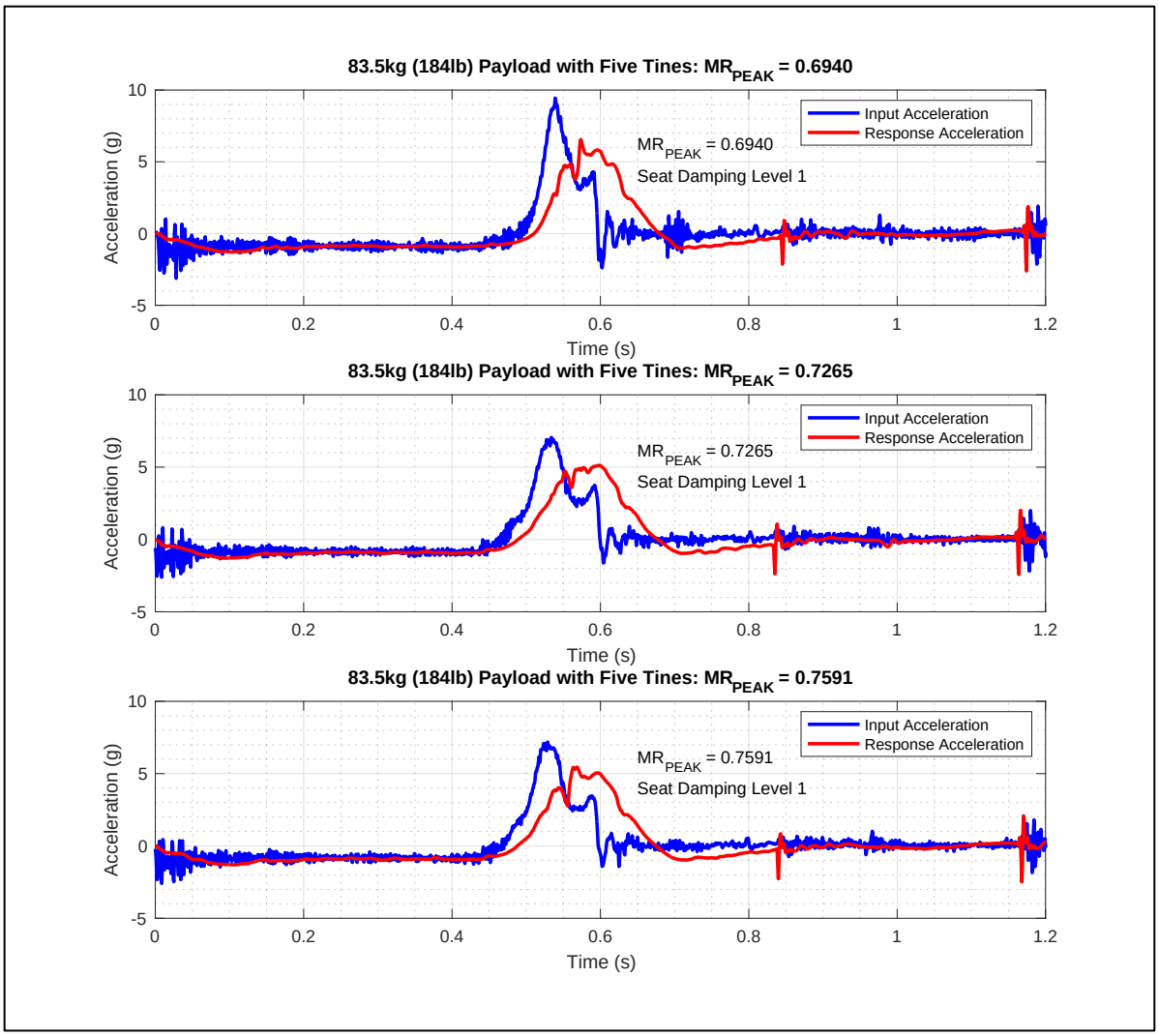

Figure A - 8: MR_{PEAK} for 83.5kg (184lb) Payload w/Tines Seat Damping 1

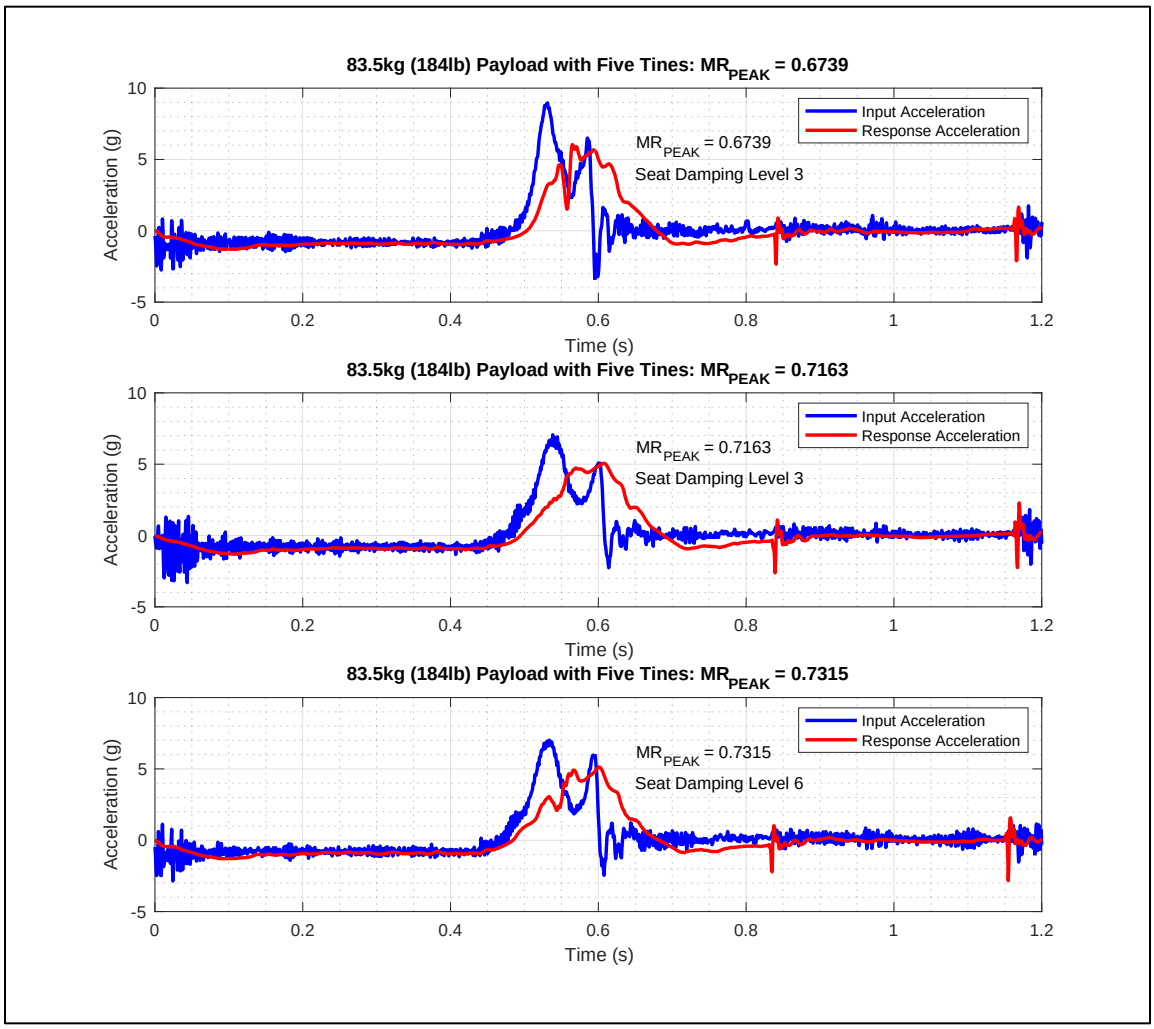

Figure A - 9: MR_{PEAK} for 83.5kg (184lb) Payload w/Tines Seat Damping 6

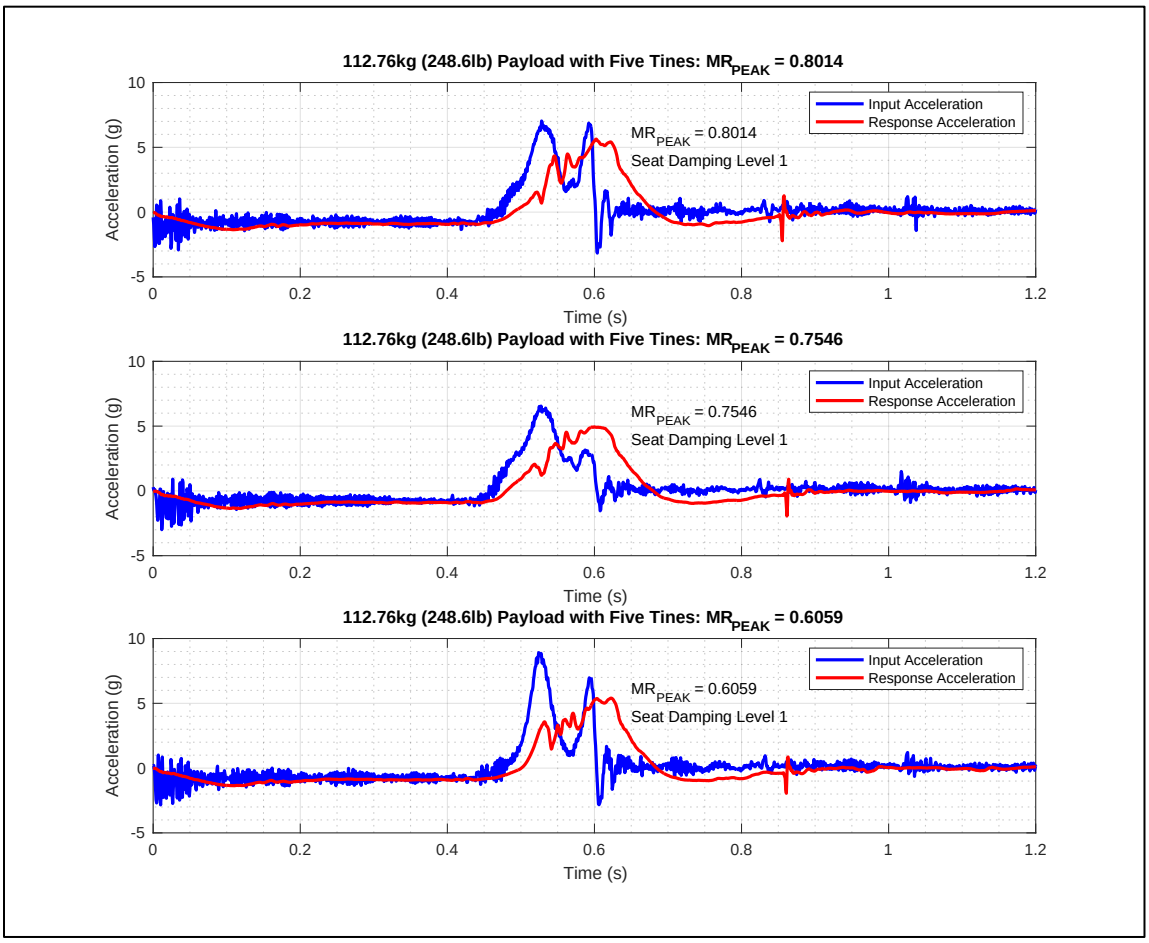

Figure A - 10: MR_{PEAK} for 112.76kg (248.6lb) Payload w/Tines Seat Damping 1

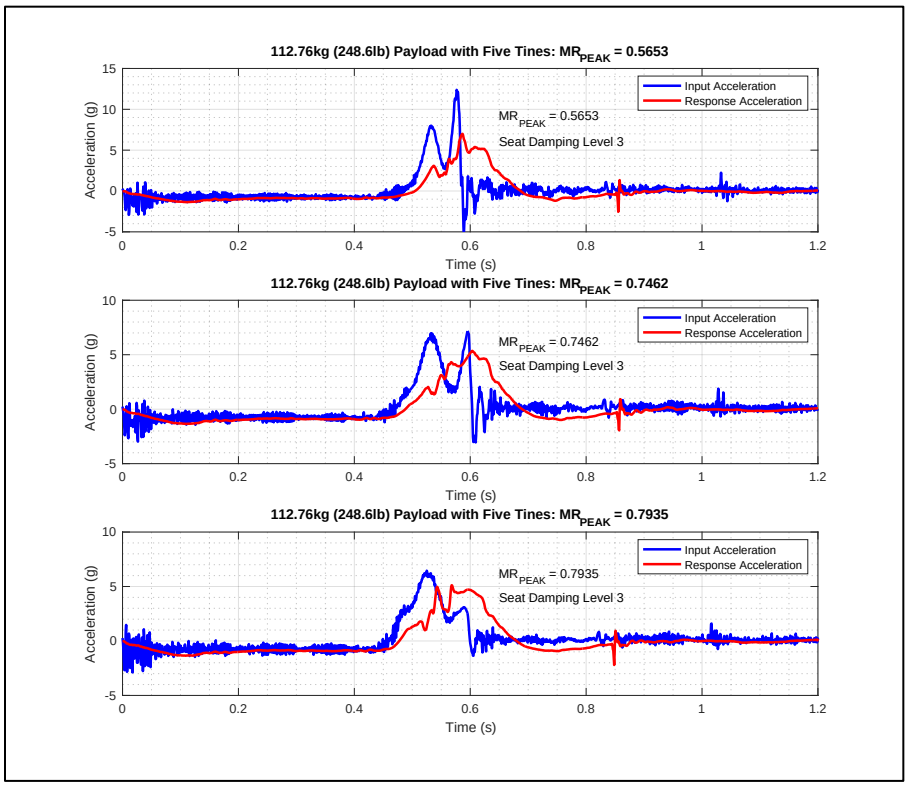

Figure A - 11: MR$_{PEAK}$ for 112.76kg (248.6lb) Payload w/Tines Seat Damping 3

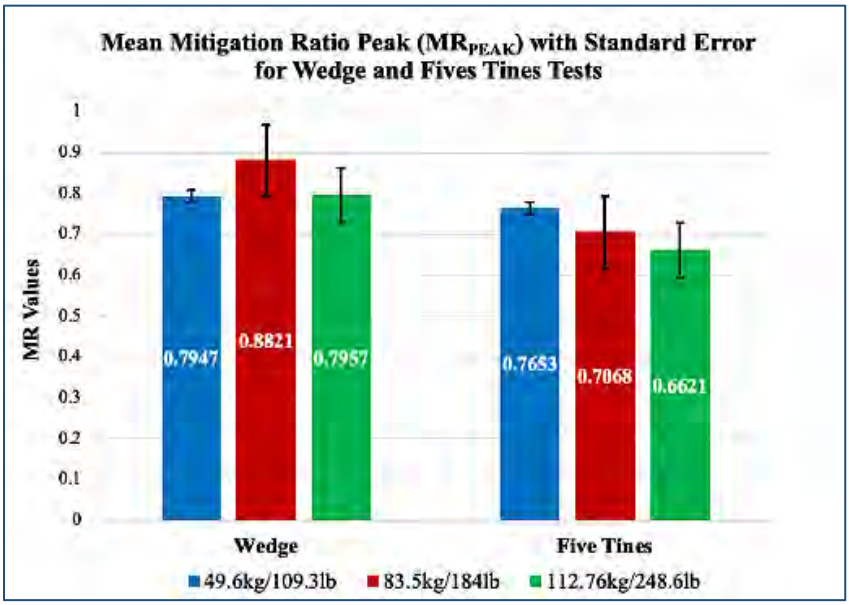

Figure A - 12: Mean MR$_{PEAK}$ Values with Standard Error for Wedge and Five Tines Test

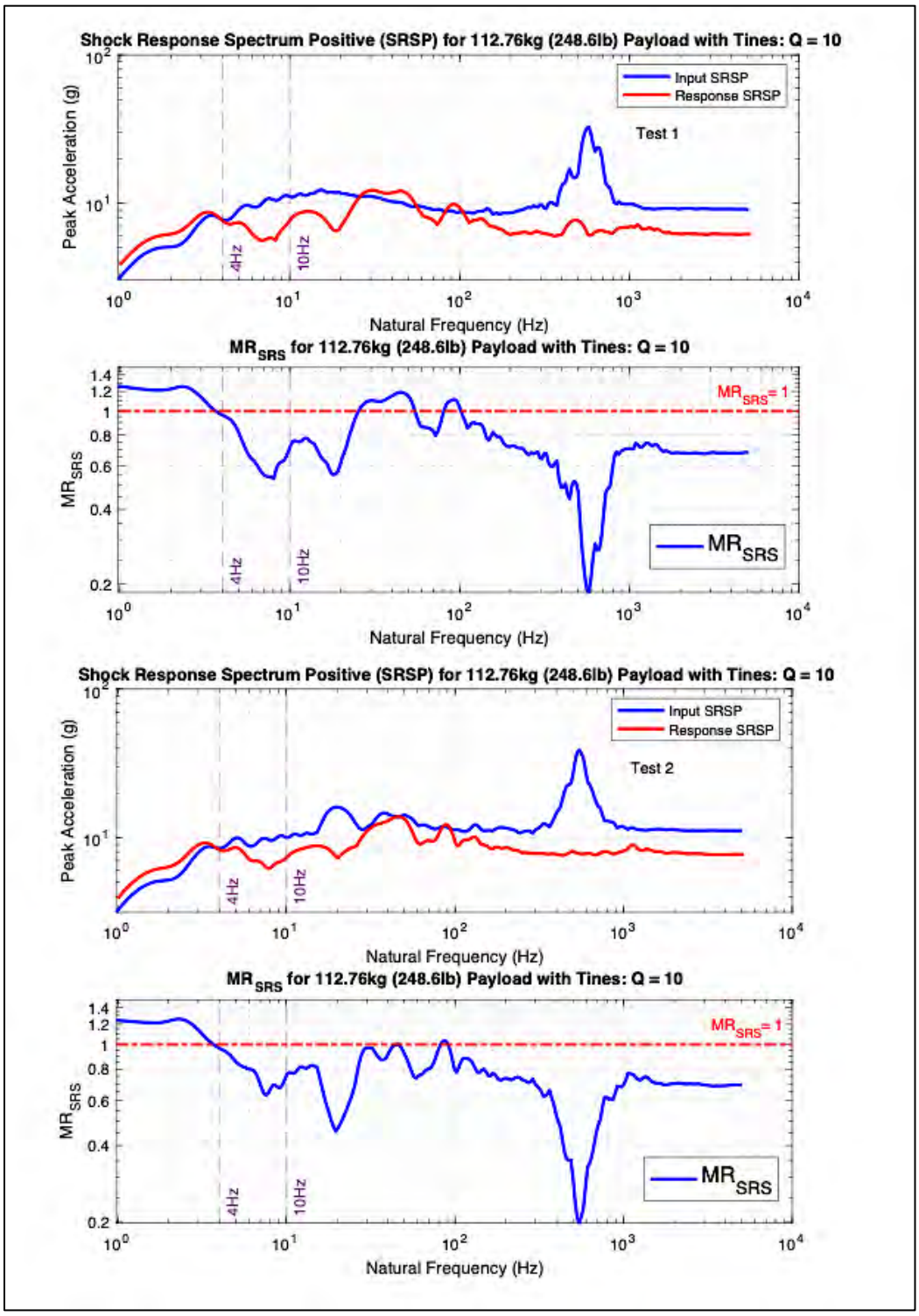

Figure A - 13: SRSP and MR_{SRS} for 112.76kg (248.6lb) Payload w/Tines Tests 1 and 2

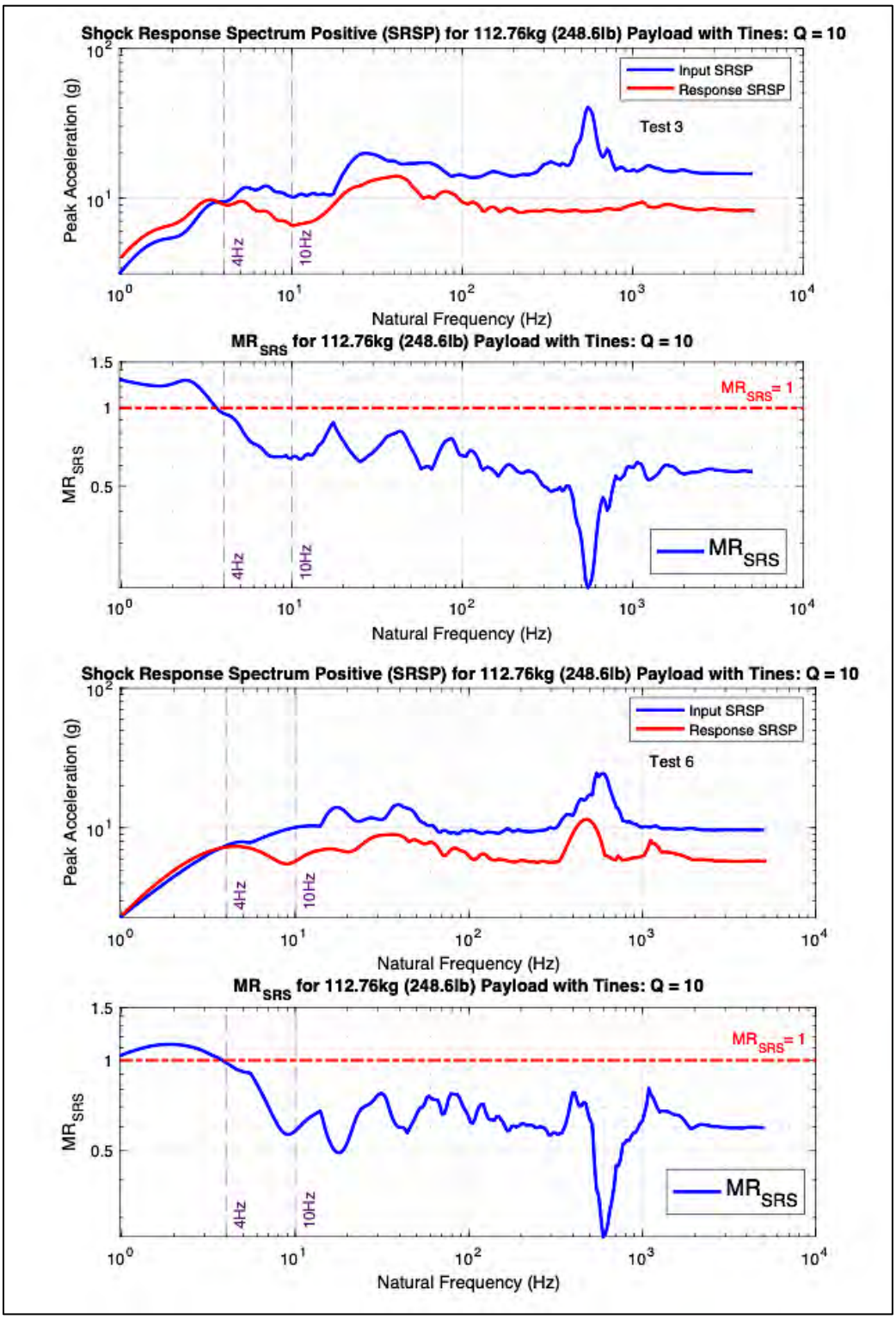

Figure A - 14: SRSP and MR_{SRS} for 112.76kg (248.6lb) Payload w/Tines Tests 3 and 6

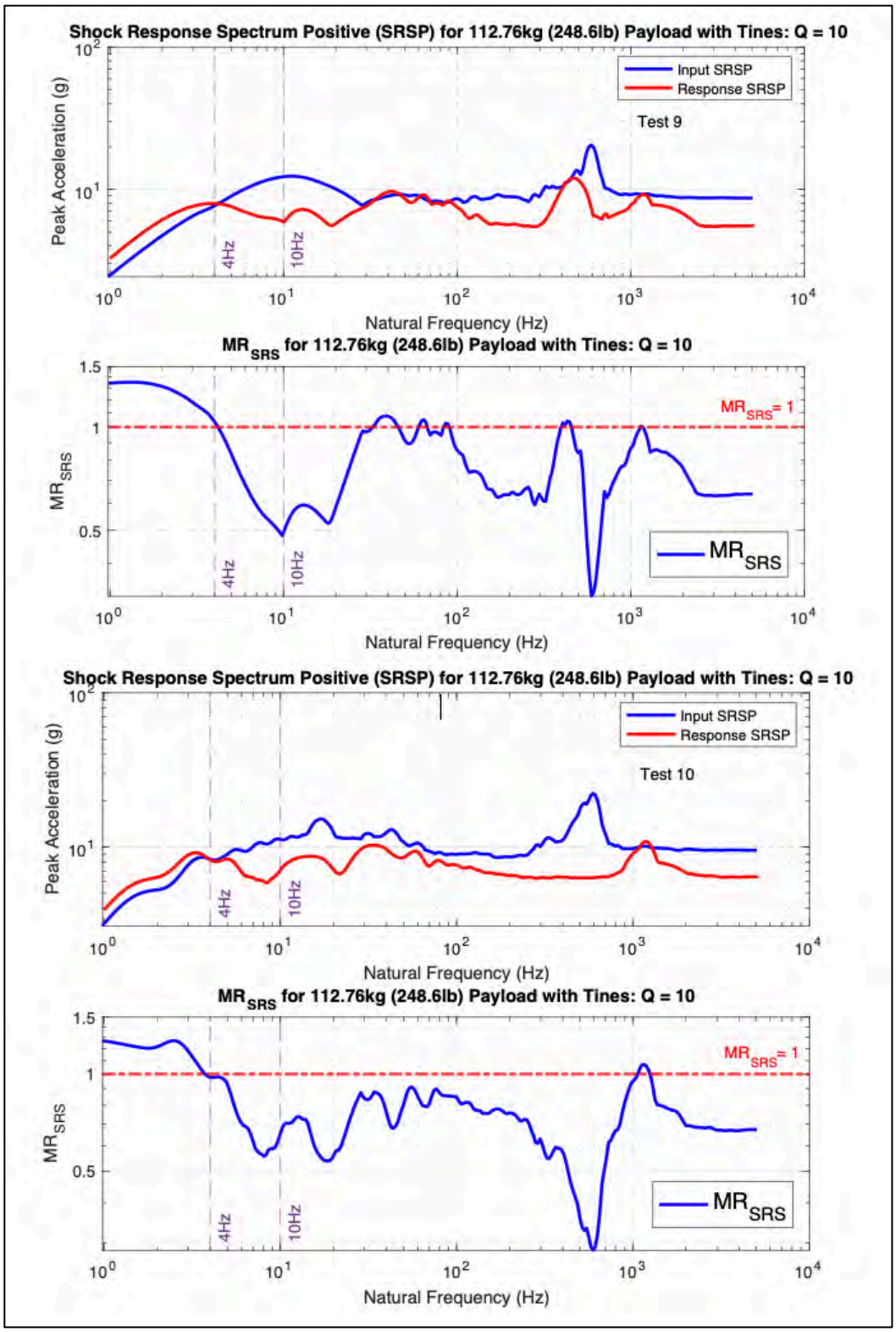

Figure A - 15: SRSP and MR_{SRS} for 112.76kg (248.6lb) Payload w/Tines Tests 9 and 10

Appendix B. Graphs for SDOF Numerical Analysis

The ‘W’ in the figure caption represents tests with the wedge, and the ‘T’ indicates tests with the five tines. The ‘SS’ is for the analysis conducted using the state space representation, and ‘NB’ is for the Newmark-Beta analysis. The light blue line represents the platform input acceleration, the dark blue line is the experimental payload response, and the red line signifies the simulated payload response acceleration. The seat damping levels are listed as ‘1’, ‘3’, or ‘6’.

SDOF State Space Analysis

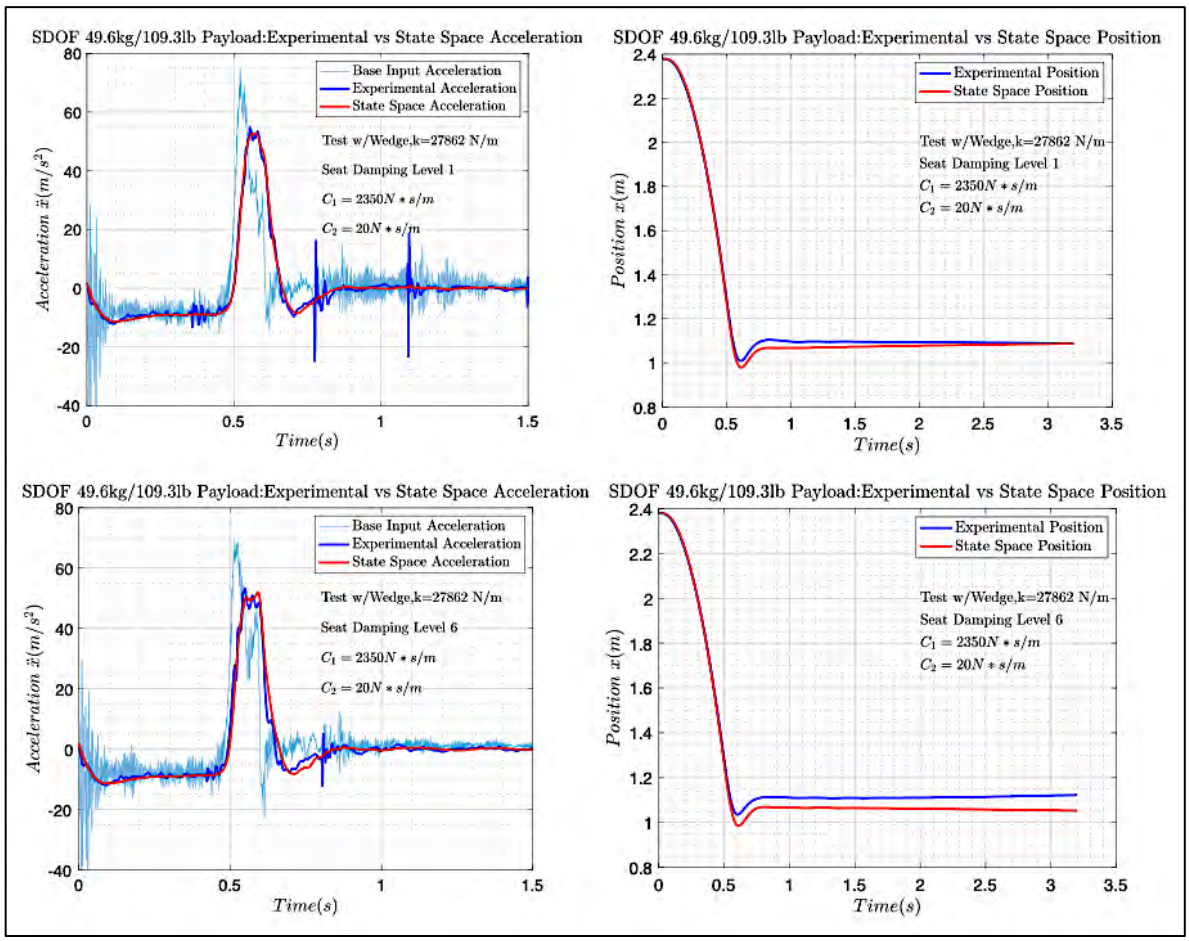

Figure B - 1: SDOF 49.6kg/109.3lb Payload (W): SS Acceleration & Position Damping 1 and 6

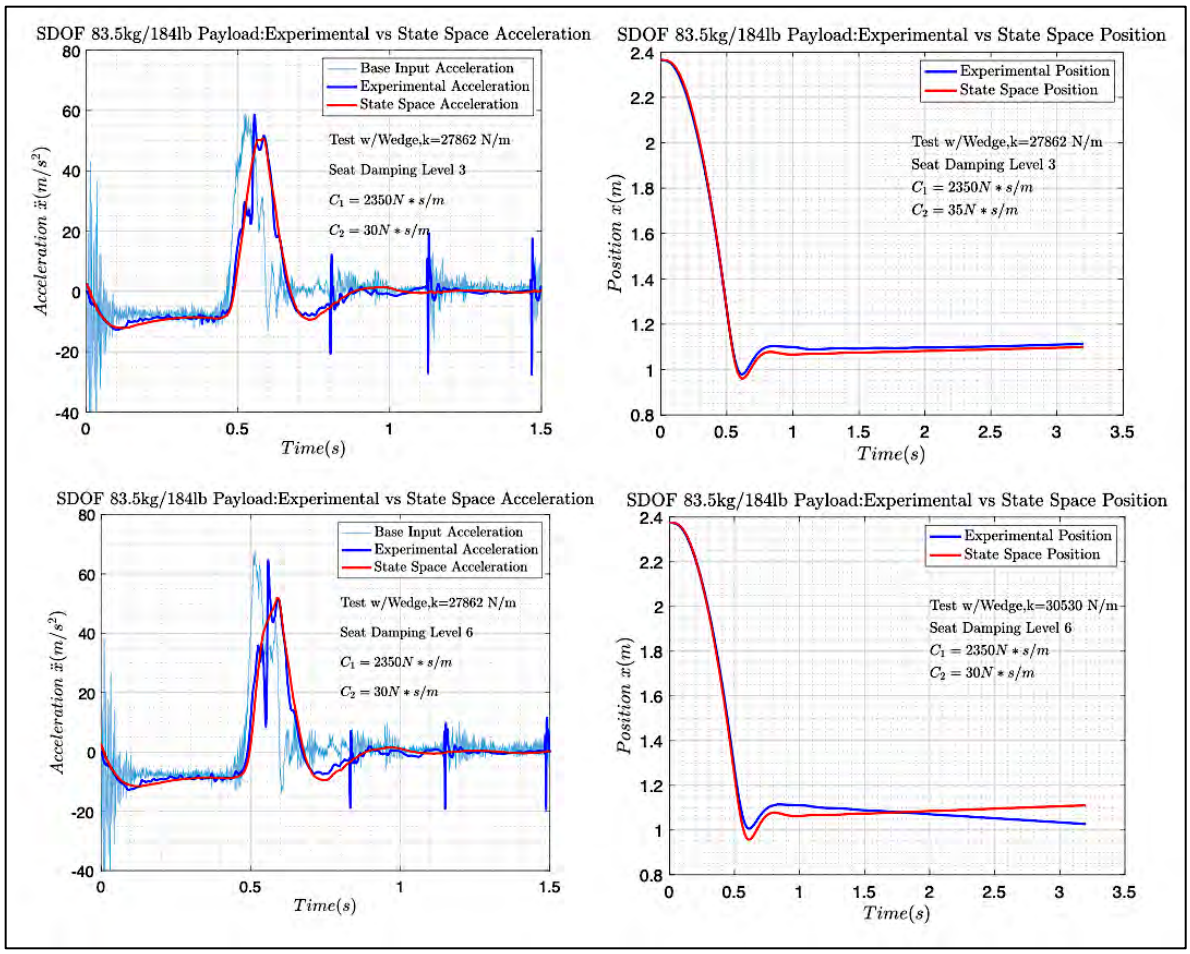

Figure B - 2: SDOF 83.5kg/184lb Payload (W): SS Acceleration & Position Damping 3 and 6

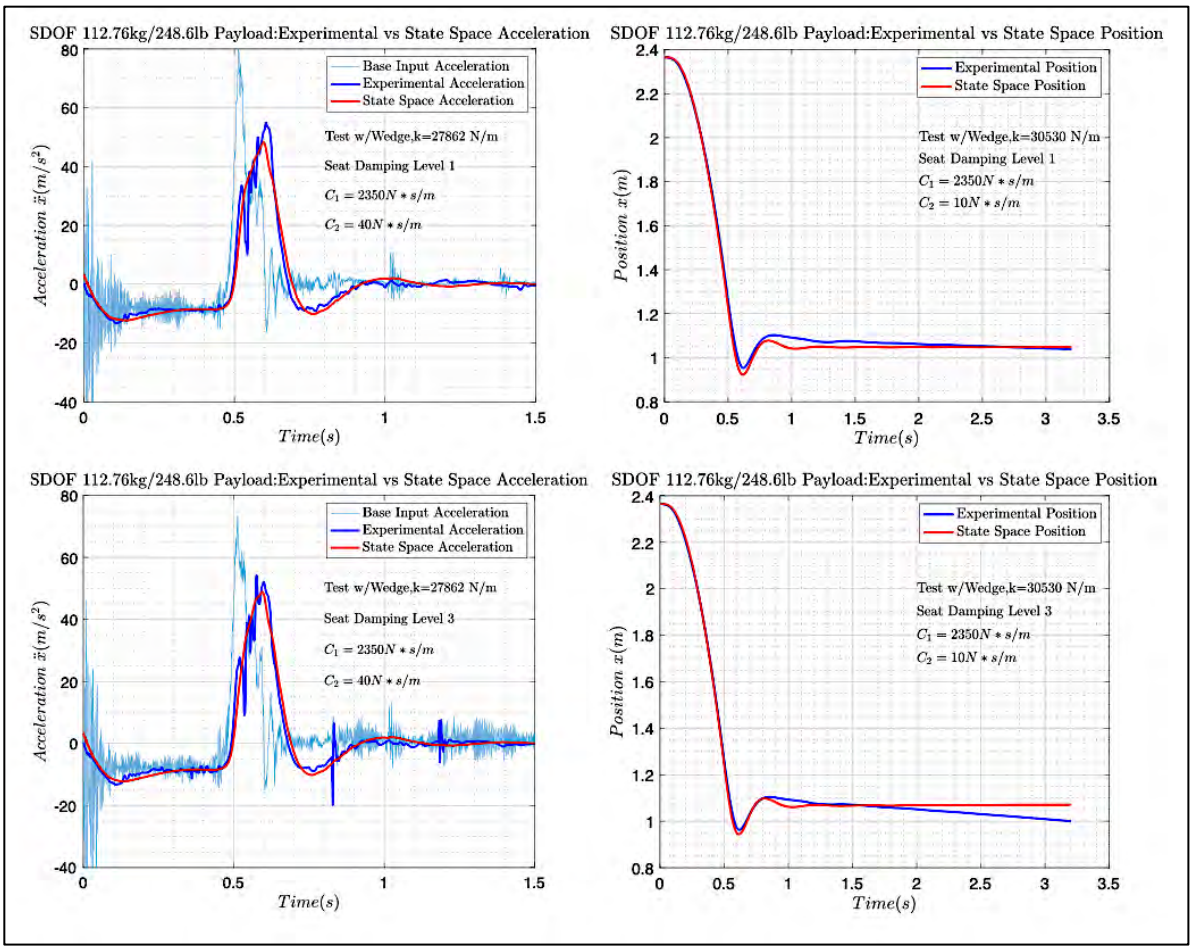

Figure B - 3: SDOF 112.76kg/248.6lb Payload (W): SS Acceleration & Position Damping 1 and 3

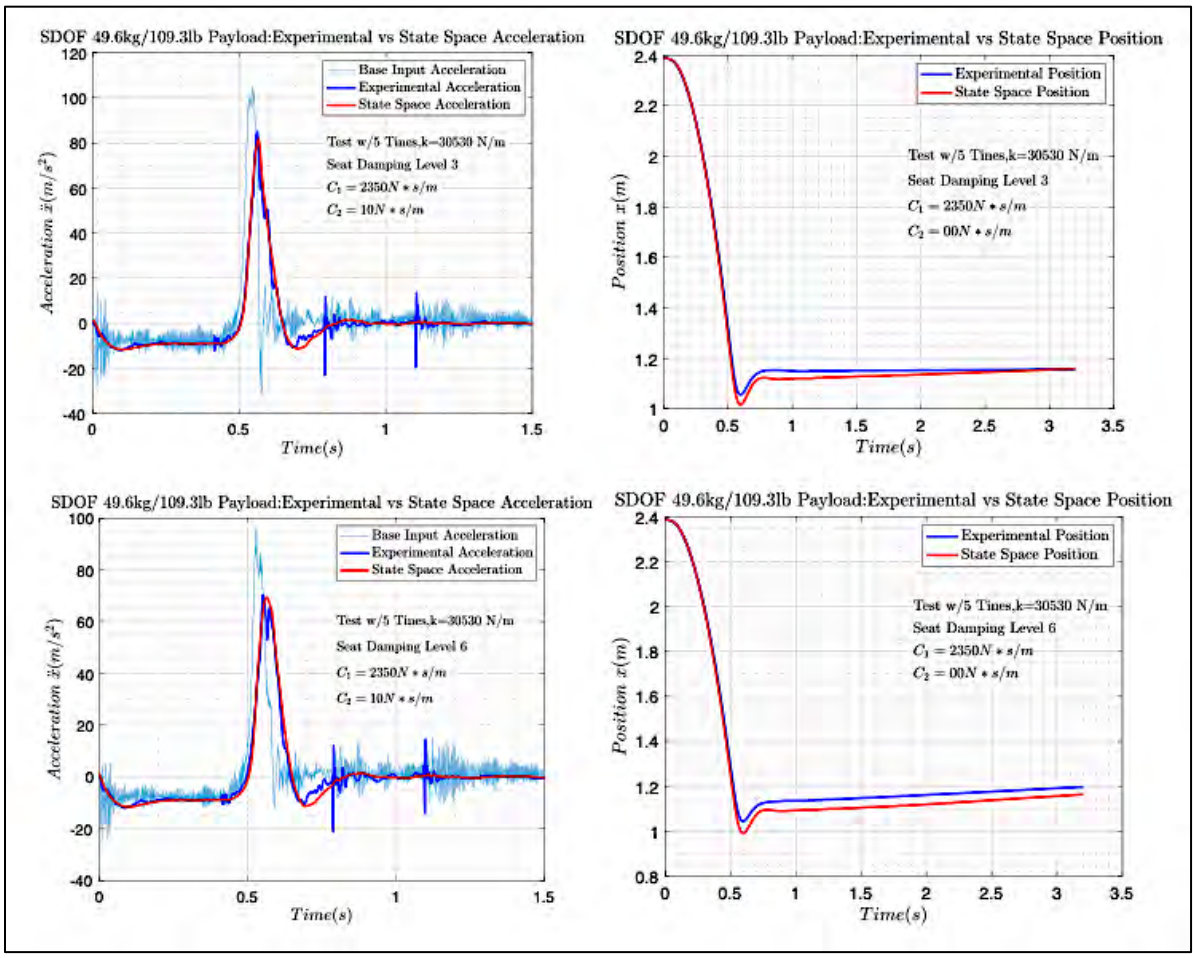

Figure B - 4: SDOF 49.6kg/109.3lb Payload (T): SS Acceleration & Position Damping 3 and 6

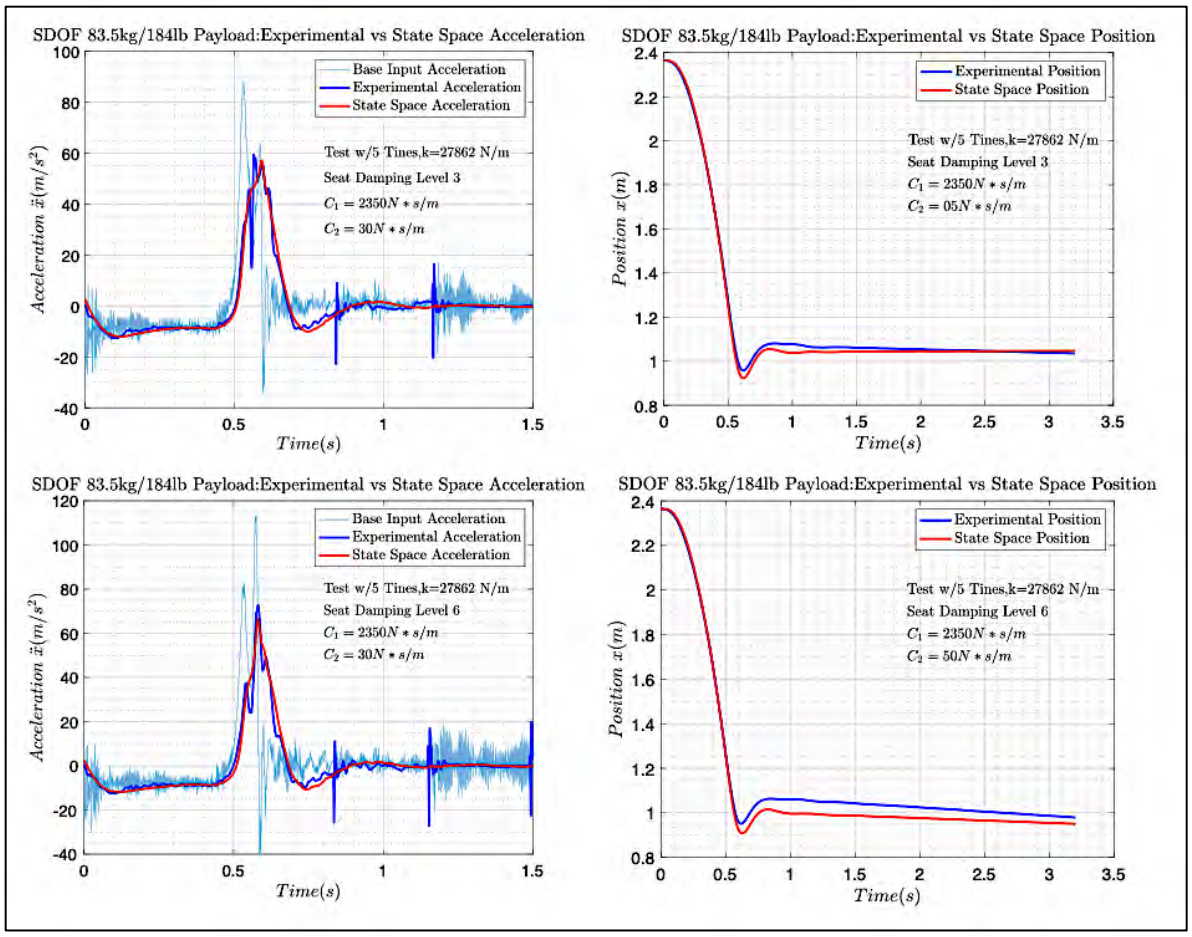

Figure B - 5: SDOF 83.5kg/184lb Payload (T): SS Acceleration & Position Damping 3 and 6

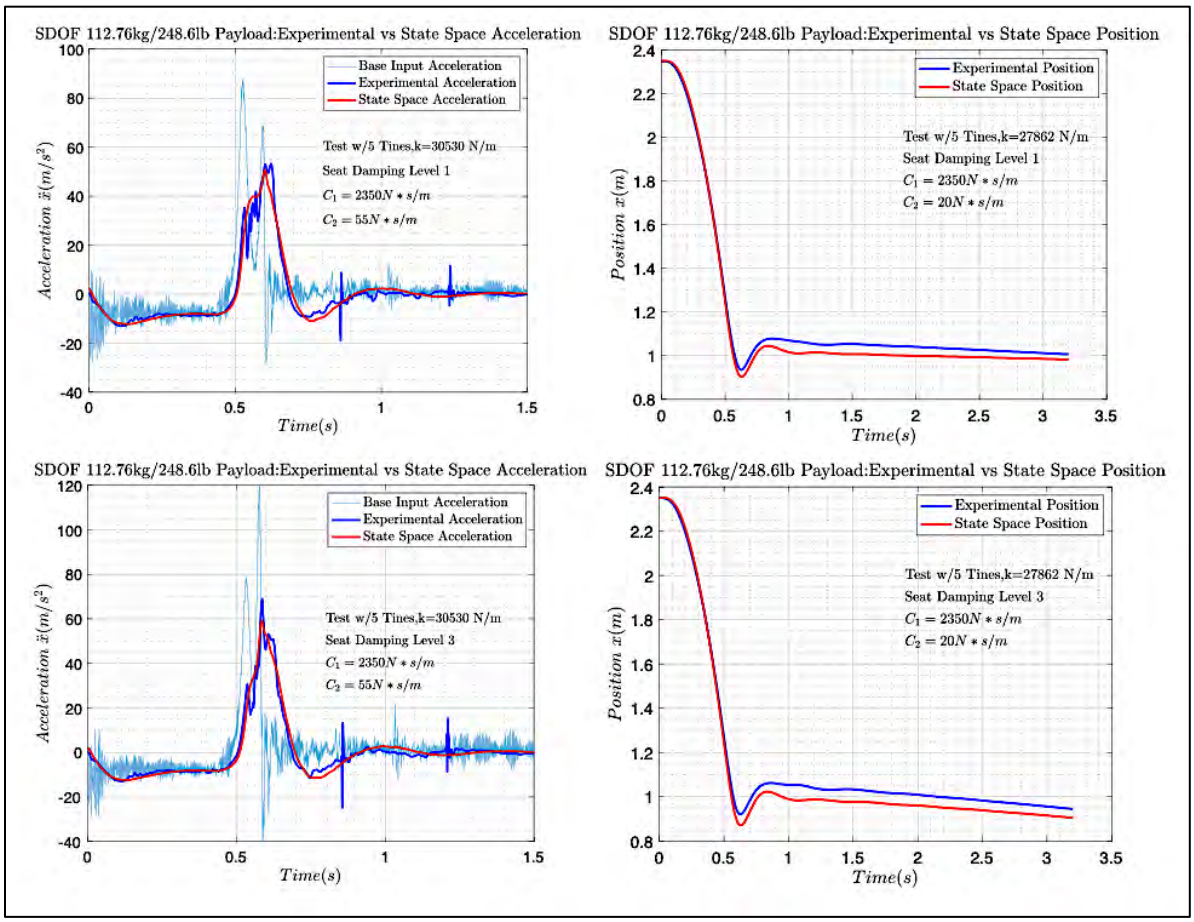

Figure B - 6: SDOF 112.76kg/248.6lb Payload (T): SS Acceleration & Position Damping 1 and 3

SDOF Newmark – Beta Analysis

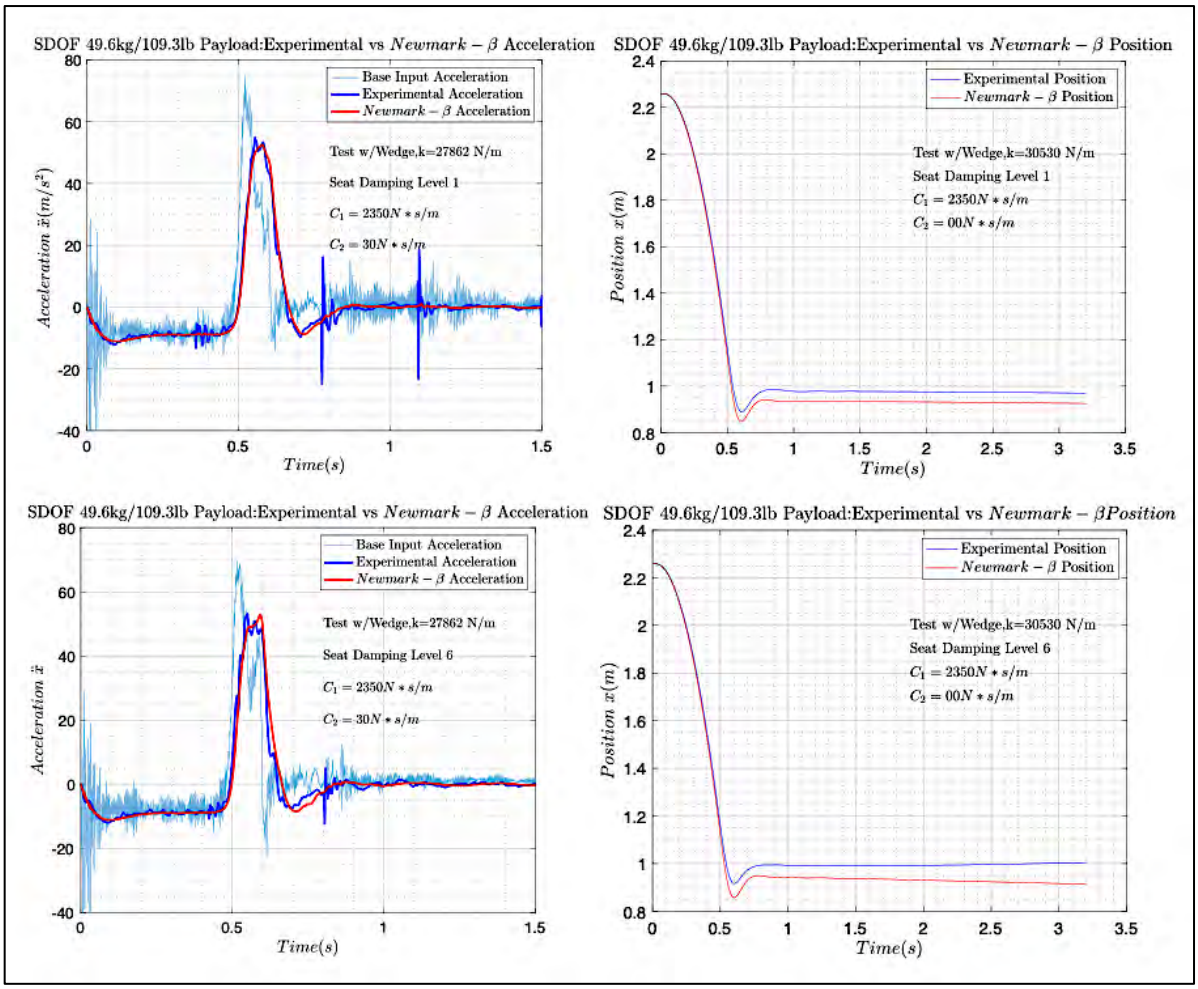

Figure B - 7: SDOF 49.6kg/109.3lb Payload (W): NB Acceleration & Position Damping 1 and 6

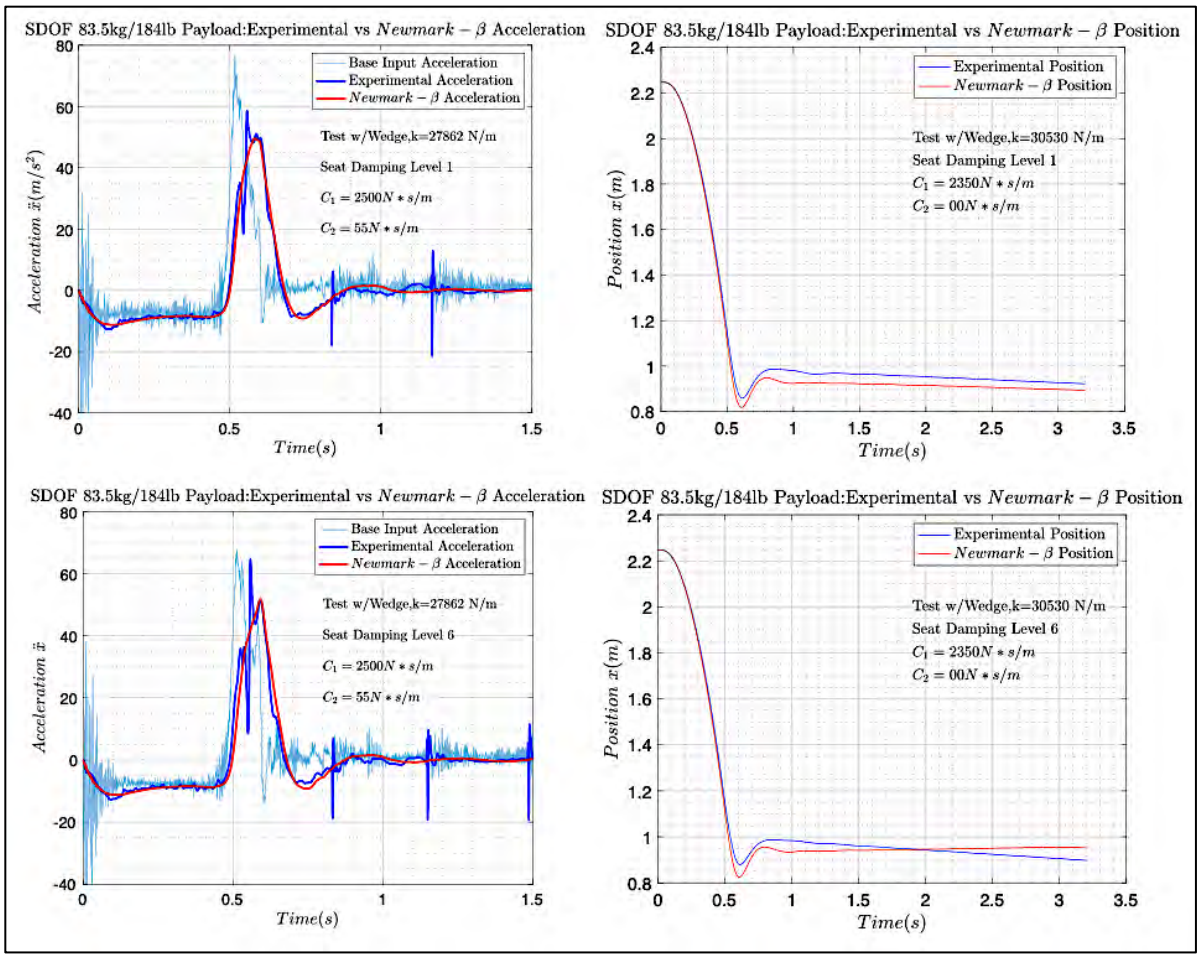

Figure B - 8: SDOF 83.5kg/184lb Payload (W): NB Acceleration & Position Damping 1 and 6

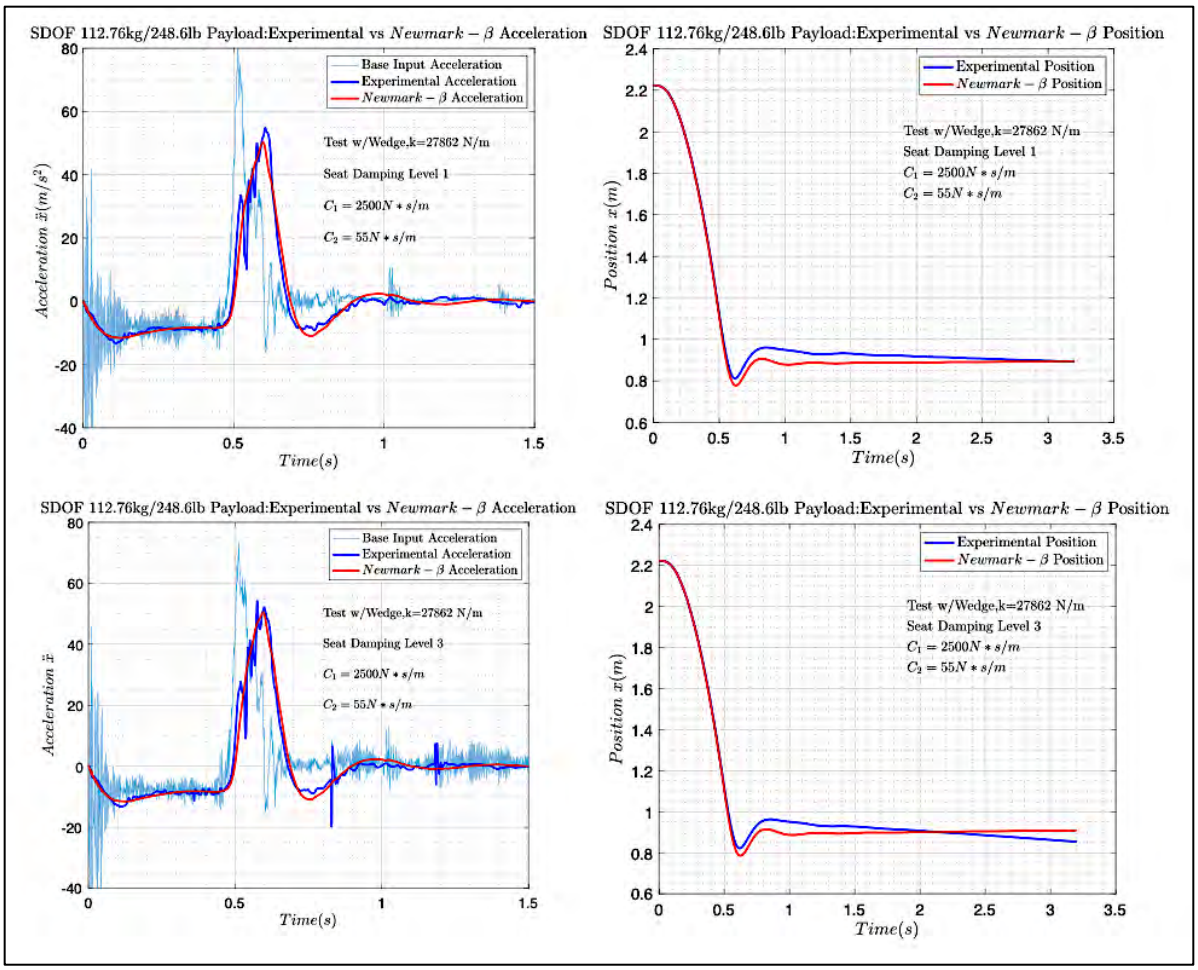

Figure B - 9: SDOF 112.76kg/248.6lb Payload (W): NB Acceleration & Position Damping 1 and 3

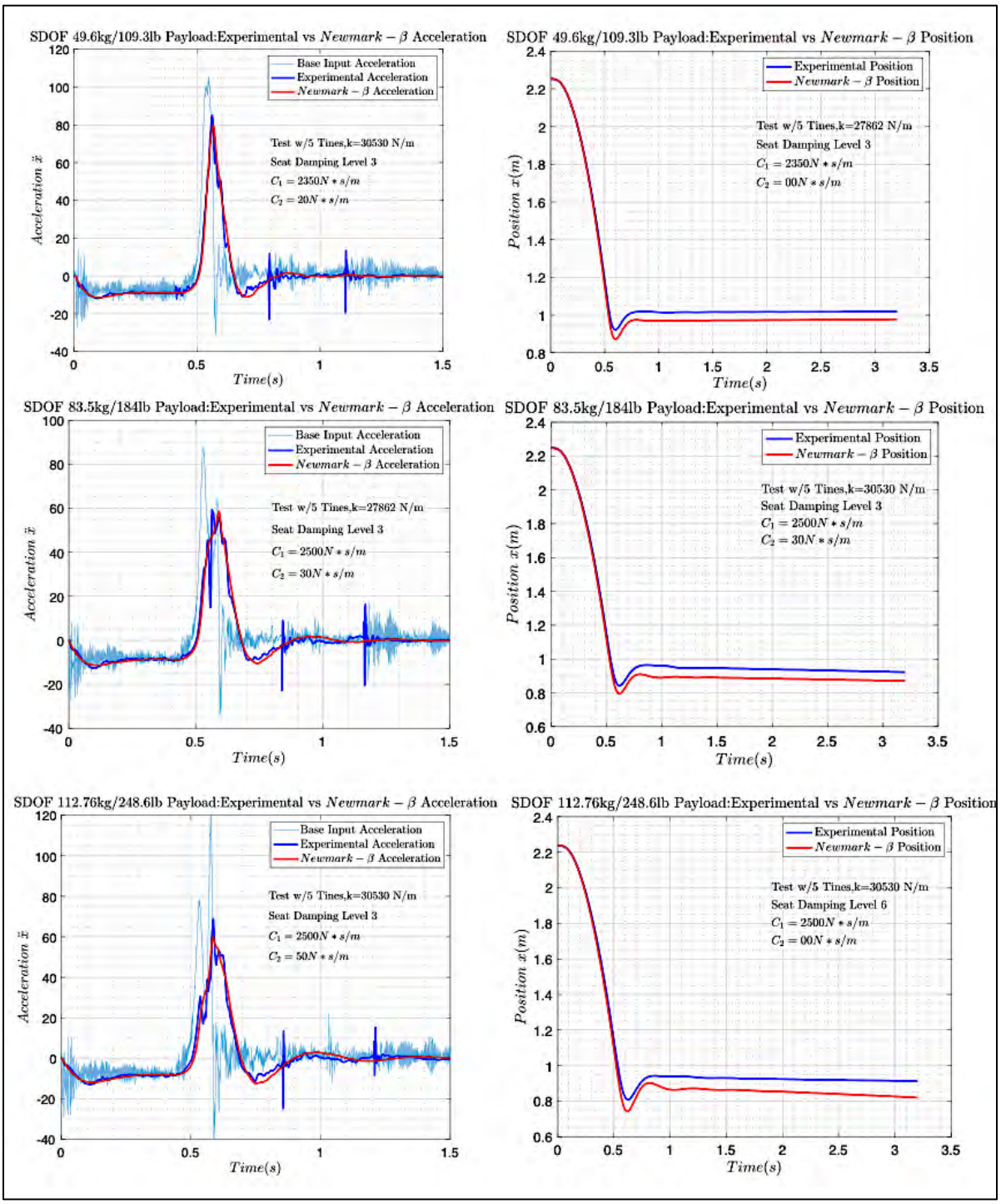

Figure B - 10: SDOF All Payloads (T): NB Acceleration & Position Damping 3 and 6

Appendix C. Graphs for 2DOF Numerical Analysis

The ‘W’ in the figure caption represents tests with the wedge, and the ‘T’ represents tests with the five tines. The ‘SS’ is for the analysis conducted using the state space representation. The light blue line represents the platform input acceleration, the gold line is the experimental payload response, the dark blue line is the simulated payload response, and the red line signifies the simulated seat response acceleration. The seat damping levels are listed as ‘1’, ‘3’, or ‘6’.

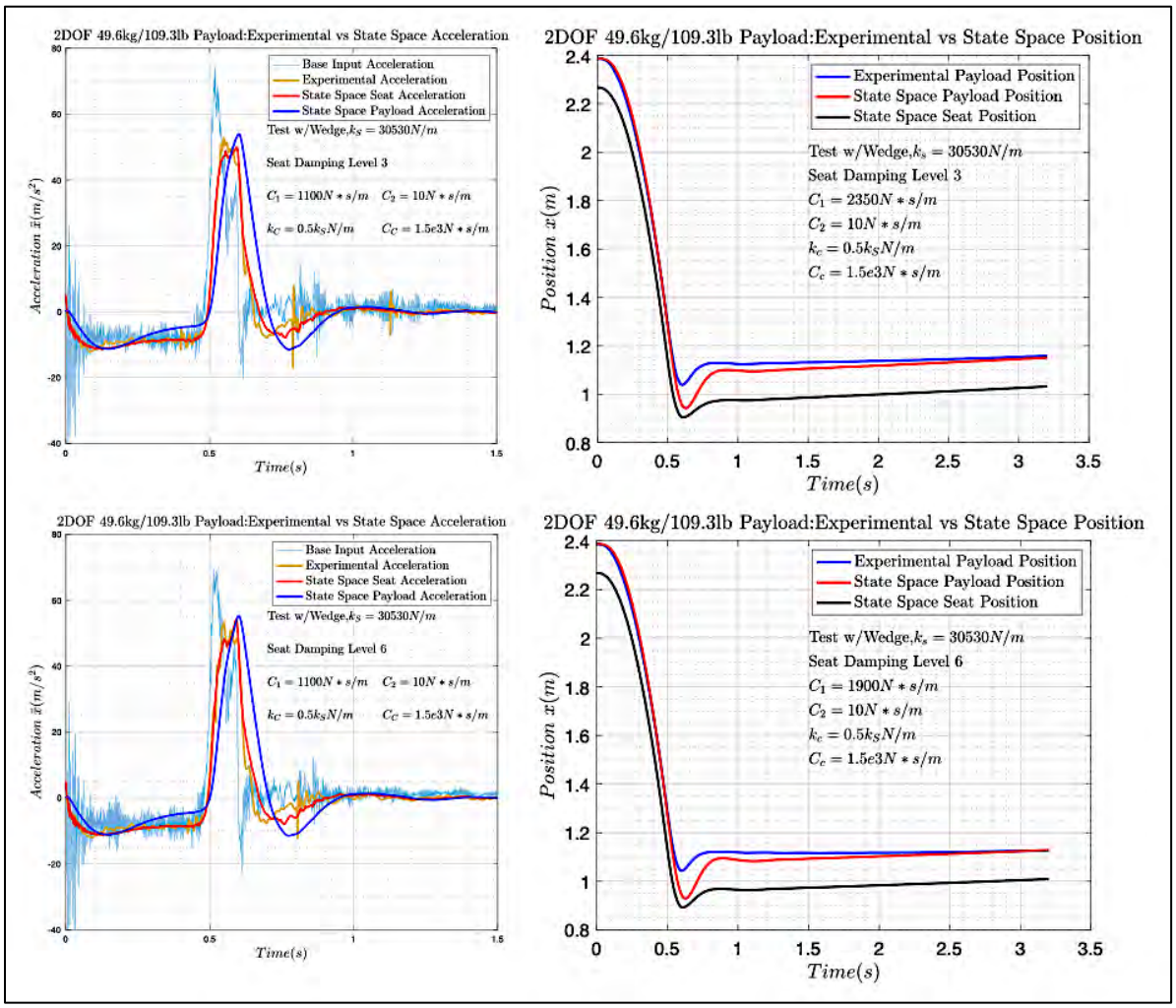

Figure C- 1: 2DOF 49.6kg/109.3lb Payload (W): SS Acceleration & Position Damping 3 and 6

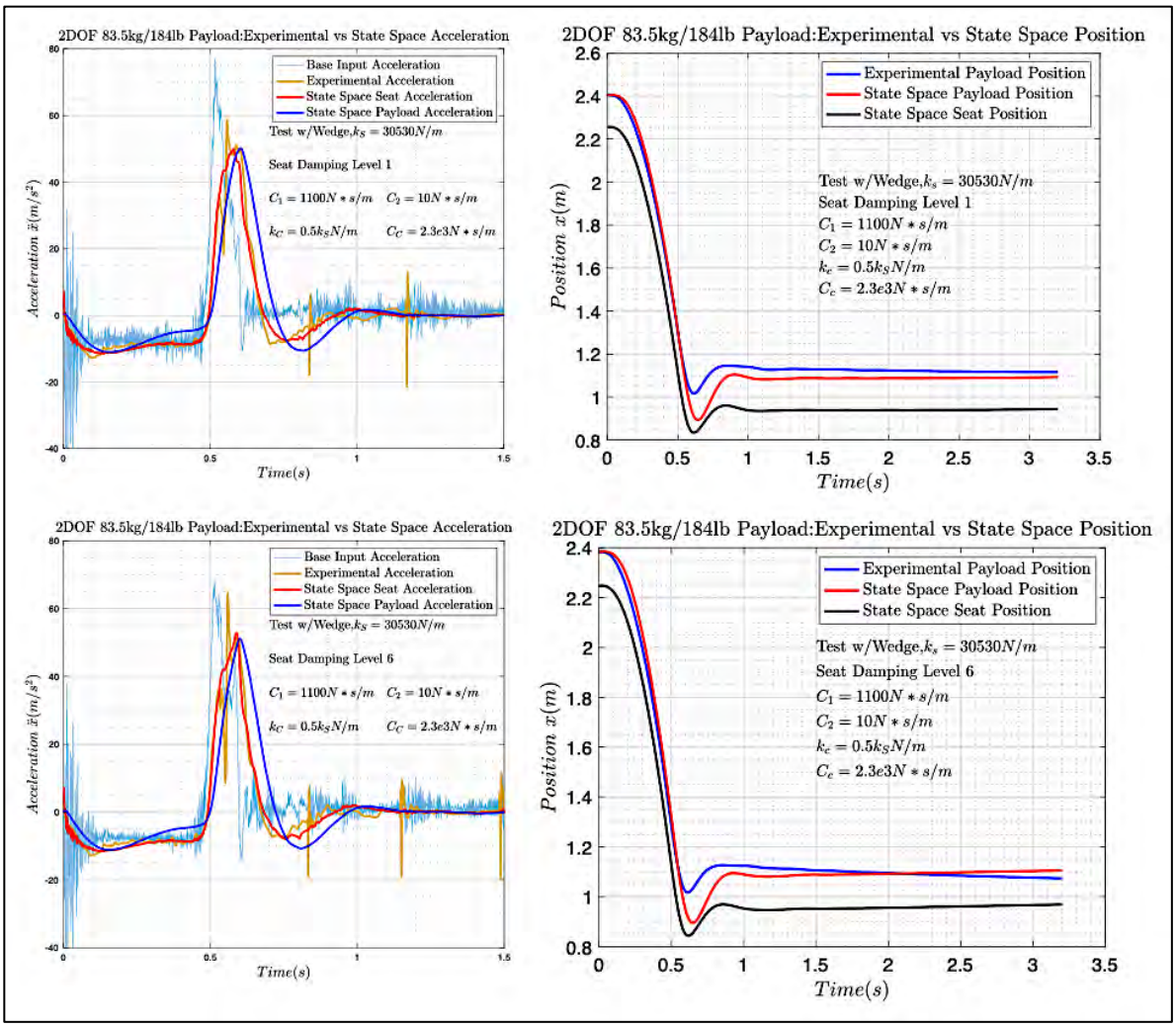

Figure C- 2: 2DOF 83.5kg/184lb Payload (W): SS Acceleration & Position Damping 1 and 6

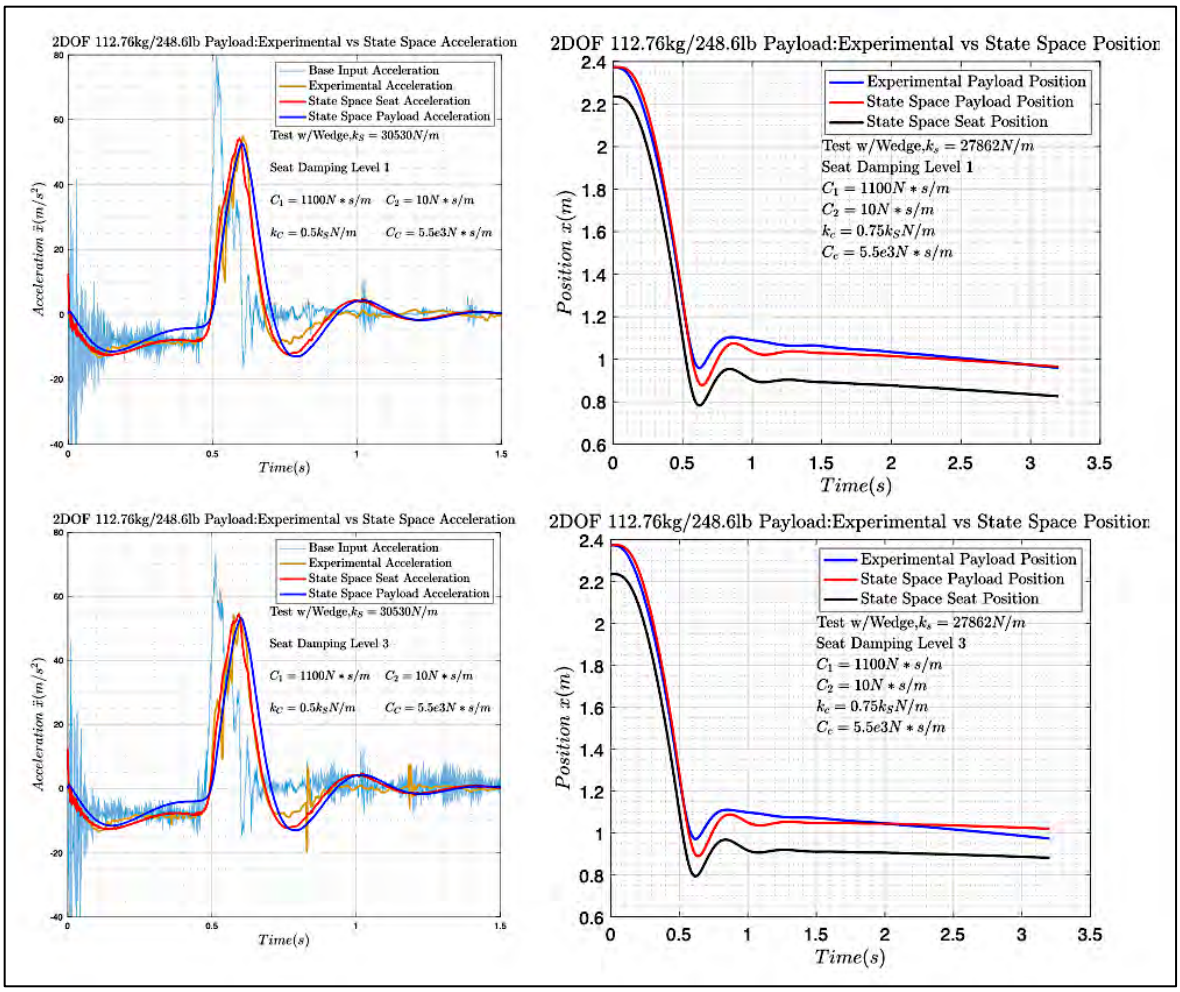

Figure C- 3: 2DOF 112.76kg/248.6lb Payload (W): SS Acceleration & Position Damping 1 and 3

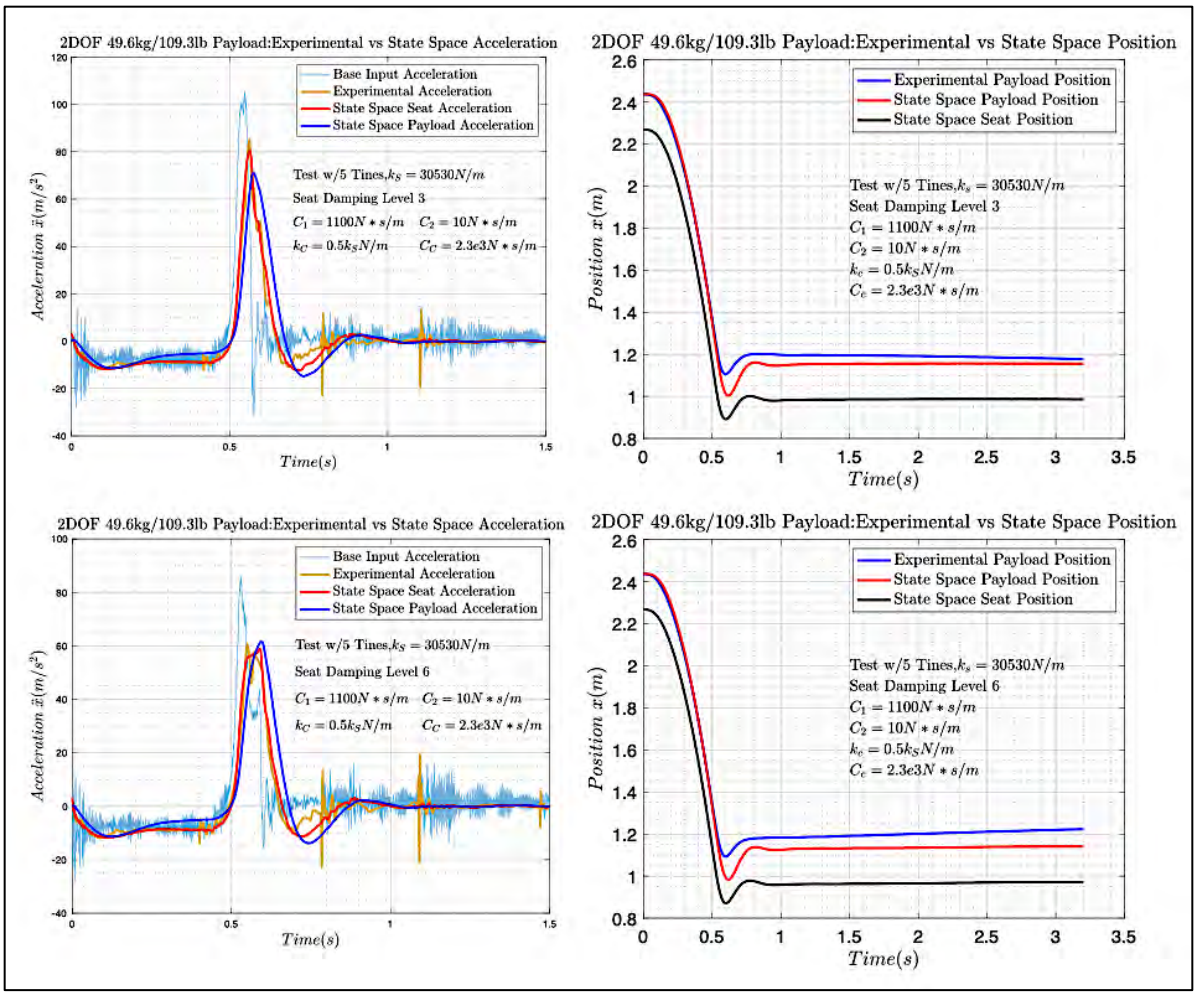

Figure C- 4: 2DOF 49.6kg/109.3lb Payload (T): SS Acceleration & Position Damping 3 and 6

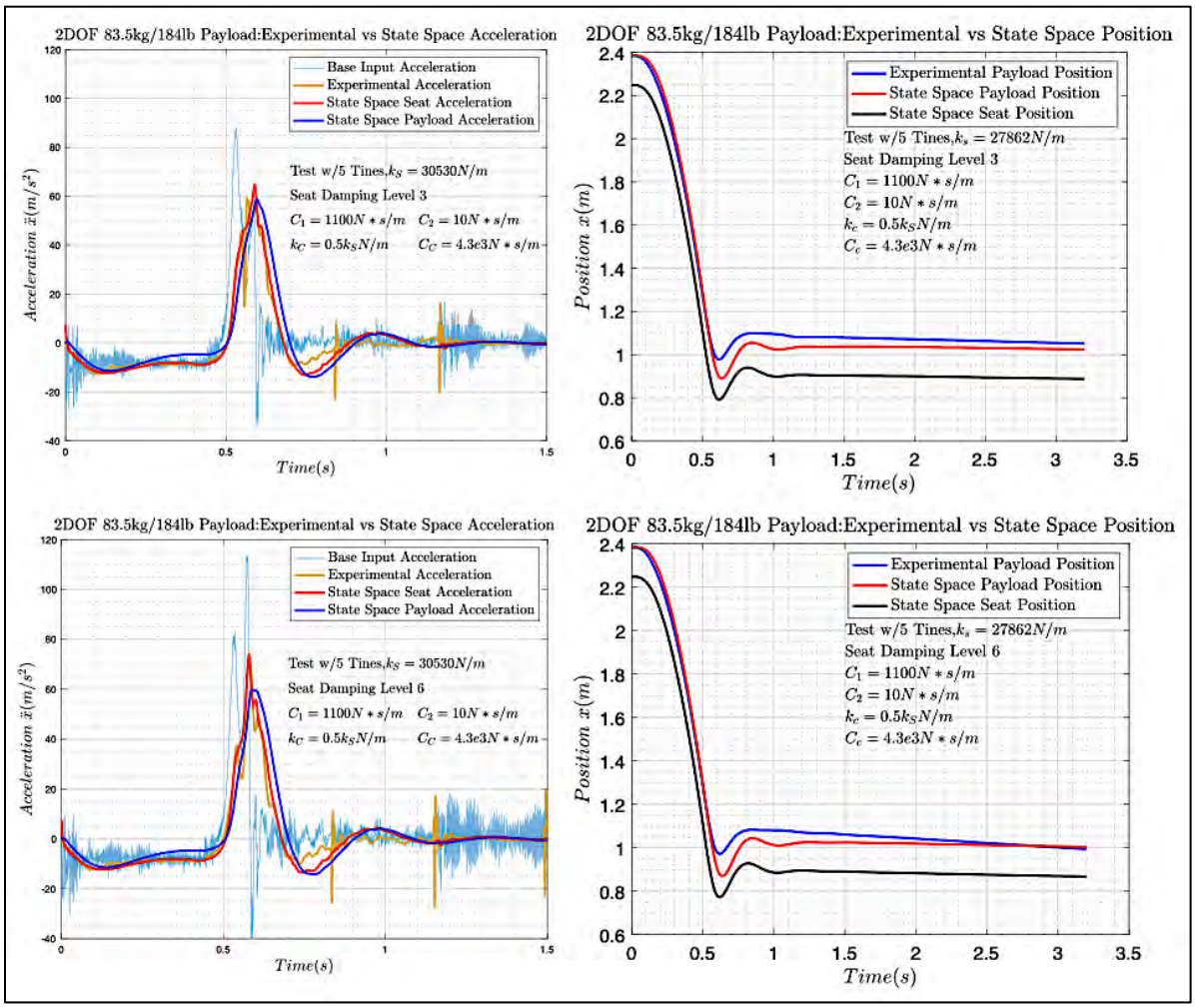

Figure C- 5: 2DOF 83.5kg/184lb Payload (T): SS Acceleration & Position Damping 3 and 6

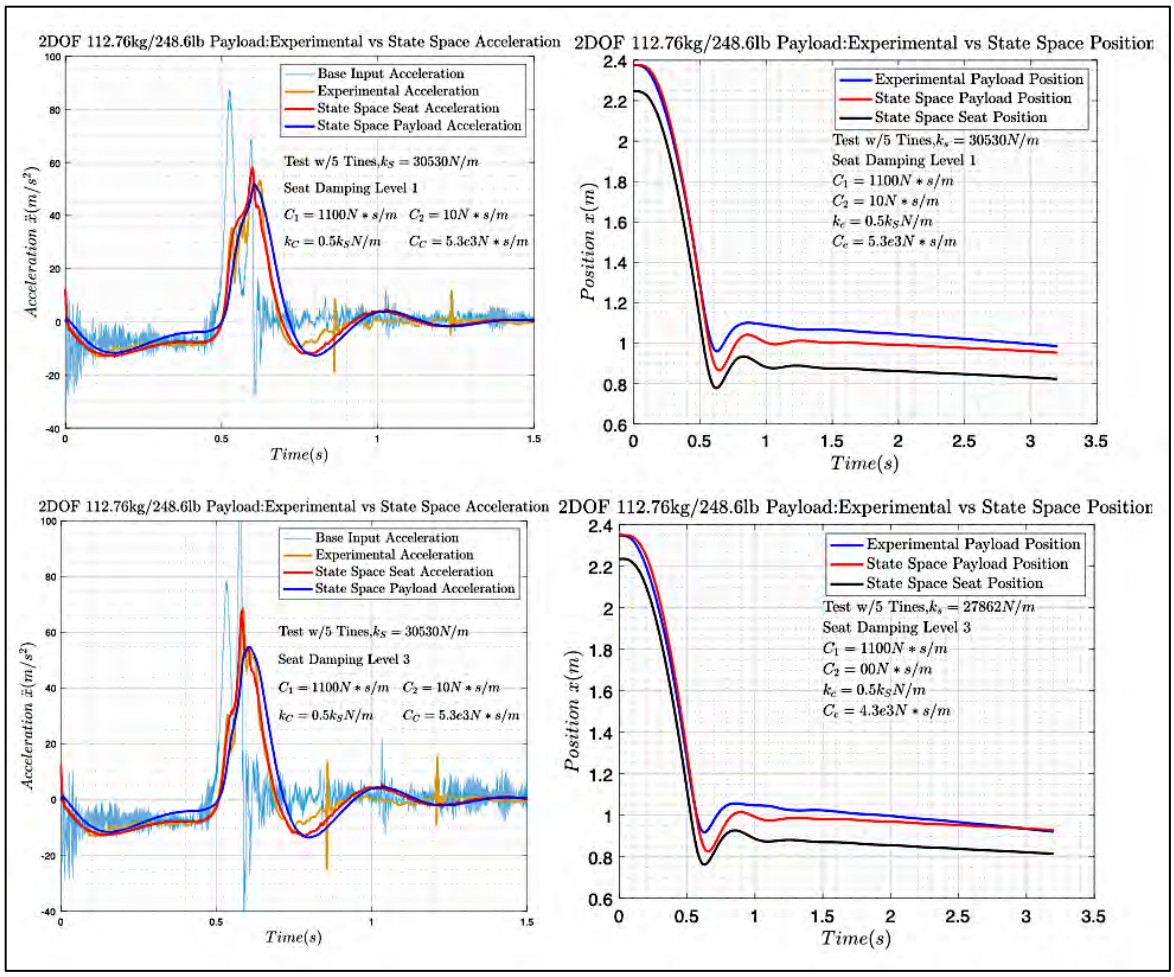

Figure C- 6: 2DOF 112.76kg/248.6lb Payload (T): SS Acceleration & Position Damping 1 and 3

Appendix D. Matlab Code

Single Degree of Freedom (SDOF) State Space Method

```
%Gravitational constant
g = 9.81; %m/s^2

%Mass(kg)
m_payload= 49.6;
m = 32.7+9.10+m_payload; %total mass held up by spring

% Restoring force
a1 = 27862;
a2 = 50.1821;
R = @(z)(a1*z + a2*z.^2);

% Uncompressed height between the base and base of the mass (m)
uncompressed_height = 0.721;

% init_spring_compression between the base and base of the mass (m)
z0 = fzero(@(z)(R(z)-m*g), m*g/a1);
init_spring_compression = z0;

data1 = readmatrix('Experimental Data');

% Time column
time_input = [data1(:, 1)];
t_idx = find(time_input(:,1)<3);

% Acceleration column
acceleration_input = [data1(:, 2)]*g;
idx1 = find(data1(:, 1)>2.5);
acceleration_input(:,1) = acceleration_input(:,1) - mean(acceleration_input(idx1,1));

acceleration_output = [data1(:, 3)]*g;
acceleration_output(:,1) = acceleration_output(:,1) -
mean(acceleration_output(idx1,1));

c_i0 = [2350 10];
c1 = c_i0(1);
c2 = c_i0(2);
c = @(zdot)(c1*zdot + c2*zdot.^2.*sign(zdot));


[t1, x1, x_accel1, y1, zdot1, zdot_accel1, xdotdot1, xdotdot_accel1, ydotdot1,Z_1] =
...
    doSimulation(time_input(:,1), acceleration_input(:,1), acceleration_output(:,1),
g, m, R, uncompressed_height,init_spring_compression, c1, c2);

------------------------------------------------------------------
-                     Plot code goes here                        -
------------------------------------------------------------------
function [t, x, x_accel, y_accel, zdot, zdot_accel, xdotdot,...
    xdotdot_accel, ydotdot_accel, Z] = doSimulation(time_input, acceleration_input,...
                                acceleration_output, g, m, R, uncompressed_height, ...
                                init_spring_compression, c1, c2)
c = @(zdot)(c1*zdot + c2*zdot.^2.*sign(zdot));
y_acc = @(t)(interp1(time_input, acceleration_input, t, 'pchip'));
x_acc = @(t)(interp1(time_input, acceleration_output, t, 'pchip'));
```

```
tspan = [time_input];

%Initial conditions
y0 = 1.397+0.17145;
x0 = y0 +  uncompressed_height - init_spring_compression;
Z0 = [x0-y0-uncompressed_height; 0; 0; y0; 0; x0];
[t,Z] = ode45(@(t,Z)calcZdot(t, Z, R, m, c1,c2, y_acc, x_acc, g), tspan, Z0);

x = Z(:,1)+Z(:,4)+uncompressed_height;
x_accel = Z(:,6);
y_accel = Z(:,4);
xdotdot = -R(Z(:,1))/m - c1*Z(:,2)/m - c2*(Z(:,2)+Z(:,3)).^2.*sign(Z(:,2)+Z(:,3))/m -
g; %simulated x acceleration
xdotdot_accel = x_acc(t); %experimental payload acceleration
ydotdot_accel = y_acc(t); %experimental platform acceleration
zdot = Z(:,2);  %simulated zdot
xdot_accel = Z(:,5); %experimental payload velocity
ydot = Z(:,3); %experimental platform velocity
zdot_accel = xdot_accel - ydot; %experimental zdot
end

function Zdot = calcZdot(t, Z, R, m, c1,c2, y_acc, x_acc, g)
    ydotdot = y_acc(t);
    Zdot = zeros(6,1);
    Zdot(1) = Z(2);
    Zdot(2) = -R(Z(1))/m - c1*Z(2)/m - c2*(Z(2)+Z(3))^2*sign(Z(2)+Z(3))/m - ydotdot -
g;
    Zdot(3) = ydotdot;
    Zdot(4) = Z(3);
    Zdot(5) = x_acc(t);
    Zdot(6) = Z(5);
end
```

Single Degree of Freedom (SDOF) Newmark-Beta Method

```
% Gravitational constant
g = 9.81; %m/s^2

% Mass (kg)
m_payload = 49.6;
m = 32.7+9.10+m_payload; %total mass held up by spring

% Restoring force constants
a1 =  30530;
a2 = -35160;
a3 = 7.7615e+04;

% Damping
c1 = 2350;
c2 = 50;

% Uncompressed height between the base and base of the mass (m)
uncompressed_height = 0.721;

% init_spring_compression between the base and base of the mass (m)
z0 = fzero(@(z)(a1*z + a2*z.^2 + a3*z.^3-m*g), m*g/a1);
init_spring_compression = z0;

data1 = readmatrix('Experimental Data');

% Time column
time = [data1(:, 1)];
t_idx = find(time(:,1)<3);

% Acceleration column
ydotdot = [data1(:, 2)]*g;
idx1 = find(data1(:, 1)>2.5);
ydotdot(:,1) = ydotdot(:,1) - mean(ydotdot(idx1,1));

xdotdot_accel = [data1(:, 3)]*g;
xdotdot_accel(:,1) = xdotdot_accel(:,1) - mean(xdotdot_accel(idx1,1));

%R function
R = @(z,zdot,ydot)(a2*z.^2+a3*z.^3 + c2*(zdot+ydot).^2.*sign(zdot+ydot));

%forcing function
f = @(ydotdot)(-m*ydotdot-m*g);


[t1, x1, x_accel1, y1, zdot1, zdot_accel1, xdotdot1, xdotdot_accel1, ydotdot1] = ...
    doSimulation(time(:,1), ydotdot(:,1), xdotdot_accel(:,1), g, m, R, f,
uncompressed_height,init_spring_compression, c1, a1);

------------------------------------------------------------------
-                     Plot code goes here                        -
------------------------------------------------------------------

function [time, x, x_accel, y_accel, zdot, zdot_accel, xdotdot,...
    xdotdot_accel, ydotdot_accel] = doSimulation(time, ydotdot,...
                                xdotdot_accel, g, m, R, f, uncompressed_height, ...
                                init_spring_compression, c1, a1)

% Initial conditions
y0 = 1.397+0.17145;
```

```
x0 = y0 +  uncompressed_height - init_spring_compression;
ydot = zeros(size(ydotdot(:,1)));
xdot_accel = zeros(size(xdotdot_accel(:,1)));
y = zeros(size(ydot));
x_accel = zeros(size(xdot_accel));
z = zeros(size(ydot));
zdot = zeros(size(ydot));
zdotdot = zeros(size(ydot));

y(1) = y0;
x_accel(1) = x0;
z(1) = -init_spring_compression;
zdotdot(1) = -ydotdot(1);
delta_Z = [0;0];

options = optimoptions('fsolve','Display','none', 'Algorithm', 'levenberg-marquardt');
for i = 1:length(time)-1
    dt = time(i+1)-time(i);

    y(i+1) = y(i) + dt*ydot(i) + dt^2*((1/4)*ydotdot(i) + (1/4)*ydotdot(i+1));
    ydot(i+1) = ydot(i) + dt*((1/2)*ydotdot(i) + (1/2)*ydotdot(i+1));

    x_accel(i+1) = x_accel(i) + dt*xdot_accel(i) + dt^2*((1/4)*xdotdot_accel(i) +
(1/4)*xdotdot_accel(i+1));
    xdot_accel(i+1) = xdot_accel(i) + dt*((1/2)*xdotdot_accel(i) +
(1/2)*xdotdot_accel(i+1));

    delta_Z = fsolve(@(delta_Z)calcResidual(delta_Z, m, c1, a1, R, f, zdotdot, zdot,
z, ydotdot, ydot, dt, i), delta_Z,options);
    delta_z = delta_Z(1);
    delta_zdot = delta_Z(2);

    z(i+1) = z(i) + delta_z;
    zdot(i+1) = -zdot(i) + (2/dt)*delta_z;
    zdotdot(i+1) = 4*delta_z/dt^2 - 4*zdot(i)/dt - zdotdot(i);
end %for i

x = z + y + uncompressed_height;
xdotdot = zdotdot + ydotdot;

ydotdot_accel = ydotdot;
y_accel = y;

zdot_accel = zdot;
end

function res = calcResidual(delta_Z, m, c1, a1, R, f, zdotdot, zdot, z, ydotdot, ydot,
dt, i)
delta_z = delta_Z(1);
delta_zdot = delta_Z(2);

LHS = (4*m/dt^2 + 2*c1/dt + a1)*delta_z;

delta_f = f(ydotdot(i+1)) - f(ydotdot(i));
delta_R = R(z(i)+delta_z, zdot(i)+delta_zdot, ydot(i+1)) - R(z(i), zdot(i), ydot(i));
RHS = delta_f - delta_R + 2*m*zdotdot(i) + (4*m/dt + 2*c1)*zdot(i);

res = LHS - RHS;
end
```

Two Degree of Freedom (2DOF) State Space Method

```
%Gravitational constant
g = 9.81; %m/s^2

% Mass (kg)
m_pay = 49.6;
m_seat = 17.6;

% Restoring force
a1 = 27862;
a2 = 50.1821;
R = @(z)(a1*z + a2*z.^2);

%Restoring force of cushion
k_cush = 0.5*a1;
R_cush = @(z_cush)(k_cush)*z_cush;


%Damping of cushion
c_cush = 1.5e3; %N-s/m

% Uncompressed height between the platform and the seat (m)
uncompressed_height = 0.721; %z_unstretched

uncompressed_cushion = 0.127; %z_cush_unstretched

% init_spring_compression between the base and base of the mass (m)
init_spring_compression = fzero(@(z)(R(z)-(m_seat+m_pay)*g), (m_seat+m_pay)*g/a1);

% init_cushion_compression between the seat and payload (m)
init_cushion_compression = fzero(@(z)(R_cush(z)- m_pay*g), 0.03);

data1 = readmatrix('Experimental Data');

% Time column
time_input = [data1(:, 1)];
t_idx = find(time_input(:,1)<3);

% Acceleration column
acceleration_input = [data1(:, 2)]*g;
idx1 = find(data1(:, 1)>1.6);
acceleration_input(:,1) = acceleration_input(:,1) - mean(acceleration_input(idx1,1));
acceleration_inputSmall = acceleration_input(t_idx, :);


acceleration_output = [data1(:, 3)]*g;
acceleration_output(:,1) = acceleration_output(:,1) -
mean(acceleration_output(idx1,1));
acceleration_outputSmall = acceleration_output(t_idx, :);

c_i0 = [2350 10];
c1 = c_i0(1);
c2 = c_i0(2);
c = @(zdot)(c1*zdot + c2*zdot.^2.*sign(zdot));
[t, x_pay, x_pay_accel, x_paydotdot, x_paydotdot_accel, xdotdot,x] = ...
    doSimulation(time_input(:,1), acceleration_input(:,1), acceleration_output(:,1),
g, m_seat, m_pay, R, R_cush, uncompressed_height, uncompressed_cushion, ...
                                init_spring_compression, init_cushion_compression, c1,
c2, c_cush);
```

```
%--------------------------------------------------------------------------
%                      Plot code goes here                                %
%--------------------------------------------------------------------------

function [t, x_pay, x_pay_accel, x_paydotdot, x_paydotdot_accel, xdotdot, x] =
doSimulation(time_input, acceleration_input,...
                                acceleration_output, g, m_seat, m_pay, R, R_cush,
uncompressed_height,uncompressed_cushion, ...
                                init_spring_compression, init_cushion_compression, c1,
c2, c_cush)
y_acc = @(t)(interp1(time_input, acceleration_input, t, 'pchip'));
x_pay_acc = @(t)(interp1(time_input, acceleration_output, t, 'pchip'));

tspan = [time_input];

% Initial Conditions
y0 = 1.397+0.17145;
x0 = y0 +  uncompressed_height - init_spring_compression;
 x_pay0 = x0 + uncompressed_cushion - init_cushion_compression;

Z0 = [x0-y0-uncompressed_height;... % z1 = z = x - y_accel - z_unstretched
    0;... %z2 = zdot = xdot - y_dot_accel
    0;... %z3 = y_dot_accel
    y0;... %z4 = y_accel
    x_pay0 - x0 - uncompressed_cushion;... %z5 = x_pay - x- z_cush_unstretched
    0;... %z6 = z_dot_pay
    0;... %z7 = x_pay_dot_accel
    x_pay0]; %z8 = x_pay_accel


[t,Z] = ode78(@(t,Z)calcZdot(t, Z, R, R_cush, m_seat, m_pay, c1,c2, c_cush, y_acc,
x_pay_acc, g), tspan, Z0);

x = Z(:,1)+Z(:,4)+uncompressed_height;
y_accel = Z(:,4);

x_pay = Z(:,5) + x + uncompressed_cushion;
x_pay_accel = Z(:,8);

xdotdot = -(c1/m_seat)*Z(:,2) - (c2/m_seat)*(Z(:,2)+Z(:,3)).^2.*sign(Z(:,2)+Z(:,3)) -
R(Z(:,1))/m_seat + R_cush(Z(:,5))/m_seat + (c_cush/m_seat)*Z(:,6) - g;
x_paydotdot = -R_cush(Z(:,5))/m_pay - (c_cush/m_pay)*Z(:,6) - g - (Z(:,2) + Z(:,3));

x_paydotdot_accel = x_pay_acc(t);

end

function Zdot = calcZdot(t, Z, R, R_cush, m_seat, m_pay, c1,c2, c_cush, y_acc,
x_pay_acc, g)
    ydotdot = y_acc(t);

    zdotdot = -(c1/m_seat)*Z(2) - (c2/m_seat)*(Z(2)+Z(3))^2*sign(Z(2)+Z(3)) -
R(Z(1))/m_seat + R_cush(Z(5))/m_seat + (c_cush/m_seat)*Z(6) - g - ydotdot;
        zpaydotdot = -R_cush(Z(5))/m_pay - (c_cush/m_pay)*Z(6) - g -
(zdotdot+ydotdot);

    Zdot = zeros(8,1);
    Zdot(1) = Z(2);
    Zdot(2) = zdotdot ;
    Zdot(3) = ydotdot;
    Zdot(4) = Z(3);
```

```
    Zdot(5) = Z(6);
    Zdot(6) = zpaydotdot;
    Zdot(7) = x_pay_acc(t);
    Zdot(8) = Z(7);
end
```

Appendix E. Tables for Test Procedure and Seat Acceleration

Table E- 1: Laboratory Test Procedure for Drop Tests

Laboratory Test Procedure for Drop Tests		
#	Action Item	Description
1	Set the Zero Offset	Before each official test session with the required payload, impacts were made on the platform (close to the lower accelerometer) at rest. Those impacts were used to set the zero offset for the accelerometers.
2	Set Seat Damping	Set the desired seat damping level to one, three, or six.
3	Set Drop Height	Raise the platform to the required drop height that corresponded with the desired severity threshold level. *Only one drop height was used in order to achieve the highest severity threshold.
4	Activate SignalCalc	Initiate the DAQ data collection sequence in the software.
5	Release Platform	The cable for the hoist was attached to the hoist frame on the platform with a quick release latch. The attached cord was pulled to release the platform.
6	Inspect/Export Data	The DAQ system was set to stop the data collection sequence after the platform came to a stop at the end of the free fall. Inspect the data to verify that the signal was captured and to ensure it was not corrupted. Archive/export data to secure drive.
7	Sensor/Cable Inspection	Visually inspect the accelerometers and cables to verify that there were no broken connections due to the drop.
8	Raise Platform	Raise the platform to a height at which the wedge (or tines) cleared the top edge of the sandbox.
9	Secure the Platform	The platform was secured with a safety chain attached to the outer frame, so in the event the hoist failed, the platform was supported by the chain and could not free fall into the sandbox.

#	Action Item	Description
10	Level Impact /Deformable Media	Rake the surface of the sand in preparation for the next drop test. Raking the sand prevented it from becoming compressed (and removed divots) between drops.
11	Raise platform	Remove the safety chain from the platform and raise the platform to the desired drop height, in preparation for the next drop.
12	Repeat	Repeat steps 2 through 11 three times for each payload weight at each desired severity threshold level.

Table E- 2: Mean Absolute Percent Error for 2DOF State Space Seat Acceleration

Mean Absolute Percent Error for 2DOF State Space Seat Acceleration						
Wedge: k_S = Seat spring , Cushion spring = 0.10 - 0.5 k_S						
Seat	49.6kg/109.3lb		83.5kg/184lb		112.76kg/248.6lb	
Damp	1100/10 (N-s/m)		1300/10 (N-s/m)		1300/10 (N-s/m)	
Level	27862 k_S (N/m)	30530 k_S (N/m)	27862 k_S (N/m)	30530 k_S (N/m)	27862 k_S (N/m)	30530 k_S (N/m)
1	329.32%	212.31%	256.73%	169.3%	207.87%	131.9%
3	664.06%	588.6%	325.47%	207.74%	208.73%	128.46%
6	187.52%	128.53%	598.19%	397.51%	133.46%	83.49%
Five Tines: k_S = Seat spring , Cushion spring = 0.10 - 0.5 k_S						
	49.6kg/109.3lb		83.5kg/184lb		112.76kg/248.6lb	
	1100/10 (N-s/m)		1300/10 (N-s/m)		1300/10 (N-s/m)	
	27862 k_S (N/m)	30530 k_S (N/m)	27862 k_S (N/m)	30530 k_S (N/m)	27862 k_S (N/m)	30530 k_S (N/m)
1	437%	279.1%	4520%	2837%	927.51%	581.28%
3	163.13%	98%	251.18%	154%	247.71%	170.1%
6	101.24%	63.46%	116.73%	79.74%	613.31%	376.86%

References

[1] Ensign, W., et al., “A Survey of Self-Reported Injuries Among Special Boat Operators,” Naval Health Research Center. Technical report No. 00-48.

[2] Riley, M. R., and Coats, T. W., “The Simulation of Wave Slam Impulses to Evaluate Shock Mitigation Seats for High-Speed Planing Craft,” NSWCCD-83-TM-2013/26, Naval Surface Warfare Center Carderock Division, May 2013.

[3] Pickford, E. V., et al., “Slam/Shock Isolation Pedestal,” US Patent: 3912248, United States Patent Office, Oct. 14, 1975.

[4] Coats, T., Haupt, K., and Lewis, J., “Shock Mitigation for personnel Onboard High-Speed Combatant Craft,” Naval Surface Warfare Center, Carderock Division, Norfolk Detachment, Combatant Craft Department.

[5] Bales, Susan L., “Designing Ships to the Natural Environment,” 19th Annual Technical Symposium 1982, Association of Scientists and Engineers, The Naval Sea Systems Command, pp. 14

[6] Riley, Michael R., et al., “Laboratory Test Requirements for Marine Shock Isolation Seats,” NSWCCD-80-TR-2015/010 Rev A, Naval Surface Warfare Center Carderock Division, June 2018.

[7] ISO/TC 108, ISO/WD 19470.6, “Laboratory evaluation of marine seat shock isolation,” Mechanical vibration, shock and condition monitoring, Subcommittee SC4, Human exposure to mechanical vibration and shock, Aug. 15, 2016.

[8] Eiband, M., “Human Tolerance to Rapidly Applied Accelerations: A Summary of the Literature,” NASA Memorandum, MEMO 5-19-59E, Lewis Research Center Cleveland, Ohio, Jun. 1959.

[9] Ilmari Karonen, “Mass-Spring-Damper,” PNG image, https://en.wikiversity.org/wiki/File:Mass-Spring-Damper.svg.

[10] Reed, W.H., et al., “UH-1B/D Armored Helicopter Seat Test Program,” USAAVSCOM Technical report 70-9, U.S. Army Aviation Systems Command St. Louis, Missouri, Feb. 1966.

[11] Kearns, Sean D., “Analysis and Mitigation of Mechanical Shock Effects on High-Speed Planing Boats,” Massachusetts Institute of Technology, Master of Science, Thesis, Sep. 2001

[12] AuCoin, C., “Shock mitigating seat single impact program,” Naval Engineering Test Establishment, Defence Research and Development Canada, Apr. 2014

[13] Gannon, L., “Single impact testing of suspension seats for high-speed craft,” Defence Research and Development Canada, Atlantic Research Centre, May 2017.

[14] Alam, Z., “Implementation of a Drop Test Impact Rig for Dynamic Testing of High-Speed Craft Shock Mitigation Seats and Extraction of Modal Parameters,” Carleton University, Master of Applied Science in Mechanical Engineering, Thesis, Sep. 2013.

[15] Liam, C., “Testing and Modeling of Shock Mitigating Seats for High-Speed Craft,” Virginia Polytechnic Institute and State University, Master of Science in Mechanical Engineering, Thesis, May 6, 2011.

[16] Wice, A., “Spatial Dynamic Modelling of High-Speed Craft Suspension Seating,” Carleton University Master of Applied Science in Mechanical Engineering, Thesis, Apr. 2015.

[17] Riley, Michael R., et al., “A Method to Quantify Mitigation Characteristics of Shock Isolation Seats Before Installation in a High-Speed Planing Craft,” Naval Surface Warfare Center, Carderock Division, Norfolk Detachment, Combatant Craft Division.

[18] ISO 2631-1, “Mechanical vibration, shock – Evaluation of human exposure to whole-body vibration – Part 1: General requirements,”, International Organization for Standardization, Second edition, Jul. 15, 1997.

[19] Ullman Dynamics Atlantic Crew Suspension Seat, https://ullmandynamics.com/suspension-seats/bolster-seats/atlantic-crew.

[20] Data Physics Dynamic Signal Analyzer, https://www.dataphysics.com/products/dynamic-signal-analyzers/.

[21] Dytran Instruments, https://www.dytran.com/Model-7500A1-High-Precision-MEMS-Accelerometer-P1381/

[22] Irvine, Tom, “Free Vibration of a Single-Degree-Of-Freedom System Revision B”, http://www.vibrationdata.com/tutorials.htm

[23] Reynolds, Douglas, ‘Engineering Principles of Mechanical Vibration’, 5th Edition. Trafford Publishing, 07/26/2019.

[24] Chopra, Anil K., ‘Dynamics of Structures Theory and Applications to Earthquake Engineering, Fourth Edition, Pearson Education Limited 2014.

[25] Irvine, Tom, “Response of a Single-Degree-Of-Freedom System Subjected to a Classical Pulse Base Excitation Revision A”, http://www.vibrationdata.com/tutorials.htm

[26] Irvine, Tom, “Simple Drop Shock Revision D”, November 10, 2004. http://www.vibrationdata.com/tutorials.htm

[27] Irvine, Tom, “An Introduction to Shock & Vibration Response Spectra”, https://enDAQ.com/pages/single-degree-of-freedom-systems-basic-concepts

[28] Geradin, M. and Rixen, D. J., ‘Mechanical Vibrations Theory and Application to Structural Dynamics’, Third Edition, John Wiley & Sons, Ltd .2015

[29] Gavin, Henri P., ‘Numerical Integration in Structural Dynamics’, CEE 541. Structural Dynamics. Department of Civil Engineering & Environmental Engineering, Duke University, Fall 2020.

[30] Irvine, T., https://www.mathworks.com/matlabcentral/fileexchange/127269-shock-response-spectrum-for-base-input-acceleration.

[31] https://www.mathworks.com/help/signal/ug/practical-introduction-to-shock-waveform-and-shock-response spectrum.html#mw_rtc_PracticalIntroToShockWaveformAndShockResponseSpectrumExample_M_7E1A38AA

[32] Smallwood, David O., 'An Improved Recursive Formula For Calculating Shock Response Spectra', Sandia National Laboratories, Albuquerque, New Mexico 87185, 1980

[33] Ahlin, Kjell,. 'Shock Response Spectrum Calculation-An Improvement of the Smallwood Algorithm', Ingemansson Technology, Box 47321, S-100 74 Stockholm, Sweden.

Curriculum Vitae

Darren Benn
Email: dibenn11@gmail.com

PROFESSIONAL EXPERIENCE

National Aeronautics and Space Administration (NASA 1)
Ames Research Center (ARC)
Aerospace Engineer/Systems Engineer
05/2020 - Present

Extensible Traffic Management (xTM)

- Supported ongoing development of xTM Systems Engineering Management Plan (SEMP) and ensured Systems Engineering (SE) practices were executed throughout the project lifecycle for xTM activities.
- Support development and management of SE processes (e.g., system requirements, system architecture design).

Vertical Motion Simulator (VMS)

- Simulation Engineer at ARC Vertical Motion Simulator (VMS).
- Support the development of IADS displays for ADS-33 tasks for the VMS.
- Simulation engineer on the Passenger Ride Quality simulation for a conceptual electric vertical takeoff and landing (eVTOL) quadrotor air taxi vehicle.

National Aeronautics and Space Administration (NASA 2)
Glenn Research Center (GRC)
Aerospace Engineer
04/2016 - 05/2020

Space Launch System (SLS)/Artemis Program

- Applied vibro-acoustic engineering theory for acoustic Statistical Energy Analysis (SEA) in support of the design and development of SLS Launch Vehicle Stage Adapter (LVSA) and Payload Fairing (PLF).
- Used NASTRAN Finite Element (FE) model of LVSA in acoustic software to create SEA structure, acoustic cavity, and applied external acoustic loads.
- Applied vibro-acoustic engineering theory for Finite Element Method (FEM) and Boundary Element Method (BEM) modeling, simulation, testing, and analysis in support of design and development of LVSA and PLF.

Hypersonic Technology Project: Combined Cycle Engine Large-scale Inlet Mode Transition (CCE-LIMX)

- Used WIND-US Computational Fluid Dynamics (CFD) analysis tool to explore the starting characteristics of streamline-traced inlets to help develop design methodology for internal supersonic diffusion for freestream flow with high Mach numbers. Development for inlet integration in Turbine Based Combine Cycle (TBCC) engine.

- Used WIND-US (CFD) to for grid generation and flow simulation to analyze the high-speed flow path and the shock-boundary layer interaction (SBLI) of the inlets that were designed with SUPIN.
- Used Supersonic Inlet Design and Analysis Tool (SUPIN®) to generate the geometry and perform the aerodynamic analysis for the design of 2D and Axisymmetric external compression supersonic inlets for Mach 2 to Mach 5.

National Aeronautics and Space Administration (NASA 3)
Armstrong Flight Research Center (AFRC)
Aerospace Engineer
10/2018 – 10/2019

Commercial Supersonic Technology (CST) Program

- Conducted specialized study to identify and support the development of trigger systems with system components that meet the requirements for an acoustic recording system for field deployment during Low-Boom Flight Demonstration (LBFD) Phase II & III test flights. Recommended implementing satellite communications as an acoustic trigger method, which was accepted and led to development of a Request for Information (RFI).
- Operated the Sonic Pressure Integrated Kit Electronics (SPIKE) field acoustic testing system to record sonic boom events during Carpet Determination In Entirety Measurements (CarpetDIEM) F-15 test flights at AFRC in support of the LBFD aircraft project.

United States Navy
Space and Warfare Systems (SPAWAR) Center Pacific
Mechanical Engineer
06/2015 – 04/2016

- Applied structural dynamics engineering theory to conduct forced vibration test and analysis on Maritime Systems and sub-components.

United States Air Force
99th Engineering Squadron, Nellis Air Force Base
Mechanical Engineer
03/2015 - 06/2015

- Applied structural dynamics engineering theory and concepts to solve mechanical engineering problems related to facilities management, general construction, and HVAC systems.

United States Air Force Reserves
926 AMX, Nellis Air Force Base
Knowledge Operations Specialist
10/2012 - 10/2014
305th Communication Squadron, McGuire Air Force Base
Cyber Operations-Client Systems
06/2002 – 06/2005

- Managed, sustained, and serviced standard voice, data, video network, and cryptographic client devices.
- Managed technologies and software to capture, organize and store tacit and explicit electronic records.

United States Army
Air Traffic Controller
05/1995 - 05/2000

- Applied air traffic control principles to aircraft operating in Class B, C, and D airspace at fixed based and tactical military installation airfields.

EDUCATION

University of Nevada Las Vegas, Las Vegas, NV United States
Doctor of Philosophy: Expected 05/2024
Major: Mechanical Engineering

University of Nevada Las Vegas, Las Vegas, NV
United States Master's Degree: 05/2015
Major: Mechanical Engineering
Minor: Aerospace Engineering

University of Nevada Las Vegas Las Vegas, NV United
States Bachelor's Degree: 05/2012
Major: Mechanical Engineering
Minor: Mathematics

DEFENSE ACQUISITION UNIVERSITY (DAWIA) CLASSES

- ACQ-101: Fundamentals of Systems Acquisition Management
- ENG-101: Fundamentals of System Engineering
- CLM-017: Risk Management
- CLE-004: Introduction to Lean Enterprise Concepts
- CLE-001: Value Engineering

SOFTWARE

- VA One®: Acoustic Modeling and Analysis
- WaveSix Vibro-Acoustic Analysis Software
- Pointwise®: Computational Fluid Dynamics (CFD) Grid Generation and Analysis
- Femap®: Finite Element Modeling and Analysis of Structural Systems
- Matlab®
- FieldView®: CFD Post-Processing, Visualization and Workflow Automation
- Comsol Multiphysics®: Finite Element based platform for modeling and simulating Multiphysics
- Tecplot-360®: CFD Visualization & Analysis Tool
- WIND-US®: Euler and Navier-Stokes Based Code for Turbulent and chemically reacting flows.
- Supersonic Inlet Design and Analysis Tool (SUPIN): Generates the geometry and performs the aerodynamic analysis for the design of supersonic inlets
- Thermal Desktop®: CAD-based thermal modeling and analysis tool

PROFESSIONAL PUBLICATIONS

- Co-authored paper with Dr. John Slater (NASA GRC-LTN) submitted to Joint Army-Navy-NASA-Air Force (JANNAF) Inter-agency Propulsion Committee Conference.
  Title: "AERODYNAMIC DESIGN OF HIGH-SPEED INLETS USING SUPIN"

PROFESSIONAL AFFILIATIONS

- American Society of Mechanical Engineers (ASME)
- American Institute of Aeronautics and Astronautics (AIAA)
- National Society of Black Engineers (NSBE)
- Member Tau Beta Pi Honor Society

PROFESSIONAL AWARDS

- NASA Aeronautics Research Mission Directorate Associate Administrator: Technology and Innovation Group Award for Quiet Supersonic Flight 2018
- NASA "Above & Beyond" Award for CFC campaign, 2017
- NASA Group Achievement Awards (2): MVF Commissioning and eSTA Environments Test Campaign, 2017
- U.S. Air Force Service Medal, Jun 2002
- U.S. Army Commendation Medal, Mar 2000
- Armed Forces Expeditionary Medal, 2000
- U.S. Army Achievement Medal (2), Jul 1998 and Jan 1999
- U.S. Army Good Conduct Medal, May 1998

LICENSE

State of Nevada Board of Professional Engineers and Land Surveyors
Engineering Intern (EI) Certificate #0T6623